SOHEIL MOHAMMADI

EXTENDED FINITE ELEMENT METHOD

Blackwell Publishing

EXTENDED FINITE ELEMENT METHOD

for Fracture Analysis of Structures

Soheil Mohammadi

School of Civil Engineering
University of Tehran
Tehran, Iran

Blackwell
Publishing

Published by Blackwell Publishing Ltd

Editorial offices:
Blackwell Publishing Ltd, 9600 Garsington Road, Oxford OX4 2DQ, UK
Tel: +44 (0) 1865 776868
Blackwell Publishing Inc., 350 Main Street, Malden, MA 02148-5020, USA
Tel: +1 781 388 8250
Blackwell Publishing Asia Pty Ltd, 550 Swanston Street, Carlton, Victoria 3053, Australia
Tel: +61 (0)3 8359 1011

First published 2008 by Blackwell Publishing Ltd

ISBN: 978-1-4051-7060-4

Library of Congress Cataloging-in-Publication Data

Mohammadi, Soheil.
Extended finite element method for fracture analysis of structures / Soheil Mohammadi.
p. cm.
Includes bibliographical references and index.
ISBN-13: 978-1-4051-7060-4 (hardback : alk. paper)
ISBN-10: 1-4051-7060-3 (hardback : alk. paper)
1. Fracture mechanics. 2. Finite element method. I. Title.
TA409.M65 2007
624.1′76–dc22
2007018717

A catalogue record for this title is available from the British Library

Typeset by Soheil Mohammadi
Printed and bound in Singapore
by Utopia Press Pte Ltd

The publisherís policy is to use permanent paper from mills that operate a sustainable forestry policy, and which has been manufactured from pulp processed using acid-free and elementary chlorine-free practices. Furthermore, the publisher ensures that the text paper and cover board used have met acceptable environmental accreditation standards.

For further information on Blackwell Publishing, visit our website:
www.blackwellpublishing.com/construction

Contents

To Mansoureh

Preface

'*I am always obliged to a person who has taught me a single word.*'

Progressive failure/fracture analysis of structures has been an active research topic for the past two decades. Historically, it has been addressed either within the framework of continuum computational plasticity and damage mechanics, or the discontinuous approach of fracture mechanics. The present form of linear elastic fracture mechanics (LEFM), with its roots a century old has since been successfully applied to various classical crack and defect problems. Nevertheless, it remains relatively limited to simple geometries and loading conditions, unless coupled with a powerful numerical tool such as the finite element method and meshless approaches.

The finite element method (FEM) has undoubtedly become the most popular and powerful analytical tool for studying a wide range of engineering and physical problems. Several general purpose finite element codes are now available and concepts of FEM are usually offered by all engineering departments in the form of postgraduate and even undergraduate courses. Singular elements, adaptive finite element procedures, and combined finite/discrete element methodologies have substantially contributed to the development and accuracy of fracture analysis of structures. Despite all achievements, the continuum basis of FEM remained a source of relative disadvantage for discontinuous fracture mechanics. After a few decades, a major breakthrough seems to have been made by the fundamental idea of partition of unity and in the form of the eXtended Finite Element Method (XFEM).

This book has been prepared primarily to introduce the concepts of the newly developed extended finite element method for fracture analysis of structures. An attempt has also been made to discuss the essential features of XFEM for other related engineering applications. The book can be divided into four parts. The first part is dedicated to the basic concepts and fundamental formulations of fracture mechanics. It covers discussions on classical problems of LEFM and their extension to elastoplastic fracture mechanics (EPFM). Issues related to the standard finite element modelling of fracture mechanics and the basics of popular singular finite elements are reviewed briefly.

The second part, which constitutes most of the book, is devoted to a detailed discussion on various aspects of XFEM. It begins by discussing fundamentals of partition of unity and basics of XFEM formulation in Chapter 3. Effects of various enrichment functions, such as crack tip, Heaviside and weak discontinuity enrichment functions are also investigated. Two commonly used level set and fast marching methods for tracking moving boundaries are explained before the chapter is concluded by examining a number of classical problems of fracture mechanics. The next chapter deals with the orthotropic fracture mechanics as an extension of XFEM for ever growing applications

of composite materials. A different set of enrichment functions for orthotropic media is presented, followed by a number of simulations of benchmark orthotropic problems. Chapter 5, devoted to simulation of cohesive cracks by XFEM, provides theoretical bases for cohesive crack models in fracture mechanics, classical FEM and XFEM. The snap-back response and the concept of critical crack path are studied by solving a number of classical cohesive crack problems.

The third part of the book (Chapter 6) provides basic information on new frontiers of application of XFEM. It begins with discussions on interface cracking, which include classical solutions from fracture mechanics and XFEM approximation. Application of XFEM for solving contact problems is explained and numerical issues are addressed. The important subject of dynamic fracture is then discussed by introducing classical formulations of fracture mechanics and the recently developed idea of time–space discretization by XFEM. New extensions of XFEM for very complex applications of multiscale and multiphase problems are explained briefly.

The final chapter explains a number of simple instructions, step-by-step procedures and algorithms for implementing an efficient XFEM. These simple guidelines, in combination with freely available XFEM source codes, can be used to further advance the existing XFEM capabilities.

This book is the result of an infinite number of brilliant research works in the field of computational mechanics for many years all over the world. I have tried to appropriately acknowledge the achievements of corresponding authors within the text, relevant figures, tables and formulae. I am much indebted to their outstanding research works and any unintentional shortcoming in sufficiently acknowledging them is sincerely regretted. Perhaps such a title should have become available earlier by one of the pioneers of the method, i.e. Professor T. Belytschko, a shining star in the universe of computational mechanics, Dr J. Dolbow, Dr N. Moës, Dr N. Sukumar and possibly others who introduced, contributed and developed most of the techniques.

I would like to extend my acknowledgement to Blackwell Publishing Limited, for facilitating the publication of the first book on XFEM; in particular N. Warnock-Smith, J. Burden, L. Alexander, A. Cohen and A. Hallam for helping me throughout the work. Also, I would like to express my sincere gratitude to my long-time friend, Professor A.R. Khoei, with whom I have had many discussions on various subjects of computational mechanics, including XFEM. Also my special thanks go to my students: Mr A. Asadpoure, to whom I owe most of Chapter 4, Mr S.H. Ebrahimi for solving isotropic examples in Chapter 3 and Mr A. Forghani for providing some of the results in Chapter 5.

This book has been completed on the eve of the new Persian year; a ‘temporal interface’ between winter and spring, and an indication of the beginning of a blooming season for XFEM, I hope.

Finally, I would like to express my gratitude to my family for their love, understanding and never-ending support. I have spent many hours on writing this book; hours that could have been devoted to my wife and little Sogol: the spring flowers that inspire the life.

Soheil Mohammadi
Tehran, Iran
Spring 2007

Nomenclature

α	Curvilinear coordinate
α_{c}	Load factor for cohesion
α_f, α_s	Thermal diffusivity of fluid and solid phases
β	Curvilinear coordinate
γ_s	Surface energy density
γ_s^{e}, γ_s^{p}	Elastic and plastic surface energies
γ_{xy}	Engineering shear strain
δ	Plastic crack tip zone
δ	Variation of a function
$\delta(\xi)$	Dirac delta function
δ_{ij}	Kronecker delta function
$\boldsymbol{\varepsilon}$	Strain tensor
$\boldsymbol{\varepsilon}_f$, $\boldsymbol{\varepsilon}_c$	Strain field at fine and coarse scales
ε_{ij}	Strain components
$\bar{\varepsilon}_{ij}$	Dimensionless angular geometric function
$\varepsilon_{ij}^{\mathrm{aux}}$	Auxiliary strain components
ε_v	Kinetic mobility coefficient
$\varepsilon_{\mathrm{yld}}$	Yield strain
η	Local curvilinear (mapping) coordinate system
θ	Crack propagation angle with respect to initial crack
θ	Angular polar coordinate
κ, κ'	Material parameters
λ	Lame modulus
λ	Eigenvalue of the characteristic equation
μ	Shear modulus
ν, ν_{ij}	Isotropic and orthotropic Poisson's ratios
ξ	Local curvilinear (mapping) coordinate system
$\xi(\mathbf{x})$	Distance function
ρ	Radius of curvature
ρ	Density
ρ_f, ρ_c	Density of fine and coarse scales
ρ_{int}	Curvature of the propagating interface
$\boldsymbol{\sigma}$	Stress tensor
$\boldsymbol{\sigma}_f$, $\boldsymbol{\sigma}_c$	Stress field at fine and coarse scales
$\boldsymbol{\sigma}_g$	Stress tensor at a Gauss point
$\boldsymbol{\sigma}_t^{\mathrm{tip}}$	Normal tensile stress at crack tip
σ_0	Applied normal traction

σ_{cr}	Critical stress for cracking
σ_{ij}	Stress components
$\bar{\sigma}_{ij}$	Dimensionless angular geometric function
$\sigma_{ij}^{\mathrm{aux}}$	Auxiliary stress components
σ_{n}	Stress component normal to an interface
σ_{n}	Stress component at time step n
σ_{yld}	Yield stress
$\boldsymbol{\tau}$	Deviatoric stress
τ_0	Applied tangential traction
τ_{c}	Cohesive shear traction
τ_{n}	Time functions
τ_n	Deviatoric stress tensor at time step n
$\phi(\mathbf{x})$	Level set function
$\phi(z)$	Complex stress function
$\phi_{\mathrm{s}}(z)$	Stress function for shear problem
φ	Angle of orthotropic axes
φ	Phase angle for interface fracture
$\chi(\mathbf{x})$	Enrichment function for weak discontinuities
$\chi(z)$	Stress function
$\boldsymbol{\psi}(\mathbf{x})$	Enrichment function
$\boldsymbol{\psi}(z)$	Stress function
ω	Oscillation index
Γ	Boundary
Γ_{c}	Crack boundary
Γ_{t}	Traction (natural) boundary
Γ_{u}	Displacement (essential) boundary
Δ	Finite variation of a function
Λ	Coefficient matrix
$\boldsymbol{\Xi}$	Homogenisation/average operator
Π	Potential energy
$\Phi_j(\mathbf{x})$	Moving least squares shape functions
$\Phi(\mathbf{x})$	Stress function
Ω	Domain
Ω_f, Ω_c	Fine and course scale domains
Ω_f, Ω_s	Fluid and solid domains
Ω_{pu}	Domain associated with the partition of unity
a	Crack length/half length
a	Semi-major axis of ellipse
a^{b}, a^{f}	Backward and forward indexes in fast marching method
$\mathbf{a}_h$	Heaviside enrichment degrees of freedom
$\mathbf{a}_i$	Enrichment degrees of freedom
$\mathbf{a}_k$	Enrichment degrees of freedom
A^*	Area associated with the domain J integral
b	Width of a plate
b	Semi-minor axis of ellipse
$\mathbf{b}_i$	Crack tip enrichment degrees of freedom

$\mathbf{B}$	Matrix of derivatives of shape functions
$\mathbf{B}^h$	Matrix of derivatives of final shape functions
$\mathbf{B}_c$	**B** matrix for coarse scale
$\mathbf{B}_f$	**B** matrix for fine scale
$\mathbf{B}_i^r$	Strain–displacement matrix (derivatives of shape functions)
$\mathbf{B}_i^{\mathbf{u}}$	Strain–displacement matrix (derivatives of shape functions)
$\mathbf{B}_i^{\mathbf{a}}$	Matrix of derivatives of enrichment (Heaviside) of shape functions
$\mathbf{B}_i^{\mathbf{b}}$	Matrix of derivatives of enrichment (crack tip) of shape functions
c	Constant parameter
c	Size of crack tip contour for J integral
c_{ij}	Material constants
c_{R}	Rayleigh speed
c_f, c_s	Specific heat for fluid and solid phases
C	Material constitutive matrix
d	Distance
$\mathrm{d}/\mathrm{d}t$	Time derivative
$\mathbf{D}$	Material modulus matrix
$\mathbf{D}_c, \mathbf{D}_f$	Material modulus in coarse and fine scales
$\mathbf{D}_{\mathrm{loc}}$	Localisation modulus
$\mathrm{D}/\mathrm{D}t$	Material time derivative
$D_x^{\mathrm{b}}, D_x^{\mathrm{f}}$	Backward and forward finite difference approximations
E, E_i	Isotropic and orthotropic Young's modulus
E'	Material parameter
f_{t}	Uniaxial tensile strength
$f(r)$	Radial function
$\mathbf{f}$	Nodal force vector
$\mathbf{f}_i^r$	Nodal force components (classic and enriched)
$\mathbf{f}^{\mathrm{b}}$	Body force vector
$\mathbf{f}^{\mathrm{t}}$	External traction vector
$\mathbf{f}^{\mathrm{c}}$	Cohesive crack traction vector
$\mathbf{f}^{\mathrm{coh}}$	Cohesive nodal force vector
$\mathbf{f}^{\mathrm{ext}}$	External force vector
$\mathbf{f}_{\mathbf{u}}^{\mathrm{int}}$	Internal nodal force vector due to external loading
$\mathbf{f}_{\mathbf{a}}^{\mathrm{int}}$	Internal nodal force vector due to cohesive force
$F_l^i(x)$	Crack tip enrichment functions
$\mathbf{g}$	Applied gravitational body force
$g(\theta)$	Angular function for a crack tip kink problem
$g_j(\theta)$	Orthotropic crack tip enrichment functions
G	Shear modulus
G	Fracture energy release rate
G_1, G_2	Mode I and II fracture energy release rates
$G_{\mathrm{I}}^{\mathrm{dyn}}$	Dynamic mode I fracture energy release
$H(\xi)$	Heaviside function
H_{l}	Latent heat
i	Complex number, $i^2 = -1$
$\mathbf{J}$	Jacobian matrix
J	J integral

J^{act}	Actual J integral
J^{aux}	Auxiliary J integral
J_k	Mode k contour integral J
k_0	Dimensionless constant for the power hardening law
k_0, k_1, k_2, k_3, k_4	Constant coefficients
k_i	Conductivity coefficient for phase i
k_s, k_f	Thermal conductivity for solid and fluid phases
$k_{\text{n}}, k_{\text{t}}$	Normal/tangential interface properties
$\mathbf{K}$	Stiffness matrix
$\mathbf{K}_{\text{hom}}$	Homogenised stiffness matrix
$\mathbf{K}_{ij}^{rs}$	Stiffness matrix components
K	Stress intensity factor
K_{C}	Critical stress intensity factor
K_{eq}	Equivalent mixed mode stress intensity factor
$K_{\text{I}}, K_{\text{II}}, K_{\text{III}}$	Mode I , II and III stress intensity factors
$\bar{K}_{\text{I}}, \bar{K}_{\text{II}}$	Normalized mode I and mode II stress intensity factors
$K_{\text{I}}^{\text{aux}}, K_{\text{II}}^{\text{aux}}$	Auxiliary mode I and mode II stress intensity factors
$K_{\text{Ic}}, K_{\text{IIc}}$	Critical mode I and mode II stress intensity factors
$K_{\text{I}}^{\text{cohesion}}$	Cohesive mode I stress intensity factor
$K_{\text{I}}^{\text{crack}}$	Crack mode I stress intensity factor
$K_{\text{I}}^{\text{dyn}}$	Dynamic mode I stress intensity factor
l_e	Characteristic length
l_c	Characteristic length for crack propagaion
m	Number of enrichment functions
mt_{i}	Number of nodes to be enriched by crack tip enrichment functions
mf	Number of crack tip enrichment functions
M_j	Mach number
M	Interaction integral
M_0	Total mass
M_i	Lumped mass component
$\mathbf{M}_{ij}$	Mass matrix component
n	Power number for the plastic model (Section 2.6.4)
ng	Number of Gauss points
$\bar{n}$	Number of nodes within each moving least squares support domain
np	Number of independent domains of partition of unity
n_n	Number of nodes in a finite element
$\mathbf{n}$	Normal vector
$\mathbf{n}_{int}$	Normal vector to an internal interface
$\mathbf{N}_j$	Matrix of shape functions
N_j	Shape function
$\bar{N}_j$	New set of generalised finite element method shape functions
$p(\mathbf{x})$	Basis function
p	Hydrostatic pressure
$\bar{p}$	Predefined hydrostatic pressure
P_i	Loading condition i
q	Arbitrary smoothing function
q	Heat flux

q_i	Nodal values of the arbitrary smoothing function
Q	Input heat to system
$\mathbf{Q}_{ij}$	Matrix of homogenous anisotropic solids
r	Radial distance/coordinate
r_g	Radial distance of a Gauss point from crack tip
r_p	Crack tip plastic zone
R	Ramp function
s_f, s_s	Heat source for fluid and solid phases
S_a	Set of accepted nodes
S_c	Set of candidate nodes
S_d	Set of distant nodes
t	Time
$\mathbf{t}$	Traction
$\mathbf{t}^{\mathrm{int}}$	Surface traction along internal boundary
T	Temperature
T_f, T_s	Temperature of fluid and solid phases
$T_i(t)$	Time shape functions
T_m	Melting/fusion temperature
$\mathbf{u}$	Displacement vector
$\hat{\mathbf{u}}$	Local symmetric displacement vector
$\dot{\mathbf{u}}$	Velocity vector
$\bar{\mathbf{u}}$	Prescribed displacement
$\bar{\dot{\mathbf{u}}}$	Prescribed velocity
$\ddot{\mathbf{u}}$	Acceleration vector
$\mathbf{u}_i^{\mathrm{aux}}$	Auxiliary displacement field
$\mathbf{u}^{\mathrm{coh}}$	Displacement field obtained from crack surface tractions
$\mathbf{u}^{\mathrm{enr}}$	Enriched displacement field
$\mathbf{u}^{\mathrm{FE}}$	Classical finite element displacement field
$\mathbf{u}^h(\mathbf{x})$	Approximated displacement field
$\bar{\mathbf{u}}_j$	Nodal displacement vector
$\tilde{\mathbf{u}}_j$	Transformed displacement
u_p	Periodic displacement
u_x, u_y	$x$and y displacement component
U^1, U^2	Symmetric and antisymmetric crack tip displacements
U_k	Kinetic energy
U_s	Strain energy
U_s^e, U_s^p	Elastic and plastic strain energies
U_Γ	Surface energy
$\mathbf{v}$	Velocity vector
$\bar{\mathbf{v}}$	Prescribed velocity
$\mathbf{v}_n$	Normal interface speed
v_1, v_2	Longitudinal and shear wave velocities
$\mathbf{V}(t)$	Vector of approximated velocity degrees of freedom
w	Crack opening
w_c	Critical crack opening
W	External work
W^{aux}	Auxiliary work

W^{coh}	Virtual work of cohesive force
W^{ext}	Virtual work of external loading
W_g	Gauss weight factor
W_g^{r}	Radial weight function at a Gauss point g
W^{int}	Internal virtual work
W^{M}	Interaction work
W_{s}	Strain energy
$W_t(t)$	Time weight function
$\mathbf{x}$	Position vector
$\mathbf{x}_c, \mathbf{x}_f$	Position vector for coarse and fine scales
$\mathbf{x}_\Gamma$	Position of projection point on an interface
x_1, x_2	Two-dimensional coordinate system
x'	Local crack tip coordinate axes
y'	Local crack tip coordinate axes
$z = x + iy$	Complex variable
$\bar{z} = x - iy$	Conjugate complex variable
z_i	Complex parameters
f', f''	First and second derivative of a function
$\bar{f}$, $\bar{\bar{f}}$	First and second integrals of a function
$\nabla = {}^{\partial}/_{\partial x}$	Nabla operator
$\langle\,\rangle$	Jump operator across an interface
BEM	Boundary Element Method
CBS	Characteristic Based Split
COD	Crack Opening Displacement
CTOD	Crack Tip Opening Displacement
DCT	Displacement Correlation Technique
DOF	Degree Of Freedom
EDI	Equivalent Domain Integral
EFG	Element-Free Galerkin
ELM	Equilibrium On Line
EPFM	Elastic Plastic Fracture Mechanics
FDM	Finite Difference Method
FE	Finite Element
FEM	Finite Element Method
FMM	Fast Marching Method
FPM	Finite Point Method
FPZ	Fracture Process Zone
GFEM	Generalised Finite Element Method
HRR	Hutchinson–Rice–Rosengren
LEFM	Linear Elastic Fracture Mechanics
LSM	Level Set Method
MCC	Modified Crack Closure
MEPU	Multiscale Enrichment Partition of Unity
MLPG	Meshless Local Petrov–Galerkin
MLS	Moving Least Squares

NURBS	Non-Uniform Rational B-Spline
OUM	Ordered Upwind Method
PU	Partition of Unity
PUFEM	Partition of Unity Finite Element Method
RKPM	Reproducing Kernel Particle Method
SAR	Statically Admissible stress Recovery
SIF	Stress Intensity Factor
SPH	Smoothed Particle Hydrodynamics
TFEM	Time Finite Element Method
TXFEM	Time eXtended Finite Element Method
WLS	Weighted Least Squares
XFEM, X-FEM	eXtended Finite Element Method

Chapter 1

Introduction

1.1 ANALYSIS OF STRUCTURES

The finite element method (FEM) has undoubtedly become the most popular and powerful analytical tool for studying the behaviour of a wide range of engineering and physical problems. Several general purpose finite element softwares have been developed, verified and calibrated over the years and are now available to almost anyone who asks and pays for them. Furthermore, concepts of FEM are usually offered by all engineering departments in the form of postgraduate and even undergraduate courses.

One of the important applications of FEM is the analysis of crack propagation problems. Fundamentals of the present form of the linear elastic fracture mechanics (LEFM) came to the existence practically in naval laboratories during the First World War. Since then, LEFM has been successfully applied to various classical crack and defect problems, but remained relatively limited to simple geometries and loading conditions.

Introduction and fast development of the finite element method drastically changed the extent of application of LEFM. FEM virtually had no limitation in solving complex geometries and loading conditions, and soon it was extended to nonlinear materials and large deformation problems (Zienkiewicz *et al.* 2005). As a result, LEFM could now rely on a powerful analytical tool in order to determine its fundamental concepts and governing criteria such as the crack energy release rate and the stress intensity factor for any complex problem. General LEFM stability criteria could then be used to assess the stability/propagation of an existing crack.

Application of FEM into linear elastic fracture mechanics and its extension to elastic plastic fracture mechanics (EPFM) has now expanded to almost all crack problems. Parametric studies and experimental observations have even resulted in the introduction of new design codes for containing a stable crack. However, the essence of analyses remained almost unchanged: LEFM basic concepts combined with classical continuum based FEM techniques through smeared or discrete crack models.

After a few decades, a major breakthrough seemed to be evolving in the fundamental idea of partition of unity and in the form of the eXtended Finite Element Method (X-FEM or XFEM).

1.2 ANALYSIS OF DISCONTINUITIES

Progressive failure/fracture analysis of structures has been an active subject of research for many years. Historically, it was addressed either within the framework of continuum mechanics, including computational plasticity and damage mechanics, or the discontinuous approach of fracture mechanics (Owen and Hinton 1980).

These methods, however, are applied to fundamentally different classes of failure problems. While the theory of plasticity and damage mechanics are basically designed for problems where the displacement field and usually the strain field remain continuous everywhere (continuous problems), fracture mechanics is essentially formulated to deal with strong discontinuities (cracks) where both the displacement and strain fields are discontinuous across a crack surface (Fig. 1.1) (Mohammadi 2003).

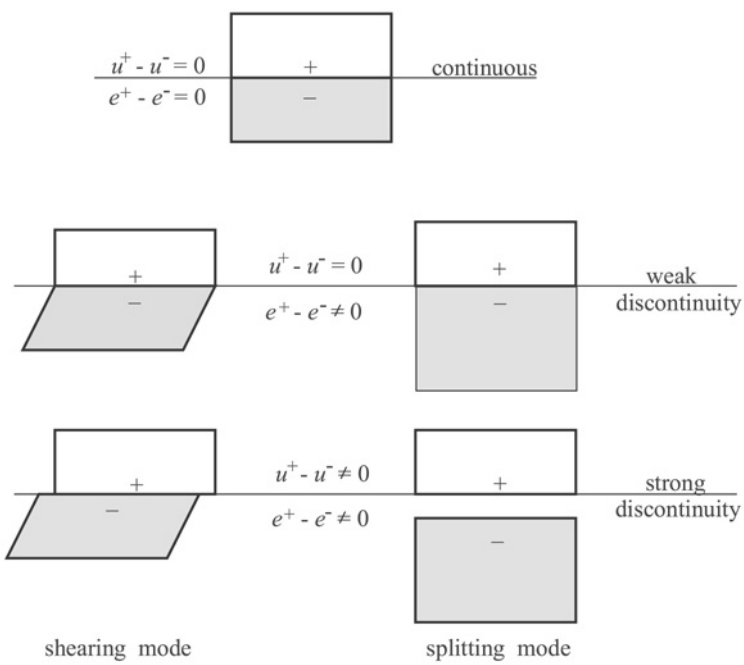

Figure 1.1 Different categories of continuities.

In practice, fracture mechanics is also used for weak discontinuity problems, and both damage mechanics and the theory of plasticity have been modified and adapted for failure/fracture analysis of structures with strong discontinuities. It is, therefore, difficult to distinguish between the practical engineering applications exclusively associated with each class of analytical methods.

Inclusion of some basic concepts from fracture mechanics such as non-local models, energy release rate, softening models in combination with adaptive remeshing techniques have allowed for successful simulations of crack problems with a certain level of accuracy.

1.3 FRACTURE MECHANICS

Fundamental concepts of fracture mechanics can be traced back to the late nineteenth and early twentieth centuries. Both experimental observations and theoretical elasticity helped to create the fundamental aspects of the theory of fracture mechanics. Major differences between the theoretical prediction of tensile strength in brittle materials and the experimentally measured one was explained by the assumption of existing minute flaws and defects; predicting drastic changes in the distribution of the stress field around each flaw, regardless of its actual size.

Introduction of the fundamental concepts of stress intensity factor, energy release rate, etc. changed the way a crack problem used to be analysed. Theoretical studies proved that even for the case of a small tiny circular hole inside an infinite tensile plate, a tensile stress concentration factor of 3 is predictable at a point adjacent to the hole, and in addition, generation of a compressive stress field for the infinite tensile plate is also anticipated.

Global (non-local) energy based methods were gradually developed and solutions for classical problems were also obtained. Energy based methods allowed the classical fracture mechanics to be extended to nonlinear problems. Introduction of the J integral was a major breakthrough that allowed powerful numerical methods such as the finite element method to be efficiently used for determining the necessary fields and variables. Future developments benefited greatly from this joint approach; basic formulations from fracture mechanics to assess the stability of cracks, and the analytical tool from the finite element method to allow simulation of problems with arbitrary geometries, boundary conditions and loadings.

1.4 CRACK MODELLING

Various methods have been developed over the years for simulation of the problems involved with creation and propagation of cracks. Analytical, semi-analytical and numerical approaches, such as the boundary integral method, the boundary element method, the finite element method and recently a number of meshless methods, have been successfully used for modelling cracks; each one provides advantages and drawbacks in handling certain parts of the simulation. Although the same concepts can be more or less applied to many numerical methods, the emphasis in this book is only put on the finite element method as a basis for its extension to the extended finite element method.

Crack simulation in the finite element method has been performed by a number of methods. They include the continuous smeared crack model and several discontinuous approaches such as the discrete inter-element crack model, the discrete crack model and the discrete element based model. Recently a new class has been proposed that simulates the singular nature of discrete models within a geometrically continuous mesh of finite elements. The extended finite element method has emerged from this class of problems, and is based on the concept of partition of unity for enriching the classical finite element approximation to include the effects of singular or discontinuous fields around a crack.

1.4.1 Local and non-local models

Early attempts to simulate crack problems by the finite element method adopted a simple plasticity based FEM. The algorithm was to check the stress state at the integration points against a material strength criterion, similar to hardening plasticity problems except for a negative hardening modulus to account for the softening effects of cracking. The behaviour of a point was only affected by its own stress state (point 1 in Fig. 1.2).

However, it was soon realised that such local results may become mesh dependent and unreliable. The conclusion was that the cracking could not solely be regarded as a local point-wise stress based criterion, and non-local models had to be adopted.

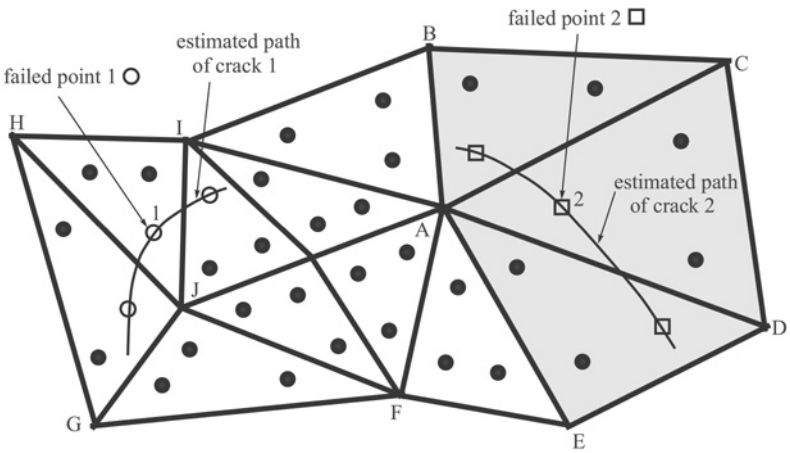

Figure 1.2 Local and non-local evaluation of stress state.

Then, non-local models were proposed to avoid mesh dependency of the plasticity based solutions for simulating crack problems (Bazant and Planas 1997). To clarify the basic idea, consider the simple case of point 2 in Fig. 1.2, where the fracture behaviour of each point is determined from a non-local criterion expressed in terms of the state variables at that point and a number of surrounding points.

1.4.2 Smeared crack model

The smeared crack model has been frequently used in the finite element simulation of fracture and crack propagation problems. Rather than trying to geometrically model a crack, the smeared crack model simulates the mechanical effects of the crack in terms of stiffness or strength reduction. It is in fact a continuous approach for a discontinuous/singular problem. In this model, the discontinuity caused by a discrete crack within an element is simulated by a distributed (smeared) equivalent field over the entire domain of the element, as depicted in Fig. 1.3a (Owen and Hinton 1980). The main advantage of the method is that it does not require any local or global remeshing in the process of crack propagation.

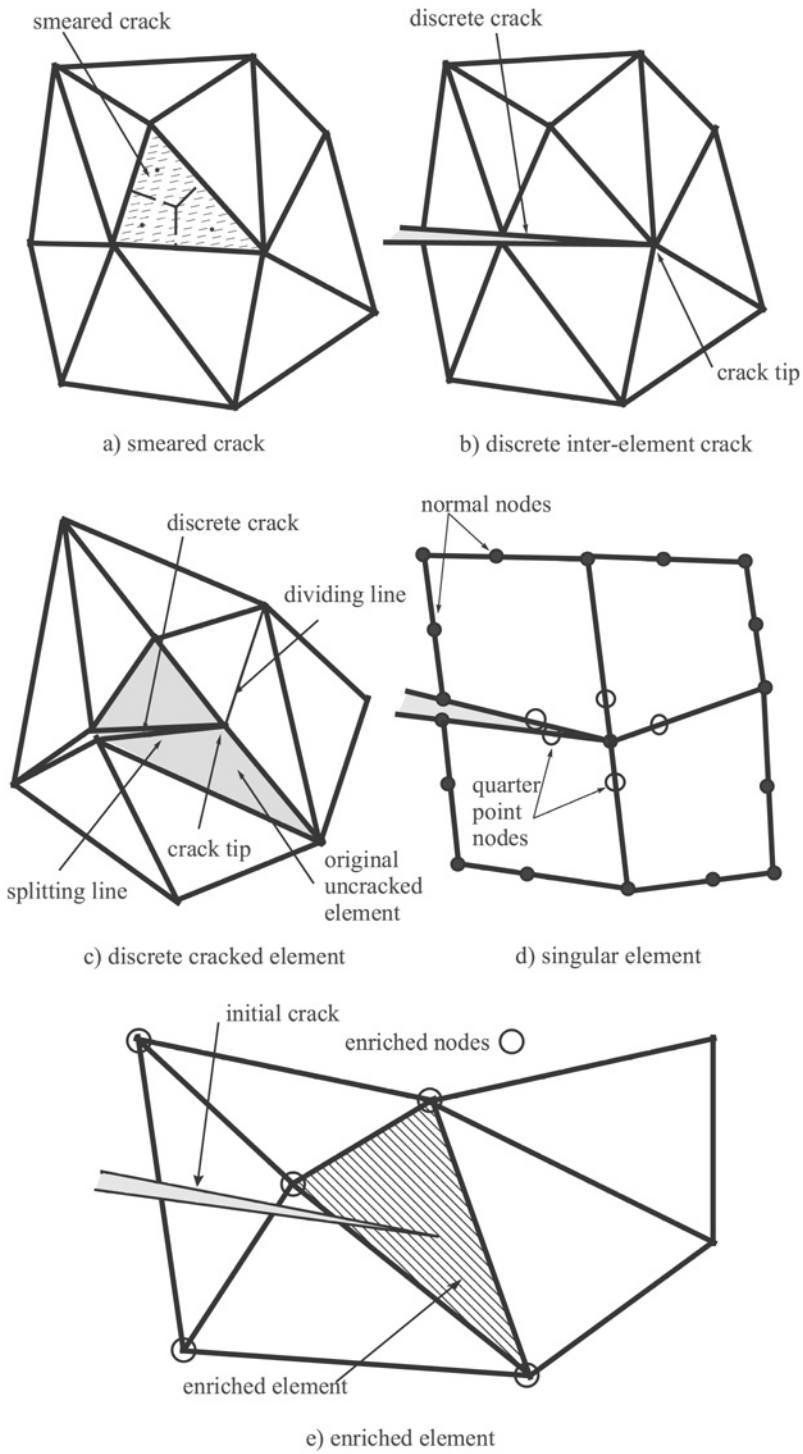

Figure 1.3 Different models for simulation of a crack.

1.4.3 Discrete inter-element crack

In this approach, existing cracks are simply defined along the finite element edges (Fig. 1.3b). The strong discontinuity is then automatically assumed in the displacement field across the crack. However, it cannot account for the singular field around the crack tip, unless special singular finite elements are used. The model is extremely simple for predefined existing crack paths along the element edges, however, it becomes rather difficult for modelling general crack propagation paths as it requires a remeshing of the model. It also dramatically increases the risk of mesh dependency.

1.4.4 Discrete cracked element

This model is an improvement on the inter-element discrete crack model, as it allows for cracks to be defined or propagated inside the finite elements. Fig. 1.3c illustrates a model in which the crack path is through the middle of a finite element. A local remeshing technique combined with adaptivity methods have to be adopted to create a new mesh by splitting the cracked element and dividing adjacent elements to ensure compatibility of the neighbouring finite elements. Adaptivity techniques are applied to compute the state variables within the newly created elements from the state variables of their parent elements.

A class of combined finite/discrete element procedures have been successfully developed in the past decade for simulation of progressive fracturing due to impact and explosive loadings. They may also take into account the effects of post-cracking interactions, including fully nonlinear frictional behaviour (Mohammadi 2003).

The method is clearly very expensive as it requires time-consuming algorithms for cracking, remeshing and contact detection/interactions every time a new crack or body is created or each time a new potential contact is anticipated. A remedy is to avoid remeshing of the whole model by gradual local remeshing and updating techniques according to the advancement of cracks.

1.4.5 Singular elements

In a major development, singular finite elements were developed for simulating crack tip singular fields. They provide major advantages; the model is simply constructed by moving the nearby midside nodes to the quarter points – absolutely no other changes in the finite element formulation are required (Fig. 1.3d). The use of these elements has considerably upgraded the level of accuracy obtained by the finite element method for simulation of crack tip fields (Owen and Fawkes 1983). Prior to the development of XFEM, singular elements have been the most popular approach for fracture analysis of structures.

Singular elements, however, lacked the capability of modelling discontinuity across a crack path. As a result, they had to be used with one of the other preceding methods to simulate the crack path.

1.4.6 Enriched elements

In this model, the singular or discontinuous displacement field within a finite element is simulated by a special set of enriched shape functions that allow for accurate approximation of the displacement field. Fig. 1.3e illustrates a model in which the crack path is through the middle of a finite element. Presence of the crack is not geometrically modelled and the mesh does not need to conform to the crack path. Additional enrichment approximation is added to the classical finite element model to account for the effects of a crack or discontinuity (Moës *et al.* 1999).

The main advantage of the method is that it does not require any remeshing in the process of crack propagation. By advancement of the crack tip location or any change in its path due to loading conditions, the method automatically determines the elements around the crack path/tip and generates necessary enrichment functions for the associated finite elements or nodal points accordingly.

Locations of initial cracks or potential propagation paths do not affect the way the initial finite element model is constructed. Multiple cracking and intersecting cracks can be similarly simulated by the same finite element mesh with comparable levels of accuracy.

1.5 ALTERNATIVE TECHNIQUES

The finite element method has been widely used for fracture analysis of structures for many years. Its earlier disadvantages have been avoided by the development of new ideas and techniques and it has now become a mature powerful approach for the analysis of many engineering and physical problems. Nevertheless, alternative methods, such as various classes of meshless methods, are increasingly being adopted.

Meshless methods have developed significantly in the last decade. The element-free Galerkin method (EFG) (Belytschko *et al.* 1994), meshless local Petrov–Galerkin (MLPG) (Atluri and Shen 2002), smoothed particle hydrodynamics (SPH) (Belytschko *et al.* 1996), finite point method (FPM) (Onate *et al.* 1995), reproducing kernel particle method (RKPM) (Liu *et al.* 1996), HP-clouds (Duarte and Oden 1995), equilibrium on line method (ELM) (Sadeghirad and Mohammadi 2007) and many other meshless methods have been used for failure and fracture analysis of structures. Discussion on these techniques is out of the scope of this book. Nevertheless, they share similar ideas and many parts of the present discussion, methodology and formulation on enrichment techniques can be extended to meshless methods and other numerical techniques.

1.6 A REVIEW OF XFEM APPLICATIONS

1.6.1 General aspects of XFEM

The basic ideas and the mathematical foundation of the partition of unity finite element method (PUFEM) were discussed by Melenk and Babuska (1996) and Duarte and Oden

(1996). Later Belytschko and Black (1999) presented a minimal remeshing finite element method by adding discontinuous enrichment functions to the finite element approximation to account for the presence of a crack. The method was then improved by Moës *et al.* (1999) and Dolbow (1999) and called the eXtended Finite Element Method (XFEM). The new methodology allowed for the entire crack to be represented independently of the mesh and constructed the enriched approximation from the interaction of the crack geometry with the mesh.

More contributions from Dolbow *et al.* (2000a, 2000b, 2000c), Daux *et al.* (2000) and Sukumar *et al.* (2000) extended the method for three-dimensional crack modelling and arbitrary branched and intersecting cracks.

The use of level set methods to represent the crack location was studied by Stolarska *et al.* (2001), Belytschko *et al.* (2001), Sukumar *et al.* (2001), Moës *et al.* (2002), Gravouil *et al.* (2002), Ventura *et al.* (2003), Zi *et al.* (2004), Budyn *et al.* (2004), Bordas and Moran (2006), and Stolarska and Chopp (2003). Alternatively, Sukumar *et al.* (2003a) and Chopp and Sukumar (2003) combined XFEM with the fast marching method (FMM).

1.6.2 Localisation and fracture

Apart from earlier works that were directed towards the development of the extended finite element method for linear elastic fracture mechanics (LEFM), simulation of localisation and fracture has been the main target. Jirásek and Zimmermann (2001a, 2001b) successfully combined XFEM with the damage theory and advocated a new concept of a model with transition from a smeared to an embedded discrete crack. Sukumar *et al.* (2003b) presented a two-dimensional numerical model of micro-structural effects in brittle fracture, while Dumstorff and Meschke (2003) and Patzak and Jirásek (2003) proposed an extended finite element model for the analysis of brittle materials in the post-cracking regime. In a fundamentally different approach, Ventura *et al.* (2005) proposed a new extended finite element method for accurately modelling the displacement and stress fields produced by a dislocation.

Simulation of growth of arbitrary cohesive cracks by XFEM was reported by Moës and Belytschko (2002a). The method was further advanced by Zi and Belytschko (2003), Mariani and Perego (2003) and Mergheim *et al.* (2005). A proper representation of the discrete character of cohesive zone formulations by the so called cohesive crack segments was proposed by de Borst *et al.* (2004a, 2004b, 2004c).

In order to develop a methodology for modelling shear bands as strong discontinuities within a continuum mechanics context, Samaniego and Belytschko (2005) and Areias and Belytschko (2006) used the enrichment ideas of XFEM. Later, Song *et al.* (2006) presented a new method for modelling of arbitrary dynamic crack and shear band propagation by a rearrangement of the extended finite element basis and the nodal degrees of freedom, describing the discontinuity superposed elements and the new concept of phantom nodes.

The idea of elastic plastic enrichments was also proposed by Elguedj *et al.* (2006) based on the Ramberg–Osgood power hardening rule and Hutchinson–Rice–Rosengren

elastoplastic fields for representing the singularities in elastic plastic fracture mechanics (EPFM).

1.6.3 Composites

Fracture of composite structures constitutes a major part of recent studies related to LEFM and EPFM. Dolbow and Nadeau (2002) employed the extended finite element method to simulate fracture behaviour of micro-structured materials with a focus on functionally graded materials. Then, Dolbow and Gosz (2002) described a new interaction energy integral method for the computation of mixed mode stress intensity factors at the tips of arbitrarily oriented cracks in functionally graded materials. In a related contribution, Remmers *et al.* (2003) presented a new formulation for the simulation of delamination growth in thin-layered composite structures.

Study of bimaterial interface cracks was performed by Sukumar *et al*. (2004) by developing partition of unity enrichment techniques. Nagashima *et al.* (2003) and Nagashima and Suemasu (2004) described the application of XFEM to stress analyses of structures containing interface cracks between dissimilar materials.

To include the effects of anisotropy on the enrichment functions, Asadpoure *et al.* (2006, 2007), and Asadpoure and Mohammadi (2007) developed three independent sets of orthotropic enrichment functions for XFEM analysis of crack in orthotropic media.

1.6.4 Contact

Dolbow *et al.* (2000c, 2001) further extended the XFEM methodology for modelling of crack growth with frictional contact on the crack faces. The subject of contact mechanics was also revisited by Belytschko *et al.* (2002a). Recently, Khoei and Nikbakht (2006) applied the extended finite element method to modelling frictional contact problems, while Shamloo *et al*. (2005), Khoei *et al.* (2006a, 2006b) presented new computational techniques based on XFEM in elastoplastic behaviour of pressure-sensitive material for powder compaction problems.

1.6.5 Dynamics

Belytschko *et al.* (2003) developed a methodology for switching from a continuum to a discrete discontinuity where the governing partial differential equation loses hyperbolicity for rate independent materials. Then, Belytschko and Chen (2004) developed a singular enrichment finite element method for elastodynamic crack propagation. Réthoré *et al*. (2005a) proposed a generalisation of XFEM to model dynamic fracture and time-dependent problems, while Zi *et al.* (2005) presented a method for modelling arbitrary growth of dynamic cracks without remeshing. Menouillard *et al.* (2006) introduced a lumped mass matrix for enriched elements, which enabled a pure explicit formulation to be used in XFEM applications.

In interesting reports, Chessa and Belytschko (2004, 2006) presented an enriched finite element method with arbitrary discontinuities in space-time. A combined space–time extended finite element method was proposed by Réthoré *et al.* (2005b), based on the idea of using a time partition of the unity method, and it was denoted the Time eXtended Finite Element Method (TXFEM).

1.6.6 Large deformation/shells

Dolbow and Devan (2004) presented a geometrically nonlinear assumed strain XFEM. Legrain *et al.* (2005) focused on the application of XFEM to large strain fracture mechanics for plane stress problems such as rubber-like materials, and Fagerström and Larsson (2006) presented a general finite element approach for the modelling of fracture for the geometrically nonlinear case.

A new XFEM formulation for the nonlinear analysis of arbitrary crack propagation in enhanced strain four-node shells was developed by Areias and Belytschko (2005a). Areias *et al.* (2006) extended the methodology for evolution of cracks in thin shells.

1.6.7 Multiscale

Multiscale analysis was also the target of Moës *et al.* (2003) who used the extended finite element method to solve scales involving complex geometries in a multiscale analysis of components. Peters *et al.* (2004) used an XFEM to study the transition from microscale damage phenomena to crack initiation and growth at the macroscale which constrains the lifetime of concrete structures. Mariano and Stazi (2004) analysed the interaction between a macrocrack and a population of microcracks by adapting XFEM to a multifield model of microcracked bodies. Later, Fish and Yuan (2005) proposed a new multiscale enrichment approach based on the partition of unity method (MEPU). It was a synthesis of mathematical homogenisation theory and the partition of unity method.

1.6.8 Multiphase/solidification

Wagner *et al.* (2001, 2003) described a new method for the simulation of particulate flows, based on the extended finite element method. The finite element basis was enriched with the Stokes flow solution for flow past a single particle and the lubrication theory solution for flow between particles.

Chessa amd Belytschko (2003a, 2003b) applied the extended finite element method with arbitrary interior discontinuous gradients to two-phase immiscible flow problems. Lin *et al*. (2005) and Gutierrez and Bermejo (2005) presented a numerical method for free surface flows that coupled the incompressible Navier–Stokes equations with the level set method in the finite element framework.

Multi-dimensional Stefan (solidification) problems were analysed by Chessa *et al.* (2002) using an enriched finite element method. Alternatively, Ji *et al.* (2002) presented a hybrid numerical method for modelling the evolution of sharp phase interfaces on fixed

grids, where the temperature field evolves according to classical heat conduction in two subdomains separated by a moving freezing front.

Ji and Dolbow (2004) and Dolbow *et al.* (2004, 2005) considered the problem of chemically induced volume phase transitions in stimulus-responsive hydrogels, wherein a sharp interface separates swelled and collapsed phases of the underlying polymer network. Alternatively, Chen *et al.* (2004) presented a coupled finite element/level set method for incompressible multiphase flows.

Modelling of multiphase materials by XEFM was performed by Hettich and Ramm (2006) and Ji *et al.* (2006), as well as Zabaras *et al.* (2006) who modelled dendrite solidification with melt convection using the extended finite element method.

1.7 SCOPE OF THE BOOK

This text is dedicated to discussing the basic ideas and formulation for the newly developed extended finite element method. Although the main goal has been set to study the application of XFEM for fracture analysis of structures, other major applications will also be considered. Therefore, in addition to fully covering the subject of fracture mechanics, an attempt has been made to introduce and address the essential features of other advanced topics related to XFEM.

The book is designed as a textbook, beginning with the basic ideas in simple one-dimensional problems, and then moving towards the general formulation for two- (and sometimes three-) dimensional problems. In order to provide a view on the wide extent of applications of XFEM, the present chapter has briefly reviewed various engineering and physical applications of XFEM, without going into detail.

Chapter 2 provides a review of fracture mechanics, which quickly reviews the basic concepts and fundamental formulations but does not provide proofs or details. Stress intensity factors, energy release rate and the J contour integral are explained and issues associated with classical finite element computations are addressed. The chapter begins with an introduction to the basics of the theory of elasticity, and is followed by a discussion on classical problems of LEFM. The same concepts are then extended to elastoplastic problems; elastoplastic fracture mechanics (EPFM). The chapter briefly reviews issues related to the finite element modelling of fracture mechanics and describes the basic formulation of popular singular finite elements. It also addresses the numerical procedures required for evaluation of the J integral, energy release rate and the stress intensity factor based on classical and singular finite elements.

Chapter 3 constitutes the main chapter of the book. It covers the formulation and implementation of XFEM, and discusses various aspects of the approach. Concepts of the partition of unity and the generalised finite element are explained, and there is a discussion on the enrichment models. Both the intrinsic and extrinsic enrichment techniques are described in detail. The extended finite element method, as a special case of local partition of unity finite element method with extrinsic enrichment, is further studied by introduction of crack tip enrichment functions. Effects of various Heaviside enrichment functions to allow for modelling discontinuous fields across a crack are also investigated. A relatively comprehensive discussion on two commonly used level set and fast marching methods for tracking moving boundaries are also provided. The chapter

concludes by examining a number of classical two-dimensional isotropic problems of fracture mechanics.

The next chapter (Chapter 4) deals with orthotropic fracture mechanics, which is important for ever growing applications of composite materials. First, the basics of anisotropic elasticity and anisotropic fracture mechanics are reviewed. Then, three different sets of enrichment functions for orthotropic media are explained. Solutions of a number of available problems of orthotropic composites are provided which also include a comprehensive sensitivity analysis of various parameters.

Chapter 5 is devoted to simulation of cohesive cracks by XFEM. It provides theoretical bases for cohesive crack models in fracture mechanics and classical finite element simulations. Then, the appropriate types of XFEM enrichments that are consistent with cohesive cracks are discussed. The snap-back behaviour, which is one of the possible modes of response in cohesive crack problems, and the concept of critical crack path are studied by solving a number of classical cohesive crack problems.

New frontiers of application of XFEM are described in Chapter 6. It begins with discussions on interface cracking, including classical solutions from fracture mechanics and the XFEM approximation. Application of XFEM for solving problems involved with contacts between two bodies is explained and numerical issues are addressed. The next section is devoted to the important subject of dynamic fracture. It starts with classical formulations of fracture mechanics and ends with the very recently developed idea of time-space discretization by XFEM. Implementation of XFEM for the very complex applications of multiscale and multiphase problems is briefly explained.

The final chapter (Chapter 7) discusses general algorithms for implementing an efficient XFEM. It provides a number of simple instructions and step-by-step procedures, based on the discussions provided in Chapters 3, 4, 5 and 6 for a wide range of engineering applications. These simple guidelines, in combination with other freely available XFEM source codes can be used to further advance the existing XFEM capabilities, and to provide a launching pad for future improvements and developments.

Chapter 2

Fracture Mechanics, a Review

2.1 INTRODUCTION

Experimental observations have shown that brittle materials tend to fracture when loaded beyond their critical stress level. It is, therefore, commonly accepted that the strength of a material to resist fracture is in fact its inherent property. This fact has resulted in a series of criteria in many design codes to ensure that the maximum stress a structure is to experience does not exceed its critical fracture stress strength (Bazant and Planas 1997).

However, experimental observations have proved that the fracture strength does depend on a number of other factors, such as the testing setup, environmental conditions and dimensions of the specimens. For example, Evans and Marathe (1968) demonstrated that the tensile strength of coal specimens, in addition to being a material property, was inversely proportional to the thickness t of specimens; $t^{-\alpha}$, where $\alpha = 0.23$.

This is also the case in predicting the strength of materials, where the theoretical strength of an ideal brittle material is estimated to be $E/10$, while the experimentally measured strength is of the order of $E/100 - E/1000$. The fracture strength is related to the specific surface energy rather than to the tensile strength of the material.

From an historic point of view, Griffith (1921, 1924) was the first to realise that the presence of internal cracks and flaws had a significant role to play in the initiation and propagation of fracture and it explained the reason for much lower tensile strength of brittle materials than the theoretical predictions. He succeeded in establishing a relationship between the fracture strength and the crack size; marking the start of the modern fracture mechanics. He derived a criterion for fracture in terms of the total change in energy during cracking.

Griffith's theory was based on the earlier works of Kirsch and Kolosoff (Meguid 1989) and Inglis (1913) who solved the problem of infinite tensile plate with circular and elliptical holes, respectively. Kirsch showed that the maximum stress around a hole is three times the applied traction, a terminology for the stress concentration factor 3. A solution for a sharp crack problem can then be obtained by degeneration of the elliptical hole into a straight line crack. A different approach was used by Westergaard (1939) to derive solutions for the stress field near a sharp crack tip.

Another major extension was to include nonlinear effects. Irwin (1957, 1958, 1960) and Irwin *et al.* (1958) extended Griffith's theory to include yielding at the crack tip, and

introduced the concept of stress intensity factor (SIF) and energy release rate, *G*. The concept of crack opening displacement (COD) was utilised by Wells (1963) as a crack strength parameter for elastoplastic analysis.

Introduction of the concept of the *J* integral by Rice (1968, 1988), Rice and Rosengren (1968) and Rice and Levy (1972) opened the way for general finite element solutions of complex fracture mechanics problems decades later. The *J* integral was defined as a path independent contour integral equal to the rate of change of the potential energy for an elastic nonlinear solid during a unit crack extension.

The finite element method (FEM) has been widely used in various problems of fracture mechanics. FEM was originally used as a simple analytical tool for obtaining the continuum based displacement and stress fields. Later, sophisticated singular elements were proposed by Barsoum (1974, 1975, 1976a, 1976b, 1977, 1981) and Henshell and Shaw (1975) and efficiently implemented by Fawkes *et al.* (1979) and Owen and Fawkes (1983) to simulate the singularity condition at crack tips. Then, it was extensively adopted as a major improvement to already available numerical techniques in LEFM.

FEM has the advantage of including various models of plasticity and large deformations, whereas classical fracture mechanics is not capable of this. In a major setback, however, Bazant, in a series of studies, proved that classical continuum mechanics and strength of materials would lead to mesh dependent results unless the concepts of fracture mechanics were embedded within the solution (Bazant and Planas 1997).

Development of the meshless methods such as the element-free Galerkin method (EFG) (Belytschko *et al.* 1994), meshless local Petrov–Galerkin (MLPG) (Atluri and Shen 2002), smoothed particle hydrodynamics (SPH) (Belytschko *et al.* 1996) and the extended finite element method (XFEM) (Dolbow *et al.* 2000b) has provided new advanced analytical tools, and a surge of revisiting the problems of fracture mechanics.

This chapter briefly reviews the basic concepts of fracture mechanics for linear and nonlinear analyses. It is not intended to be a comprehensive discussion on all related topics. Instead, the goal has been set to provide the theoretical basics and a quick review of the main topics as a precursor to the main subject of the book, XFEM for fracture analysis of structures.

2.2 BASICS OF ELASTICITY

2.2.1 Stress–strain relations

In the seventeenth century, Hooke proposed his fundamental stress–strain relationship for one-dimensional linear elastic materials:

$$\sigma = E\varepsilon \tag{2.1}$$

where σ and ε are unidirectional stress and strain, respectively, and E is the elasticity (Young's) modulus. The generalised Hooke's law can be written as:

$$\boldsymbol{\sigma} = \mathbf{D}\boldsymbol{\varepsilon} \tag{2.2}$$

or in indicial form,

$$\sigma_{ij} = D_{ijkl}\varepsilon_{kl} \tag{2.3}$$

The symmetry property of both $\boldsymbol{\sigma}$ and $\boldsymbol{\varepsilon}$ reduces the number of constants of the fourth order elastic tensor, D_{ijkl}, from 81 components to only 36 independent terms.

Hooke's law for isotropic materials can be written as:

$$\sigma_{ij} = \frac{E}{1+\nu}\left(\varepsilon_{ij} + \frac{\nu}{1-2\nu}\delta_{ij}\varepsilon_{kk}\right) \tag{2.4}$$

and in the form of strain–stress relations:

$$\varepsilon_{ij} = \frac{1+\nu}{E}\sigma_{ij} - \frac{\nu}{E}\delta_{ij}\sigma_{kk} \tag{2.5}$$

where δ_{ij} is the Kronecker delta function.

The expanded form for 3D isotropic materials can then be written as:

$$\begin{Bmatrix} \varepsilon_{xx} \\ \varepsilon_{yy} \\ \varepsilon_{zz} \\ \varepsilon_{xy} \\ \varepsilon_{yz} \\ \varepsilon_{zx} \end{Bmatrix} = \frac{1}{E}\begin{bmatrix} 1 & -\nu & -\nu & 0 & 0 & 0 \\ -\nu & 1 & -\nu & 0 & 0 & 0 \\ -\nu & -\nu & 1 & 0 & 0 & 0 \\ 0 & 0 & 0 & 1+\nu & 0 & 0 \\ 0 & 0 & 0 & 0 & 1+\nu & 0 \\ 0 & 0 & 0 & 0 & 0 & 1+\nu \end{bmatrix}\begin{Bmatrix} \sigma_{xx} \\ \sigma_{yy} \\ \sigma_{zz} \\ \sigma_{xy} \\ \sigma_{yz} \\ \sigma_{zx} \end{Bmatrix} \tag{2.6}$$

or

$$\begin{Bmatrix} \sigma_{xx} \\ \sigma_{yy} \\ \sigma_{zz} \\ \sigma_{xy} \\ \sigma_{yz} \\ \sigma_{zx} \end{Bmatrix} = \begin{bmatrix} \lambda+2\mu & \lambda & \lambda & 0 & 0 & 0 \\ \lambda & \lambda+2\mu & \lambda & 0 & 0 & 0 \\ \lambda & \lambda & \lambda+2\mu & 0 & 0 & 0 \\ 0 & 0 & 0 & \mu & 0 & 0 \\ 0 & 0 & 0 & 0 & \mu & 0 \\ 0 & 0 & 0 & 0 & 0 & \mu \end{bmatrix}\begin{Bmatrix} \varepsilon_{xx} \\ \varepsilon_{yy} \\ \varepsilon_{zz} \\ \varepsilon_{xy} \\ \varepsilon_{yz} \\ \varepsilon_{zx} \end{Bmatrix} \tag{2.7}$$

where λ and μ are the Lame and shear modules, defined as:

$$\lambda = \frac{\nu E}{(1+\nu)(1-2\nu)} \tag{2.8}$$

$$\mu = \frac{E}{2(1+\nu)} \tag{2.9}$$

Eqs. (2.6)–(2.7) are further simplified for the plane stress, plane strain and two-dimensional axisymmetric cases. For the plane stress case, the dimension in one direction (thickness) is neglected compared to the two others, and

$$\begin{Bmatrix}\sigma_{xx}\\ \sigma_{yy}\\ \sigma_{xy}\end{Bmatrix}=\frac{1}{1-\nu^2}\begin{bmatrix}1 & \nu & 0\\ \nu & 1 & 0\\ 0 & 0 & \frac{1-\nu}{2}\end{bmatrix}\begin{Bmatrix}\varepsilon_{xx}\\ \varepsilon_{yy}\\ \gamma_{xy}\end{Bmatrix} \tag{2.10}$$

where $\gamma_{xy}=2\varepsilon_{xy}$ is the engineering shear strain component. The strain component along the thickness direction, ε_{zz}, can also be derived from the Poisson's effect:

$$\varepsilon_{zz}=-\frac{\nu}{1-\nu}(\varepsilon_{xx}+\varepsilon_{yy}) \tag{2.11}$$

A plane strain case resembles a long body undergoing no variation in load or geometry in the longitudinal direction. As a result,

$$\begin{Bmatrix}\sigma_{xx}\\ \sigma_{yy}\\ \sigma_{zz}\\ \sigma_{xy}\end{Bmatrix}=\frac{E}{(1+\nu)(1-2\nu)}\begin{bmatrix}1-\nu & \nu & 0\\ \nu & 1-\nu & 0\\ \nu & \nu & 0\\ 0 & 0 & \frac{1-2\nu}{2}\end{bmatrix}\begin{Bmatrix}\varepsilon_{xx}\\ \varepsilon_{yy}\\ \gamma_{xy}\end{Bmatrix} \tag{2.12}$$

Here, some other useful definitions are presented. First, the effective Young's modulus, E', is defined as:

$$E'=\begin{cases}E & \text{plane stress}\\ \dfrac{E}{1-\nu^2} & \text{plane strain}\end{cases} \tag{2.13}$$

and another frequently used parameter κ

$$\kappa=\begin{cases}\dfrac{3-\nu}{1+\nu} & \text{plane stress}\\ 3-4\nu & \text{plane strain}\end{cases} \tag{2.14}$$

For an axisymmetric solid of revolution, a form almost similar to the plane strain relation is derived in terms of polar coordinate systems:

$$\begin{Bmatrix}\sigma_{zz}\\ \sigma_{rr}\\ \sigma_{\theta\theta}\\ \sigma_{rz}\end{Bmatrix}=\frac{E}{(1+\nu)(1-2\nu)}\begin{bmatrix}1-\nu & \nu & \nu & 0\\ \nu & 1-\nu & \nu & 0\\ \nu & \nu & 1-\nu & 0\\ 0 & 0 & 0 & \frac{1-2\nu}{2}\end{bmatrix}\begin{Bmatrix}\varepsilon_{zz}\\ \varepsilon_{rr}\\ \varepsilon_{\theta\theta}\\ \gamma_{rz}\end{Bmatrix} \tag{2.15}$$

When an elastic body is subjected to a loading, the body undergoes displacements which are linearly related to the applied loading. As a result, a certain amount of work is

stored in the body in the form of potential strain energy. The strain energy density can be defined as:

$$U_s = \int \sigma_{ij} \mathrm{d}\varepsilon_{ij} = \frac{1}{2}\sigma^T \varepsilon \tag{2.16}$$

The strain energy will be directly used in the definitions of a number of fundamental concepts of fracture mechanics, such as the *J* integral.

2.2.2 Airy stress function

Airy developed the idea of a stress function which can satisfy both the equilibrium and the compatibility conditions (Sharifabadi 1990). He showed that in absence of body forces, such a function Φ must satisfy the Laplace equation:

$$\nabla^4 \Phi = \nabla^2 \left(\nabla^2 \Phi \right) = 0 \tag{2.17}$$

where

$$\nabla^2 = \frac{\partial^2}{\partial x^2} + \frac{\partial^2}{\partial y^2} \tag{2.18}$$

and

$$\sigma_{xx} = \frac{\partial^2 \Phi}{\partial x^2} \tag{2.19}$$

$$\sigma_{yy} = \frac{\partial^2 \Phi}{\partial y^2} \tag{2.20}$$

$$\sigma_{xy} = -\frac{\partial^2 \Phi}{\partial x \partial y} \tag{2.21}$$

Eq. (2.17) can then be written as:

$$\nabla^4 \Phi = \nabla^2 \left(\sigma_{xx}^2 + \sigma_{yy}^2 \right) = 0 \tag{2.22}$$

or in polar coordinates:

$$\nabla^4 \Phi = \nabla^2 \left(\sigma_{rr} + \sigma_{\theta\theta} \right) = 0 \tag{2.23}$$

The Airy function must also satisfy the natural (stress) boundary conditions, which further limits its application for complex problems. The Airy stress function will be used in Section 2.3.2 for a stress field around a circular hole.

2.2.3 Complex stress functions

Kolonov and Muskheshvili (1953) developed the idea of complex stress functions, which enables finding solutions for more general problems including sharp corners, cracks and openings. Assuming $\psi(z)$ and $\chi(z)$ to be two harmonic analytic functions of x and y,

$$\nabla^2(\psi)=\nabla^2(\chi)=0 \tag{2.24}$$

$$z=x+iy=re^{i\theta} \tag{2.25}$$

Any stress function Φ can be expressed as:

$$\Phi=\mathrm{Re}\left[(x-iy)\,\psi(z)+\chi(z)\right] \tag{2.26}$$

or in terms of the conjugate function $\bar{z}=x-iy$:

$$\Phi=\mathrm{Re}\left[\bar{z}\psi(z)+\chi(z)\right] \tag{2.27}$$

Substituting Eq. (2.27) into Eqs. (2.19)–(2.21) results in:

$$\sigma_{xx}+\sigma_{yy}=4\,\mathrm{Re}\left[\psi'(z)\right] \tag{2.28}$$

$$-\sigma_{xx}+\sigma_{yy}+2i\sigma_{xy}=2\left[\bar{z}\psi''(z)+\chi''(z)\right] \tag{2.29}$$

which can be solved for the three stress components σ_{xx}, σ_{yy} and σ_{xy}. The expressions f' and f'' denote the first and second derivatives of the function f.

Cartesian displacements u_x and u_y can also be expressed in terms of the complex functions:

$$u_x+iu_y=\frac{3-\nu}{E}\psi(z)-\frac{1+\nu}{E}\left[\bar{z}\psi'(\bar{z})+\chi'(\bar{z})\right] \tag{2.30}$$

In a general curvilinear coordinate system any point can be represented by (α,β), where α and β are functions of coordinates (x,y). The stress components in terms of curvilinear coordinates can then be defined as:

$$\sigma_{\alpha\alpha}+\sigma_{\beta\beta}=4\,\mathrm{Re}\left[\psi'(z)\right] \tag{2.31}$$

$$-\sigma_{\alpha\alpha}+\sigma_{\beta\beta}+2i\sigma_{\alpha\beta}=\left[\bar{z}\psi''(z)+\chi''(z)\right]e^{2i\theta} \tag{2.32}$$

and for displacements

$$2\mu(u_\alpha-iu_\beta)=\left[\frac{3-\nu}{1+\nu}\psi(z)-z\psi'(\bar{z})-\chi'(\bar{z})\right]e^{-i\theta} \tag{2.33}$$

The special case of polar coordinates is obtained by setting:

$$\alpha \rightarrow r = \sqrt{x^2 + y^2} \tag{2.34}$$

$$\beta \rightarrow \theta = \tan^{-1}\left(\frac{y}{x}\right) \tag{2.35}$$

It should be noted that the present form of the stress function (Eq.(2.27)) can be further generalised as:

$$\Phi = \bar{z}\psi(z) + \chi(z) \tag{2.36}$$

2.3 BASICS OF LEFM

2.3.1 Fracture mechanics

A detailed investigation of a large number of catastrophic failures of structures indicates that the main source of failure can be attributed to some kind of geometric discontinuity or stress concentration. This form of discontinuity can be a sharp change of geometry, opening, hole, notch, crack, etc.

In order to explain the fundamental differences of fracture mechanics and conventional theory of strength of material, consider a simple example as depicted in Fig. 2.1. An infinite tensile plate is considered in two cases: a flawless plate and a plate with a tiny circular hole (flaw).

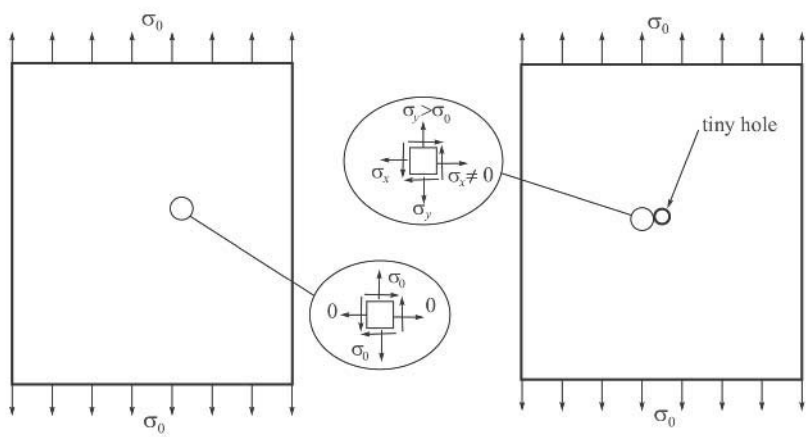

Figure 2.1 An infinite tensile plate with and without a flaw.

At the centre of the flawless plate, the stress field remains equal to the applied tensile stress, σ_0. Therefore, the maximum allowable traction can be determined from the

condition that the internal stress field should be limited to the material yield stress, as a measure of material failure strength:

$$\sigma_0 = \sigma_{\text{yld}} \tag{2.37}$$

In contrast, the elasticity solution for an infinite plate with a circular defect/hole (as will be discussed in Section 2.3.2) predicts a biaxial non-uniform stress field with a stress concentration factor of 3 at the centre of the plate, regardless of the size of the hole. In a limiting case of a line crack, the solution from a degenerated elliptical hole shows an infinite stress state at the crack tip. No material can withstand such an infinite stress state. Therefore, instead of comparing the existing stress field with a strength criterion, fracture mechanics adopts a local stress intensity factor or a global fracture energy release and compares them with their critical values.

In the following, a number of classical problems of fracture mechanics are reviewed.

2.3.2 Circular hole

In 1898, Kirsch analysed the problem of an infinite plate with a circular hole under uniform tensile stress, as depicted in Fig. 2.2a.

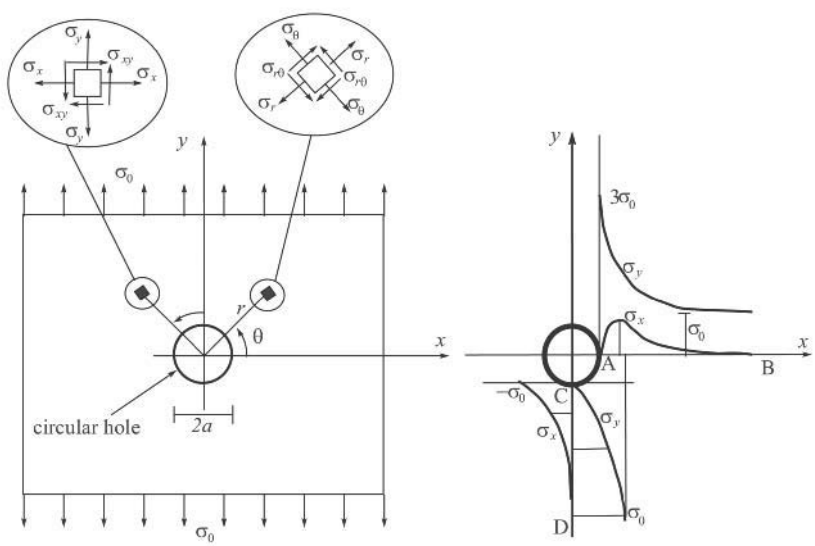

a) circular hole in an infinite plate b) stress distribution around the hole

Figure 2.2 Infinite tensile plate with a circular hole. a) geometry, b) distribution of stress components.

The problem is difficult to analyse in a single coordinate system. The boundary conditions around the circular hole can naturally be expressed in polar coordinate

systems, whereas the far field Cartesian boundary conditions are better expressed in the xy coordinate system.

Recalling the definition of the stress, σ_{yy}, in terms of the Airy stress function $\sigma_{yy} = \partial^2\Phi/\partial x^2$ would suggest a stress function of the form $\Phi = \sigma_0 x^2$ to represent the far field boundary condition $\sigma_{yy} = \sigma_0$. Alternatively, a polar representation of Φ is required to suit the circular hole with $x = r\cos\theta$:

$$\Phi = \sigma_0 r^2 \cos^2\theta \quad or \quad \Phi = \sigma_0 f(r)\cos 2\theta \tag{2.38}$$

After some manipulations, the following solutions are obtained (Meguid 1989):

$$\sigma_{rr} = \frac{\sigma_0}{2}\left(1-\frac{a^2}{r^2}\right)\left[1-\left(1-3\frac{a^2}{r^2}\right)\cos 2\theta\right] \tag{2.39}$$

$$\sigma_{\theta\theta} = \frac{\sigma_0}{2}\left[\left(1+\frac{a^2}{r^2}\right)+\left(1+3\frac{a^4}{r^4}\right)\cos 2\theta\right] \tag{2.40}$$

$$\sigma_{r\theta} = \frac{\sigma_0}{2}\left[\left(1-\frac{a^2}{r^2}\right)\left(1+3\frac{a^2}{r^2}\right)\sin 2\theta\right] \tag{2.41}$$

It is of interest to examine the stress values at the edge of the hole, $r = a$:

$$\begin{cases} \sigma_{rr} = 0 \\ \sigma_{\theta\theta} = \sigma_0(1-2\cos 2\theta) \\ \sigma_{r\theta} = 0 \end{cases} \tag{2.42}$$

which shows that despite application of a uniform unidirectional tensile traction, a non-uniform biaxial stress state is generated around the hole, which may even become compressive at $\theta = \pi/2, 3\pi/2$ ($\sigma_{\theta\theta} = \sigma_{xx} = -\sigma_0$). The stress concentration factor for $\sigma_{\theta\theta}$ is 3 at $\theta = 0, \pi$ ($\sigma_{\theta\theta} = \sigma_{yy} = 3\sigma_0$). Fig. 2.2b illustrates the distribution of stress components along the major axes of the plate.

2.3.3 Elliptical hole

Inglis (1913), a professor of naval architecture, independent of an earlier work by Kolosov, solved the problem of stress concentration around an elliptical hole in an infinite plate subjected to uniform stress loading, as depicted in Fig. 2.3.

The following complex stress potential functions, proposed by Inglis in the curvilinear coordinate system α and β, satisfy the boundary conditions and are periodic in β:

$$\psi(z) = \frac{1}{4}\sigma_0 c\left[\left(1+e^{2\alpha_0}\right)\sinh p - e^{2\alpha_0}\cosh p\right] \tag{2.43}$$

$$\chi(z) = -\frac{1}{4}\sigma_0 c^2\left[\left(\cosh 2\alpha_0 - \cosh\pi\right)p + \frac{1}{2}e^{2\alpha_0} - \cosh 2\left(p-\alpha_0 - i\frac{\pi}{2}\right)\right] \tag{2.44}$$

where $p=\alpha+i\beta$. The solution at $\alpha=\alpha_0$ is:

$$\left(\sigma_{\beta\beta}\right)_{\alpha=\alpha_0}=\sigma_0 e^{2\alpha_0}\left[\frac{\sinh 2\alpha_0\left(1+e^{-2\alpha_0}\right)}{\cosh 2\alpha_0-\cos 2\beta}-1\right] \tag{2.45}$$

and for points located at the end of the ellipse in terms of a and b,

$$\left(\sigma_{\beta\beta}\right)_{\substack{\alpha=\alpha_0\\ \beta=0,\pi}}=\sigma_0\left(1+2\frac{a}{b}\right) \tag{2.46}$$

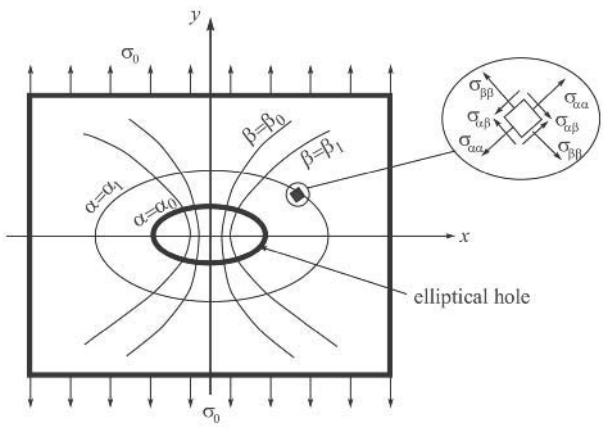

Figure 2.3 An elliptical hole in an infinite plate.

Eq. (2.46) shows that for a circular hole ($a=b$) the stress concentration factor becomes 3, similar to the conclusion made from the circular hole problem. Another extreme case is where the ellipse is degenerated into a crack ($b=0$), generating an infinite stress. For a crack propagating along the applied tensile stress ($a=0$), however, the stress at the crack tip remains at the finite value σ_0.

It has been shown that Eq. (2.46) can be rewritten in terms of the radius of curvature ρ:

$$\left(\sigma_{\beta\beta}\right)_{\substack{\alpha=\alpha_0\\ \beta=0,\pi}}=\sigma_0\left(1+2\sqrt{\frac{a}{\rho}}\right) \tag{2.47}$$

which shows that the stress concentration factor is proportional to $\rho^{-1/2}$.

2.3.4 Westergaard analysis of a sharp crack

Consider an infinite plate with a central traction-free crack of length $2a$ subjected to uniform biaxial stress σ_0, as depicted in Fig. 2.4a.

One solution is to superimpose Inglis solutions in the two cases of $a = 0$ and $b = 0$. As an alternative approach, Westergaard (1939) proposed the following biharmonic stress function Φ as a solution to the crack problem:

$$\Phi = \mathrm{Re}\,\bar{\bar{\phi}}(z) + y\ \mathrm{Im}\,\bar{\phi}(z) \tag{2.48}$$

where $\bar{\phi}$ and $\bar{\bar{\phi}}$ are the first and second integrals of $\phi(z)$, respectively. The stress components then become:

$$\sigma_{xx} = \mathrm{Re}\,\phi(z) - y\ \mathrm{Im}\,\phi'(z) \tag{2.49}$$

$$\sigma_{yy} = \mathrm{Re}\,\phi(z) + y\ \mathrm{Im}\,\phi'(z) \tag{2.50}$$

$$\sigma_{xy} = -y\,\mathrm{Re}\,\phi'(z) \tag{2.51}$$

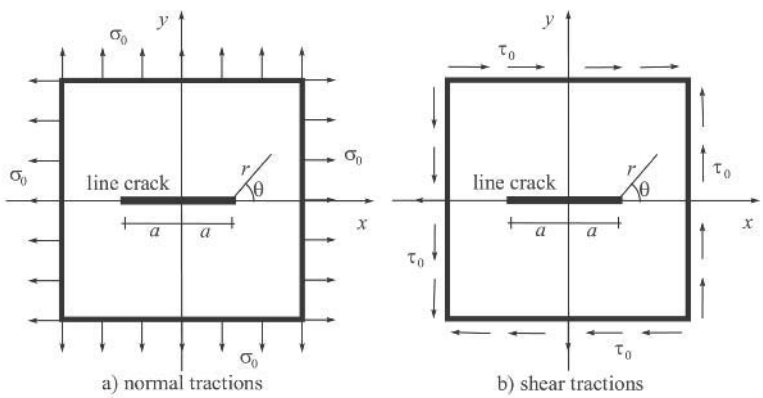

Figure 2.4 An infinite plate with a crack subjected to uniform normal and shear tractions.

The complex function ϕ is determined so that the boundary conditions are satisfied along the crack and at infinity (σ_0):

$$\phi(z) = \frac{\sigma_0}{\sqrt{1 - \dfrac{a^2}{z^2}}} \tag{2.52}$$

Then, the final near crack tip solutions are obtained ($r << a$) (Meguid 1989):

$$\sigma_{xx} = \sigma_0 \sqrt{\frac{a}{2r}}\ \cos\frac{\theta}{2}\left(1 - \sin\frac{\theta}{2}\ \sin\frac{3\theta}{2}\right) + \cdots \tag{2.53}$$

$$\sigma_{yy} = \sigma_0 \sqrt{\frac{a}{2r}}\ \cos\frac{\theta}{2}\left(1 + \sin\frac{\theta}{2}\ \sin\frac{3\theta}{2}\right) + \cdots \tag{2.54}$$

$$\sigma_{xy} = \sigma_0 \sqrt{\frac{a}{2r}}\ \sin\frac{\theta}{2}\ \cos\frac{\theta}{2}\ \cos\frac{3\theta}{2} + \cdots \tag{2.55}$$

Neglecting the higher order terms in Eqs. (2.53)–(2.55) is only acceptable for small values of r around the crack tip. A comparison with the exact solution:

$$\sigma_{yy} = \frac{\sigma_0}{\sqrt{1-\frac{a^2}{x^2}}} \tag{2.56}$$

shows that by increasing (r/a) from a small number 0.5 to a larger value 15, the relative error increases from 0.37 to about $10\,\%$.

Using a similar approach, the stress field around a crack tip in an infinite plate subjected to shear stresses τ_0 (Fig. 2.4b) can be expressed as:

$$\phi_s(z) = \frac{\tau_0}{\sqrt{1-\frac{a^2}{z^2}}} \tag{2.57}$$

and

$$\Phi_s(z) = -y\ \mathrm{Re}\,\bar{\phi}_s(z) \tag{2.58}$$

2.4 STRESS INTENSITY FACTOR, *K*

2.4.1 Definition of the stress intensity factor

Irwin (1957) introduced the concept of stress intensity factor K (SIF), as a measure of the strength of the singularity. He illustrated that all elastic stress fields around a crack tip are distributed similarly, and $K \propto \sigma\sqrt{\pi r}$ controls the local stress quantity.

Recalling Eqs. (2.53)–(2.55), the elastic stress state around a crack can now be represented by:

$$\sigma_{xx} = \sigma_0\sqrt{\frac{a}{2r}}\cos\frac{\theta}{2}\left(1-\sin\frac{\theta}{2}\sin\frac{3\theta}{2}\right)+\cdots=\sigma_0\sqrt{\frac{1}{r}}f(\theta)+\cdots \tag{2.59}$$

or in the more general form of:

$$\sigma_{ij} = r^{-\frac{1}{2}}\left\{K_{\mathrm{I}}f_{ij}^{\mathrm{I}}(\theta)+K_{\mathrm{II}}f_{ij}^{\mathrm{II}}(\theta)+K_{\mathrm{III}}f_{ij}^{\mathrm{III}}(\theta)\right\}+\text{higher order terms} \tag{2.60}$$

where σ_{ij} are the near crack tip stresses, and K_{I}, K_{II}, K_{III} are the stress intensity factors associated with three independent modes of movement of crack surfaces,

$$K_{\mathrm{I}} = \lim_{\substack{r\to 0\\ \theta=0}} \sigma_{yy}\sqrt{2\pi r} \tag{2.61}$$

$$K_{\mathrm{II}} = \lim_{\substack{r\to 0\\ \theta=0}} \sigma_{xy}\sqrt{2\pi r} \tag{2.62}$$

$$K_{\mathrm{III}} = \lim_{\substack{r\to 0\\ \theta=0}} \sigma_{yz}\sqrt{2\pi r} \tag{2.63}$$

The first mode stress intensity factor based on Eq. (2.61) can then be simplified to:

$$K_{\mathrm{I}} = \lim_{\substack{r\to 0\\ \theta=0}} \sigma_{yy}\sqrt{2\pi r} = \lim_{\substack{r\to 0\\ \theta=0}} \sqrt{2\pi r}\sigma_0\sqrt{\frac{a}{2r}}\cos\frac{\theta}{2}\left(1-\sin\frac{\theta}{2}\sin\frac{3\theta}{2}\right) = \sigma_0\sqrt{\pi a} \tag{2.64}$$

Fig. 2.5 illustrates these independent crack opening modes. In the opening mode *I,* crack surfaces are pulled apart in the normal direction (*y*) but remain symmetric about the *xz* and *xy* planes. The shearing mode II represents the sliding mode of movement of crack surfaces in the *x* direction, while remaining symmetric about the *xy* plane and skew symmetric about the *xz* plane. Finally, in the tearing mode III, the crack surfaces slide over each other in the *z* direction, while remaining skew symmetric about the *xy* and *xz* planes.

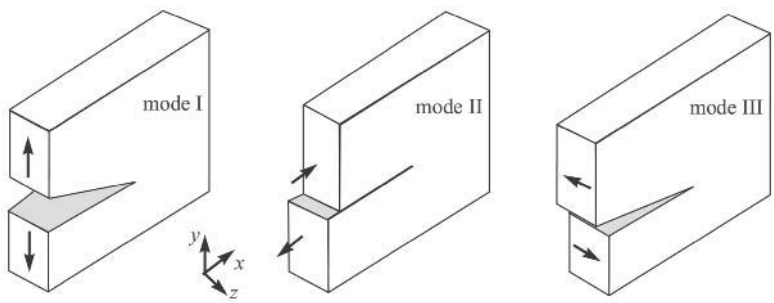

Figure 2.5 Different modes of crack displacement.

Similar to the conventional theory of strength of materials where the existing stress is compared to an allowable material stress/strength, fracture mechanics states that unstable fracture occurs when one of the stress intensity factors, K_i, or a mixed mode of them reaches a critical value, K_{ic}. This critical value, K_{ic}, is called fracture toughness and represents the potential ability of a material to withstand a given stress field at the tip of a crack and to resist progressive tensile crack extension.

Substituting Eqs. (2.61)–(2.63) into Eqs. (2.53)–(2.55) at the crack tip $\theta = 0$, allows the final stress and displacement fields to be described in terms of the stress intensity factors. They are categorised into three pure modes of fracture (Saouma 2000).

For pure opening mode I, the stress field is given by:

$$\sigma_{xx} = \frac{K_{\mathrm{I}}}{\sqrt{2\pi r}} \cos\frac{\theta}{2}\left(1 - \sin\frac{\theta}{2}\sin\frac{3\theta}{2}\right) \tag{2.65}$$

$$\sigma_{yy} = \frac{K_{\mathrm{I}}}{\sqrt{2\pi r}} \cos\frac{\theta}{2}\left(1 + \sin\frac{\theta}{2}\sin\frac{3\theta}{2}\right) \tag{2.66}$$

$$\sigma_{xy} = \frac{K_{\mathrm{I}}}{\sqrt{2\pi r}} \sin\frac{\theta}{2}\cos\frac{\theta}{2}\cos\frac{3\theta}{2} \tag{2.67}$$

$$\sigma_{zz} = \begin{cases} \nu(\sigma_{xx} + \sigma_{yy}) & \text{plane strain} \\ 0 & \text{plane stress} \end{cases} \tag{2.68}$$

$$\sigma_{xz} = \sigma_{yz} = 0 \tag{2.69}$$

and the displacement field:

$$u_x = \frac{K_{\mathrm{I}}}{2\mu}\sqrt{\frac{r}{2\pi}} \cos\frac{\theta}{2}\left(\kappa - 1 + 2\sin^2\frac{\theta}{2}\right) \tag{2.70}$$

$$u_y = \frac{K_{\mathrm{I}}}{2\mu}\sqrt{\frac{r}{2\pi}} \sin\frac{\theta}{2}\left(\kappa + 1 - 2\cos^2\frac{\theta}{2}\right) \tag{2.71}$$

$$u_z = 0 \tag{2.72}$$

The pure mode II is governed by the following stress fields:

$$\sigma_{xx} = \frac{K_{\mathrm{II}}}{\sqrt{2\pi r}} \sin\frac{\theta}{2}\left(2 + \cos\frac{\theta}{2}\cos\frac{3\theta}{2}\right) \tag{2.73}$$

$$\sigma_{yy} = \frac{K_{\mathrm{II}}}{\sqrt{2\pi r}} \sin\frac{\theta}{2}\cos\frac{\theta}{2}\cos\frac{3\theta}{2} \tag{2.74}$$

$$\sigma_{xy} = \frac{K_{\mathrm{II}}}{\sqrt{2\pi r}} \cos\frac{\theta}{2}\left(1 - \sin\frac{\theta}{2}\sin\frac{3\theta}{2}\right) \tag{2.75}$$

$$\sigma_{zz} = \nu(\sigma_{xx} + \sigma_{yy}) \tag{2.76}$$

$$\sigma_{xz} = \sigma_{yz} = 0 \tag{2.77}$$

with the displacement fields u_x and u_y,

$$u_x = \frac{K_{\mathrm{II}}}{2\mu}\sqrt{\frac{r}{2\pi}}\,\sin\frac{\theta}{2}\left(\kappa + 1 + 2\cos^2\frac{\theta}{2}\right) \tag{2.78}$$

$$u_y = -\frac{K_{\mathrm{II}}}{2\mu}\sqrt{\frac{r}{2\pi}}\,\cos\frac{\theta}{2}\left(\kappa - 1 - 2\sin^2\frac{\theta}{2}\right) \tag{2.79}$$

$$u_z = 0 \tag{2.80}$$

The tearing mode III, has only two non-zero stress components and one non-zero displacement:

$$\sigma_{xx} = \sigma_{yy} = \sigma_{zz} = \tau_{xy} = 0 \tag{2.81}$$

$$\sigma_{xz} = -\frac{K_{\mathrm{III}}}{\sqrt{2\pi r}}\sin\frac{\theta}{2} \tag{2.82}$$

$$\sigma_{yz} = \frac{K_{\mathrm{III}}}{\sqrt{2\pi r}}\cos\frac{\theta}{2} \tag{2.83}$$

$$u_x = u_y = 0 \tag{2.84}$$

$$u_z = \frac{K_{\mathrm{III}}}{2\mu}\sqrt{\frac{r}{2\pi}}\,\sin\frac{\theta}{2} \tag{2.85}$$

Finally, Eqs. (2.65)–(2.80) can be expressed in polar coordinates σ_{rr}, $\sigma_{\theta\theta}$ and $\sigma_{r\theta}$. In the opening mode I:

$$\sigma_{rr} = \frac{K_{\mathrm{I}}}{\sqrt{2\pi r}}\cos\frac{\theta}{2}\left(1 + \sin^2\frac{\theta}{2}\right) \tag{2.86}$$

$$\sigma_{\theta\theta} = \frac{K_{\mathrm{I}}}{\sqrt{2\pi r}}\cos\frac{\theta}{2}\left(1 - \sin^2\frac{\theta}{2}\right) \tag{2.87}$$

$$\sigma_{r\theta} = \frac{K_{\mathrm{I}}}{\sqrt{2\pi r}}\sin\frac{\theta}{2}\cos^2\frac{\theta}{2} \tag{2.88}$$

and for the shear mode II:

$$\sigma_{rr} = \frac{K_{\mathrm{II}}}{\sqrt{2\pi r}}\left(-\frac{5}{4}\sin\frac{\theta}{2} + \frac{3}{4}\sin\frac{3\theta}{2}\right) \tag{2.89}$$

$$\sigma_{\theta\theta} = \frac{K_{II}}{\sqrt{2\pi r}}\left(-\frac{3}{4}\sin\frac{\theta}{2} - \frac{3}{4}\sin\frac{3\theta}{2}\right) \tag{2.90}$$

$$\sigma_{r\theta} = \frac{K_{II}}{\sqrt{2\pi r}}\left(\frac{1}{4}\sin\frac{\theta}{2} + \frac{3}{4}\sin\frac{3\theta}{2}\right) \tag{2.91}$$

2.4.2 Examples of stress intensity factors for LEFM

In this section some of the basic problems of fracture mechanics with available analytical SIF solutions are illustrated. First a finite tensile plate problem that includes a central crack will be considered, as depicted in Fig. 2.6a. The mode I stress intensity factor can be defined as:

$$K_I = \sqrt{\sec\frac{\pi a}{b}}\,\sigma\sqrt{\pi a} = \left[1 + 0.256\left(\frac{a}{b}\right) - 1.152\left(\frac{a}{b}\right)^2 + 12.2\left(\frac{a}{b}\right)^3\right]\sigma_0\sqrt{\pi a} \tag{2.92}$$

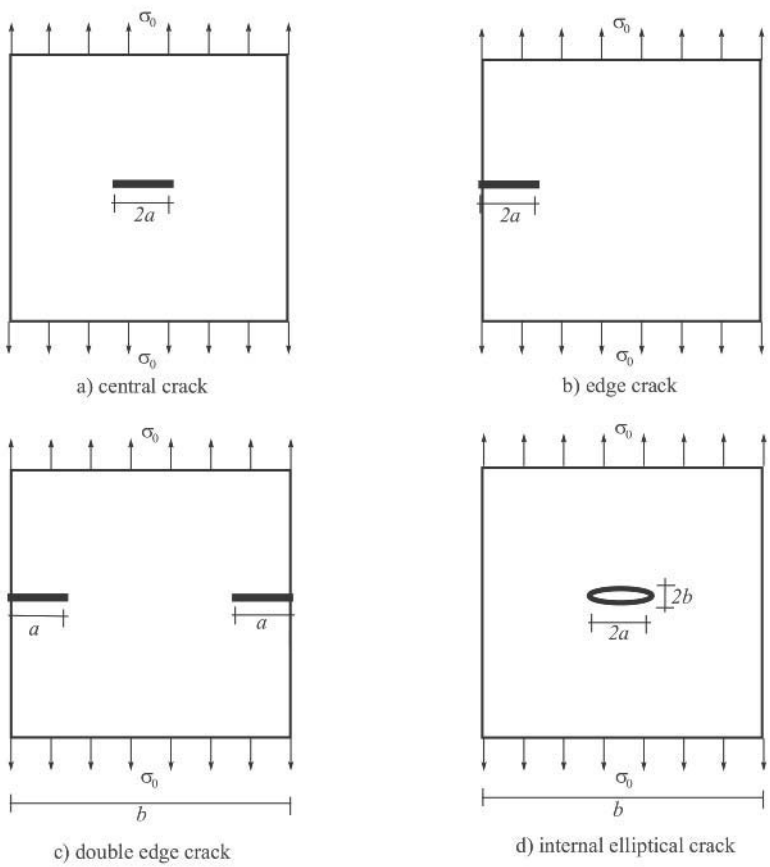

Figure 2.6 Classical problems of fracture mechanics.

The second problem is similar to the previous one except that it has an edge crack, as shown in Fig. 2.6b. The stress intensity factor for the fracture mode I can be obtained as:

$$K_{\mathrm{I}}=\left[1.12-0.23\left(\frac{a}{b}\right)+10.56\left(\frac{a}{b}\right)^{2}-21.74\left(\frac{a}{b}\right)^{3}+30.42\left(\frac{a}{b}\right)^{4}\right]\sigma_{0}\sqrt{\pi a} \tag{2.93}$$

Now, if the edge crack is doubled, as illustrated in Fig. 2.6c, the stress intensity factor has to be modified accordingly,

$$K_{\mathrm{I}}=\left[1.12+0.43\left(\frac{a}{b}\right)-4.79\left(\frac{a}{b}\right)^{2}+15.46\left(\frac{a}{b}\right)^{3}\right]\sigma_{0}\sqrt{\pi a} \tag{2.94}$$

The final example in this section describes the stress intensity factor for an embedded elliptical crack within a finite tensile plate, as depicted in Fig. 2.6d.

$$K_{\mathrm{I}}(\theta)=\left(\int_{0}^{\pi/2}\sqrt{1-\frac{a^{2}-b^{2}}{a^{2}}\sin^{2}\theta}\,\mathrm{d}\theta\right)^{-1}\left(\sin^{2}\theta+\frac{b^{2}}{a^{2}}\cos^{2}\theta\right)^{\frac{1}{4}}\sigma_{0}\sqrt{\pi b} \tag{2.95}$$

To simplify the process of determining the SIF, an approximate solution can be obtained by omitting the first term:

$$K_{\mathrm{I}}=\left(\sin^{2}\theta+\frac{b^{2}}{a^{2}}\cos^{2}\theta\right)^{\frac{1}{4}}\sigma_{0}\sqrt{\pi b}\qquad 0\le\frac{b}{a}\le 1 \tag{2.96}$$

A comprehensive list of different problems with their analytic or approximate stress intensity factors can be found in handbooks and textbooks on fracture mechanics.

2.4.3 Griffith theories of strength and energy

While exploring the theoretical strength of solids by performing a series of experiments on glass rods of various diameters, Griffith observed that the tensile strength of glass decreased with an increase in diameter. He realised that something different from a simple inherent material property had caused the size dependency of the tensile strength.

While studying the solution of the elliptical hole problem, Inglis initiated the idea that the theoretical strength of a solid has to be reduced due to the presence of internal flaws. In other words, he assumed that the theoretical strength of a material must be compared with the concentrated stress field, which is much higher than the average stress or the flawless based stress field.

Instead of using a stress based criterion, Griffith derived a thermodynamic criterion for fracture by considering the total change in energy of a cracked body in terms of the crack length increase. His model described the failure of a solid material in terms of satisfying a critical energy criterion rather than a maximum stress based failure control.

Consider a crack in a deformable continuum subjected to arbitrary loading. The first law of thermodynamics states that the change in total energy is proportional to the amount of performed work and the change of heat content:

$$\frac{\mathrm{d}}{\mathrm{d}t}\left(U_{\mathrm{k}}+U_{\mathrm{s}}+U_{\Gamma}\right)=\frac{\mathrm{d}}{\mathrm{d}t}\left(W+Q\right) \tag{2.97}$$

where U_{k} is the kinetic energy, U_{s} is the total internal strain energy, U_{Γ} is the surface energy, W is the external work and Q is the heat input to the system.

For an adiabatic quasi-static system, Q and K are equal to zero:

$$\frac{\mathrm{d}}{\mathrm{d}t}\left(U_{\mathrm{s}}+U_{\Gamma}\right)=\frac{\mathrm{d}}{\mathrm{d}t}\left(W\right) \tag{2.98}$$

Rewriting Eq. (2.98) in terms of crack half length, a,

$$\frac{\partial W}{\partial a}=\frac{\partial U_{\mathrm{s}}}{\partial a}+\frac{\partial U_{\Gamma}}{\partial a} \tag{2.99}$$

This equation represents the energy balance during crack growth, and indicates that the work rate supplied to the continuum by the applied external load is equal to the surface energy dissipated during crack propagation, U_{Γ}, plus the rate of strain energy, U_{s}, decomposed into elastic $U_{\mathrm{s}}^{\mathrm{e}}$ and plastic $U_{\mathrm{s}}^{\mathrm{p}}$ parts

$$U_{\mathrm{s}}=U_{\mathrm{s}}^{\mathrm{e}}+U_{\mathrm{s}}^{\mathrm{p}} \tag{2.100}$$

Eq. (2.99) can be expressed in terms of the potential energy, Π:

$$\Pi=U_{\mathrm{s}}^{\mathrm{e}}-W \tag{2.101}$$

$$-\frac{\partial \Pi}{\partial a}=-\frac{\partial U_{\mathrm{s}}^{\mathrm{e}}}{\partial a}+\frac{\partial W}{\partial a}=-\frac{\partial U_{\mathrm{s}}^{\mathrm{e}}}{\partial a}+\frac{\partial U_{\mathrm{s}}}{\partial a}+\frac{\partial U_{\Gamma}}{\partial a}=\frac{\partial U_{\mathrm{s}}^{\mathrm{p}}}{\partial a}+\frac{\partial U_{\Gamma}}{\partial a} \tag{2.102}$$

Therefore, the energy available for crack growth is compared with the resistance of the material that must be overcome for crack growth. It also indicates that the decrease rate of potential energy during crack growth is equal to the rate of energy dissipated in plastic deformation and crack growth.

2.4.4 Brittle material

For a perfectly brittle material, $U_{\mathrm{s}}^{\mathrm{p}}$ vanishes and Eqs. (2.101)–(2.102) reduce to:

$$-\frac{\partial \Pi}{\partial a}=\frac{\partial W}{\partial a}-\frac{\partial U_{\mathrm{s}}^{\mathrm{e}}}{\partial a}=\frac{\partial U_{\Gamma}}{\partial a}=2\gamma_{\mathrm{s}} \tag{2.103}$$

where γ_s is the surface energy and the factor 2 represents the existence of two material surfaces upon fracture. The value of γ_s is experimentally measured for different materials. Water has a value of $\gamma_s = 0.077$, while for most of the metals, $\gamma_s = 1$ (Saouma 2000). Eq. (2.103) is defined as the Griffith crack growth energy, G

$$G = -\frac{\partial \Pi}{\partial a} = 2\gamma_s \tag{2.104}$$

Thus a criterion for crack propagation can be expressed as an inequality between the energy release rate per unit crack extension and the surface energy:

$$\frac{\mathrm{d}\Pi}{\mathrm{d}a} \geq 2\gamma_s \tag{2.105}$$

or

$$\mathrm{d}\Pi \geq 2\gamma_s \, \mathrm{d}a \tag{2.106}$$

Griffith has shown that for a plane stress infinite plate with a central crack of length $2a$ and unit thickness subjected to unilateral tensile loading, the strain energy required to introduce the crack is equal in magnitude to the work required to close the crack by the stresses acting on it,

$$\Pi = 4\int_0^a \frac{1}{2}\sigma \, u_y(x)\mathrm{d}x \tag{2.107}$$

According to Mushkelishvili or Westergaard solutions, displacements for the free surface of one of the crack faces can be expressed as:

$$u_x(x) = -\frac{2\sigma x}{E'} \tag{2.108}$$

$$u_y(x) = \frac{2\sigma\sqrt{a^2 - x^2}}{E'} \tag{2.109}$$

Eq. (2.107) can then be further simplified to:

$$\Pi = \frac{\pi\sigma^2 a^2}{2E'} \tag{2.110}$$

Therefore, going back to Eq. (2.104) gives,

$$G = -\frac{\mathrm{d}\Pi}{\mathrm{d}a} = \frac{\pi a \sigma^2}{E'} \tag{2.111}$$

Also, the total energy consumed over a crack extension, da, can be determined:

$$\mathrm{d}\Pi = \int_0^{\mathrm{d}a} G\,\mathrm{d}x = \int_0^{\mathrm{d}a} \frac{\sigma^2 \pi a}{E'}\,\mathrm{d}x = \frac{\sigma^2 \pi a}{E'}\,\mathrm{d}a \tag{2.112}$$

The critical stress for cracking that satisfies Eq. (2.110) is denoted by σ_{cr},

$$\sigma_{\mathrm{cr}} = \sqrt{\frac{2E'\gamma_{\mathrm{s}}}{\pi a}} \tag{2.113}$$

The critical stress intensity factor K_{C} can then be defined as:

$$K_{\mathrm{C}} = \sigma_{\mathrm{cr}}\sqrt{\pi a} \tag{2.114}$$

and an unstable crack extension occurs if:

$$K = K_{\mathrm{C}} \tag{2.115}$$

2.4.5 Quasi-brittle material

In order to extend the Griffith model further to quasi-brittle materials, a modification to Eq. (2.103) can be written as:

$$\frac{\partial U_\Gamma}{\partial a} = 2(\gamma_{\mathrm{s}}^{\mathrm{e}} + \gamma_{\mathrm{s}}^{\mathrm{p}}) \tag{2.116}$$

where $\gamma_{\mathrm{s}}^{\mathrm{e}}$ and $\gamma_{\mathrm{s}}^{\mathrm{p}}$ are the elastic and plastic parts of the work associated with crack extension, respectively. For ductile metals, $\gamma_{\mathrm{s}}^{\mathrm{p}} >> \gamma_{\mathrm{s}}^{\mathrm{e}}$. Alternatively, a simple modification to Eq. (2.113) can be assumed:

$$\sigma_{\mathrm{cr}} = \sqrt{\frac{2E'\alpha_{\mathrm{p}}\gamma}{\pi a}} \tag{2.117}$$

where α_{p} is a correction factor.

It is also important to observe that the potential energy and surface energy scale differently, the former scales with a^2 ($U_{\mathrm{s}} = \pm\pi\sigma^2 a^2 / E$), whereas the later is a function of a ($U_\Gamma = 4a\gamma_{\mathrm{s}}$). This further complicates the solution and can have serious implications on the stability of cracks and on size effects.

2.4.6 Crack stability

Eq. (2.102) can be rewritten as:

$$\frac{\partial}{\partial a}\left(\Pi + U_\Gamma\right) = 0 \tag{2.118}$$

Therefore, a crack's growth can be considered unstable or stable when the energy at equilibrium is a maximum or minimum, respectively. Therefore, a sufficient condition for crack stability is obtained from the second derivative of $\left(\Pi + U_\Gamma\right)$ (Gtoudos 1993):

$$\frac{\partial^2\left(\Pi + U_\Gamma\right)}{\partial a^2}\begin{cases} < 0 & \text{unstable fracture} \\ = 0 & \text{stable fracture} \\ > 0 & \text{neutral equilibrium} \end{cases} \tag{2.119}$$

To conclude the discussion on crack propagation criteria, for a crack to extend in a linear elastic flawed structure, two criteria can be considered:

1. A local criterion based on comparing the stress intensity factor, K, determined from the near crack tip stress field, with a material property K_C (critical stress intensity factor or fracture toughness).
2. A global approach for comparing the energy release rate, G, determined from the crack global transfer of energy, with a material property, G_C (critical energy release rate).

2.4.7 Fixed grip versus fixed load

An infinite plate with a crack of length $2a$ subjected to the loading P is now considered. The change in potential energy is determined as the crack length is increased to $2(a + \mathrm{d}a)$. Two limiting cases of the fixed grip (displacement control) and the fixed load (load control) are analysed (Fig. 2.7).

In the first case ($u_2 = u_1$), the external work is zero ($\Delta W = 0$) and any increase in crack length results in a decrease in stored elastic strain energy:

$$\Delta U = \frac{1}{2}P_2 u_1 - \frac{1}{2}P_1 u_1 < 0 \tag{2.120}$$

and

$$\Pi_2 - \Pi_1 = \Delta W - \Delta U = \frac{1}{2}\left(P_1 - P_2\right)u_1 \tag{2.121}$$

This release of excess energy is consumed to form the surface energy.

Under the fixed loading condition ($P_2 = P_1$), neither the external work nor the release of internal strain energy is zero,

$$\Delta W = P_1(u_2 - u_1) \tag{2.122}$$

and the change in potential energy:

$$\Pi_2 - \Pi_1 = \Delta W - \Delta U = P_1(u_2 - u_1) - \frac{1}{2}P_1(u_2 - u_1) = \frac{1}{2}P_1(u_2 - u_1) \tag{2.123}$$

Half of the produced external work is consumed into strain energy, and the other half is released to form surface energy.

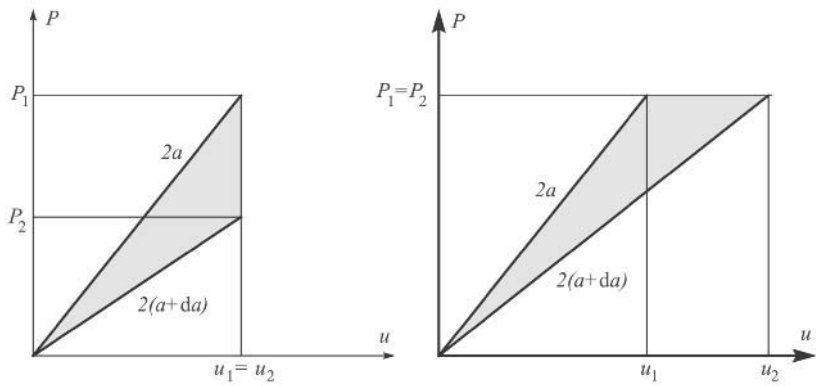

Figure 2.7 Load–displacement curves for displacement control and load control problems.

2.4.8 Mixed mode crack propagation

The problems discussed so far were mainly in fracture mode I. Practical engineering problems, however, rarely fall into this category. They usually include inclined or curvilinear crack propagations and are subjected to multiaxial loadings (Fig. 2.8), creating non-zero K_{I} and K_{II} stress intensity factors. The effect of the tearing mode is neglected in this section.

The analytical solution for an inclined crack in an infinite plate can be written as:

$$K_{\mathrm{I}} = \sigma \sin^2 \theta_0 \sqrt{\pi a} \tag{2.124}$$

$$K_{\mathrm{II}} = \sigma \sin \theta_0 \cos \theta_0 \sqrt{\pi a} \tag{2.125}$$

Generalisation of the original SIF based collinear crack propagation criterion ($K_{\mathrm{I}} > K_{\mathrm{Ic}}$) to include mixed mode effects can be defined in terms of K_{I} and K_{II} stress intensity factors, and K_{Ic} and K_{IIc} fracture toughness factors:

$$f(K_{\mathrm{I}}, K_{\mathrm{Ic}}, K_{\mathrm{II}}, K_{\mathrm{IIc}}) = 0 \tag{2.126}$$

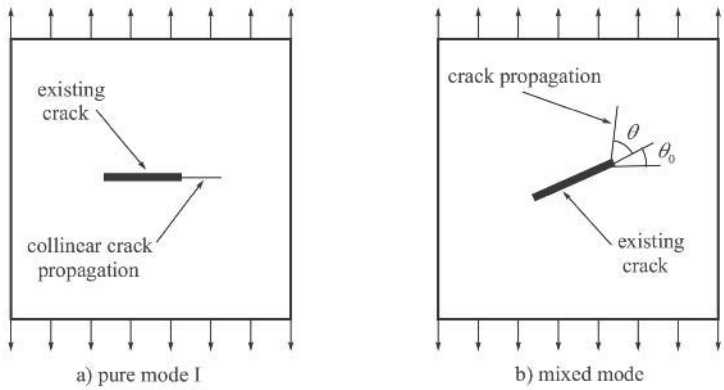

Figure 2.8 Mixed mode crack propagation.

Eq. (2.126) is further simplified because usually only the mode I fracture toughness K_{Ic} is experimentally measured:

$$f(K_I, K_{Ic}, K_{II}) = 0 \tag{2.127}$$

In the following sections (2.4.8.1–2.4.8.5), some of the most widely used mixed mode criteria are briefly reviewed.

2.4.8.1 *Maximum circumferential tensile stress*

Erdogan and Sih (1963) developed the first theory of mixed mode stress intensity factor based on the solution of stress state near a crack tip. They assumed that the crack propagates at its tip in a radial direction within a plane perpendicular to the direction of maximum tension when the maximum circumferential tensile stress, $(\sigma_\theta)_{max}$, reaches a critical material constant.

The mixed mode criterion for a crack angle θ can then be defined as (Fig. 2.8b):

$$\frac{K_I}{K_{Ic}} \cos^3 \frac{\theta}{2} - \frac{3}{2} \frac{K_{II}}{K_{Ic}} \cos \frac{\theta}{2} \sin \theta = 1 \tag{2.128}$$

or

$$K_{eq} = K_I \cos^3 \frac{\theta}{2} - \frac{3}{2} K_{II} \cos \frac{\theta}{2} \sin \theta \tag{2.129}$$

2.4.8.2 *Minimum strain energy density criterion*

The maximum strain energy density criterion is based on this idea that a crack propagates along the minimum resistance path. It determines the crack propagation from the crack tip

in a direction θ, along which the strain energy density at a critical distance is minimum. Occurrence of crack propagation is controlled by checking such a minimum resistance until it reaches a critical value.

The final form of the criterion according to Sih (1973, 1974) can be defined as:

$$\frac{8\mu}{(\kappa-1)}\left[a_{11}\left(\frac{K_{\mathrm{I}}}{K_{\mathrm{Ic}}}\right)^2+2a_{12}\left(\frac{K_{\mathrm{I}}K_{\mathrm{II}}}{K_{\mathrm{Ic}}^2}\right)+a_{22}\left(\frac{K_{\mathrm{II}}}{K_{\mathrm{Ic}}}\right)^2\right]=1 \tag{2.130}$$

where

$$\begin{cases} a_{11}=\dfrac{1}{16\mu}\left[(1+\cos\theta)(\kappa-\cos\theta)\right] \\ a_{12}=\dfrac{\sin\theta}{16\mu}\left[2\cos\theta-(\kappa-1)\right] \\ a_{22}=\dfrac{1}{16\mu}\left[(\kappa+1)(1-\cos\theta)+(1+\cos\theta)(3\cos\theta-1)\right] \end{cases} \tag{2.131}$$

2.4.8.3 *Maximum energy release rate*

Another alternative model, the maximum energy release rate, is based on the work of Hussain *et al.* (1974) who solved for the stress intensity factors $K_{\mathrm{I}}(\theta)$ and $K_{\mathrm{II}}(\theta)$ of a major existing crack with an infinitesimal tip kink at an angle θ (Fig. 2.9) in terms of the stress intensity factors of the original crack K_{I} and K_{II}:

$$K_{\mathrm{I}}(\theta)=g(\theta)\left(K_{\mathrm{I}}\cos\theta+\frac{3}{2}K_{\mathrm{II}}\sin\theta\right) \tag{2.132}$$

$$K_{\mathrm{II}}(\theta)=g(\theta)\left(K_{\mathrm{II}}\cos\theta-\frac{3}{2}K_{\mathrm{I}}\sin\theta\right) \tag{2.133}$$

with

$$g(\theta)=\left(\frac{4}{3+\cos^2\theta}\right)\left(\frac{1-\theta/\pi}{1+\theta/\pi}\right)^{\frac{\theta}{2\pi}} \tag{2.134}$$

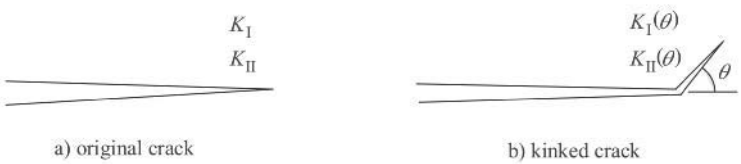

Figure 2.9 A crack with an infinitesimal kink.

Adopting Irwin's generalised expression for the energy release rate,

$$G(\theta) = \frac{1}{E'}\left(K_{\mathrm{I}}^2(\theta) + K_{\mathrm{II}}^2(\theta)\right) \tag{2.135}$$

the evaluation of $G(\theta)$ for the kinked crack becomes:

$$G(\theta) = \frac{1}{4E'} g^2(\theta)\left[\left(1 + 3\cos^2\theta\right)K_{\mathrm{I}}^2\right) + 8\sin\theta\cos\theta K_{\mathrm{I}}K_{\mathrm{II}} + \left(9 - 5\cos^2\theta\right)K_{\mathrm{II}}^2\right)\Big] \tag{2.136}$$

and the angle of crack propagation is found by minimizing $G(\theta)$:

$$\frac{\partial G(\theta)}{\partial \theta} = 0 \tag{2.137}$$

and satisfying the instability condition,

$$\frac{\partial^2 G(\theta)}{\partial \theta^2} < 0 \tag{2.138}$$

The general form of Eq. (2.136) takes the following form,

$$G(\theta) = \frac{1}{E'}\left[A_{11}K_{\mathrm{I}}^2(\theta) + 2A_{12}K_{\mathrm{I}}(\theta)K_{\mathrm{II}}(\theta) + A_{22}K_{\mathrm{II}}^2(\theta)\right] \tag{2.139}$$

where

$$\begin{bmatrix} A_{11} \\ A_{12} \\ A_{22} \end{bmatrix} = g^2(\theta)\begin{bmatrix} 4 - 3\sin^2\theta \\ -2\sin 2\theta \\ 4 + 5\sin^2\theta \end{bmatrix} \tag{2.140}$$

2.4.8.4 *Zero K_{II} criterion*

In this model, the criterion is to set the in-plane stress intensity factor K_{II} to vanish in shear mode for infinitesimal small crack extensions. For further details see Whittaker and Singh (1992).

2.4.8.5 *Other empirical models*

The following formulae define a number of mixed mode stress intensity criteria that are basically developed from experimental observations rather than theoretical bases. Many of them are valid only for specific problems in concrete, rock and composite problems, where the models have been experimentally obtained or calibrated.

$$\left(\frac{K_{\mathrm{I}}}{K_{\mathrm{Ic}}}\right)+\left(\frac{K_{\mathrm{II}}}{K_{\mathrm{IIc}}}\right)=1 \quad \text{: linear model} \tag{2.141}$$

$$\left(\frac{K_{\mathrm{I}}}{K_{\mathrm{Ic}}}\right)^2+\left(\frac{K_{\mathrm{II}}}{K_{\mathrm{IIc}}}\right)^2=1 \quad \text{: elliptical model} \tag{2.142}$$

$$\left(\frac{K_{\mathrm{I}}}{K_{\mathrm{Ic}}}\right)^2+c\left(\frac{K_{\mathrm{I}}K_{\mathrm{II}}}{K_{\mathrm{Ic}}K_{\mathrm{IIc}}}\right)+\left(\frac{K_{\mathrm{II}}}{K_{\mathrm{IIc}}}\right)^2=1, \quad c\neq 2 \quad \text{: quadratic model} \tag{2.143}$$

$$\left(\frac{K_{\mathrm{I}}}{K_{\mathrm{Ic}}}\right)+\left(\frac{K_{\mathrm{II}}}{2K_{\mathrm{Ic}}}\right)^2=1 \quad \text{: Advani/Lee model} \tag{2.144}$$

$$\left(\frac{K_{\mathrm{I}}}{K_{\mathrm{Ic}}}\right)^c+\left(\frac{K_{\mathrm{II}}}{K_{\mathrm{IIc}}}\right)^c=1, \quad c\cong 1.6 \quad \text{: Awaji/Sato model} \tag{2.145}$$

$$\left(\frac{K_{\mathrm{I}}}{K_{\mathrm{Ic}}}\right)+1.5\left(\frac{K_{\mathrm{II}}}{K_{\mathrm{Ic}}}\right)^2=1 \quad \text{: Palanisawamy/Knauss model} \tag{2.146}$$

2.5 SOLUTION PROCEDURES FOR *K* AND *G*

For most practical problems no analytical solution is available, and numerical techniques such as the finite element method, boundary element method, and more recently the meshless method should be used. In this section, a review of available solutions related to the finite element method is provided. These include:

1. Classical methods using the finite element method solely as a continuum based analytical tool.
2. Techniques in which the SIFs are directly evaluated as part of the global stiffness matrix.
3. Techniques through which the SIF can be computed from a standard finite element analysis via a special purpose post-processing technique.
4. Methods in which the singularity of the stress field at the crack tip is modelled.

2.5.1 Displacement extrapolation/correlation method

The stress field at a crack tip is singular and conventional finite elements cannot represent it no matter how fine they are. Nevertheless, it was recognised in earlier simulations of LEFM that a very fine mesh is required at the crack tip if it is to be used to approximate the stress field for evaluation of the stress intensity factor (Chan *et al.* 1970).

Stress intensity factors can be determined at different radial distances from the crack tip by equating the numerically obtained displacements with their analytical expression in terms of the SIF. For plane stress problems in the *xy* plane (Fig. 2.10):

$$K_{\mathrm{I}} = \mu\sqrt{\frac{2\pi}{r}}\frac{u_y^b - u_y^a}{2(1-\nu)} \tag{2.147}$$

$$K_{\mathrm{II}} = \mu\sqrt{\frac{2\pi}{r}}\frac{u_x^b - u_x^a}{2(1-\nu)} \tag{2.148}$$

$$K_{\mathrm{III}} = \mu\sqrt{\frac{\pi}{2r}}\left(u_z^b - u_z^a\right) \tag{2.149}$$

and for plane stress problems, the following replacement is required:

$$\nu \to \frac{\nu}{1+\nu} \tag{2.150}$$

A simple extrapolation technique, as depicted in Fig. 2.10, can then be used to approximately evaluate the value of SIF at the crack tip. The same procedure for stresses can also be used, although it is likely to yield less accurate predictions.

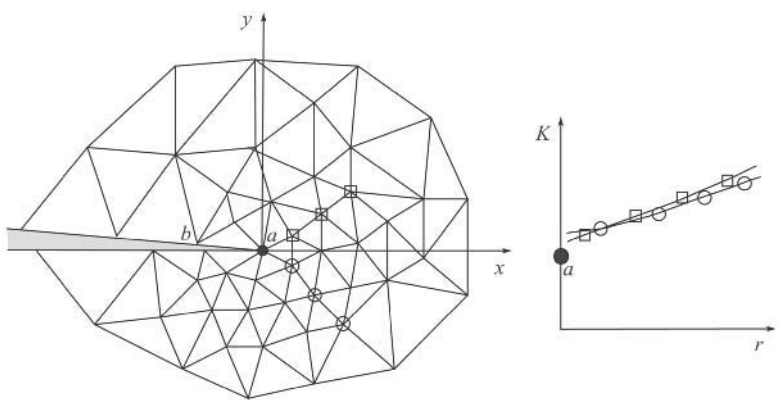

Figure 2.10 Extrapolation of stress intensity factor.

2.5.2 Mode I energy release rate

A direct method for evaluation of the mode I stress intensity factor and the energy release rate is based on the direct definition of G:

$$G = \frac{K_I^2}{E'} = -\frac{\partial \Pi}{\partial a} \cong \frac{\Delta \Pi}{\Delta a} \tag{2.151}$$

and finding the difference in the total strain energy, $\Delta\Pi$, of the system for initial and extended crack lengths a and $a + \Delta a$, respectively. Therefore, the algorithm requires two completely separate analyses, which is a computationally expensive task. The strain energy can be determined from either $\Pi = \mathbf{u}^{\mathrm{T}}\mathbf{K}\mathbf{u}$ in terms of the nodal displacement $\mathbf{u}$ and the global stiffness matrix $\mathbf{K}$, or $\Pi = \mathbf{u}^{\mathrm{T}}P$ in terms of the external load P and displacements $\mathbf{u}$.

2.5.3 Mode I stiffness derivative/virtual crack model

A major problem with the previous method is the requirement for two complete analyses for the evaluation of G. It should be noted, however, that the stiffness matrix of the second analysis (associated with $a + \Delta a$) is only slightly altered from the first one (associated with a). A remedy, therefore, is to use relaxation methods to reduce the computational costs for the second analysis, as independently proposed by Parks (1974) and Hellen and Blackburn (1975), who called the method stiffness derivative and virtual crack model, respectively.

Beginning with the definition of the potential energy:

$$\Pi = \frac{1}{2}\mathbf{u}^{\mathrm{T}}\mathbf{K}\mathbf{u} - \mathbf{u}^{\mathrm{T}}\mathbf{P} \tag{2.152}$$

and

$$-G = \frac{\partial \Pi}{\partial a} = \frac{\partial \mathbf{u}^{\mathrm{T}}}{\partial a}\mathbf{K}\mathbf{u} + \frac{1}{2}\mathbf{u}^{\mathrm{T}}\frac{\partial \mathbf{K}}{\partial a}\mathbf{u} - \frac{\partial \mathbf{u}^{\mathrm{T}}}{\partial a}\mathbf{P} - \mathbf{u}^{\mathrm{T}}\frac{\partial \mathbf{P}}{\partial a} \tag{2.153}$$

and holding the equilibrium condition, results in:

$$G = -\frac{1}{2}\mathbf{u}^{\mathrm{T}}\frac{\partial \mathbf{K}}{\partial a}\mathbf{u} + \mathbf{u}^{\mathrm{T}}\frac{\partial \mathbf{P}}{\partial a} \tag{2.154}$$

The method can be further simplified if the loading is assumed unaltered during the crack extension, $\partial\mathbf{P}/\partial a = 0$:

$$G = -\frac{1}{2}\mathbf{u}^{\mathrm{T}}\frac{\partial \mathbf{K}}{\partial a}\mathbf{u} \tag{2.155}$$

Therefore, the derivative of the stiffness matrix is required for evaluation of G. Instead of cumbersome numerical differentiations, this is usually computed by perturbing the elements around the crack tip (Fig. 2.11) and evaluating the modified part of the stiffness matrix associated with the nodes of elements along the crack extension.

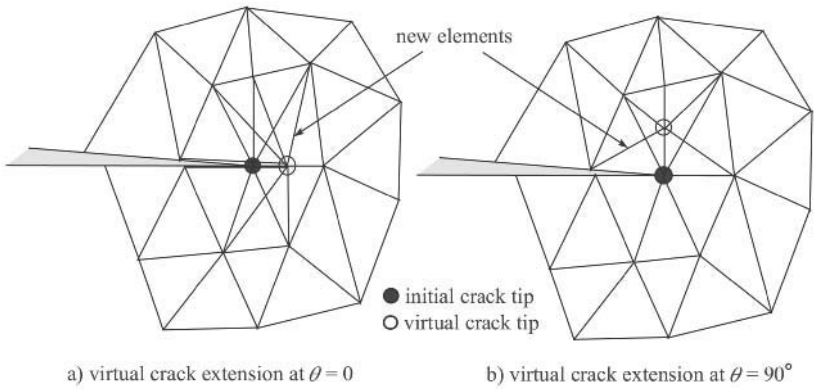

Figure 2.11 Virtual crack models.

In the case of multiple cracking, G can then be numerically evaluated from:

$$G = -\frac{1}{2}\mathbf{u}^{\mathrm{T}}\left\{\sum_{i=1}^{nc}\left(\frac{\partial \mathbf{K}}{\partial a}\right)_i\right\}\mathbf{u} \tag{2.156}$$

where nc is the number of discrete cracks.

2.5.4 Two virtual crack extensions for mixed mode cases

A natural extension to the virtual crack model to include effects of mixed mode fracture is to use the two virtual crack extensions model. This is achieved by applying the virtual crack model to two independent crack extensions, θ_1 and θ_2:

$$G(\theta) = f\left(G_1(\theta_1) + G_2(\theta_2)\right) \tag{2.157}$$

Alternatively, from the known values of G_1 and G_2 at two distinct values of θ, which are not necessarily 0 or $\pi/2$, the value of the mixed $G(\theta)$ can be defined as:

$$G(\theta) = G_1 \cos\theta + G_2 \sin\theta \tag{2.158}$$

A rather simple case with a closed form solution was proposed by Hellen and Blackburn (1975) based on the following expressions of the energy release rates for virtual crack extensions at $\theta = 0$ and $\theta = \pi/2$:

$$G_1 = \frac{K_{\mathrm{I}}^2 + K_{\mathrm{II}}^2}{E'} + \frac{K_{\mathrm{III}}^2}{2\mu} \tag{2.159}$$

$$G_2 = \frac{-2K_{\mathrm{I}}K_{\mathrm{II}}}{E'} \tag{2.160}$$

The procedure can be started by computing the total strain energy U_s for an initial crack length a. Then the crack length is extended to $a+\Delta a$ along $\theta=0$ and $\theta=\pi/2$ to determine G_1 and G_2, respectively. The stress intensity factors are computed from solving simultaneous Eqs. (2.159) and (2.160):

$$K_{\mathrm{I}}=\frac{1}{2}\left(s\pm\sqrt{s^2+\frac{8G_2}{\kappa'}}\right) \tag{2.161}$$

$$K_{\mathrm{II}}=\frac{1}{2}\left(s\mp\sqrt{s^2+\frac{8G_2}{\kappa'}}\right) \tag{2.162}$$

where

$$s=2\sqrt{\frac{G_1-G_2}{\alpha}} \tag{2.163}$$

$$\kappa'=\frac{(1+\nu)(1+\kappa)}{E} \tag{2.164}$$

2.5.5 Single virtual crack extension based on displacement decomposition

Previous techniques were computationally expensive and inefficient because they required at least one complete finite element analysis, followed by two separate analyses or two virtual crack extensions. The present approach, proposed by Ishikawa (1980) and Sha (1984), requires only one analysis (or one virtual crack extension) but it is limited to symmetrical local elements around the crack tip.

With reference to Fig. 2.12, the nodal displacements for a symmetrical local mesh around the crack tip can be decomposed into two local symmetric U^1 and anti-symmetric U^2 components about the crack plane:

$$U=U^1+U^2 \tag{2.165}$$

where

$$U^1=\begin{Bmatrix}u_x^1\\u_y^1\end{Bmatrix}=\frac{1}{2}\begin{Bmatrix}u_x+\hat{u}_x\\u_y-\hat{u}_y\end{Bmatrix} \tag{2.166}$$

$$U^2=\begin{Bmatrix}u_x^2\\u_y^2\end{Bmatrix}=\frac{1}{2}\begin{Bmatrix}u_x-\hat{u}_x\\u_y+\hat{u}_y\end{Bmatrix} \tag{2.167}$$

and

$$\hat{\mathbf{u}}(x, y) = \mathbf{u}(x, -y) \tag{2.168}$$

The fracture energy release rates can also be decomposed into:

$$G_i = G_i(U^i) \qquad i = 1, 2 \tag{2.169}$$

The following solutions based on two local conjugates (U^1, P^1) and (U^2, P^2) can be obtained:

$$G_i = -\frac{1}{2} U^i \frac{\partial \mathbf{K}}{\partial a} U^i + U^i \frac{\partial \mathbf{P}i}{\partial a} \qquad i = 1, 2 \tag{2.170}$$

The two stress intensity factors can then be simply determined:

$$K_i = \sqrt{E' G_i} \qquad i = 1, 2 \tag{2.171}$$

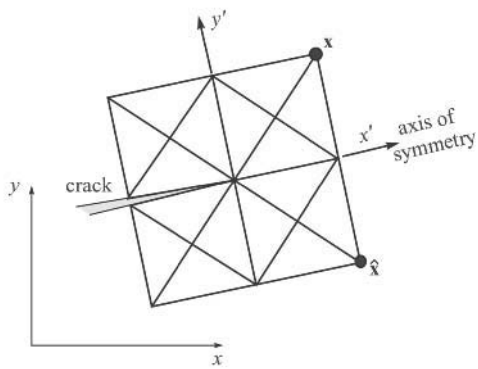

Figure 2.12 Displacement decomposition for a symmetric local mesh around the crack tip.

2.5.6 Quarter point singular elements

Development of the sophisticated singular elements to simulate the singularity condition at crack tips has had an enormous impact on increasing the accuracy of various numerical analyses of LEFM. It was first proposed by Barsoum (1974, 1975, 1976a, 1976b, 1977, 1981) and independently by Henshell and Shaw (1975), as they demonstrated that the $r^{-1/2}$ singularity characteristic of LEFM can be obtained by two-dimensional 8-node isoparametric elements when the midside nodes near the crack tip are placed at the quarter points. A direct consequence was the additional capability of an existing continuum based finite element code for modelling a stress singularity just by shifting the midside nodes of elements adjacent to the crack tip to their quarter point positions. This provides one of the easiest and most powerful techniques for modelling a stress singularity.

Hibbit (1977) and Ying (1982) studied the singularity of rectangular and triangular quarter elements and concluded that the singularity of a rectangular quarter point element is along the edges and diagonal only, whereas in a triangular element it occurs in all radial directions emanating from the crack tip.

Owen and Fawkes (1983) implemented and compared different crack tip elements. They illustrated how those elements can be implemented within a finite element code and discussed various related numerical issues.

In order to demonstrate the way a singular element performs, a simple one-dimensional element with three nodes is considered, as depicted in Fig. 2.13. The physical location of the middle node x_2 may be anywhere in between the other nodes: $-1 < x_2 < 1$, while its location in the mapping parametric space is always at $\xi_2 = 0$. Assuming a second-order basis function, leads to the following position vector x (Macneal 1994),

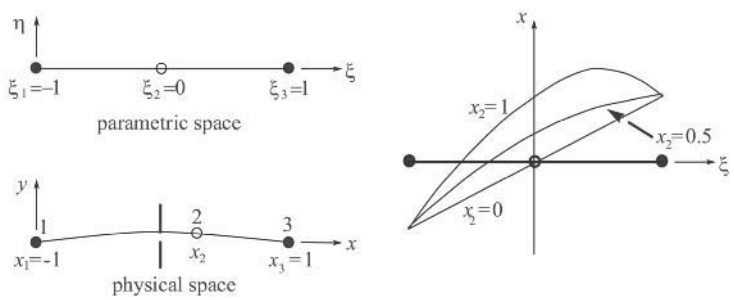

Figure 2.13 1D finite element with three nodes.

$$x = \xi + (1-\xi^2)x_2 \tag{2.172}$$

Eq. (2.172) illustrates that for values of $x_2 > 1/2$, the value of x can lie outside the range of $[-1,+1]$. Physically, the middle node crosses the corner nodes and the element spills over its boundaries.

It can also be observed that placing the middle node at the quarter point ($x_2 = \pm 1/2$) allows the element to simulate a stress singularity at the corner. The strain can be determined from:

$$\varepsilon_x = u_{,x} = u_{,\xi}\xi_{,x} \tag{2.173}$$

which becomes infinity at the corner point $\xi = 1$, provided that the middle point is at the quarter point $x_2 = 1/2$:

$$x_{,\xi} = 0\,,\ \xi_{,x} = \infty \tag{2.174}$$

The same conclusion can be made for two- and three-dimensional elements. The stress tensor in an isoparametric finite element is given by (see Section 3.3):

$$\boldsymbol{\sigma} = \mathbf{D}\mathbf{B}\bar{\mathbf{u}}_i \tag{2.175}$$

where the components of the $\mathbf{B}$ matrix is evaluated from the components of jacobian $\mathbf{J}$. In order to simulate a singular stress field, Eq. (2.175) requires $\mathbf{B}$ to be singular, as the other two components are constants. Consequently, from Eq. (3.7) the determinant of $\mathbf{J}$ must vanish at the crack tip. This is possible only if either one of the diagonal terms becomes zero.

$$\mathbf{J} = \begin{bmatrix} \dfrac{\partial x}{\partial \xi} & \dfrac{\partial y}{\partial \xi} \\ \dfrac{\partial x}{\partial \eta} & \dfrac{\partial y}{\partial \eta} \end{bmatrix}, \quad \mathbf{J}^{-1} = \frac{1}{\det \mathbf{J}} \begin{bmatrix} \dfrac{\partial y}{\partial \eta} & \dfrac{\partial y}{\partial \xi} \\ -\dfrac{\partial x}{\partial \eta} & \dfrac{\partial x}{\partial \xi} \end{bmatrix} \tag{2.176}$$

Now referring to Eq. (2.176), it is found that this is achieved only if the midside node of the element is located at $x_2 = 1/2\ (l/4)$ instead of $x_2 = 0\ (l/2)$. As a result, the stresses and strains at the nearby corner node will become singular (Fig. 2.14).

It can be proved that the quarter point element approximates to the displacement field along $\eta = -1$ in the general form of:

$$u = A_1 + A_2 x + A_3 \left(\frac{x}{l}\right)^{\frac{1}{2}} \tag{2.177}$$

which is an indication of the order of singularity of $r^{-1/2}$ for the strain (derivative of displacement) and so the stress field.

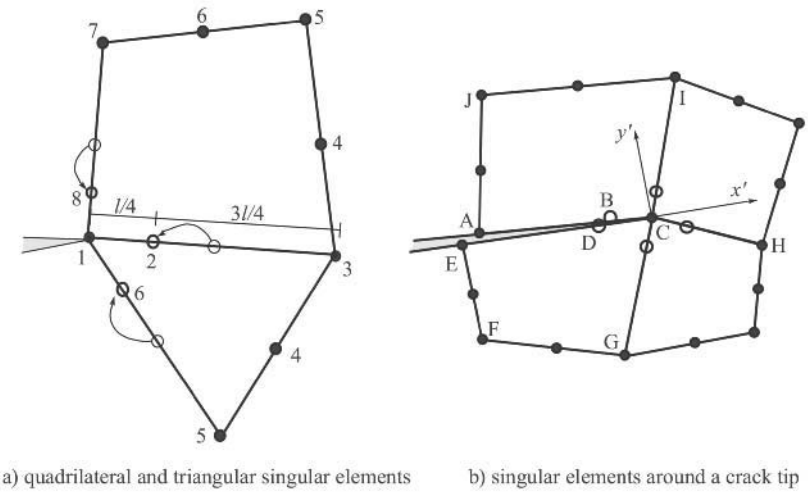

a) quadrilateral and triangular singular elements b) singular elements around a crack tip

Figure 2.14 a) Quarter point (singular) quadrilateral and triangular finite elements and b) four quarter point elements around a crack tip.

It should be mentioned that the quarter point singular quadrilateral elements provide radial singular strain and stress fields along the corresponding edge and diagonal only, and the strain and stress fields remain finite (not singular) in other directions. Therefore, using four singular elements around node C in Fig. 2.14b generates four independent radial strain fields along edges CA, CI, CH, CG and CE, and non-singular strain fields elsewhere.

In contrast, triangular quarter elements create singularity in all radial directions (inside the element) emanating from the crack tip. They also raise the number of radial rays around a crack tip representing singular strain fields.

Singular finite elements allow for an efficient and fast approach for evaluation of the stress intensity factors (Shih *et al.* 1976). Referring to Fig. 2.14b, the basic idea is to equate the local displacement field in the quarter point singular element with the theoretical solution:

$$u_i = u_{i\mathrm{C}} + (-3u_{i\mathrm{C}} + 4u_{i\mathrm{B}} - u_{i\mathrm{A}})\sqrt{\frac{r}{l}} + (2u_{i\mathrm{C}} - 4u_{i\mathrm{B}} + 2u_{i\mathrm{A}})\frac{r}{l} \qquad i = x', y' \tag{2.178}$$

$$u_i = u_{i\mathrm{C}} + (-3u_{i\mathrm{C}} + 4u_{i\mathrm{D}} - u_{i\mathrm{E}})\sqrt{\frac{r}{l}} + (2u_{i\mathrm{C}} - 4u_{i\mathrm{D}} + 2u_{i\mathrm{E}})\frac{r}{l} \qquad i = x', y' \tag{2.179}$$

where $u_{x'}$ and $u_{y'}$ are the local displacements of the nodes along the crack in the singular element, with x' aligned with the crack axis, as depicted in Fig. 2.14b.

On the other hand, the analytical solution for u_y can be obtained from Eq. (2.71) along the crack axis:

$$u_y = K_{\mathrm{I}}\frac{\kappa+1}{2\mu}\sqrt{\frac{r}{2\pi}} \tag{2.180}$$

Equating $u_{y'} = u_y$, results in:

$$K_{\mathrm{I}} = \frac{1}{2}\frac{2\mu}{\kappa+1}\sqrt{\frac{2\pi}{l}}(-3u_{y'\mathrm{C}} + 4u_{y'\mathrm{B}} - u_{y'\mathrm{A}}) \tag{2.181}$$

which can be generalised for mixed mode problems,

$$K_{\mathrm{I}} = \frac{1}{2}\frac{2\mu}{\kappa+1}\sqrt{\frac{2\pi}{l}}\left[-3u_{y'\mathrm{C}} + 4(u_{y'\mathrm{B}} - u_{y'\mathrm{D}}) - (u_{y'\mathrm{A}} - u_{y'\mathrm{E}})\right] \tag{2.182}$$

$$K_{\mathrm{II}} = \frac{1}{2}\frac{2G}{\kappa+1}\sqrt{\frac{2\pi}{l}}\left[-3u_{x'\mathrm{C}} + 4(u_{x'\mathrm{B}} - u_{x'\mathrm{D}}) - (u_{x'\mathrm{A}} - u_{x'\mathrm{E}})\right] \tag{2.183}$$

Theoretically, the same procedure may be performed on stress components. The problem is that the stress field is discontinuous across element edges. In any case, extension of the method to the case of more than one singular element, and possible

discrepancy of the results obtained from different singular elements, remains unresolved. Nevertheless, the method has remained popular because of the advantage of being exceptionally simple and fast.

2.6 ELASTOPLASTIC FRACTURE MECHANICS (EPFM)

Under the assumptions of linear elastic fracture mechanics, the stress at the crack tip is theoretically infinite. Consequently, it may usually lead to conservative and expensive solutions as it does not account for plastification at the crack tip. From a physical point of view, however, no material can withstand infinite stress, and a small plastic/fractured zone will be formed around the crack tip. As a result, an extension to ductile fracture or elastoplastic fracture mechanics (EFPM) is required.

In this section, first the problem of the size of the plastic zone is addressed, using various levels of approximations. Then the concepts of the crack opening displacement (COD) and the *J* integral are discussed. Theoretically, the models can be extended to more sophisticated plasticity models for simulation of material nonlinear behaviour around the crack tip.

2.6.1 Plastic zone

2.6.1.1 *First-order uniaxial stress criterion*

Here, only the uniaxial stress state normal to the crack axis is considered. The simplest estimate of the size of the plastic zone is obtained by equating the uniaxial stress σ_{yy} to the yield stress σ_{yld}. Recalling Eq. (2.66) (for plane stress problems),

$$\sigma_{yy} = \frac{K_{\text{I}}}{\sqrt{2\pi r}} \cos\frac{\theta}{2}\left(1+\sin\frac{\theta}{2}\sin\frac{3\theta}{2}\right) \tag{2.184}$$

the size of the plastic zone, $r = r_{\text{p}}$, can be obtained at $\theta = 0$,

$$\sigma_{yy} = \frac{K_{\text{I}}}{\sqrt{2\pi r_{\text{p}}}} = \sigma_{\text{yld}} \tag{2.185}$$

or in terms of the stress intensity factor, $K_{\text{I}} = \sigma_0\sqrt{\pi a}$

$$r_{\text{p}} = \frac{1}{2\pi}\frac{K_{\text{I}}^2}{\sigma_{\text{yld}}^2} = \frac{a}{2}\left(\frac{\sigma_0}{\sigma_{\text{yld}}}\right)^2 \tag{2.186}$$

Similarly, the size of the plastic zone for mode II for both plane stress and plane strain problems can be obtained from:

$$r_{\mathrm{p}} = \frac{3}{2\pi}\frac{K_{\mathrm{II}}^2}{\sigma_{\mathrm{yld}}^2} \tag{2.187}$$

The main problem with this approximation is that it simply ignores all stresses exceeding σ_{yld} (Fig. 2.15a). As a result, equilibrium is no longer satisfied.

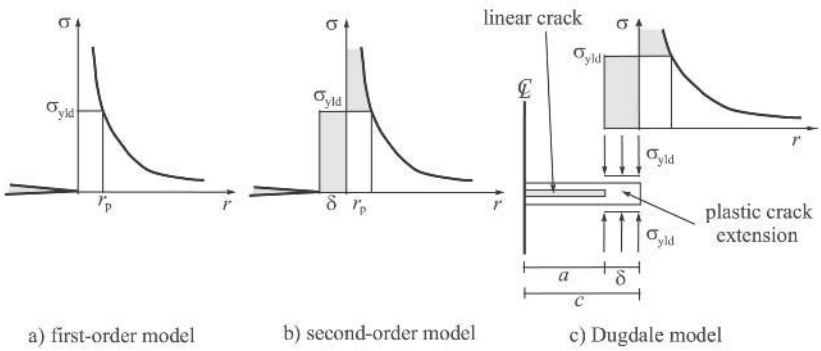

Figure 2.15 First- and second-order approximations of the plastic zone, and the Dugdale model.

2.6.1.2 *Second-order uniaxial stress criterion*

In an alternative approach to avoid violation of equilibrium equations, Irwin (1960) developed a second-order approximation for the plastic zone based on the stress redistribution occurring at the crack tip. In this model, the area under the stress curve which was eliminated in the first order approach, is redistributed to satisfy equilibrium requirements (Fig. 2.15b),

$$\int_0^{r_{\mathrm{p}}} \frac{K_{\mathrm{I}}}{\sqrt{2\pi r}}\,\mathrm{d}r = \left(r_{\mathrm{p}} + \delta\right)\sigma_{\mathrm{yld}} \tag{2.188}$$

The final solution is then obtained as:

$$\delta = r_{\mathrm{p}} = \frac{1}{\pi}\frac{K_{\mathrm{I}}^2}{\sigma_{\mathrm{yld}}^2} = a\left(\frac{\sigma_0}{\sigma_{\mathrm{yld}}}\right)^2 \tag{2.189}$$

implying that the second-order size is twice the first-order size. Thus, the first-order solution r_{p} (Eq.(2.187)) may still be used with an effective crack length of $a + r_{\mathrm{p}}$ extending to the centre of the plastic zone. Thus,

$$K_{\mathrm{I}} = \sigma_0\sqrt{\pi(a + r_{\mathrm{p}})} \tag{2.190}$$

2.6.1.3 *Dugdale criterion*

Another alternative to satisfy equilibrium equations was proposed by Dugdale (1960) based on the assumption of replacing the actual physical crack length ($2a$) by a total effective crack length $2c$, where $c = a + \delta$ (Fig. 2.15c). Dugdale assumed that a closing constant stress σ_{yld} is applied over the length δ, causing a negative K_{yld}. As a result, the combined model requires the overall stress intensity factor to vanish: $K_{\text{combined}} = K + K_{\text{yld}} = 0$, determining the length c or δ.

Using the Westergaard's approach, the solution for c is obtained from:

$$\frac{a}{c} = \cos\left(\frac{\pi}{2}\frac{\sigma_0}{\sigma_{\text{yld}}}\right) \tag{2.191}$$

Then, applying Taylor's expansion and neglecting higher order terms results in (for plane stress):

$$r_{\text{p}} = \frac{\pi^2}{8}\left(\frac{\sigma_0}{\sigma_{\text{yld}}}\right)^2 a = \frac{\pi}{8}\left(\frac{K_{\text{I}}}{\sigma_{\text{yld}}}\right)^2 \tag{2.192}$$

and for plane strains,

$$r_{\text{p}} = \frac{\pi}{8}\left(\frac{K_{\text{I}}}{\sqrt{3}\sigma_{\text{yld}}}\right)^2 \tag{2.193}$$

2.6.1.4 *First-order multiaxial yield criterion*

In this section, the idea of a plastic zone is further extended to the first-order multiaxial conditions to include points other than $\theta = 0$. The idea is to assume that yielding would occur when the effective stress σ_{eff} computed from any specified yield criterion reaches σ_{yld}.

In order to provide sample explicit solutions, the Von Mises yield criterion is considered:

$$\sigma_{\text{eff}} = \frac{1}{\sqrt{2}}\left[(\sigma_1 - \sigma_2)^2 + (\sigma_2 - \sigma_3)^2 + (\sigma_3 - \sigma_1)^2\right] \tag{2.194}$$

where principal stresses σ_1, σ_2 and σ_3 are related to K_{I} through Eqs. (2.65)–(2.67). The size of the plastic zone $r_{\text{p}}(\theta)$ can be evaluated for plane strain problems as:

$$r_{\text{p}}(\theta) = \frac{1}{4\pi}\frac{K_{\text{I}}}{\sigma_{\text{yld}}^2}\left[\frac{3}{2}\sin^2\theta + (1-2\nu)^2(1+\cos\theta)\right] \tag{2.195}$$

and a much larger size for plane stress conditions:

$$r_{\mathrm{p}}(\theta)=\frac{1}{4\pi}\frac{K_{\mathrm{I}}}{\sigma_{\mathrm{yld}}^{2}}\left[1+\frac{3}{2}\sin^{2}\theta+\cos\theta\right] \tag{2.196}$$

2.6.2 Crack tip opening displacements (CTOD)

In a totally different approach, a local criterion based on the crack tip opening displacement (CTOD) has been proposed to account for elastoplastic behaviour around the crack tip (Cottrell 1961, Wells 1963). In LEFM and brittle fracture, sharp cracks are considered and the CTOD is always zero. In contrast, CTOD is not negligible in ductile fracture and elastoplastic fracture mechanics due to relatively large deformation and blunting of the crack (Fig. 2.16).

Similar to the method of determining the size of the plastic zone, two first- and second-order CTOD approaches are available.

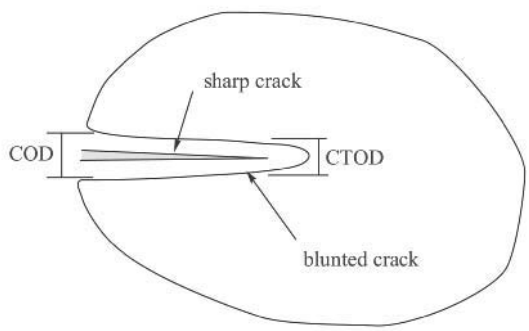

Figure 2.16 Estimation of the CTOD.

2.6.2.1 *First-order* CTOD

The first-order solution for CTOD is based on Irwin's solution for the mode I vertical displacement of a point next to the crack tip, as depicted in Fig. 2.16.

$$u_{y}=\frac{K_{\mathrm{I}}}{2\mu}\left[\frac{r}{2\pi}\right]^{\frac{1}{2}}\sin\frac{\theta}{2}\left[\kappa+1-2\cos^{2}\frac{\theta}{2}\right] \tag{2.197}$$

Substituting $\theta=\pm\pi$ results in the evaluation of crack tip opening (COD) at a distance r:

$$\mathrm{COD}=2u_{y}=\frac{\kappa+1}{\mu}K_{\mathrm{I}}\sqrt{\frac{r}{2\pi}} \tag{2.198}$$

For $r = r_p$, where r_p is the Irwin plastic zone, the final crack tip opening (CTOD) estimation is obtained:

$$\mathrm{CTOD} = \frac{4}{\pi}\frac{K_I^2}{E\sigma_{yld}} \tag{2.199}$$

2.6.2.2 *Second-order* CTOD

The second-order CTOD formulation is based on the application of the second-order Dugdale model along the crack for determination of COD (Kanninen 1984):

$$u_y(x) = \frac{2}{\pi}\frac{a\sigma_{yld}}{E}\left\{\log\left|\frac{e+\sqrt{c^2-x^2}}{e-\sqrt{c^2-x^2}}\right| + \frac{x}{a}\log\left|\frac{xe+a\sqrt{c^2-x^2}}{xe-a\sqrt{c^2-x^2}}\right|\right\} \qquad 0 \le x \le c \tag{2.200}$$

with $e^2 = c^2 - a^2$. Eq. (2.200) is further simplified for $x = a$

$$u_y(a) = \frac{4}{\pi}\frac{a\sigma_{yld}}{E}\log\frac{c}{a} \tag{2.201}$$

Using Eq. (2.191) results in:

$$\mathrm{CTOD} = 2u_y = \frac{8}{\pi}\frac{a\sigma_{yld}}{E}\log\left[\sec\frac{\pi}{2}\frac{\sigma}{\sigma_{yld}}\right] \tag{2.202}$$

and adopting a series expansion leads to:

$$\mathrm{CTOD} = \frac{K^2}{E\sigma_{yld}}\left[1 + \frac{\pi^2}{24}\frac{\sigma^2}{\sigma_{yld}^2} + \cdots\right] \tag{2.203}$$

Recalling the definition of the energy release rate as $G = K^2/E'$, the following approximation can be assumed:

$$\mathrm{CTOD} = \frac{G}{\sigma_{yld}} \tag{2.204}$$

2.6.3 *J* integral

In a pioneering work, Eshelby (1956, 1974) defined a number of contour integrals that were path independent by virtue of the theorem of energy conservation. This was achieved while he was studying dislocations in elastic domains, and he did not realise its

importance or applications in fracture mechanics. It was up to Rice and Rosengren (1968) to notice the importance of the J integral as a criterion for crack growth in fracture mechanics (Anderson 1995). While the original introduction of the J integral was limited to problems with no unloading, no internal stress/strains and no crack face tractions, the new developments have now been well extended to cohesive crack and dynamic problems. Path independency of J also allows for evaluation of linear and nonlinear elastic energy release rates and elastoplastic work far from the crack tip.

First, the problem is considered without the presence of the body force and crack tractions ($\mathbf{f}^{\mathrm{b}} = \mathbf{f}^{\mathrm{c}} = 0$). The two-dimensional form of one of these integrals can be written as:

$$J = \oint_{\Gamma} \left(W_{\mathrm{s}} \mathrm{d}y - \mathbf{t} \frac{\partial \mathbf{u}}{\partial x} \mathrm{d}\Gamma \right) \tag{2.205}$$

and

$$W_{\mathrm{s}} = \int_0^{\varepsilon} \sigma_{ij} \mathrm{d}\varepsilon_{ij} \tag{2.206}$$

is the strain energy density, Γ is a closed counter-clockwise contour, $\mathrm{d}\Gamma$ is the differential element of the arc along the path Γ, $\mathbf{t} = \boldsymbol{\sigma}\mathbf{n}$ is the traction vector on a plane defined by the outward normal $\mathbf{n}$, and $\mathbf{u}$ is the displacement vector (Fig. 2.17a).

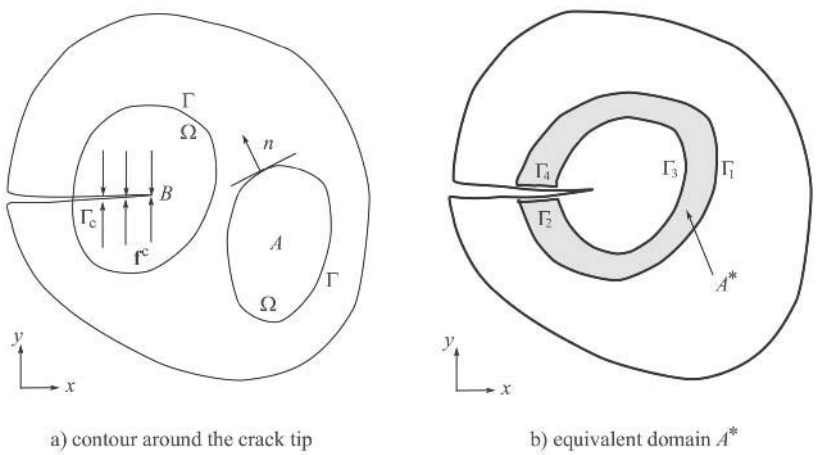

a) contour around the crack tip b) equivalent domain A^*

Figure 2.17 Definition of the J integral around a crack, and the equivalent domain A^*.

To elaborate the path independency of the J integral for crack problems, consider a body in the state of equilibrium with continuous stress and displacement gradients, as depicted in Fig. 2.17. For this body, Eq. (2.205) is equal to zero for any closed contour; $J = 0$. With reference to Fig. 2.17b, a closed path $\Gamma = \Gamma_1 + \Gamma_2 + \Gamma_3 + \Gamma_4$ is constructed, where Γ_1 and Γ_3 are arbitrary contours, and Γ_2 and Γ_4 are placed on opposite faces of the traction free crack:

$$J = J_{\Gamma 1} + J_{\Gamma 2} + J_{\Gamma 3} + J_{\Gamma 4} = 0 \tag{2.207}$$

The contributions to J from Γ_2 and Γ_4 vanish, because both $\mathrm{d}y$ and t_i are zero on Γ_2 and Γ_4.

$$J = J_{\Gamma 1} + J_{\Gamma 3} = 0 \tag{2.208}$$

It can be concluded that the absolute values of the J integral evaluated over arbitrary paths Γ_1 and Γ_3 remain identical; an indication of the path independency of J. As a result, if a contour begins from one crack surface and ends at the other face, it can be used to determine of the J integral.

Selection of the size and shape of the appropriate contour curve for a specific problem requires complementary numerical studies. Practically, they should also be related to the geometry of the crack and the finite element model, as will be further discussed in the following sections.

It can be shown that when J is applied along a contour around a crack tip, it represents the change in potential energy for a virtual crack extension $\mathrm{d}a$. The total potential energy of a two-dimensional domain including a traction free crack that is surrounded by a contour curve Γ under quasi-static conditions and in the absence of body forces can be defined as:

$$\Pi = \int_{\Omega} W_{\mathrm{s}} \mathrm{d}\Omega - \int_{\Gamma} t_i u_i \mathrm{d}\Gamma \tag{2.209}$$

For a virtual crack extension $\mathrm{d}a$, the change in potential energy is

$$\frac{\mathrm{d}\Pi}{\mathrm{d}a} = \int_{\Omega} \frac{\mathrm{d}W_{\mathrm{s}}}{\mathrm{d}a} \mathrm{d}\Omega - \oint_{\Gamma} \left[t_i \frac{\mathrm{d}u_i}{\mathrm{d}a} + \frac{\mathrm{d}t_i}{\mathrm{d}a} u_i \right] \mathrm{d}\Gamma \tag{2.210}$$

Applying the divergence theorem and omitting zero terms, results in

$$-\frac{\mathrm{d}\Pi}{\mathrm{d}a} = \oint_{\Gamma} \left(W_{\mathrm{s}} \mathrm{d}y - \mathbf{t} \frac{\partial \mathbf{u}}{\partial x} \mathrm{d}\Gamma \right) \tag{2.211}$$

which is similar to Eq. (2.205), hence

$$J = -\frac{\mathrm{d}\Pi}{\mathrm{d}a} \tag{2.212}$$

This is equivalent to the definition of the fracture energy release for linear elastic materials, $-\partial\Pi / \partial a = G$,

$$J = G \tag{2.213}$$

Eq. (2.212) can also be used to define the energy release rate for a unit crack extension in nonlinear elastic materials.

2.6.4 Plastic crack tip fields

In order to illustrate how the concept of the *J* integral can be used in nonlinear analysis, a typical elastoplastic problem based on the Ramberg–Osgood power hardening law is considered (Hutchinson 1968, 1990),

$$\frac{\varepsilon}{\varepsilon_{\text{yld}}} = \frac{\sigma}{\sigma_{\text{yld}}} + k_0 \left(\frac{\sigma}{\sigma_{\text{yld}}} \right)^n \tag{2.214}$$

where n is the strain hardening exponent, and k_0 is a dimensionless constant. Neglecting the elastic strain in the vicinity of the crack tip,

$$\varepsilon(r) = \frac{k_1}{r^{\frac{n}{n+1}}} \qquad \sigma(r) = \frac{k_2}{r^{\frac{1}{n+1}}} \tag{2.215}$$

or

$$\varepsilon_{ij} = k_3 \left(\frac{J}{r} \right)^{\frac{1}{n+1}} \tag{2.216}$$

$$\sigma_{ij} = k_4 \left(\frac{J}{r} \right)^{\frac{n}{n+1}} \tag{2.217}$$

where coefficients k_i are constants. The relationship between J and the crack tip displacement, stress and strain fields can be expressed as:

$$u_i = k_0 \varepsilon_{\text{yld}} r \left(\frac{J}{k_0 \sigma_{\text{yld}} \varepsilon_{\text{yld}} I_n r} \right)^{\frac{n}{n+1}} \overline{u}_i(\theta, n) \tag{2.218}$$

$$\sigma_{ij} = \sigma_{\text{yld}} \left(\frac{EJ}{k_0 \sigma_{\text{yld}}^2 I_n r} \right)^{\frac{1}{n+1}} \overline{\sigma}_{ij}(\theta, n) \tag{2.219}$$

$$\varepsilon_{ij} = \frac{k_0 \sigma_{\text{yld}}}{E} \left(\frac{EJ}{k_0 \sigma_{\text{yld}}^2 I_n r} \right)^{\frac{n}{n+1}} \overline{\varepsilon}_{ij}(\theta, n) \tag{2.220}$$

where I_n is an integration constant which depends on the stress–strain curve, and $\overline{\sigma}$ and $\overline{\varepsilon}$ are dimensionless geometric functions of n and θ.

2.6.5 Generalisation of J

The original definition of J can be regarded as the first component of a more general path independent vector:

$$J_k = \int_{\Gamma} \left\{ W_s n_k - \mathbf{t} \frac{\partial \mathbf{u}}{\partial x_k} \right\} \mathrm{d}\Gamma \tag{2.221}$$

or simply

$$J_1 = \int_{\Gamma} \left\{ W_s \mathrm{d}y - \mathbf{t} \frac{\partial \mathbf{u}}{\partial x} \mathrm{d}\Gamma \right\} \tag{2.222}$$

$$J_2 = \int_{\Gamma} \left\{ W_s \mathrm{d}x - \mathbf{t} \frac{\partial \mathbf{u}}{\partial y} \mathrm{d}\Gamma \right\} \tag{2.223}$$

The generalised J also satisfies the following relation for crack extensions parallel and perpendicular to the crack (Hellen and Blackburn 1975)

$$J = J_1 - iJ_2 = \frac{1}{E'} (K_{\mathrm{I}}^2 + K_{\mathrm{II}}^2 + 2iK_{\mathrm{I}}K_{\mathrm{II}}) \tag{2.224}$$

2.6.5.1 *Effect of crack surface traction*

Karlsson and Backlund (1978) extended the concept of the J integral to account for the effect of crack surface tractions by simply extending the definition of the contour path to include the crack surfaces:

$$J = \int_{\Gamma} \left\{ W_s \mathrm{d}y - \mathbf{t} \frac{\partial \mathbf{u}}{\partial x} \mathrm{d}\Gamma \right\} - \int_{\Gamma_c} \mathbf{f}^c \frac{\partial \mathbf{u}}{\partial x} \mathrm{d}\Gamma \tag{2.225}$$

where Γ_c is the portion of the crack surfaces between the points in between the two ends of Γ and $\mathbf{f}^c$ is the crack surface traction vector, as depicted in Fig. 2.17a.

2.6.5.2 *Effect of body force*

In the case of present body force, $\mathbf{f}^b$, the equilibrium equation can be written as:

$$\sigma_{ij,j} + \mathbf{f}_i^b = 0 \tag{2.226}$$

and a modified J integral has to be defined (Atluri 1982):

$$J = \int_{\Gamma} \left\{ W_s \mathrm{d}y - \mathbf{t} \frac{\partial \mathbf{u}}{\partial x} \mathrm{d}\Gamma \right\} - \int_{\Omega} \mathbf{f}^b \frac{\partial \mathbf{u}}{\partial x} \mathrm{d}\Omega \tag{2.227}$$

2.7 NUMERICAL METHODS BASED ON THE *J* INTEGRAL

The equivalency of the J integral and G within the context of LEFM allows for evaluation of J according to the available approaches previously discussed for the energy release rate. In this section, however, algorithms for direct evaluation of J are presented.

At present, most simulations are based on the direct evaluation of the J integral, which is more compatible with the structure of the finite element method. The results will then be used to determine the stress intensity factor and the energy release rate from the classical concepts of fracture mechanics.

2.7.1 Nodal solution

First consider the rather simple case where stresses are known at the nodes, then the numerical evaluation of J would become relatively simple (Fig. 2.18a).

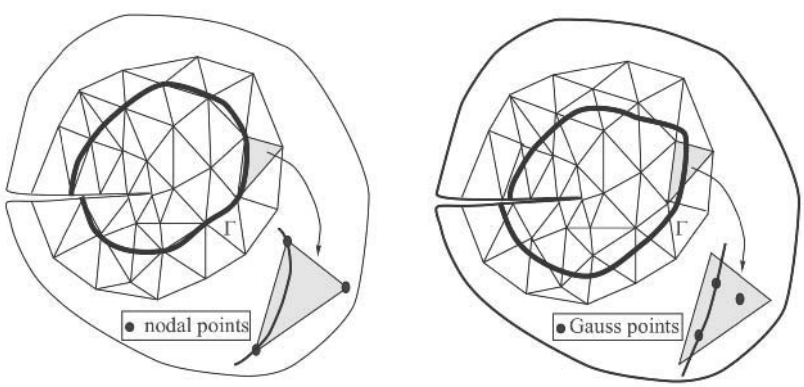

Figure 2.18 Contour of J integral passing through finite element nodes or Gauss points.

Beginning with a modification of Eq. (2.222) for a crack along the ξ in a plane stress problem:

$$J = \int_{\Gamma} W_s \mathrm{d}\eta - \int_{\Gamma} \mathbf{t} \cdot \frac{\partial \mathbf{u}}{\partial \xi} \mathrm{d}\Gamma \tag{2.228}$$

or

$$J = \int_{\Gamma} W_{\mathrm{s}} \mathrm{d}\eta - \int_{\Gamma} (\sigma_n, \sigma_t) \begin{bmatrix} \dfrac{\partial u_n}{\partial \xi} \\ \dfrac{\partial u_t}{\partial \xi} \end{bmatrix} \mathrm{d}\Gamma \tag{2.229}$$

where

$$W_{\mathrm{s}} = \frac{1}{2E}(\sigma_{xx} + \sigma_{yy})^2 + \frac{1+2\nu}{E}(\sigma_{xy}^2 - \sigma_{xx}\sigma_{yy}) \tag{2.230}$$

$$\sigma_n = \sigma_{xx} \cos^2 \theta + \sigma_{xy} \sin\theta \cos\theta + \sigma_{yy} \sin^2 \theta \tag{2.231}$$

$$\tau_t = (\sigma_{yy} - \sigma_{xx}) \sin\theta \cos\theta + \sigma_{xy}(\cos^2 \theta - \sin^2 \theta) \tag{2.232}$$

$$u_n = u_x \cos\theta + u_y \sin\theta \tag{2.233}$$

$$u_t = -u_x \sin\theta + u_y \sin\theta \cos\theta \tag{2.234}$$

The J integral can be calculated by evaluation of the values of the following expression between adjacent nodes and computing the total sum around the contour,

$$\begin{aligned} J = & \int w(\sin\theta \mathrm{d}x + \cos\theta \mathrm{d}y) \\ & - \int [\sigma_{xx}\varepsilon_{xx} \cos\theta \mathrm{d}y + \sigma_{xy}\varepsilon_{yy} \sin\theta \mathrm{d}y - \sigma_{xy}\varepsilon_{xx} \cos\theta \mathrm{d}x - \sigma_{yy}\varepsilon_{yy} \sin\theta \mathrm{d}x \\ & + \sigma_{xy}\varepsilon_{xy} \cos\theta \mathrm{d}y - \sigma_{xy}\varepsilon_{xy} \sin\theta \mathrm{d}x + (\sigma_{xx} \sin\theta - \sigma_{xy} \cos\theta) \mathrm{d}u_n \\ & - (\sigma_{yy} \sin\theta + \sigma_{xy} \sin\theta) \mathrm{d}u_t] \end{aligned} \tag{2.235}$$

where θ is the angle between the normal to the contour and x direction at each node.

2.7.2 General finite element solution

Most standard finite element codes, however, only provide Gauss point stresses, and hence care must be exercised in properly determining the J integral along a path passing through them. Consider a crack to be along the x axis as illustrated in Fig. 2.18b. From the definition of J,

$$J = -\frac{\partial \Pi}{\partial a} = \int_{\Gamma} \left(W_{\mathrm{s}} \mathrm{d}y - \mathbf{t} \frac{\partial \mathbf{u}}{\partial x} \mathrm{d}\Gamma \right) \tag{2.236}$$

Defining the traction and displacement vectors, the strain energy density and the arc length in terms of the problem specifications,

$$W_{\mathrm{s}} = \frac{1}{2}\left[\sigma_{xx}\frac{\partial u_x}{\partial x} + \sigma_{xy}\left(\frac{\partial u_x}{\partial y} + \frac{\partial u_y}{\partial x}\right)\frac{\partial u_x}{\partial x} + \sigma_{yy}\frac{\partial u_y}{\partial y}\right] \tag{2.237}$$

$$\mathrm{d}y = \frac{\partial y}{\partial \eta}\mathrm{d}\eta \tag{2.238}$$

$$\mathbf{t}\cdot\frac{\partial \mathbf{u}}{\partial x} = \left[\left(\sigma_{xx}n_1 + \sigma_{xy}n_2\right)\frac{\partial u_x}{\partial x} + \left(\sigma_{xy}n_1 + \sigma_{yy}n_2\right)\frac{\partial u_y}{\partial x}\right] \tag{2.239}$$

$$\mathrm{d}\Gamma = \sqrt{\left(\frac{\partial x}{\partial \eta}\right)^2 + \left(\frac{\partial y}{\partial \eta}\right)^2}\,\mathrm{d}\eta \qquad (\text{at} \quad \mathrm{d}\xi = \text{constant}) \tag{2.240}$$

results in,

$$\begin{aligned} J = \int_{\Gamma}\Bigg\{&\frac{1}{2}\left[\sigma_{xx}\frac{\partial u_x}{\partial x} + \sigma_{xy}\left(\frac{\partial u_x}{\partial y} + \frac{\partial u_y}{\partial x}\right)\frac{\partial u_x}{\partial x} + \sigma_{yy}\frac{\partial u_y}{\partial y}\right]\frac{\partial y}{\partial \eta} \\ &-\left[\left(\sigma_{xx}n_1 + \sigma_{xy}n_2\right)\frac{\partial u_x}{\partial x} + \left(\sigma_{xy}n_1 + \sigma_{yy}n_2\right)\frac{\partial u_y}{\partial x}\right]\sqrt{\left(\frac{\partial x}{\partial \eta}\right)^2 + \left(\frac{\partial y}{\partial \eta}\right)^2}\Bigg\}\mathrm{d}\eta \end{aligned} \tag{2.241}$$

Evaluation of Eq. (2.241) is performed by a Gauss integration rule along the contour path Γ:

$$J = \sum_{g=1}^{ng} W_g I_g(\xi_g, \eta_g) \tag{2.242}$$

where W_g is the Gauss weighting factor, ng is the number of integration points and I_g is the integrand evaluated at each Gauss point g:

$$\begin{aligned} I_g = \Bigg\{&\frac{1}{2}\left[\sigma_{xx}\frac{\partial u_x}{\partial x} + \sigma_{xy}\left(\frac{\partial u_x}{\partial y} + \frac{\partial u_y}{\partial x}\right)\frac{\partial u_x}{\partial x} + \sigma_{yy}\frac{\partial u_y}{\partial y}\right]\frac{\partial y}{\partial \eta} \\ &-\left[\left(\sigma_{xx}n_1 + \sigma_{xy}n_2\right)\frac{\partial u_x}{\partial x} + \left(\sigma_{xy}n_1 + \sigma_{yy}n_2\right)\frac{\partial u_y}{\partial x}\right]\sqrt{\left(\frac{\partial x}{\partial \eta}\right)^2 + \left(\frac{\partial y}{\partial \eta}\right)^2}\Bigg\}_g \end{aligned} \tag{2.243}$$

The path is intentionally designed so the same integration points associated with the element stiffness matrix can be used. Therefore, the contour path must pass through the finite element Gauss points, as depicted in Fig. 2.18b. Consequently, all the terms of Eq. (2.243) are known: the stress components are available at the Gauss points, strains can be determined from derivatives of the shape functions (**B** matrix), and $\partial y/\partial \eta$ is a component of the known Jacobian matrix **J**.

2.7.3 Equivalent domain integral (EDI) method

Li *et al.* (1985) proposed the equivalent domain integral method as an alternative approach, which requires only one analysis. According to Fig. 2.17b, the J integral can be defined as (Li *et al.* 1985, Babuska and Miller 1984):

$$J = \int_{A^*} \left[\sigma_{ij} \frac{\partial u_i}{\partial x_1} - W_s \delta_{1i} \right] \frac{\partial q}{\partial x_i} \mathrm{d}A \tag{2.244}$$

where q is an arbitrary smoothing function which is equal to unity on Γ_3 and zero on Γ_1. In fact, the contour integral has been replaced by an equivalent area integral, which is more suited to finite element solutions.

The value of q within an element can be interpolated as

$$q(\mathbf{x}) = \sum_{i=1}^{n} N_i(\mathbf{x}) q_i \tag{2.245}$$

where n is the number of nodes per element, q_i are the nodal values of q, and N_i are the element shape functions. Evaluation of J then follows:

$$J = \sum_{A^*} \sum_{g=1}^{ng} \left\{ \left[\left(\sigma_{ij} \frac{\partial u_i}{\partial x_1} - W_s \delta_{1i} \right) \frac{\partial q}{\partial x_i} \right] \det\left(\frac{\partial x_j}{\partial \xi_k} \right) \right\}_g W_g \tag{2.246}$$

In FEM, the inner contour Γ_3 is often taken as the crack tip, and so A^* naturally corresponds to the area inside Γ_1. The boundary Γ_1 should also coincide with element boundaries to facilitate numerical calculations.

2.7.4 Interaction integral method

In the interaction integral method, auxiliary fields are introduced and superimposed onto the actual fields satisfying the boundary value problem (Sih *et al.* 1965). Stresses and strains for the auxiliary state should be chosen so as to satisfy both the equilibrium equation and the traction free boundary condition on the crack surface in the A^* area. These auxiliary fields are suitably selected in order to find a relationship between the mixed mode stress intensity factors and the interaction integrals. The contour J integral for the sum of the two states can be defined as

$$J = J^{\mathrm{act}} + J^{\mathrm{aux}} + M \tag{2.247}$$

where J^{act} and J^{aux} are associated with the actual and auxiliary states, respectively, and M is the interaction integral:

$$J^{\text{act}} = \int_{A^*} \left[\sigma_{ij} \frac{\partial u_i}{\partial x_1} - W_{\text{s}} \delta_{1i} \right] \frac{\partial q}{\partial x_i} \mathrm{d}\Gamma \tag{2.248}$$

$$J^{\text{aux}} = \int_{A^*} \left[\sigma_{ij}^{\text{aux}} \frac{\partial u_i^{\text{aux}}}{\partial x_1} - W^{\text{aux}} \delta_{1i} \right] \frac{\partial q}{\partial x_i} \mathrm{d}\Gamma \tag{2.249}$$

$$M = \int_{A^*} \left[\sigma_{ij} \frac{\partial u_i^{\text{aux}}}{\partial x_1} + \sigma_{ij}^{\text{aux}} \frac{\partial u_i}{\partial x_1} - W^{\text{M}} \delta_{1j} \right] \frac{\partial q}{\partial x_j} \mathrm{d}\Gamma \tag{2.250}$$

with the actual, auxiliary and interaction works defined as:

$$W_{\text{s}} = \sigma_{ij} \varepsilon_{ij} \tag{2.251}$$

$$W^{\text{aux}} = \sigma_{ij}^{\text{aux}} \varepsilon_{ij}^{\text{aux}} \tag{2.252}$$

$$W^{\text{M}} = \frac{1}{2} \left(\sigma_{ij} \varepsilon_{ij}^{\text{aux}} + \sigma_{ij}^{\text{aux}} \varepsilon_{ij} \right) \tag{2.253}$$

One of the choices for the auxiliary state is the displacement and stress fields in the vicinity of the crack tip. From the relation of the J integral and mode I and II stress intensity factors,

$$J = \frac{1}{E'} (K_{\text{I}}^2 + K_{\text{II}}^2) \tag{2.254}$$

the following relationship is obtained:

$$M = \frac{2}{E'} (K_{\text{I}} K_{\text{I}}^{\text{aux}} + K_{\text{II}} K_{\text{II}}^{\text{aux}}) \tag{2.255}$$

Therefore, the mode I and II stress intensity factors can be obtained from:

$$K = \frac{E'}{2} M \tag{2.256}$$

by choosing $K_{\text{I}}^{\text{aux}} = 1,\ K_{\text{II}}^{\text{aux}} = 0$ for mode I and $K_{\text{I}}^{\text{aux}} = 0,\ K_{\text{II}}^{\text{aux}} = 1$ for mode II.

Chapter 3

Extended Finite Element Method for Isotropic Problems

3.1 INTRODUCTION

This chapter is devoted to a full discussion on various aspects of the extended finite element method. The goal has been set to describe in detail all theoretical and computational bases of the approach, including advantages and potential drawbacks. The discussion is limited to two-dimensional XFEM, although many of the basic formulations can be similarly extended to three-dimensional problems.

The chapter begins with a comprehensive review of the development of the XFEM methodology. Specific applications may have been left out of the present chapter, which is mainly dedicated to the basic formulations. More advanced topics will be discussed in the next three chapters.

The main discussion starts with the definition of the partition of unity and its extension to more advanced frameworks. The concept of enrichment will then be explained in detail based on the concept of partition of unity and the extended finite element method. It covers a wide range of available techniques and enrichment functions, comprising asymptotic crack tip enrichments and jump functions to approximate field discontinuity across a crack within a finite element.

Weak formulation of the boundary value problem and its discretization using the XFEM methodology will be explained and associated numerical implications regarding Gauss integration rules, sub-quad and sub-triangle methods, multiple crack paths and branching will be addressed.

Level set and fast marching methods, as powerful alternatives to classical approaches for representing crack paths and crack intersections, will be discussed. The chapter concludes with illustrative examples that provide comparable results for a number of well known problems in fracture mechanics.

3.2 A REVIEW OF XFEM DEVELOPMENT

In this section, a brief review of the development of the extended finite element method is presented. This overview is dedicated to the basic ideas of XFEM and does not cover application issues. They have already been reviewed in Chapter 1 and will be dealt with in

more detail in Chapters 4, 5 and 6. There are also a number of available review papers and comprehensive documents published by Moës and Belytschko (2002b), Karihaloo and Xiao (2003), Bordas and Legay (2005) and Rabczuk and Wall (2006).

The basic mathematical foundation of the partition of unity finite element method (PUFEM) was discussed by Melenk and Babuska (1996). They illustrated that PUFEM can be used to employ the structure of the differential equation under consideration to construct effective and robust methods. The global solution of PUFEM has been the theoretical basis of the local partition of unity finite element method, to be called later the extended finite element method.

The first effort for developing the extended finite element methodology can be traced back to 1999 when Belytschko and Black (1999) presented a minimal remeshing finite element method for crack growth. They added discontinuous enrichment functions to the finite element approximation to account for the presence of the crack. The method allowed the crack to be arbitrarily aligned within the mesh, though it required remeshing for severely curved cracks.

Later, Moës *et al.* (1999) improved the method and called it the extended finite element method (XFEM). The improved methodology allowed for independent representation of the entire crack from the mesh, based on the construction of the enriched approximation from the interaction of the crack geometry with the mesh.

A major step forward was probably achieved by Dolbow (1999) with his PhD thesis at Northwestern University (Extended finite element method with discontinuous enrichment for applied mechanics). This work resulted in a number of papers for solution of two-dimensional elasticity and Mindlin–Reissner plates using both a jump function and the asymptotic near tip fields using XFEM (Dolbow *et al.* 2000a), presenting a technique to model arbitrary discontinuities in the finite element framework by locally enriching a displacement based approximation through a partition of unity method (Dolbow *et al.* 2000b, 2000c).

Sukumar *et al.* (2000) then extended the XFEM for three-dimensional crack modelling and addressed geometric issues associated with the representation of the crack and the enrichment of the finite element approximation. Modelling of arbitrary branched and intersecting cracks with multiple branches, multiple holes and cracks emanating from holes, was the subject of another study by Daux *et al.* (2000) as extensions to the original XFEM.

Level set methods gradually evolved to represent the crack location, including the location of crack tips. Stolarska *et al.* (2001) introduced coupling the level set method (LSM) with XFEM to model crack growth. Belytschko *et al.* (2001) presented a technique for modelling arbitrary discontinuities in the function and its derivatives in finite elements. The discontinuous approximation was constructed in terms of a signed distance function, so level sets could be used to update the position of the discontinuities. Also, Sukumar *et al.* (2001) described modelling holes and inclusions by level sets in the extended finite element method. At the same time, Moës *et al.* (2002) and Gravouil *et al.* (2002) discussed the mechanical model and level set update for non-planar three-dimensional crack growth, based on a Hamilton–Jacobi equation to update the level sets with a velocity extension approach to preserve the old crack surface.

Sukumar *et al.* (2003a) developed a numerical technique for planar three-dimensional fatigue crack growth simulations that couples the extended finite element method to the fast marching method (FMM). Chopp and Sukumar (2003) extended the method to multiple coplanar cracks, where the entire multiple crack geometry was represented by a single signed distance (level set) function and merging of distinct cracks could be handled by the FMM with no necessity of collision detection or mesh reconstruction procedures. A different approach for tackling the same set of problems was proposed by Ventura *et al.* (2003)

A major number of developments followed the initial success of the method, including extension to strong and weak discontinuities by Sukumar and Prevost (2003), Huang *et al.* (2003) and Legay *et al.* (2005), discussion on ways of construction of blending elements by Chessa *et al.* (2003) and formulating higher order elements for curved cracks by Stazi *et al.* (2003). Liu *et al.* (2004) proposed an improved XFEM by direct evaluation of mixed mode stress intensity factors (SIFs) without extra post-processing. The main idea was to include the higher order terms of the crack tip asymptotic field for enriching the finite element approximation of the nodes surrounding the crack tip and applying a penalty function method, thus ensuring that the displacement approximations reduce to the actual asymptotic fields adjacent to the crack tip.

Other contributions include Bellec and Dolbow (2003) and Mariani and Perego (2003) for simulation of cohesive crack propagation by assuming a cubic displacement discontinuity that allowed reproduction of the typical cusp-like shape of the process zone at the tip of a cohesive crack, Areias and Belytschko (2005a, 2005b) presenting a viscosity-regularised continuum damage constitutive model coupled with the XFEM formulation resulting in a regularised 'crack-band' version of XFEM. Alternatively, Lee *et al.* (2004) combined the extended finite element method and the mesh superposition method (s-version FEM) for modelling of stationary and growing cracks. In a different approach, Mergheim *et al.* (2006) presented a geometrically nonlinear XFEM by doubling the degrees of freedom in the discontinuous elements. In contrast to the standard XFEM, the suggested approach thus relies exclusively on displacement degrees of freedom.

Simulation of growth of multiple cracks was the goal of several other studies. Budyn *et al.* (2004) presented a combined XFEM/level set method for modelling homogeneous and inhomogeneous linear elastic media. Zi *et al.* (2004) discussed the junction of two cracks and presented a numerical XFEM model to analyse the growth and the coalescence of cracks in a quasi-brittle cell containing multiple cracks. Béchet *et al.* (2005) proposed a geometrical enrichment instead of the usual topological one in which a given domain size would be enriched even if the elements did not touch the crack front.

Accuracy, stabitity and convergence were also the target of Laborde *et al.* (2005) and Chahine *et al.* (2006), who studied the convergence for a variety of XFEM on cracked domains. Peters and Hack (2005) discussed the ways that a singular stiffness matrix may be avoided by deleting some of the enhanced degrees of freedom. Ventura (2006) showed how standard Gauss quadrature can be accurately used in the elements containing the discontinuity without splitting the elements into subcells or introducing any additional approximation.

Xiao and Karihaloo (2006) discussed improving the accuracy of XFEM crack tip fields using higher order quadrature and statically admissible stress recovery procedures. They proposed a statically admissible stress recovery (SAR) scheme to be constructed by basis functions and moving least squares (MLS) to fit the stresses at sampling points (e.g. quadrature points) obtained by XFEM. Imposition of Dirichlet-type conditions was studied by Moës *et al.* (2006), who introduced a strategy to impose Dirichlet boundary conditions while preserving the optimal rate of convergence. The key aspect was the construction of the correct Lagrange multiplier space on the boundary.

XFEM and meshless methods have used the partition of unity enrichment for solving the crack problems. Belytschko *et al.* (2002b) and Xu (2005) described methods based on the partition of unity for approximating discontinuous functions in finite element and meshless formulations. Recently, Fries and Belytschko (2006) presented a new intrinsic enrichment method for treating arbitrary discontinuities in a finite element (FE) context. Unlike the standard XFEM, no additional unknowns were introduced at the nodes whose supports were crossed by discontinuities. An approximation space was constructed consisting of mesh based, enriched moving least squares (MLS) functions near discontinuities and standard FE shape functions elsewhere.

XFEM has been successfully adopted for simulation of various engineering problems. The localisation problem has been solved by Jirásek and Zimmermann (2001a, 2001b), Jirásek (2002), Sukumar *et al.* (2003b), Patzak and Jirásek (2003), Dumstorff and Meschke (2003), Samaniego and Belytschko (2005), Areias and Belytschko (2006), Song *et al.* (2006), Ferrie *et al.* (2006), Ventura *et al.* (2005), Larsson and Fagerström (2005) and Stolarska and Chopp (2003).

The problem of cohesive cracks has been studied by Moës and Belytschko (2002a), Zi and Belytschko (2003), Mergheim *et al.* (2005) and de Borst *et al.* (2004a, 2004b, 2004c), while Dolbow and Nadeau (2002), Dolbow and Gosz (2002), Remmers *et al.* (2003), Sukumar *et al.* (2004), Nagashima *et al.* (2003), Nagashima and Suemasu (2004), Asadpoure *et al.* (2006), Asadpoure *et al.* (2007) and Asadpoure and Mohammadi (2007) have extensively studied the behaviour of crack in composites using XFEM.

Contact, plasticity and large deformation have always been regarded as difficult computational obstacles to overcome. Modelling contact by XFEM was first introduced by Dolbow *et al.* (2000c, 2001) and revisited by Belytschko *et al.* (2002a). Khoei and Nikbakht (2006) applied the available formulation to modelling frictional contact problems. Introduction of plastic enrichment terms into XFEM was first reported by Elguedj *et al.* (2006) based on the Hutchinson–Rice–Rosengren (HRR) fields to represent the singularities in EPFM. Many researchers have tackled the XFEM within large deformation regime, among them Dolbow and Devan (2004), Legrain *et al.* (2005) and Fagerström and Larsson (2006) presented a geometrically nonlinear XFEM.

Areias and Belytschko (2005a) developed a new XFEM formulation for arbitrary crack propagation in shells with a new enrichment of the rotation field. Areias *et al.* (2006) then presented a XFEM methodology similar to the Hansbo and Hansbo approach for evolution of cracks in thin shells using midsurface displacement and director field discontinuities.

Dynamic XFEM was proposed by Belytschko *et al.* (2003), Belytschko and Chen (2004) and Zi *et al.* (2005) based on the singular enrichment finite element method for

elastodynamic crack propagation. Also, Réthoré *et al.* (2005a) proposed a generalised XFEM to model dynamic fracture and time dependent problems. Later, Menouillard *et al.* (2006) presented an explicit XFEM by introduction of a lumped mass matrix for enriched elements.

In an interesting development, Chessa and Belytschko (2004, 2006) presented a locally enriched space–time extended finite element method for solving hyperbolic problems with discontinuities. The coupling was implemented through a weak enforcement of the continuity of the flux between the space–time and semi-discrete domains in a manner similar to discontinuous Galerkin methods. They successfully applied the TXFEM to the Rankine–Hugoniot jump conditions to linear first order wave and nonlinear Burgers' equations. Furthermore, Réthoré *et al.* (2005b) proposed a combined space–time extended finite element method, based on the idea of the time extended finite element method, allowing a suitable form of the time stepping formulae to study stability and energy conservation.

3.3 BASICS OF FEM

3.3.1 Isoparametric finite elements, a short review

Consider a domain in the state of equilibrium descretized by a four-node quadrilateral finite element mesh, as depicted in Fig. 3.1. According to the finite element methodology, the coordinates $\mathbf{x}^{\mathrm{T}} = (x, y)$ are interpolated from the nodal values $\bar{\mathbf{x}}^{\mathrm{T}} = (\bar{x}, \bar{y})$:

$$\mathbf{x} = \sum_{j=1}^{4} \mathbf{N}_j \bar{\mathbf{x}}_j \tag{3.1}$$

where $\mathbf{N}_j$ is the matrix of finite element shape functions,

$$\mathbf{N}_j = \begin{bmatrix} N_j & 0 \\ 0 & N_j \end{bmatrix} \tag{3.2}$$

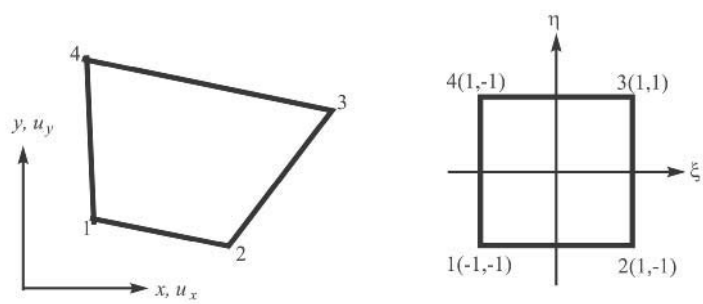

Figure 3.1 An isoparametric finite element.

In an isoparametric finite element representation, displacement fields $\mathbf{u}^{\mathrm{T}} = (u_x, u_y)$ are similarly interpolated from the nodal displacements nodal values $\overline{\mathbf{u}}^{\mathrm{T}} = (\overline{u}_x, \overline{u}_y)$:

$$\mathbf{u} = \sum_{j=1}^{4} \mathbf{N}_j \overline{\mathbf{u}}_j \tag{3.3}$$

The strain field is computed directly from Eq. (3.2):

$$\boldsymbol{\varepsilon} = \sum_{j=1}^{4} \mathbf{B}_j \overline{\mathbf{u}}_j \tag{3.4}$$

where the matrix $\mathbf{B}_j$ is defined in terms of derivatives of the shape functions $\mathbf{N}_j$,

$$\mathbf{B}_j = \begin{bmatrix} \dfrac{\partial N_j}{\partial x} & 0 \\ 0 & \dfrac{\partial N_j}{\partial y} \\ \dfrac{\partial N_j}{\partial y} & \dfrac{\partial N_j}{\partial x} \end{bmatrix} \tag{3.5}$$

and the chain rule is invoked to determine the coefficients of $\mathbf{B}_j$:

$$\begin{Bmatrix} \dfrac{\partial N}{\partial x} \\ \dfrac{\partial N}{\partial y} \end{Bmatrix} = \mathbf{J}^{-1} \begin{Bmatrix} \dfrac{\partial N}{\partial \xi} \\ \dfrac{\partial N}{\partial \eta} \end{Bmatrix} \tag{3.6}$$

where $\mathbf{J}$ is the Jacobian matrix

$$\mathbf{J} = \begin{bmatrix} \dfrac{\partial x}{\partial \xi} & \dfrac{\partial y}{\partial \xi} \\ \dfrac{\partial x}{\partial \eta} & \dfrac{\partial y}{\partial \eta} \end{bmatrix} \qquad \mathbf{J}^{-1} = \frac{1}{\det \mathbf{J}} \begin{bmatrix} \dfrac{\partial y}{\partial \eta} & \dfrac{\partial y}{\partial \xi} \\ -\dfrac{\partial x}{\partial \eta} & \dfrac{\partial x}{\partial \xi} \end{bmatrix} \tag{3.7}$$

Finally, the stiffness matrix $\mathbf{K}_e$ of an element Ω_e can be determined from:

$$\mathbf{K}_e = \int_{\Omega_e} \mathbf{B}^{\mathrm{T}} \mathbf{D} \mathbf{B} \, \mathrm{d}\Omega \tag{3.8}$$

where $\mathbf{D}$ is the material stress–strain or constitutive matrix ($\boldsymbol{\sigma} = \mathbf{D}\mathbf{B}\overline{\mathbf{u}}_i$). Eq. (3.8) can be rewritten in local curvilinear coordinates ξ, η:

$$\mathbf{K} = \int_{-1}^{1} \int_{-1}^{1} \mathbf{B}(\xi, \eta)^{\mathrm{T}} \mathbf{D} \mathbf{B}(\xi, \eta) \left(\det \mathbf{J} \right) \mathrm{d}\xi \, \mathrm{d}\eta \tag{3.9}$$

3.3.2 Finite element solutions for fracture mechanics

The classical contribution of the finite element method in fracture mechanics is to provide an analytical tool for determination of the displacement, strain and stress fields. Those will then be used for evaluation of the stress intensity factor K and the energy release rate G. Available two-step solutions and the simplified one-step method have been discussed in a previous chapter.

Another major contribution has been the development of singular finite elements which resemble crack tip stress fields. They have already been discussed in Section 2.5.6, and are expected to provide more accurate results with a lower number of finite elements.

Evaluation of the J integral is different, in the sense that the calculations have to be carried out over a contour curve. Such a contour, in general, may neither pass through the nodal points of the finite elements nor include the predefined Gauss points.

First assume the contour path passes through the finite element Gauss points. Recalling Eq. (2.236), J for a crack along the x axis (Fig. 2.18b) can be defined as,

$$J = \int_{\Gamma}\left(W_s \mathrm{d}y - \mathbf{t}\frac{\partial \mathbf{u}}{\partial x}\mathrm{d}\Gamma \right) \tag{3.10}$$

In a direct approach, Eq. (3.10) is expressed in terms of the stress and strain components (Eqs. (2.241)),

$$\begin{aligned} J = \int_{\Gamma}\Bigg\{ & \frac{1}{2}\left[\sigma_{xx}\frac{\partial u_x}{\partial x} + \sigma_{xy}\left(\frac{\partial u_x}{\partial y} + \frac{\partial u_y}{\partial x} \right)\frac{\partial u_x}{\partial x} + \sigma_{yy}\frac{\partial u_y}{\partial y} \right]\frac{\partial y}{\partial \eta} \\ & - \left[\left(\sigma_{xx}n_1 + \sigma_{xy}n_2 \right)\frac{\partial u_x}{\partial x} + \left(\sigma_{xy}n_1 + \sigma_{yy}n_2 \right)\frac{\partial u_y}{\partial x} \right]\sqrt{\left(\frac{\partial x}{\partial \eta} \right)^2 + \left(\frac{\partial y}{\partial \eta} \right)^2} \Bigg\}\mathrm{d}\eta \end{aligned} \tag{3.11}$$

Evaluation of Eq. (3.11) is performed by the Gauss integration rule along the path Γ,

$$J = \sum_{g=1}^{ng} W_g I(\xi_g, \eta_g) \tag{3.12}$$

where W_g is the Gauss weighting factor, ng is the order of integration, and the integrand I is defined as:

$$\begin{aligned} I_g = \Bigg\{ & \frac{1}{2}\left[\sigma_{xx}\frac{\partial u_x}{\partial x} + \sigma_{xy}\left(\frac{\partial u_x}{\partial y} + \frac{\partial u_y}{\partial x} \right)\frac{\partial u_x}{\partial x} + \sigma_{yy}\frac{\partial u_y}{\partial y} \right]\frac{\partial y}{\partial \eta} \\ & - \left[\left(\sigma_{xx}n_1 + \sigma_{xy}n_2 \right)\frac{\partial u_x}{\partial x} + \left(\sigma_{xy}n_1 + \sigma_{yy}n_2 \right)\frac{\partial u_y}{\partial x} \right]\sqrt{\left(\frac{\partial x}{\partial \eta} \right)^2 + \left(\frac{\partial y}{\partial \eta} \right)^2} \Bigg\}_g \end{aligned} \tag{3.13}$$

In an alternative approach, the equivalent domain integral method is increasingly preferred for determination of the contour J integral. Recalling Eqs. (2.244)–(2.245) and referring to Fig. 2.17b, the J integral can be defined as:

$$J = \int_{A^*} \left[\sigma_{ij} \frac{\partial u_i}{\partial x_1} - W_s \delta_{1i} \right] \frac{\partial q}{\partial x_i} \mathrm{d}\Gamma \tag{3.14}$$

where q is an arbitrary smoothing function which is equal to unity on the inner contour and zero on the outer one. Discretization of q in terms of its nodal values, $q(\mathbf{x}) = \sum N_i(\mathbf{x}) q_i$, leads to the following form of the domain integral:

$$J = \sum_{\substack{elements \\ in\ A^*}} \left(\sum_{g=1}^{ng} \left\{ \left[\left(\sigma_{ij} \frac{\partial u_j}{\partial x_1} - W_s \delta_{1i} \right) \frac{\partial q}{\partial x_i} \right] \det\left(\frac{\partial x_j}{\partial \xi_k} \right) \right\}_g W_g \right) \tag{3.15}$$

Finally, application of the finite element method for evaluation of the J integral by the interaction integral method (M integral) is based on Eq. (2.247)

$$J = \int_{A^*} \left[\sigma_{ij} \frac{\partial u_i^{\mathrm{aux}}}{\partial x_1} - \sigma_{ij}^{\mathrm{aux}} \frac{\partial u_i}{\partial x_1} - \sigma_{ij} \varepsilon_{ij}^{\mathrm{aux}} \delta_{1j} \right] \frac{\partial q}{\partial x_j} \mathrm{d}\Gamma \tag{3.16}$$

or in a discretized form is obtained through a Gauss integration scheme,

$$J = \sum_{A^*} \left(\sum_{g=1}^{ng} \left\{ \left[\left(\sigma_{ij} \frac{\partial u_i^{\mathrm{aux}}}{\partial x_1} - \sigma_{ij}^{\mathrm{aux}} \frac{\partial u_i}{\partial x_1} - \sigma_{ij} \varepsilon_{ij}^{\mathrm{aux}} \delta_{1j} \right) \frac{\partial q}{\partial x_j} \right] \det J \right\}_g W_g \right) \tag{3.17}$$

where the superscript $^{\mathrm{aux}}$ respresents the auxiliary state in comparison to the actual states (without superscript).

3.4 PARTITION OF UNITY

The concept of partition of unity has been used in various computational disciplines (Melenk and Babuska 1996). A partition of unity is defined as a set of m functions $f_k(\mathbf{x})$ within a domain Ω_{pu} such that

$$\sum_{k=1}^{m} f_k(\mathbf{x}) = 1 \tag{3.18}$$

It can easily be shown that by selection of any arbitrary function $\psi(\mathbf{x})$, the following property is automatically satisfied:

$$\sum_{k=1}^{m} f_k(\mathbf{x})\psi(\mathbf{x}) = \psi(\mathbf{x}) \tag{3.19}$$

This is equivalent to the definition of the reproducing condition or completeness. Completeness is expressed in terms of the order of the polynomial $\psi(\mathbf{x}) = p(\mathbf{x})$, which must be represented exactly by approximating functions $f_k(\mathbf{x})$. Then, zero completeness is achieved if Eq. (3.19) holds for a constant $p(\mathbf{x})$.

The set of isoparametric finite element shape functions, N_j, also satisfy the condition of partition of unity,

$$\sum_{j=1}^{n} N_j(\mathbf{x}) = 1 \tag{3.20}$$

where n is the number of nodes for each finite element. The concept of partition of unity provides a mathematical framework for the development of an enriched solution, as will be discussed in the next section.

3.5 ENRICHMENT

Theoretically, enrichment can be regarded as the principal of increasing the order of completeness that can be achieved. Computationally, it may simply target higher accuracy of the approximation by including the information obtained from the analytical solution. The choice of the enriched functions depends on the *a priori* solution of the problem. For instance, in a crack analysis this is equivalent to an increase in accuracy of the approximation if analytical near crack tip solutions are somehow included in the enrichment terms.

Let us begin with the classical approximation of a field variable $\mathbf{u}$ within a finite element method:

$$\mathbf{u} = \sum_{j=1}^{n} \mathbf{N}_j \bar{\mathbf{u}}_j \tag{3.21}$$

or in a more appropriate form in terms of the m basis functions $\mathbf{p}$,

$$\mathbf{u} = \mathbf{p}^{\mathrm{T}}\mathbf{a} = \sum_{k=1}^{m} p_k \mathbf{a}_k \tag{3.22}$$

where unknowns $\mathbf{a}_k$ are determined from the approximation at nodal points.

For one- and two-dimensional problems, the basis function may be defined for different orders of completeness:

$$\begin{cases} 1D: & \begin{cases} \mathbf{p}^{\mathrm{T}} = \{1, x\} & \text{1st order} \\ \mathbf{p}^{\mathrm{T}} = \{1, x, x^2\} & \text{2nd order} \end{cases} \\ 2D: & \begin{cases} \mathbf{p}^{\mathrm{T}} = \{1, x, y\} & \text{1st order} \\ \mathbf{p}^{\mathrm{T}} = \{1, x, y, x^2, xy, y^2\} & \text{2nd order} \end{cases} \end{cases} \tag{3.23}$$

The basic idea of the enrichment is to transform Eqs. (3.21) or (3.22) into a more appropriate form to enhance the way approximation is constructed. The enhancement may be attributed to the degree of consistency of the approximation, or to the capability of approximation to reproduce a given complex field of interest.

There are basically two ways of enriching an approximation: enriching the basis vector (intrinsic enrichment) and enriching the approximation (extrinsic enrichment). The following sections discuss both approaches.

3.5.1 Intrinsic enrichment

In this approach, the idea is to enhance approximation Eq. (3.22) by transforming the basis function $\mathbf{p}$ to include new terms to satisfy a certain condition of reproducing a complex field (Fries and Belytschko 2006). For instance, for a first-order standard linear basis function $\mathbf{p}^{\mathrm{lin}} = \{1, x, y\}$, new enrichment terms $\mathbf{p}^{\mathrm{enr}} = \{f_1, f_2\}$ are added:

$$\mathbf{p} = \{\mathbf{p}^{\mathrm{lin}}, \mathbf{p}^{\mathrm{enr}}\} = \{1, x, y, f_1, f_2\} \tag{3.24}$$

To further elaborate the concept of enrichment, consider the classical crack problem of Section 2.4. The asymptotic near tip displacement field can be written as:

$$u_x = \frac{1}{\mu}\sqrt{\frac{r}{2\pi}}\left(K_{\mathrm{I}}\cos\frac{\theta}{2}(\kappa - \cos\theta) + K_{\mathrm{II}}\sin\frac{\theta}{2}(\kappa + \cos\theta + 2)\right) \tag{3.25}$$

$$u_y = \frac{1}{\mu}\sqrt{\frac{r}{2\pi}}\left(K_{\mathrm{I}}\sin\frac{\theta}{2}(\kappa - \cos\theta) - K_{\mathrm{II}}\cos\frac{\theta}{2}(\kappa + \cos\theta - 2)\right) \tag{3.26}$$

where r and θ are defined in Fig. 3.2, and K_{I} and K_{II} are the mode I and II stress intensity factors, respectively.

It can be shown that the asymptotic near crack tip displacement field (Eqs. (3.26)–(3.27)) can be expressed by the following basis function $\mathbf{p}(\mathbf{x})$, defined in the polar coordinate system,

$$\mathbf{p}^{\mathrm{T}}(\mathbf{x}) = [P_1, P_2, P_3, P_4] = \left[\sqrt{r}\sin\frac{\theta}{2}, \sqrt{r}\cos\frac{\theta}{2}, \sqrt{r}\sin\theta\sin\frac{\theta}{2}, \sqrt{r}\sin\theta\cos\frac{\theta}{2}\right] \tag{3.27}$$

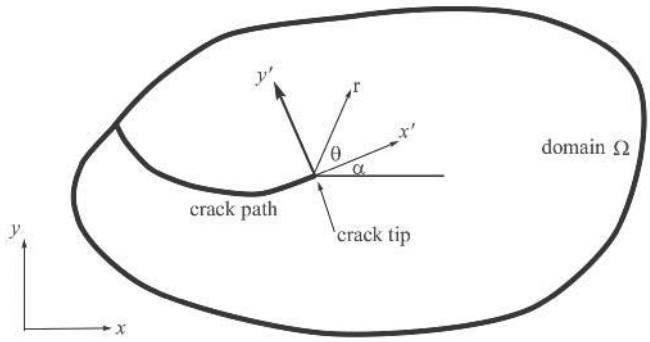

Figure 3.2 Polar coordinates at the crack tip.

The basis function for the total solution must include the constant and linear terms:

$$\mathbf{p}^{\mathrm{T}}(\mathbf{x}) = \left[1, x, y, \sqrt{r}\sin\frac{\theta}{2}, \sqrt{r}\cos\frac{\theta}{2}, \sqrt{r}\sin\theta\sin\frac{\theta}{2}, \sqrt{r}\sin\theta\cos\frac{\theta}{2}\right] \tag{3.28}$$

which is a familiar basis function previously used for fracture analysis by the meshless element-free Galerkin (EFG) method (Belytschko *et al.* 1994),

$$\mathbf{u}^h(\mathbf{x}) = \mathbf{p}^{\mathrm{T}}(\mathbf{x})\mathbf{a}(\mathbf{x}) \tag{3.29}$$

where $\mathbf{a}(\mathbf{x})$ is a vector of coefficients obtained from one of the least square techniques for minimizing the overall error of approximation. The vector $\mathbf{a}(\mathbf{x})$ can be set as constants or variables depending on the adoption of weighted least squares (WLS) or moving least squares (MLS) techniques, respectively (Onate *et al.* 1995).

3.5.2 Extrinsic enrichment

Another form of enrichment is based on a so-called extrinsic enrichment. This uses extrinsic bases $p_k(\mathbf{x})$ to increase the order of completeness.

$$\mathbf{u}^h(\mathbf{x}) = \sum_{j=1}^{n} N_j(\mathbf{x})\mathbf{u}_j + \sum_{k=1}^{m} p_k(\mathbf{x})\mathbf{a}_k \tag{3.30}$$

where $\mathbf{a}_k$ are additional unknowns or degrees of freedom associated to the enriched solution. In a general partition of unity enrichment, Eq. (3.30) is rewritten as,

$$\mathbf{u}^h(\mathbf{x}) = \sum_{j=1}^{n} N_j(\mathbf{x})\mathbf{u}_j + \sum_{k=1}^{m} f_k^{\mathrm{pu}}(\mathbf{x})p(\mathbf{x})\mathbf{a}_k \tag{3.31}$$

where $f_k^{\text{pu}}(\mathbf{x})$ are set of the partition of unity functions defined over the support domain of the partition of unity enrichment Ω_{pu}, as illustrated in Fig. 3.3.

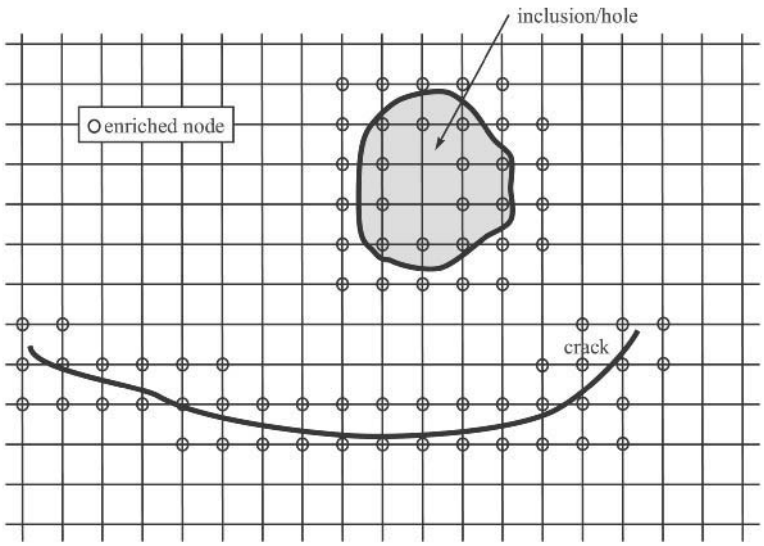

Figure 3.3 Definition of the enrichment support domain Ω_{pu}.

3.5.3 Partition of unity finite element method

Similar methodology is followed in the partition of unity finite element method (PUFEM) (Melenk and Babuska 1996) using the classical finite element shape functions $N_j(\mathbf{x})$. For a general point $\mathbf{x}$ within a finite element,

$$\mathbf{u}^h(\mathbf{x}) = \sum_{j=1}^{n} N_j(\mathbf{x}) \left(\mathbf{u}_j + \sum_{k=1}^{m} p_k(\mathbf{x}) \mathbf{a}_{jk} \right) \tag{3.32}$$

The approximation (3.32) is clearly a partition of unity. As a result, a compatible solution is guaranteed. Examining the approximate solution (3.32) for a typical enriched node $\mathbf{x}_i$ leads to:

$$\mathbf{u}^h(\mathbf{x}_i) = \sum_{j=1}^{n} N_j(\mathbf{x}_i) \left(\mathbf{u}_j + \sum_{k=1}^{m} p_k(\mathbf{x}_i) \mathbf{a}_{jk} \right) \tag{3.33}$$

where the first part vanishes, except for $N_i(\mathbf{x}_i)\mathbf{u}_i = \mathbf{u}_i$. Therefore,

$$\mathbf{u}^h(\mathbf{x}_i) = \mathbf{u}_i + \sum_{k=1}^{m} p_k(\mathbf{x}_i) \mathbf{a}_{jk} \tag{3.34}$$

which is not a feasible conclusion. To satisfy interpolation at nodal points, Eq. (3.32) is transformed to:

$$\mathbf{u}^h(\mathbf{x}) = \sum_{j=1}^{n} N_j(\mathbf{x}) \left(\mathbf{u}_j + \sum_{k=1}^{m} \left(p_k(\mathbf{x}) - p_k(\mathbf{x}_j) \right) \mathbf{a}_j \right) \tag{3.35}$$

which ensures $\mathbf{u}^h(\mathbf{x}_i) = \mathbf{u}_i$.

3.5.4 Generalised finite element method

In the generalised finite element method (GFEM), different shape functions are used for the classical and enriched parts of the approximation. Beginning with Eq. (3.32),

$$\mathbf{u}^h(\mathbf{x}) = \sum_{j=1}^{n} N_j(\mathbf{x}) \mathbf{u}_j + \sum_{j=1}^{n} N_j(\mathbf{x}) \left(\sum_{k=1}^{m} p_k(\mathbf{x}) \mathbf{a}_{jk} \right) \tag{3.36}$$

The generalised form can then be written as:

$$\mathbf{u}^h(\mathbf{x}) = \sum_{j=1}^{n} N_j(\mathbf{x}) \mathbf{u}_j + \sum_{j=1}^{n} \overline{N}_j(\mathbf{x}) \left(\sum_{k=1}^{m} p_k(\mathbf{x}) \mathbf{a}_{jk} \right) \tag{3.37}$$

where $\overline{N}_j(\mathbf{x})$ are the new set of shape functions associated with the enrichment part of the approximation.

3.5.5 Extended finite element method

In contrast to PUFEM and GFEM, where the enrichments are usually employed on a global level and over the entire domain, the extended finite element method adopts the same procedure on a local level.

Assumption of the approximation (3.36) generates a compatible solution even if a local partition of unity is adopted. This is a considerable computational advantage as it is equivalent to enriching only nodes close to a crack tip; a basis for the extended finite element solution. The extended finite element method will be comprehensively discussed in Section 3.6.

3.5.6 Hp-clouds enrichment

The meshless Hp-cloud (Duarte and Oden 1995) uses extrinsic bases $p_k(\mathbf{x})$ to increase the order of completeness within a moving least squares (MLS) approximation,

$$\mathbf{u}^h(\mathbf{x}) = \sum_{j=1}^{\bar{n}} \Phi_j(\mathbf{x}) \left(\mathbf{u}_j + \sum_{k=1}^{m} p_k(\mathbf{x}) \mathbf{a}_{jk} \right) \tag{3.38}$$

where $\bar{n}$ is the number of nodes within each MLS support domain, $\mathbf{a}_{jk}$ are additional degrees of freedom introduced to enrich the domain of interest and $\Phi_j(\mathbf{x})$ are the MLS shape functions evaluated over a moving support domain procedure.

3.5.7 Generalisation of the PU enrichment

The original PU enrichment (3.35) can be further generalised if a number of different PU support domains Ω_{pu}^l and associated partition of unity functions $f_k^l(\mathbf{x})$ are used for the enrichment:

$$\mathbf{u}^h(\mathbf{x}) = \sum_{j=1}^{n} N_j(\mathbf{x}) \mathbf{u}_j + \sum_{l=1}^{np} \sum_{k=1}^{m} f_k^l(\mathbf{x}) p^l(\mathbf{x}) \mathbf{a}_k^l \tag{3.39}$$

where $\mathbf{a}_k^l$ are the additional unknowns associated with each set of np domains of partition of unity.

3.5.8 Transition from standard to enriched approximation

Application of the enrichment for near crack tip analysis may lead to solution incompatibility and interior discontinuities, if it is not employed in the entire domain of consideration. The reason can be attributed to different orders of approximation for neighbouring domains while each domain follows a different basis function. As a result, different values may be obtained for the common nodes; an indication of occurrence of internal discontinuities.

A remedy to this drawback is to design a blending procedure over a transition domain connecting the domains with and without enrichment (Fig. 3.4):

$$\mathbf{u}^h(\mathbf{x}) = (1 - R)\mathbf{u}(\mathbf{x}) + R\mathbf{u}^{\text{enr}}(\mathbf{x}) \tag{3.40}$$

where R is a blending ramp function set to 1 on the enriched boundary and 0 on the linear boundary. A linear blending ramp function R ensures the continuity of the displacement field, while it cannot guarantee the continuity of the strain field. Higher order blending functions are therefore required to ensure continuous strain (displacement derivative) fields.

The same problem of internal discontinuities may occur in both intrinsic and extrinsic enrichments, if different types of approximations are to be used for modelling near and far fields.

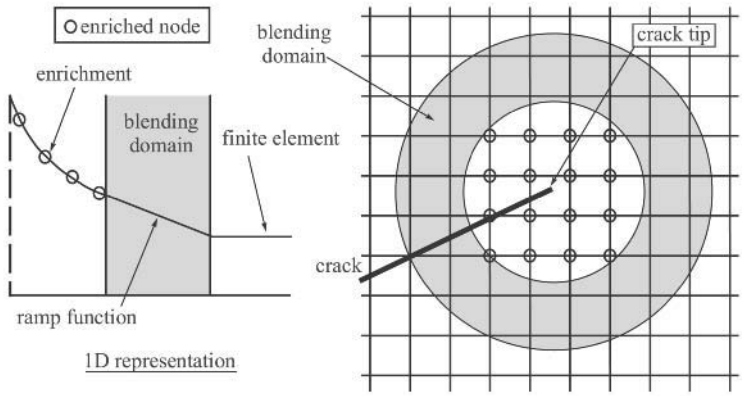

Figure 3.4 A smooth transition between the enriched and linear approximations.

From a different point of view, finite elements used for modelling an entire domain may be classified into three categories: standard finite elements, elements with enriched nodes and partially enriched elements which consist of standard and enriched nodes (Fig. 3.5). The first two categories are fully governed by either the classic FEM or XFEM approximations, whereas the third category (blending elements) is only partially involved with XFEM.

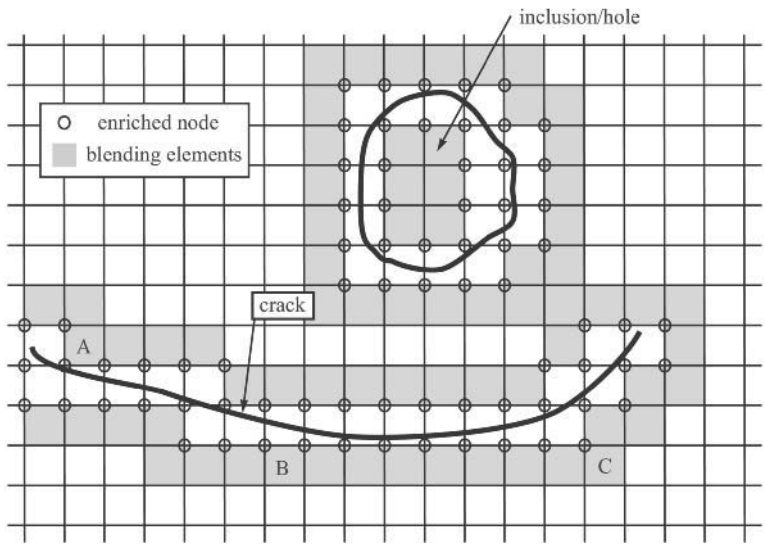

Figure 3.5 Standard, enriched and blending elements.

Three different types of blending elements are shown in Fig. 3.5. Typical element A has three enriched nodes and one standard node, while element B has two enriched and two standard nodes. Element C has the least number of enriched nodes in comparison to the number of standard nodes.

Now, consider a typical blending element B. Approximation of the displacement field for this element can be expressed as,

$$\mathbf{u}^h(\mathbf{x}) = \sum_{j=1}^{4} N_j(\mathbf{x})\mathbf{u}_j + \sum_{k=1}^{2} N_k(\mathbf{x})\psi(\mathbf{x})\mathbf{a}_k \tag{3.41}$$

The second part of Eq. (3.41) is no longer a partition of unity. Neverthelss, it has little direct effect on the approximation because such a blending element does not include any singularity at all.

3.6 ISOTROPIC XFEM

The basic concept of XFEM is to enrich the approximation space so that it is capable of reproducing certain features of the problem of interest, in particular discontinuities such as cracks or interfaces. Although it is a local version of the partition of unity finite element enrichment applied only in a certain local subdomain, it has strongly relied on the development of extrinsic enrichments for crack simulations by a number of meshless methods such as EFG and Hp-clouds. Naturally, the first XFEM approximations were also developed for simulation of strong discontinuities in fracture mechanics. This was later extended to include weak discontinuity and interface problems. XFEM can be assumed to be a classical FEM capable of handling arbitrary strong and weak discontinuities.

In the extended finite element method, first, the usual finite element mesh is produced. Then, by considering the location of discontinuities, a few degrees of freedom are added to the classical finite element model in selected nodes near to the discontinuities to provide a higher level of accuracy.

3.6.1 Basic XFEM approximation

Consider **x,** a point in a finite element model. Also assume there is a discontinuity in the arbitrary domain discretized into some n node finite elements. In the extended finite element method, the following approximation is utilised to calculate the displacement for the point **x** locating within the domain (Belytschko and Black 1999)

$$\mathbf{u}^h(\mathbf{x}) = \mathbf{u}^{\mathrm{FE}} + \mathbf{u}^{\mathrm{enr}} = \sum_{j=1}^{n} N_j(\mathbf{x})\mathbf{u}_j + \sum_{k=1}^{m} N_k(\mathbf{x})\psi(\mathbf{x})\mathbf{a}_k \tag{3.42}$$

where $\mathbf{u}_j$ is the vector of regular degrees of nodal freedom in the finite element method, $\mathbf{a}_k$ is the added set of degrees of freedom to the standard finite element model and $\psi(\mathbf{x})$ is the discontinuous enrichment function defined for the set of nodes that the discontinuity has in its influence (support) domain.

The influence domain associated to a node, located on an edge, consists of the elements containing that node, whereas for an interior node (in higher order elements) it is the element surrounding the node. Fig. 3.6 illustrates definitions of the influence domain for a node located on edges of elements (a corner node) as well as an internal node.

The enrichment function $\psi(\mathbf{x})$ can be chosen by applying appropriate analytical solutions according to the type of discontinuity. The main objectives for using various types of enrichment functions within an XFEM procedure can be expressed as the following:

1. Reproducing the singular field around a crack tip.
2. Continuity in displacement between adjacent finite elements.
3. Independent strain fields in two different sides of a crack surface.
4. Other features according to the specific discontinuity problem.

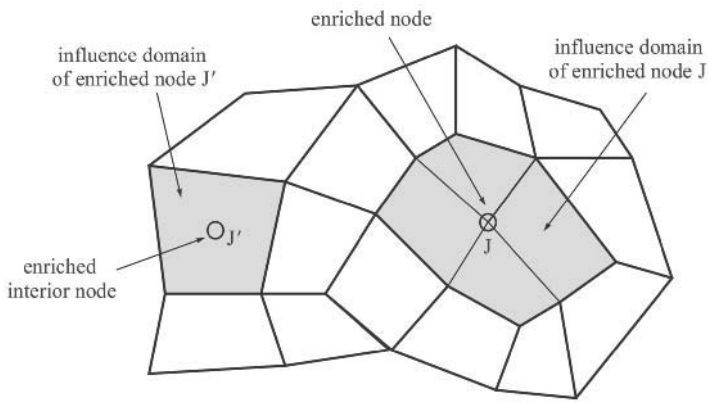

Figure 3.6 Influence (support) domains of an edge node J and an internal node J′ in an arbitrary finite element mesh.

The first term on the right-hand side of Eq. (3.42) is the classical finite element approximation to determine the displacement field, while the second term is the enrichment approximation which takes into account the existence of any discontinuities. The second term utilises additional degrees of freedom to facilitate modelling the existence of any discontinuous field, such as a crack, without modelling it explicitly in the finite element mesh.

For *np* multiple discontinuities within a finite element, the approximation (3.42) can be further extended to:

$$\mathbf{u}^h(\mathbf{x}) = \mathbf{u}^{\mathrm{FE}} + \mathbf{u}^{\mathrm{enr}} = \sum_{j=1}^{n} N_j(\mathbf{x})\mathbf{u}_j + \sum_{l=1}^{np}\sum_{k=1}^{m} N_k(\mathbf{x})\psi^l(\mathbf{x})\mathbf{a}_k^l \tag{3.43}$$

3.6.2 Signed distance function

The distance d from a point $\mathbf{x}$ to an interface Γ is defined as,

$$d = \left\| \mathbf{x} - \mathbf{x}_\Gamma \right\| \tag{3.44}$$

where $\mathbf{x}_\Gamma$ is the normal projection of $\mathbf{x}$ on Γ (Fig. 3.7). The signed distance function $\xi(\mathbf{x})$ can then be defined as,

$$\xi(\mathbf{x}) = \underbrace{\min_{\mathbf{x}_\Gamma \in \Gamma} \left\| \mathbf{x} - \mathbf{x}_\Gamma \right\|}\ sign\left(\mathbf{n} \cdot (\mathbf{x} - \mathbf{x}_\Gamma)\right) \tag{3.45}$$

where $\mathbf{n}$ is the unit normal vector.

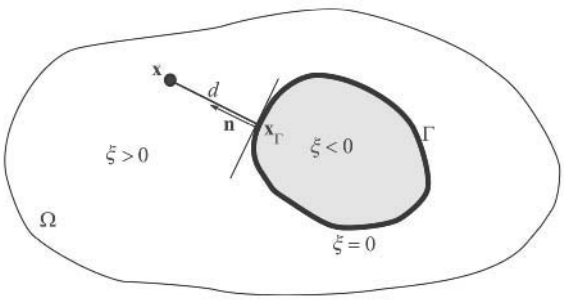

Figure 3.7 Definition of the signed distance function.

3.6.3 Modelling strong discontinuous fields

In the extended finite element method, approximation of a discontinuous displacement field is based on the definition of specially designed shape functions by the use of enrichment functions. The method operates on additional independent virtual degrees of freedom for the definition of the crack boundary and approximation of the displacement field. It will then be combined with the classical finite element method to approximate the overall solution.

In order to discuss various effects of the modelling, a one-dimensional problem is considered which consists of four nodes and three finite elements with a strong discontinuity (crack) in an arbitrary location $x_c(\xi_c)$ within the middle element, as depicted in Fig. 3.8. Similar one-dimensional examples can be found almost in all XFEM-related documents and references.

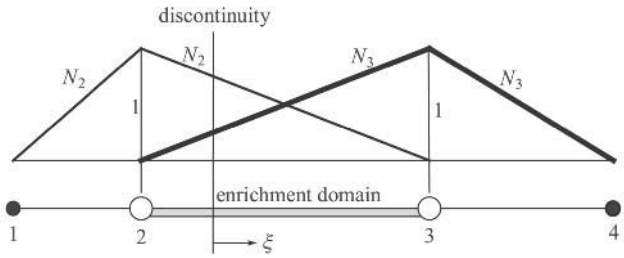

Figure 3.8 Simulation of a crack in a one-dimensional problem using the standard linear finite element shape functions.

Only nodes 2 and 3 are required to be enriched, whereas nodes 1 and 4 are not influenced by the crack.

There have been a number of possible choices for the enrichment function $\psi(\mathbf{x})$ in Eq. (3.42). The following sections explain the basic ideas and discuss the various effects of enrichment on this simple one-dimensional problem.

3.6.3.1 *A simple model*

Earlier models used a simple enriched shape function in the form of:

$$N_i^h = \begin{cases} N_i - 1 & \mathbf{x} \in \Omega_i \\ N_i & \mathbf{x} \notin \Omega_i \end{cases} \tag{3.46}$$

where N_i is the conventional finite element shape function and Ω_i is part of the element in between the crack and node i, as illustrated in Fig. 3.9.

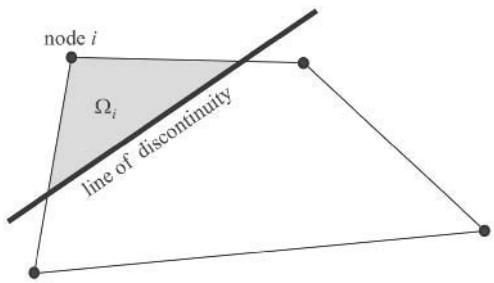

Figure 3.9 An element cut across by a crack.

Fig. 3.10 shows how this jump enrichment can affect the shape functions for a simple one-dimensional case of Fig. 3.8.

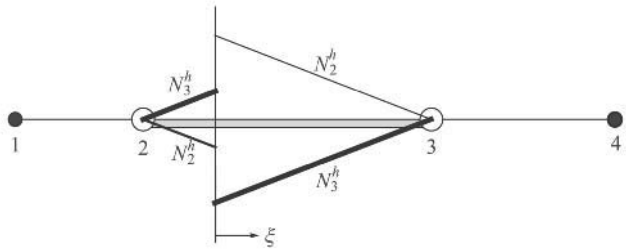

Figure 3.10 A simple description of discontinuity by a jump function.

One problem with this type of jump function is that it provides similar strain fields (derivative of the displacement field) in both sides of the discontinuity (Fig. 3.11). This is in contrast to the independent physical response of the segments anticipated in a cracked element.

Another drawback is the lower number of degrees of freedom required by approximation (3.46) than other recently available techniques. This may directly affect the quality of approximation field and the crack analysis.

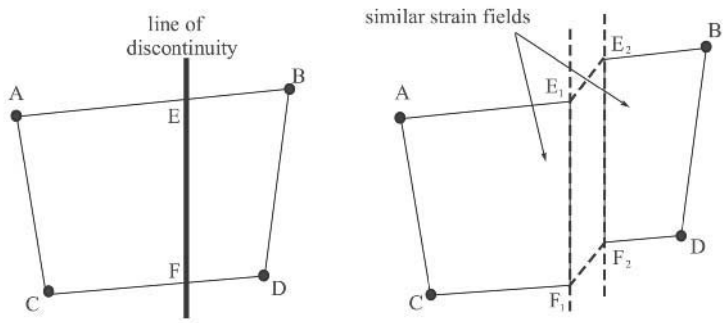

Figure 3.11 Deformation of a quadrilateral element with the first jump function.

3.6.3.2 *The Heaviside function*

Different definitions have been adopted for the Heaviside function over the years. The first type of Heaviside function $H(\xi)$ can be defined as a step function,

$$H(\xi)=\begin{cases}1 & \forall \xi > 0\\ 0 & \forall \xi < 0\end{cases} \tag{3.47}$$

A simple one-dimensional representation of this step function is depicted in Fig. 3.12a.

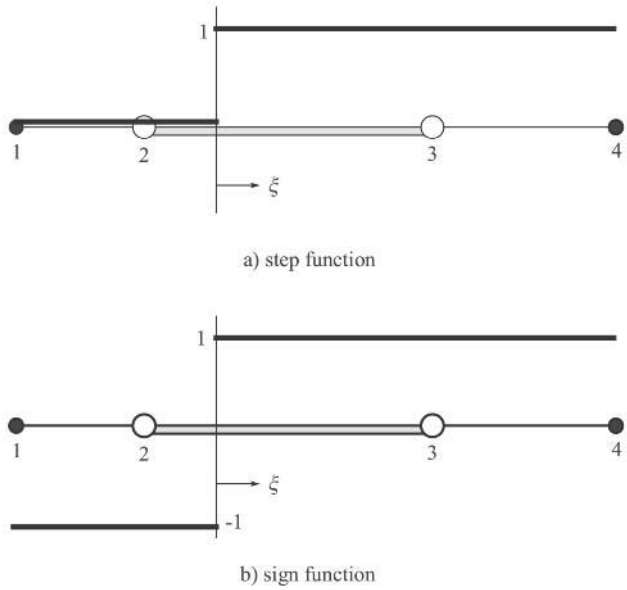

Figure 3.12 Different types of Heaviside function $H(\xi)$.

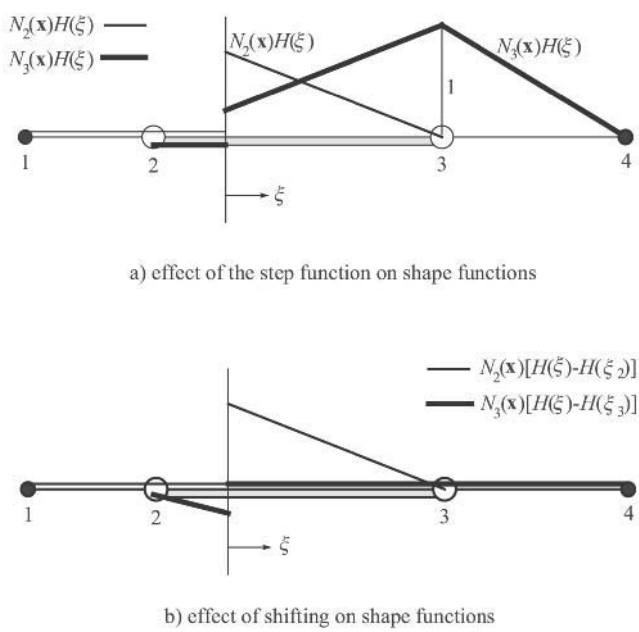

Figure 3.13 Enriched shape functions for nodes 2 and 3 and application of the shifting Heaviside function.

Approximation (3.42) then reads,

$$\mathbf{u}^h(\mathbf{x}) = \sum_{j=1}^{n} N_j(\mathbf{x})\mathbf{u}_j + \sum_{k=1}^{m} N_k(\mathbf{x})H(\xi)\mathbf{a}_k \tag{3.48}$$

Fig. 3.13a illustrates the way the step function simulates the discontinuity.

To examine whether the approximation (3.48) is an interpolation, the value of the field variable $\mathbf{u}(\mathbf{x})$ on an enriched node i can be obtained as:

$$\mathbf{u}^h(\mathbf{x}_i) = \mathbf{u}_i + H(\xi_i)\mathbf{a}_i \tag{3.49}$$

which means that approximation (3.48) is not an interpolation and the nodal parameter $\mathbf{u}_i$ is not the real displacement value on the enriched node i. A simple remedy to this shortcoming is to shift the step function around the node of interest:

$$\mathbf{u}^h(\mathbf{x}) = \sum_{j=1}^{n} N_j(\mathbf{x})\,\mathbf{u}_j + \sum_{k=1}^{m} N_k(\mathbf{x})\big(H(\xi) - H(\xi_k)\big)\mathbf{a}_k \tag{3.50}$$

Consequently, interpolation can be automatically guaranteed. Fig. 3.13b illustrates the effect of the modified approximation on the one-dimensional crack problem. The overall jump in the displacement field can be obtained from:

$$\left\langle \mathbf{u}^h(\mathbf{x}) \right\rangle = \mathbf{u}^h(\mathbf{x}^+) - \mathbf{u}^h(\mathbf{x}^-) = \cdots = \sum_{k=1}^{m} N_k(\mathbf{x})\ \mathbf{a}_k \tag{3.51}$$

Application of the aforementioned jump function on a quadrilateral element may lead to a discontinuous field, as depicted in Fig. 3.14. The deformation field includes all potential displacement fields independently for both sides of the crack. The strain fields also remain independent for both sides of the crack, compared with the previous case illustrated in Fig. 3.11.

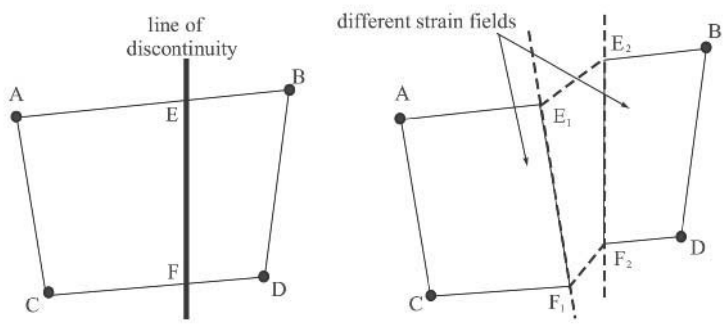

Figure 3.14 Deformation of a quadrilateral element with a jump function.

In order to avoid numerical instabilities, the following smoothed Heaviside functions can also be used for a small value of β less than the element size (Bordas and Legay 2005):

$$H(\xi)=\begin{cases}0 & \xi<-\beta \\ \frac{1}{2}+\frac{\xi}{2\beta}+\frac{1}{2\pi}\sin\frac{\pi\xi}{\beta} & -\beta<\xi<\beta \\ 1 & \xi>\beta\end{cases} \tag{3.52}$$

or

$$H(\xi)=\begin{cases}0 & \xi<-\beta \\ \frac{1}{2}+\frac{1}{8}\left(9\frac{\xi}{\beta}-5\frac{\xi^3}{\beta^3}\right) & -\beta<\xi<\beta \\ 1 & \xi>\beta\end{cases} \tag{3.53}$$

The derivative of the Heaviside function is the Dirac delta function $\delta(\xi)$

$$H_{,i}(\xi)=\delta(\xi) \tag{3.54}$$

which can be approximated by the following smoothed functions

$$\delta(\xi)=\begin{cases}\frac{1}{2\beta}+\frac{1}{2\beta}\sin\frac{\pi\xi}{\beta} & -\beta<\xi<\beta \\ 0 & \text{otherwise}\end{cases} \tag{3.55}$$

or

$$\delta(\xi)=\begin{cases}\frac{1}{8}\left(\frac{9}{\beta}-15\frac{\xi^2}{\beta^3}\right) & -\beta<\xi<\beta \\ 0 & \text{otherwise}\end{cases} \tag{3.56}$$

An alternative form has also been proposed by Chessa and Belytschko (2003a).

3.6.3.3 *The signed function*

An alternative Heaviside enrichment function is assumed to be the signed function

$$H(\xi)=\text{sign}(\xi)=\begin{cases}1 & \forall\xi>0 \\ -1 & \forall\xi<0\end{cases} \tag{3.57}$$

A simple one-dimensional representation of the step function is depicted in Fig. 3.12b. Fig. 3.15a illustrates the way the step function simulates the discontinuity.

Again, approximation (3.48) is no longer an interpolation and the value of the field variable $u(\mathbf{x})$ on an enriched node i is not equal to the nodal value $\mathbf{u}_i$

$$\mathbf{u}^h(\mathbf{x}_i) = \mathbf{u}_i + H(\xi_i)\,\mathbf{a}_i \neq \mathbf{u}_i \tag{3.58}$$

A simple shifting procedure guarantees the interpolation:

$$\mathbf{u}^h(\mathbf{x}) = \sum_{j=1}^{n} N_j(\mathbf{x})\,\mathbf{u}_j + \sum_{k=1}^{m} N_k(\mathbf{x})\big(H(\xi) - H(\xi_k)\big)\,\mathbf{a}_k \tag{3.59}$$

Fig. 3.15b illustrates the effect of the modified approximation on the one-dimensional crack problem. The overall jump in the displacement field can be obtained from:

$$\left\langle \mathbf{u}^h(\mathbf{x}) \right\rangle = \mathbf{u}^h(\mathbf{x}^+) - \mathbf{u}^h(\mathbf{x}^-) = \cdots = 2\sum_{k=1}^{m} N_k(\mathbf{x})\,\mathbf{a}_k \tag{3.60}$$

It is important to note that the choice of the jump in the enrichment function does not affect the overall solution. Similar forms as Eqs. (3.52)–(3.53) can be derived for smoothed equivalent functions for the Heaviside sign function.

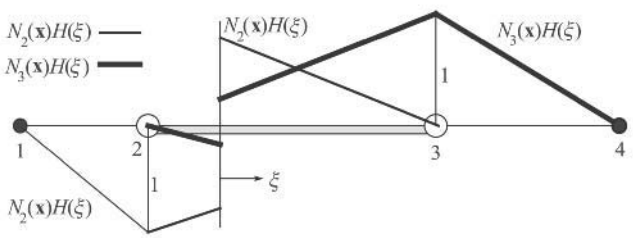

a) effect of the sign function on shape functions

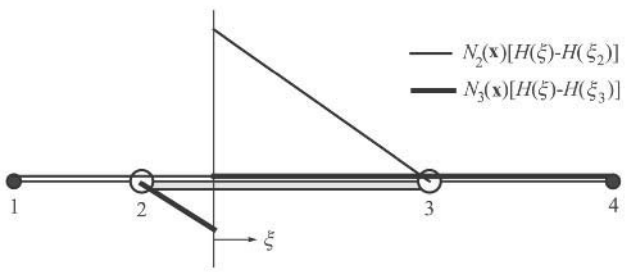

b) effect of shifting on shape functions

Figure 3.15 Enriched shape functions for nodes 2 and 3 and application of the shifting Heaviside function.

3.6.4 Modelling weak discontinuous fields

The same one-dimensional problem as discussed in Section 3.6.3 is considered (Fig. 3.8). The only difference is the assumption of a weak discontinuity in an arbitrary location $\mathbf{x}_c(\xi_c)$ within the middle element.

The XFEM approximation (3.48) can now be defined by replacing the Heaviside function $H(\xi)$ with an appropriate enrichment function $\chi(\mathbf{x})$ (Bordas and Legay 2005)

$$\mathbf{u}^h(\mathbf{x}) = \sum_{j=1}^{n} N_j(\mathbf{x})\mathbf{u}_j + \sum_{k=1}^{m} N_k(\mathbf{x})\chi(\mathbf{x})\mathbf{a}_k \tag{3.61}$$

where $\chi(\mathbf{x})$ is the weak discontinuous enrichment function defined in terms of the signed distance function $\xi(\mathbf{x})$:

$$\chi_k(\mathbf{x}) = |\xi(\mathbf{x})| - |\xi(\mathbf{x}_k)| \tag{3.62}$$

Fig. 3.16a illustrates these signed distance functions for the simple problem.

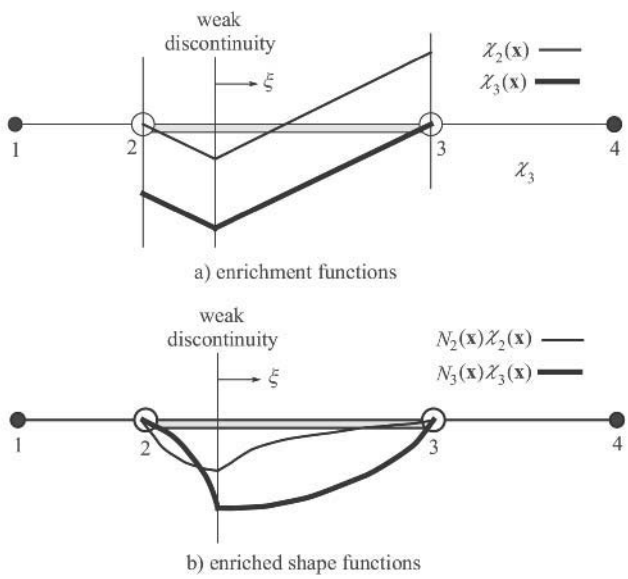

Figure 3.16 Weak discontinuous enrichment functions, and final enriched shape functions.

Fig. 3.16b depicts how the original shape functions are transformed as an effect of enrichment by the weak discontinuous enrichment functions. According to this figure, a kink in the displacement field is introduced. As a result, a jump in its derivative, i.e. a discontinuity in the gradient of the function is anticipated.

The normal jump in the gradient field, seen clearly in Fig. 3.16b at the position of weak discontinuity, can be computed as:

$$\left\langle \nabla \mathbf{u}^h(\mathbf{x}) \right\rangle = 2\sum_{k=1}^{m} N_k(\mathbf{x})\mathbf{a}_k \tag{3.63}$$

3.6.5 Plastic enrichment

Elguedj *et al.* (2006) have recently proposed the concept of plastic enrichment to include effects of crack tip platstification based on the Ramberg–Osgood plasticity model. In principle, other plasticity models may also be adopted with some modifications. Beginning with the Hutchinson–Rice–Rosengren power law hardening material model (2.214) (Hutchinson 1968):

$$\frac{\varepsilon}{\varepsilon_{\text{yld}}} = \frac{\sigma}{\sigma_{\text{yld}}} + k_0\left(\frac{\sigma}{\sigma_{\text{yld}}}\right)^n \tag{3.64}$$

Asymptotic crack tip displacement, strain and stress fields can be defined according to Eqs. (2.219)–(2.220) (Elguedj *et al.* 2006):

$$u_i = k_0\varepsilon_{\text{yld}} r\left(\frac{J}{k_0\sigma_{\text{yld}}\varepsilon_{\text{yld}} I_n r}\right)^{\frac{n}{n+1}} \overline{u}_i(\theta, n) \tag{3.65}$$

$$\varepsilon_{ij} = k_0\varepsilon_{\text{yld}}\left(\frac{J}{k_0\sigma_{\text{yld}}\varepsilon_{\text{yld}} I_n r}\right)^{\frac{n}{n+1}} \overline{\varepsilon}_{ij}(\theta, n) \tag{3.66}$$

$$\sigma_{ij} = \sigma_{\text{yld}}\left(\frac{J}{k_0\sigma_{\text{yld}}\varepsilon_{\text{yld}} I_n r}\right)^{\frac{1}{n+1}} \overline{\sigma}_{ij}(\theta, n) \tag{3.67}$$

where J is the well known contour integral and I_n is a dimensionless constant that depends on n. The terms $\overline{\sigma}_{ij}$, $\overline{\varepsilon}_{ij}$ and $\overline{u}_{ij}$ are dimensionless angular functions. Applying a Fourier decomposition on $\overline{u}_{ij}$ for modes I and II allows for the pure mode I and II displacement fields to be defined from the following basis function

$$r^{\frac{1}{n+1}}\left\{\left(\cos\frac{k\theta}{2}, \sin\frac{k\theta}{2}\right); k \in [1,3,5,7]\right\} \tag{3.68}$$

In practice, Elguedj *et al.* (2006) have used and compared the following options derived from Eq. (3.68):

$$\frac{1}{r^{\frac{1}{n+1}}}\left\{\sin\frac{\theta}{2},\cos\frac{\theta}{2},\sin\frac{\theta}{2}\sin\theta,\cos\frac{\theta}{2}\sin\theta,\sin\frac{\theta}{2}\sin 2\theta,\cos\frac{\theta}{2}\sin 2\theta\right\} \tag{3.69}$$

$$\frac{1}{r^{\frac{1}{n+1}}}\left\{\sin\frac{\theta}{2},\cos\frac{\theta}{2},\sin\frac{\theta}{2}\sin\theta,\cos\frac{\theta}{2}\sin\theta,\sin\frac{\theta}{2}\sin 3\theta,\cos\frac{\theta}{2}\sin 3\theta\right\} \tag{3.70}$$

$$\begin{aligned}\frac{1}{r^{\frac{1}{n+1}}}\Bigg\{&\sin\frac{\theta}{2},\cos\frac{\theta}{2},\sin\frac{\theta}{2}\sin\theta,\cos\frac{\theta}{2}\sin\theta,\\&\sin\frac{\theta}{2}\sin 2\theta,\cos\frac{\theta}{2}\sin 2\theta,\sin\frac{\theta}{2}\sin 3\theta,\cos\frac{\theta}{2}\sin 3\theta\Bigg\}\end{aligned} \tag{3.71}$$

3.6.6 Selection of nodes for discontinuity enrichment

There have been different approaches for the selection of nodes to be enriched by the Heaviside function. The procedure discussed in this section is only related to the Heaviside enrichment, and crack tip enrichments are separately applied to all nodes of the element that contains the crack tip.

One method allows for the discontinuity to be modelled across the crack over the points along the crack surface. The value of the modified (enriched) shape function N_i^h remains zero at all nodes and edges that do not intersect with the crack. This is important in satisfying the inter-element continuity requirements. This method only affects the element containing a crack, and does not directly influence other elements, even if they share a common node with the enriched element.

Fig. 3.17 illustrates this simple procedure for selection of nodes for enrichment. At each stage of the propagation, nodes on edges cut by the crack path are enriched. Even if the crack tip locates just on an edge, the corresponding nodes are not enriched. A potential source of instability and divergence is when a crack path passes along the finite element edges.

This technique adds two enrichment degrees of freedom to an element per any enriched node. As a result, for a quadrilateral element on the path of a crack, sixteen degrees of freedom (DOF) are assigned: eight classical DOFs and eight enriched DOFs.

The XFEM using classical jump functions, applies the enrichment onto the nodal points. As a result, elements containing an enriched node are affected by the enrichment degrees of freedom. Fig. 3.18 illustrates the procedure of node selection for enrichment based on this formulation.

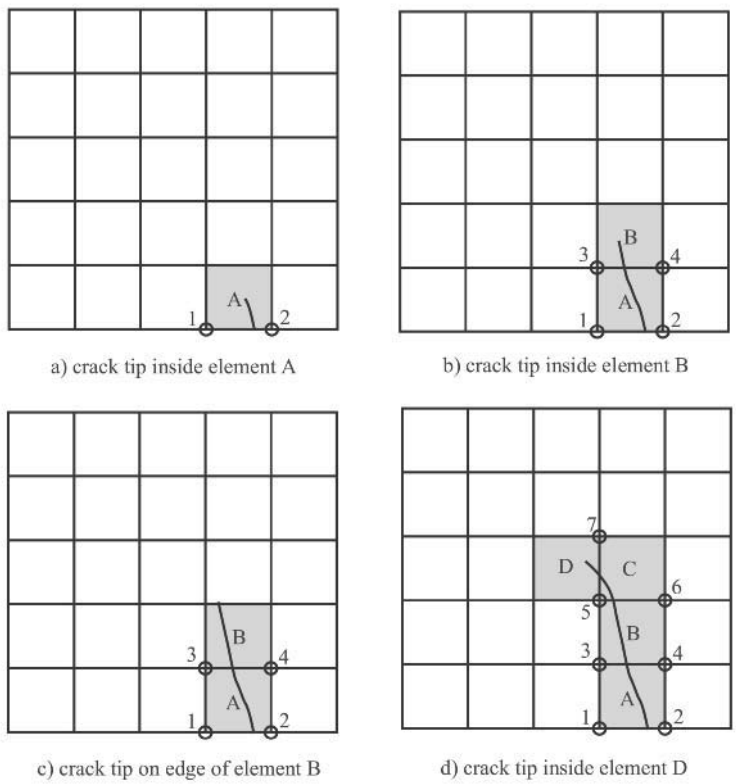

Figure 3.17 Enrichment nodes at different stages of crack propagation.

Other effects include the influence of external forces on the enrichment degrees of freedom in classical jump functions, while this approach avoids these direct interaction effects.

In a finite element mesh, as depicted in Fig. 3.19, the set of nodes that must be enriched with Heaviside or crack tip functions are marked by circles and squares, respectively. The crack does not affect other nodes and their associated classical finite element degrees of freedom.

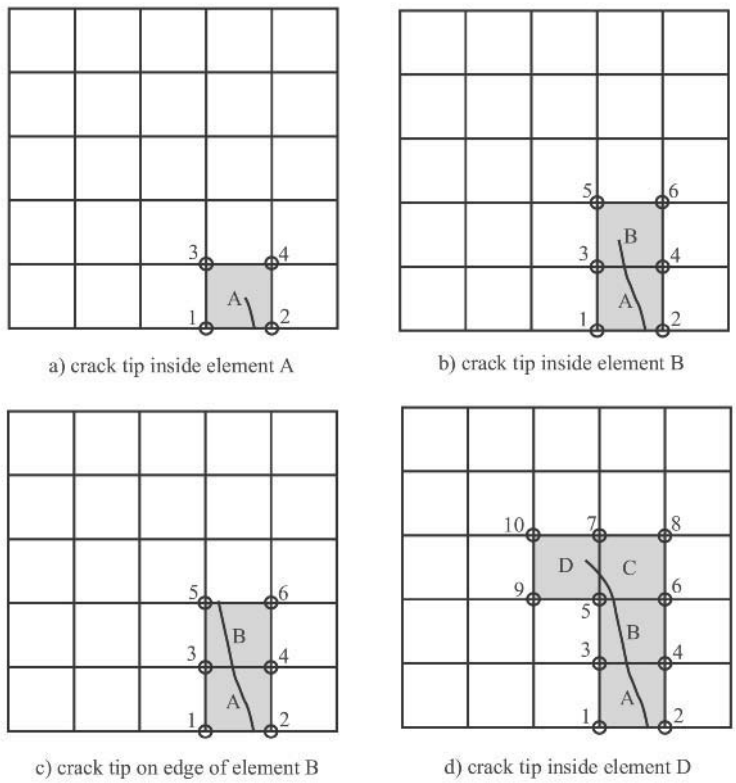

Figure 3.18 Enrichment nodes at different stages of crack propagation.

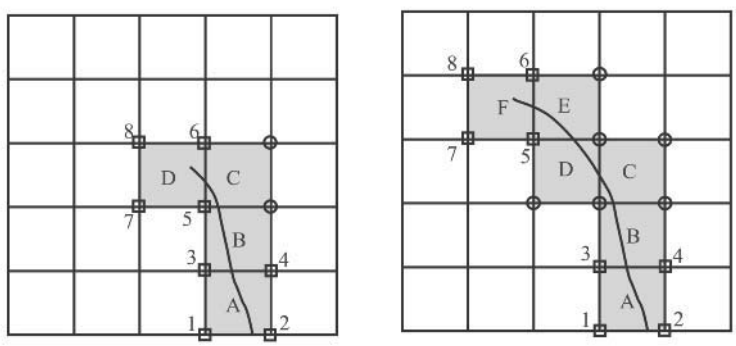

Figure 3.19 Node selection for enrichment at different stages of a crack propagation; nodes marked by squares are enriched by crack tip functions and the circled ones are enriched by the Heaviside function.

3.6.7 Modelling the crack

Moës *et al.* (1999) proposed that Eq. (3.42) be rearranged in order to model crack surfaces and tips in the extended finite element method as below

$$\begin{aligned}\mathbf{u}^h(\mathbf{x}) = &\sum_{j=1}^{n} N_j(\mathbf{x})\mathbf{u}_j + \sum_{h=1}^{m} N_h(\mathbf{x})H(\xi(x))\mathbf{a}_h \\ &+ \sum_{k=1}^{mt_1} N_k(\mathbf{x})\left(\sum_{l=1}^{mf} F_l^1(x)\mathbf{b}_k^{l1}\right) \\ &+ \sum_{k=1}^{mt_2} N_k(\mathbf{x})\left(\sum_{l=1}^{mf} F_l^2(x)\mathbf{b}_k^{l2}\right)\end{aligned} \tag{3.72}$$

where m is the set of nodes that have the crack face (but not the crack tip) in their support domain, while mt_1 and mt_2 are the sets of nodes associated with crack tips 1 and 2 in their influence domain, respectively; $\mathbf{u}_j$ are the nodal displacements (standard degrees of freedom). $\mathbf{a}_h$, $\mathbf{b}_k^1$ and $\mathbf{b}_k^2$ are vectors of additional degrees of nodal freedom for modelling crack faces and the two crack tips, respectively, and $F_l^i(\mathbf{x})$, $i = 1, 2$ represent mf crack tip enrichment functions.

To include the corrections related to interpolation failure of the enrichment, Eq. (3.72) can be rewritten as:

$$\begin{aligned}\mathbf{u}^h(\mathbf{x}) = &\sum_{j=1}^{n} N_j(\mathbf{x})\mathbf{u}_j + \sum_{h=1}^{m} N_h(\mathbf{x})\big(H(\xi(x)) - H(\xi(x_h))\big)\mathbf{a}_h \\ &+ \sum_{k=1}^{mt_1} N_k(\mathbf{x})\left(\sum_{l=1}^{mf} \big(F_l^1(x) - F_l^1(x_k)\big)\mathbf{b}_k^{l1}\right) \\ &+ \sum_{k=1}^{mt_2} N_k(\mathbf{x})\left(\sum_{l=1}^{mf} \big(F_l^2(x) - F_l^2(x_k)\big)\mathbf{b}_k^{l2}\right)\end{aligned} \tag{3.73}$$

Despite the fact that Eq. (3.72) lacks the interpolation property, it has been frequently used for XFEM fracture analysis.

3.7 DISCRETIZATION AND INTEGRATION

3.7.1 Governing equation

Consider a body in the state of equilibrium with the boundary conditions in the form of traction and displacement conditions, as depicted in Fig. 3.20.

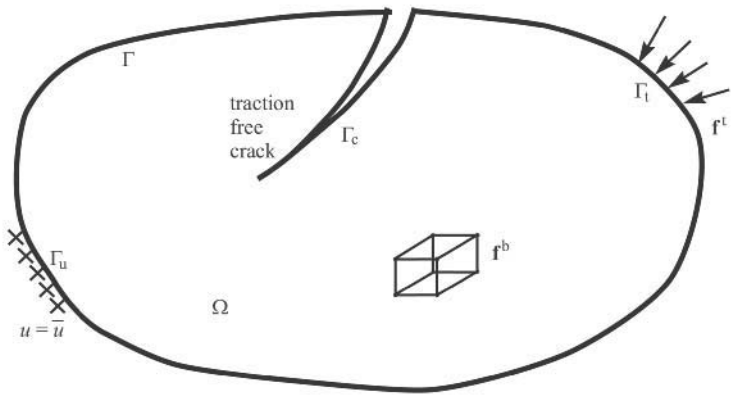

Figure 3.20 A body in a state of elastostatic equilibrium.

The strong form of the equilibrium equation can be written as:

$$\nabla.\boldsymbol{\sigma} + \mathbf{f}^{\mathrm{b}} = 0 \qquad \text{in } \Omega \tag{3.74}$$

with the following boundary conditions:

$$\boldsymbol{\sigma} \cdot \mathbf{n} = \mathbf{f}^{\mathrm{t}} \qquad \text{on } \Gamma_{\mathrm{t}} \tag{3.75}$$

$$\mathbf{u} = \bar{\mathbf{u}} \qquad \text{on } \Gamma_{\mathrm{u}} \tag{3.76}$$

$$\boldsymbol{\sigma} \cdot \mathbf{n} = 0 \qquad \text{on } \Gamma_{\mathrm{c}} \tag{3.77}$$

where Γ_{t}, Γ_{u} and Γ_{c} are traction, displacement and crack boundaries, respectively, $\boldsymbol{\sigma}$ is the stress tensor and $\mathbf{f}^{\mathrm{b}}$ and $\mathbf{f}^{\mathrm{t}}$ are the body force and external traction vectors, respectively.

The variational formulation of the boundary value problem can be defined as:

$$W^{\mathrm{int}} = W^{\mathrm{ext}} \tag{3.78}$$

or

$$\int_{\Omega} \boldsymbol{\sigma} \cdot \delta\boldsymbol{\varepsilon} \; \mathrm{d}\Omega = \int_{\Omega} \mathbf{f}^{\mathrm{b}} \cdot \delta\mathbf{u} \; \mathrm{d}\Omega + \int_{\Gamma} \mathbf{f}^{\mathrm{t}} \cdot \delta\mathbf{u} \; \mathrm{d}\Gamma \tag{3.79}$$

3.7.2 XFEM discretization

Discretization of Eq. (3.79) using the XFEM procedure (Eq. (3.72)) results in a discrete system of linear equilibrium equations:

$$\mathbf{K}\mathbf{u}^h = \mathbf{f} \tag{3.80}$$

where $\mathbf{K}$ is the stiffness matrix, $\mathbf{u}^h$ is the vector of degrees of nodal freedom (for both classical and enriched ones) and $\mathbf{f}$ is the vector of external force. The global matrix and vectors are calculated by assembling the matrix and vectors of each element. $\mathbf{K}$ and $\mathbf{f}$ for each element e are defined as

$$\mathbf{K}_{ij}^e = \begin{bmatrix} \mathbf{K}_{ij}^{\mathbf{uu}} & \mathbf{K}_{ij}^{\mathbf{ua}} & \mathbf{K}_{ij}^{\mathbf{ub}} \\ \mathbf{K}_{ij}^{\mathbf{au}} & \mathbf{K}_{ij}^{\mathbf{aa}} & \mathbf{K}_{ij}^{\mathbf{ab}} \\ \mathbf{K}_{ij}^{\mathbf{bu}} & \mathbf{K}_{ij}^{\mathbf{ba}} & \mathbf{K}_{ij}^{\mathbf{bb}} \end{bmatrix} \tag{3.81}$$

$$\mathbf{f}_i^e = \left\{ \mathbf{f}_i^u \quad \mathbf{f}_i^{\mathbf{a}} \quad \mathbf{f}_i^{\mathbf{b}1} \quad \mathbf{f}_i^{\mathbf{b}2} \quad \mathbf{f}_i^{\mathbf{b}3} \quad \mathbf{f}_i^{\mathbf{b}4} \right\}^{\mathrm{T}} \tag{3.82}$$

and $\mathbf{u}^h$ is the vector of nodal parameters:

$$\mathbf{u}^h = \left\{ \mathbf{u} \quad \mathbf{a} \quad \mathbf{b}_1 \quad \mathbf{b}_2 \quad \mathbf{b}_3 \quad \mathbf{b}_4 \right\}^{\mathrm{T}} \tag{3.83}$$

with

$$\mathbf{K}_{ij}^{rs} = \int_{\Omega^e} (\mathbf{B}_i^r)^{\mathrm{T}} \mathbf{D} \mathbf{B}_j^s \, \mathrm{d}\Omega \qquad (r, s = \mathbf{u}, \mathbf{a}, \mathbf{b}) \tag{3.84}$$

$$\mathbf{f}_i^{\mathbf{u}} = \int_{\Gamma_t} N_i \mathbf{f}^{\mathrm{t}} \, \mathrm{d}\Gamma + \int_{\Omega^e} N_i \mathbf{f}^{\mathrm{b}} \, \mathrm{d}\Omega \tag{3.85}$$

$$\mathbf{f}_i^{\mathbf{a}} = \int_{\Gamma_t} N_i H \mathbf{f}^{\mathrm{t}} \, \mathrm{d}\Gamma + \int_{\Omega^e} N_i H \mathbf{f}^{\mathrm{b}} \, \mathrm{d}\Omega \tag{3.86}$$

$$\mathbf{f}_i^{\mathbf{b}\alpha} = \int_{\Gamma_t} N_i F_\alpha \mathbf{f}^{\mathrm{t}} \, \mathrm{d}\Gamma + \int_{\Omega^e} N_i F_\alpha \mathbf{f}^{\mathrm{b}} \, \mathrm{d}\Omega \qquad (\alpha = 1, 2, 3 \text{ and } 4) \tag{3.87}$$

In Eq. (3.84), $\mathbf{B}$ is the matrix of shape function derivatives,

$$\mathbf{B}_i^{\mathbf{u}} = \begin{bmatrix} N_{i,x} & 0 \\ 0 & N_{i,y} \\ N_{i,y} & N_{i,x} \end{bmatrix} \tag{3.88}$$

$$\mathbf{B}_i^{\mathbf{a}} = \begin{bmatrix} (N_i H)_{,x} & 0 \\ 0 & (N_i H)_{,y} \\ (N_i H)_{,y} & (N_i H)_{,x} \end{bmatrix} \tag{3.89}$$

$$\mathbf{B}_i^{\mathbf{b}} = \left[\mathbf{B}_i^{\mathbf{b}1} \quad \mathbf{B}_i^{\mathbf{b}2} \quad \mathbf{B}_i^{\mathbf{b}3} \quad \mathbf{B}_i^{\mathbf{b}4}\right] \tag{3.90}$$

$$\mathbf{B}_i^{\alpha} = \begin{bmatrix} \left(N_i F_\alpha\right)_{,x} & 0 \\ 0 & \left(N_i F_\alpha\right)_{,y} \\ \left(N_i F_\alpha\right)_{,y} & \left(N_i F_\alpha\right)_{,x} \end{bmatrix} \quad (\alpha = 1,2,3 \text{ and } 4) \tag{3.91}$$

To include the effects of interpolation, the following shifting amendments are required:

$$\mathbf{B}_i^{\mathbf{a}} = \begin{bmatrix} \left(N_i\left[H(\xi) - H(\xi)\right]\right)_{,x} & 0 \\ 0 & \left(N_i\left[H(\xi) - H(\xi_i)\right]\right)_{,y} \\ \left(N_i\left[H(\xi) - H(\xi)\right]\right)_{,y} & \left(N_i\left[H(\xi) - H(\xi_i)\right]\right)_{,x} \end{bmatrix} \tag{3.92}$$

$$\mathbf{B}_i^{\alpha} = \begin{bmatrix} \left[N_i\left(F_\alpha - F_{\alpha i}\right)\right]_{,x} & 0 \\ 0 & \left[N_i\left(F_\alpha - F_{\alpha i}\right)\right]_{,y} \\ \left[N_i\left(F_\alpha - F_{\alpha i}\right)\right]_{,y} & \left[N_i\left(F_\alpha - F_{\alpha i}\right)\right]_{,x} \end{bmatrix} \quad (\alpha = 1,2,3 \text{ and } 4) \tag{3.93}$$

The rest of the computation depends on the definition of the enrichment function. The following types are considered:

1. The Heaviside function $\psi(x) = H(\xi)$

Derivative of the Heaviside function is the Dirac delta function:

$$H_{,i}(\xi) = \delta(\xi) \tag{3.94}$$

which vanishes except at the position of the crack interface:

$$H_{,i}(\xi) = \begin{cases} 1 & \text{at crack tip} \\ 0 & \text{otherwise} \end{cases} \tag{3.95}$$

As a result, Eq. (3.89) can be rewritten as:

$$\mathbf{B}_i^{\mathbf{a}} = \begin{bmatrix} N_{i,x}H & 0 \\ 0 & N_{i,y}H \\ N_{i,y}H & N_{i,x}H \end{bmatrix} \tag{3.96}$$

To include the effects of interpolation, $H(\xi)$ should be replaced by $H(\xi) - H(\xi_i)$.

2. The weak discontinuity function $\psi(\mathbf{x}) = \chi(\mathbf{x}) = \left|\xi(\mathbf{x})\right|$

Derivative of the weak discontinuity enrichment function can be obtained from

$$\psi_{,i}(\mathbf{x}) = sign(\xi)\ \xi_{,i}(\mathbf{x}) \tag{3.97}$$

Derivatives of $\xi(\mathbf{x})$ are calculated from the derivatives of the shape functions if a standard finite element interpolation is adopted to define the function in terms of its nodal values:

$$\xi(\mathbf{x}) = \sum_{j=1}^{4} N_j(\mathbf{x})\ \xi_j \tag{3.98}$$

$$\xi_{,i}(\mathbf{x}) = \sum_{j=1}^{4} N_{j,i}(\mathbf{x})\ \xi_j \tag{3.99}$$

3. The near tip enrichment functions $\psi = F_\alpha(r,\theta)$

The near tip enrichment functions have already been defined in terms of the local crack tip coordinate system (r,θ), (Fig. 3.2)

$$F_\alpha(r,\theta) = \left\{\sqrt{r}\sin\frac{\theta}{2}, \sqrt{r}\cos\frac{\theta}{2}, \sqrt{r}\sin\theta\sin\frac{\theta}{2}, \sqrt{r}\sin\theta\cos\frac{\theta}{2}\right\} \tag{3.100}$$

Derivatives of $F_\alpha(r,\theta)$ with respect to the crack tip polar coordinates (r,θ) become

$$F_{1,r} = \frac{1}{2\sqrt{r}}\sin\frac{\theta}{2}, \qquad F_{1,\theta} = \frac{\sqrt{r}}{2}\cos\frac{\theta}{2} \tag{3.101}$$

$$F_{2,r} = \frac{1}{2\sqrt{r}}\cos\frac{\theta}{2}, \qquad F_{2,\theta} = -\frac{\sqrt{r}}{2}\sin\frac{\theta}{2} \tag{3.102}$$

$$F_{3,r} = \frac{1}{2\sqrt{r}}\sin\frac{\theta}{2}\sin\theta, \quad F_{3,\theta} = \sqrt{r}\left(\frac{1}{2}\cos\frac{\theta}{2}\sin\theta + \sin\frac{\theta}{2}\cos\theta\right) \tag{3.103}$$

$$F_{4,r} = \frac{1}{2\sqrt{r}}\cos\frac{\theta}{2}\sin\theta, \quad F_{4,\theta} = \sqrt{r}\left(-\frac{1}{2}\sin\frac{\theta}{2}\sin\theta + \cos\frac{\theta}{2}\cos\theta\right) \tag{3.104}$$

and the derivatives of $F_\alpha(r,\theta)$ with respect to the local crack coordinate system (x',y') can then be defined as:

$$F_{1,x'} = -\frac{1}{2\sqrt{r}}\sin\frac{\theta}{2}, \qquad F_{1,y'} = \frac{1}{2\sqrt{r}}\cos\frac{\theta}{2} \tag{3.105}$$

$$F_{2,x'} = \frac{1}{2\sqrt{r}}\cos\frac{\theta}{2}, \qquad F_{2,y'} = \frac{1}{2\sqrt{r}}\sin\frac{\theta}{2} \tag{3.106}$$

$$F_{3,x'} = -\frac{1}{2\sqrt{r}}\sin\frac{3\theta}{2}\sin\theta, \quad F_{3,y'} = \frac{1}{2\sqrt{r}}\left(\sin\frac{\theta}{2} + \sin\frac{3\theta}{2}\cos\theta\right) \tag{3.107}$$

$$F_{4,x'} = -\frac{1}{2\sqrt{r}}\cos\frac{3\theta}{2}\sin\theta, \quad F_{4,y'} = \frac{1}{2\sqrt{r}}\left(\cos\frac{\theta}{2} + \cos\frac{3\theta}{2}\cos\theta\right) \tag{3.108}$$

Finally, the derivatives in the global coordinate system are obtained,

$$F_{\alpha,x} = F_{\alpha,x'}\cos(\alpha) - F_{\alpha,y'}\sin(\alpha) \tag{3.109}$$

$$F_{\alpha,y} = F_{\alpha,x'}\sin(\alpha) + F_{\alpha,y'}\cos(\alpha) \tag{3.110}$$

where α is the angle of crack path with respect to the x axis.

3.7.3 Element partitioning and numerical integration

The Gauss quadrature rule is widely used in finite element analysis for numerical evaluation of various integrals over a specified domain of interest such as a finite element. For polynomial integrands, the Gauss quadrature is proved to be exact. However, for non-polynomial integrands, it may result in substantial accuracy reduction.

Even for a specified integrand, using a small number of Gauss points may introduce excessive error. Introduction of discontinuity within a finite element transforms the displacement and stress fields into highly nonlinear fields. This is further complicated as the crack path turns to be substantially curved. As a result, an efficient approach is required to define the necessary points needed for the integration within an enriched element. The approach has to be consistent with the geometry of the crack as well as the order of the enrichment functions.

Because the ordinary Gauss rules do not accurately calculate the integration of enrichment functions in elements cut by a crack, Dolbow (1999) proposed two methods to overcome this numerical difficulty. The first method is to subdivide the element at both sides of the crack into sub-triangles whose edges are adapted to crack faces and the second one is to subdivide the element into sub-quads. Both methods are illustrated in Fig. 3.21.

In both methods, if values of $A^-/(A^+ + A^-)$ and $A^+/(A^+ + A^-)$, where A^+ and A^- are the area of the influence domain of a node above and below the crack, respectively (see Fig. 3.22a), are smaller than an allowable tolerance value, the node must not be

enriched. A tolerance of 0.01% was proposed by Dolbow (1999), although it should be set according to each specific problem. In an alternative approach, a node is enriched if each side of the crack in its influence domain includes at least one Gauss point. Fig. 3.22b shows a mesh that contains a crack while the sub-quad partitioning was applied. Although the crack cuts the element in Fig. 3.22b, node J must not be enriched because there is no Gaussian point above the crack. On the contrary, node J in Fig. 3.22a has to be enriched.

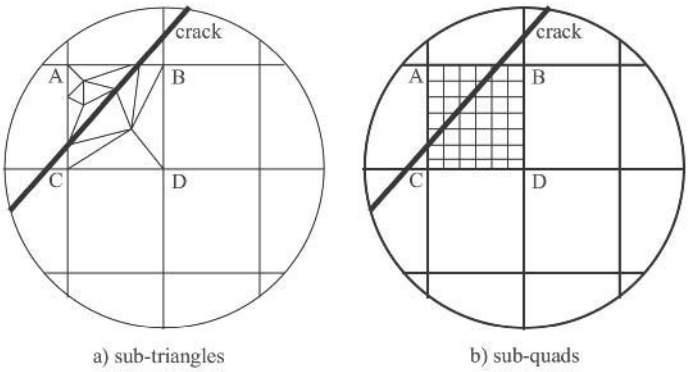

Figure 3.21 Two methods for partitioning the cracked element.

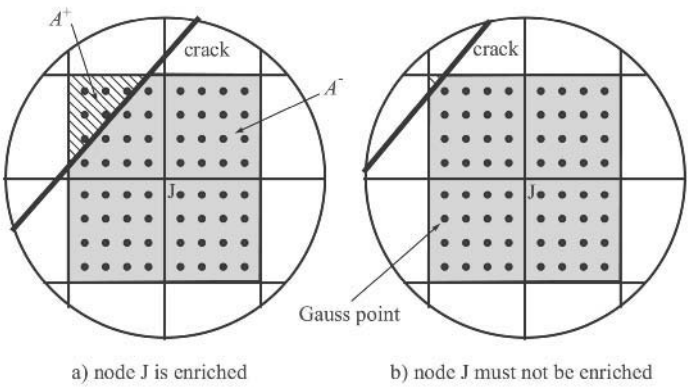

Figure 3.22 Criteria for node enrichment: a) based on definitions of A^+ and A^- in its support domain, b) based on the existence of Gauss points within its support domain.

The final point is that in XFEM analysis of fracture mechanics problems, elements containing a crack tip should also have a singularity at the crack tip. Hence, a sub-triangulation procedure might not be accurate enough if Gauss points of the sub-triangles are close to the stress singularity.

3.7.4 Crack intersection

The basic equation for XFEM enrichment requires further modification if two or more cracks intersect within a finite element, as illustrated in Fig. 3.23.

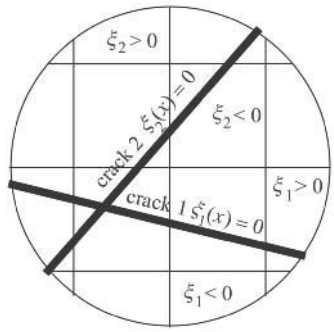

Figure 3.23 Intersecting cracks within a finite element.

The XFEM approximation of the displacement may be written as (Daux *et al.* 2000):

$$\begin{aligned}\mathbf{u}^h(\mathbf{x}) = &\sum_{j=1}^{n} N_j(\mathbf{x})\mathbf{u}_j \\ &+ \sum_{h=1}^{m} N_h(\mathbf{x})H(\xi_1)\mathbf{a}_h^1 + \sum_{h=1}^{m} N_h(\mathbf{x})H(\xi_2)\mathbf{a}_h^2 \\ &+ \sum_{h=1}^{m} N_h(\mathbf{x})H(\xi_1)H(\xi_2)\mathbf{a}_h^3 \\ &+ \sum_{k=1}^{mt_1} N_k(\mathbf{x})\left(\sum_{l=1}^{mf} F_l^1(x)\mathbf{b}_k^{l1}\right) \\ &+ \sum_{k=1}^{mt_2} N_k(\mathbf{x})\left(\sum_{l=1}^{mf} F_l^2(x)\mathbf{b}_k^{l2}\right)\end{aligned} \tag{3.111}$$

Some researchers have proposed a more efficient approach that avoids the cross terms by introduction of modified signed distance functions (Zi *et al.* 2004).

3.8 TRACKING MOVING BOUNDARIES

One important aspect of problems with moving interfaces is to track them as they evolve. Most conventional numerical techniques attempt to follow moving boundaries by putting a collection of marker points on the evolving front. This is usually performed by the use of general B-spline or non-uniform rational B-spline (NURBS) functions (Fig. 3.24) (Patrikalakis 2003). Positions of the particles are then advanced in accordance with a set of finite difference approximations to the equations of motion (Fig. 3.24). Such schemes usually become unstable around points of high curvature and cusps. The reason can be attributed to the fact that any small error in determining the position may produce large

errors in the evaluation of the curvature (Sethian 1987, 1996, 1999a, 1999b, Adalsteinsson and Sethian 2003).

One alternative is to consider the reformulation of the equations of motion as a conservation law with viscosity, and solve these equations with the techniques developed for gas dynamics. These techniques, based on high-order upwind formulations, are particularly attractive, since they are highly stable, accurate, and preserve monotonicity (Sukumar *et al.* 2001).

This idea forms one cornerstone of numerical methods based on partial differential equations for tracking evolving fronts. It has contributed to two different, yet complementary techniques: (1) a more general but slower general-purpose time-dependent level set method; (2) an extremely efficient but limited-purpose fast marching method for certain front problems. Both methods are designed to handle problems in which the separating interfaces develop sharp corners and cusps, change topology, break apart and merge together. These techniques have a wide range of applications, including problems in fluid mechanics, combustion, manufacturing computer chips, computer animation, image processing, structure of snowflakes, and the shape of soap bubbles (Sethian 1987).

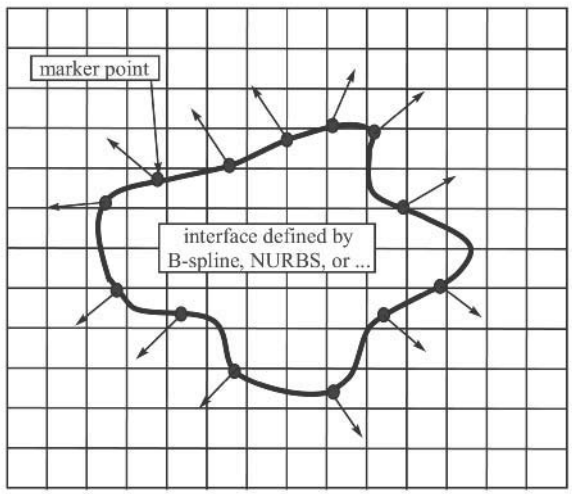

Figure 3.24 Tracking marker points on a moving boundary.

3.8.1 Level set method

A powerful tool for tracking interfaces is the level set method (LSM). Though it is not mandatory to use level sets in XFEM, many XFEM formulations take advantages of the level set method.

The level set approach, introduced by Osher and Sethian (1988), instead of following the interface itself, takes the original curve and builds it into a surface. A major property of this cone shaped surface is that it intersects the *xy* plane exactly where the curve sits.

Such a surface is called the level set function because it accepts a point in the plane and generates back its height (level) (Fig. 3.25).

It seems odd to replace the problem of a moving curve with a moving surface. However, the level set function is well behaved and all the complicated problems of breaking and merging can be easily handled.

In LSM, the interface of interest is represented as the zero level set of a function $\phi(\mathbf{x})$. This function is one dimension higher than the dimension of the interface. The evolution equation for the interface can then be expressed as an equation for the evolution of ϕ.

There are many advantages to using LSM for tracking interfaces. First, unlike many other interface tracking schemes, the motion of the interface is computed on a fixed Eulerian mesh. Second, the method handles changes in the topology of the interface naturally. Third, the method can be easily extended to higher dimensions. Finally, the geometric properties of the interface can be obtained from the level set function ϕ.

One drawback of LSM is that the level set representation requires a function of a higher dimension than the original crack, potentially leading to higher storage and computational costs.

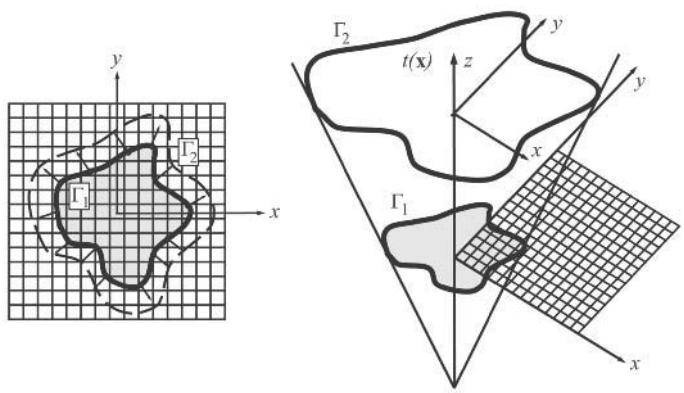

Figure 3.25 A simple description of LSM and FMM, including the original front projected on the *xy* plane and the level set function as the intersection of surface and *xy* plane.

3.8.1.1 *Definition of the level set function*

Consider a domain Ω divided into two non-overlapping subdomains, Ω_1 and Ω_2, sharing an interface Γ, as illustrated in Fig. 3.26. The level set function $\phi(\mathbf{x})$ is defined as:

$$\phi(\mathbf{x}) = \begin{cases} > 0 & \mathbf{x} \in \Omega_1 \\ = 0 & \mathbf{x} \in \Gamma \\ < 0 & \mathbf{x} \in \Omega_2 \end{cases} \tag{3.112}$$

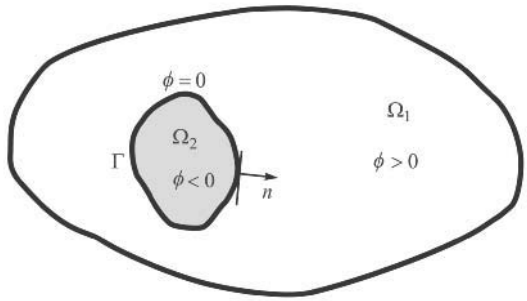

Figure 3.26 Definition of the level set function.

An interpretation of Eq. (3.112) is that the interface Γ can be regarded as the zero level contour of the level set function $\phi(\mathbf{x})$.

One of the common choices for the level set function, $\phi(\mathbf{x})$, can then be simply defined in terms of the signed distance function:

$$\phi(\mathbf{x}) = \xi(\mathbf{x}) = \begin{cases} d & \mathbf{x} \in \Omega_1 \\ -d & \mathbf{x} \in \Omega_2 \end{cases} \tag{3.113}$$

where d is the normal distance from a point $\mathbf{x}$ to the interface Γ. Note that the signed distance function satisfies the unity property:

$$\|\nabla \phi(\mathbf{x})\| = 1 \tag{3.114}$$

Using the definition of the Heaviside function, $H(\xi)$,

$$H(\xi) = \begin{cases} 1 & \forall \xi > 0 \\ 0 & \forall \xi < 0 \end{cases} \tag{3.115}$$

domains Ω_1 and Ω_2 can then be defined as

$$\begin{cases} \Omega_1 = \{\mathbf{x} \in \Omega, H(\phi(\mathbf{x})) = 1\} \\ \Omega_2 = \{\mathbf{x} \in \Omega, H(\phi(\mathbf{x})) = 0\} \end{cases} \tag{3.116}$$

or in a more appropriate form

$$\begin{cases} \Omega_1 = \{\mathbf{x} \in \Omega, H(\phi(\mathbf{x})) = 1\} \\ \Omega_2 = \{\mathbf{x} \in \Omega, H(-\phi(\mathbf{x})) = 1\} \end{cases} \tag{3.117}$$

The normal vector $\mathbf{n}$ to the interface Γ at a point $\mathbf{x} \in \Gamma$ can then be defined as:

$$\mathbf{n} = \frac{\nabla \phi(\mathbf{x})}{\left\| \nabla \phi(\mathbf{x}) \right\|} \tag{3.118}$$

For the special case of $\left\| \nabla \phi(\mathbf{x}) \right\| = 1$,

$$\mathbf{n} = \nabla \phi(\mathbf{x}) \tag{3.119}$$

Discretization of the level set allows for the evaluation of the level set at the element level based on the nodal level set values $\phi_j = \phi(\mathbf{x}_j)$ and known finite element shape functions $N_j(\mathbf{x})$:

$$\phi(\mathbf{x}) = \sum_{j=1}^{n} N_j(\mathbf{x}) \phi_j \tag{3.120}$$

This is practically an important concept for implicitly defining the level set function for describing a general solid shape. This simple procedure of defining the level set function can also be extended to other meshless methods and even other arbitrary distributions of points, providing that the value of the level set function at each point is known. Convex and concave boundaries, cracks, holes and multiple surfaces can be similarly prepared (Sukumar *et al.* 2001).

Another major advantage of this approximation is that it avoids the necessity for derivatives of the level set function at nodal points by expressing it in terms of derivatives of the finite element shape functions:

$$\phi_{,i}(\mathbf{x}) = \sum_{j=1}^{n} N_{j,i}(\mathbf{x}) \phi_j \tag{3.121}$$

3.8.1.2 *Other types of level sets*

The signed distance function is perhaps the most favourite type of level set function. However, there are other types, such as circular, elliptical and polygonal functions. The circular level set function can be defined as (Sukumar *et al.* 2001):

$$\phi_i(\mathbf{x}) = \underbrace{\min_{\mathbf{x}_c^j \in \Omega^j}}_{j=1,\ldots,n_c} \left\{ \left\| \mathbf{x}_i - \mathbf{x}_c^j \right\| - r_c^j \right\} \tag{3.122}$$

where Ω^j is the domain of the jth void, n_c is the number of circular holes, and $\mathbf{x}_c^j$ is the location of the centre of the jth circular hole with radius r_c^j.

The elliptical level set function can be expressed as (Sukumar *et al.* 2001):

$$\phi_i(\mathbf{x}) = \underbrace{\min}_{j=1,\ldots,n_c} \left\{ f(\xi^j) \right\} \tag{3.123}$$

where $f(\xi^j)$ is the equation of ellipse j in the local coordinate system,

$$f(\xi^j) = \left\| \xi^j \right\| - 1 \tag{3.124}$$

and

$$\xi^j = \left(\frac{\bar{x}^j}{a_j}, \frac{\bar{y}^j}{b_j} \right) \tag{3.125}$$

where a_j, b_j are the semi-major and semi-minor axes of ellipse with centre $\mathbf{x}_c^j$,

$$\bar{\mathbf{x}}^j = R^j (\mathbf{x}_i - \mathbf{x}_c^j) \tag{3.126}$$

Finally, the polygonal level set function takes the form of a polygon (Sukumar *et al.* 2001):

$$\phi_i(\mathbf{x}) = \left\| \mathbf{x}_i - \mathbf{x}_{\min} \right\| \text{sign}\left[\mathbf{n}_{\min} \cdot (\mathbf{x}_i - \mathbf{x}_{\min}) \right] \tag{3.127}$$

$$\left\| \mathbf{x}_i - \mathbf{x}_{\min} \right\| = \underbrace{\min}_{\substack{\mathbf{x}_j \in \Gamma_j \\ j=1,\ldots,p}} \left\| \mathbf{x}_i - \mathbf{x}_j \right\| \tag{3.128}$$

where $\mathbf{x}_{\min}$ is the orthogonal projection of x on the interface Γ and $\mathbf{n}_{\min}$ is its associated normal to the interface. The polygonal interface Γ consists of p segments Γ_p:

$$\Gamma = \cup_{i=1}^{p} \Gamma_i, \quad \Gamma_1 = [\mathbf{x}_1, \mathbf{x}_2], \Gamma_2 = [\mathbf{x}_2, \mathbf{x}_3], \ldots, \Gamma_p = [\mathbf{x}_p, \mathbf{x}_1] \tag{3.129}$$

3.8.1.3 *Evolving surfaces*

In the case of a moving surface, its position is no longer known *a priori*. From the fact that the level set is zero on the surface, its material time derivative has to vanish:

$$\frac{\mathrm{D}\phi(\mathbf{x},t)}{\mathrm{D}t} = 0 \tag{3.130}$$

which can be written in the form of the Hamilton–Jacobi equation of motion:

$$\frac{\partial \phi(\mathbf{x},t)}{\partial t} + \nabla \phi(\mathbf{x},t) \cdot \mathbf{v}(\mathbf{x},t) = 0 \tag{3.131}$$

or simply,

$$\dot{\phi} + \phi_{,i} \mathbf{v}_i = 0 \tag{3.132}$$

where $\mathbf{v}$ is the velocity of the interface. Eq. (3.132) can be transformed into a more appropriate incremental form using a first-order time integration scheme within a time step Δt:

$$\phi^{n+1} = \phi^n - \Delta t \, \phi^n_{,i} \, \mathbf{v}^n_i \tag{3.133}$$

This, however, is unlikely to be appropriate for crack propagation analyses, as the crack speed is not generally known.

3.8.1.4 *Level sets for a crack*

One of the main difficulties in the application of the level set method to crack problems is constraining the evolution of the signed distance function while the crack propagates so that the existing crack surface remains frozen. Since level sets are generally updated by the integration of the Hamilton–Jacobi equation, special techniques have to be adopted for cracks so the level sets describing the existing crack are not modified (Ventura *et al.* 2003). Another reason for a new approach may be attributed to this fact that the level set functions are not updated with the speed of an interface in the direction normal to itself but with the speed at the crack fronts.

A different approach proposed by Ventura *et al.* (2003) is based on the vector level set formulation and avoids the difficulty mentioned above. In this method, the level set is only defined on a narrow band around the crack and the evolution of the level set function does not alter the previously formed crack. The method takes into consideration the effect of new points having a geometric closest point projection onto a segment when a crack advances. A simple updating procedure will then allow for the inclusion of advancing cracks.

The previous definition of the level set for closed interfaces must be modified or altered if it is to be used for an open curve such as a crack. One level set ϕ is not generally sufficient to describe the crack, and another level set ψ at the crack tip is required. A one-dimensional crack growth in a level set framework is modelled by representing the crack as the zero level set of a function $\psi(\mathbf{x},t)$. An endpoint of the crack is represented as the intersection of the zero level set of $\psi(\mathbf{x},t)$ with a zero level set of the function $\phi^k(\mathbf{x},t)$, where k is the number of tips on a given crack. The crack tip level set ψ is generally assumed to be orthogonal to ϕ

$$\phi_{,i}\psi_{,i} = 0 \tag{3.134}$$

The values of the level set functions are stored only at the nodes. The functions can be interpolated over the mesh by the same finite element shape functions (Stolarska and Chopp 2003),

$$\phi^k(\mathbf{x},t) = \sum_{j=1}^{n} N_j(\mathbf{x})\left(\phi^k(\mathbf{x},t)\right)_j \tag{3.135}$$

$$\psi(\mathbf{x},t) = \sum N_j(\mathbf{x})\psi_j(\mathbf{x},t) \tag{3.136}$$

An important consideration is that although the actual crack is embedded inside a domain, the zero level set of ψ cuts through the entire domain. It is also assumed that once a part of a crack has formed, that part will no longer change shape or move.

Crack growth is modelled by appropriately updating the ϕ^k and ψ functions, then reconstructing the updated ϕ function. The evolution of ϕ^k and ψ is determined by the crack growth direction θ. In each step, the displacement of the crack tip is given by the prescribed velocity vector $\mathbf{v} = (\mathbf{v}_x, \mathbf{v}_y)$, which is always normal to the interface. The following steps describe the simple procedure of evolution of the level set functions ϕ_n^k and ψ_n at the step n (Stolarska and Chopp 2003):

Step 1: Determine the rotated level set of ϕ_n^k : $\phi^{k,r}$

$$\phi^{k,r} = (x - x_k)\frac{\mathbf{v}_x}{\|\mathbf{v}\|} + (y - y_k)\frac{\mathbf{v}_y}{\|\mathbf{v}\|} \tag{3.137}$$

Step 2: Determine ψ_{n+1}

$$\psi_{n+1} = \pm\left|(x - x_k)\frac{\mathbf{v}_y}{\|\mathbf{v}\|} + (y - y_k)\frac{\mathbf{v}_x}{\|\mathbf{v}\|}\right| \tag{3.138}$$

Step 3: The updated location of the crack tip can be computed:

$$\phi_{n+1}^k = \phi^{k,r} - \Delta t\|\mathbf{v}\| \tag{3.139}$$

Step 4: ϕ_{n+1} is updated, if more than one crack tip exists:

$$\phi(\mathbf{x},t) = \max_k(\phi^k) \tag{3.140}$$

Step 5: The location of the new crack tip k can now be determined by finding the intersection of the zero level sets of ϕ_{n+1}^{k} and ψ_{n+1}.

At a point $\mathbf{x}$, the polar coordinates with respect to the tangent to the crack tip are defined as:

$$r = \left[\phi(\mathbf{x},t)^2 + \psi(\mathbf{x},t)^2 \right]^{1/2} \tag{3.141}$$

and

$$\theta = \tan^{-1}\left[\frac{\psi(\mathbf{x},t)}{\phi(\mathbf{x},t)} \right] \tag{3.142}$$

3.8.2 Fast marching method

The fast marching method (FMM) was first introduced by Sethian (1996) and later improved by Sethian (1999a) and Chopp (2001). FMMs are designed to track a propagating interface and to find the first arrival of the interface as it passes a point. They are limited to problems in which the speed of propagation is isotropic*;* the speed function never changes sign, so that the front is always moving forward or backward. That speed can change from point to point, but there is no preferred direction. This allows the problem to be converted into a stationary formulation, which provides a tremendous speed. This is in contrast to level set methods that are designed for problems in which the speed function can be positive in some places and negative in others. As a result, the front may move forwards and backwards.

At first glance, it seems, surprisingly, that FMM transforms the problem of a moving boundary into a new non-moving problem. To illustrate the procedure, consider a structured background grid for a closed curve initial disturbance model propagating outwards, as depicted in Fig. 3.25, and suppose that somebody is standing at each grid point $\mathbf{x}$ to measure the time, $t(\mathbf{x})$, for the front to cross that point. The function $t(\mathbf{x})$ gives a cone-shaped surface that has the property of intersecting the *xy* plane exactly where the curve was initially placed. Also, at any height $t(\mathbf{x})$, the surface gives the set of points to which the curve has reached at time t (Sethian 2006).

FMM is closely related to Dijkstra's method, which is a well known method for computing the shortest path on a network of weighted graph edges and nodes. To explain the approach, consider a network in which a different cost has been assigned for reaching each node. In an optimal control, the cost of reaching a point depends on both where the present standing point is and the direction of movement.

Here, the basic idea is briefly explained. First, the starting point is placed in a set of accepted nodes. Grid points which are one link away are considered as neighbour or candidate nodes. Then the correct cost of reaching each of these candidates is computed.

The node with smallest cost is removed from the set of candidates and added to the set of accepted nodes. The procedure continues by computing the cost and adding any new candidates that are not already accepted. The process terminates when all points are accepted. The algorithm is in fact a systematic ordering procedure for determining the cost of reaching points from a known starting point.

Fast marching methods have many desirable qualities. They do not require any iterative procedure and provide the solution in one pass, which allows a systematic ordering update of the points so that each point is touched only once. As a result, the method allows for very fast computation of order $O(n_t \log n_t)$, where n_t is the total number of grid points.

For a set of distributed finite element nodes, the methodology described by Sukumar *et al.* (2003) is followed. Fig. 3.27 illustrates the procedure of nodal classification into three non-overlapping sets; the set of accepted nodes S_a, whose values of $\phi(\mathbf{x})$ (replacing $t(\mathbf{x})$) have been computed, the set of all candidate (neighbour) nodes S_c that are candidates for inclusion into the set S_a, and the set of all distant nodes S_d that are too far from S_a to be candidates. The method begins by systematically moving the nodes from the set S_d into the set S_c and consequently into the set S_a, and terminates when all nodes are accepted.

FMM computes the unique crossing time $\phi(\mathbf{x})$ for a monotonically advancing front when it crosses the point $\mathbf{x}$. Thus $\phi^{-1}(0)$ defines the initial position of the front and at any later time t, the front can be described by $\phi^{-1}(t)$. The crossing time is computed by solving the following equation,

$$\|\nabla\phi(\mathbf{x})\| = \frac{1}{\mathbf{v}(\mathbf{x})} \tag{3.143}$$

where $\mathbf{v}(\mathbf{x})$ is the front speed at the point $\mathbf{x}$.

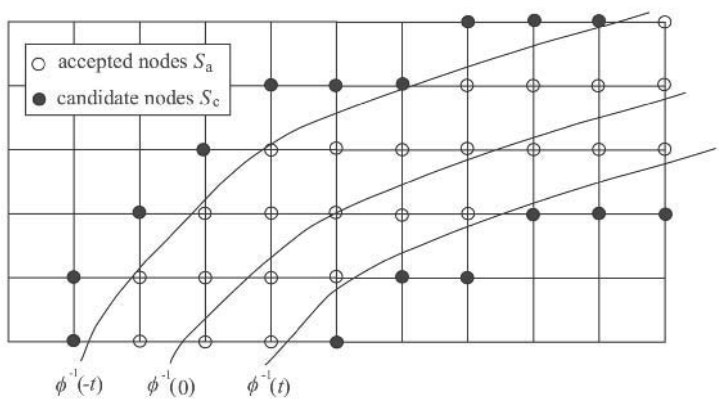

Figure 3.27 Classification of nodes into accepted, candidate (neighbour) and distant nodes (Sukumar *et al.* 2003).

FMM solves Eq. (3.143) by replacing the gradient with suitable upwind operators, and then systematically advancing the front by marching outwards from the boundary data.

A candidate value for a node $\mathbf{x}$ of the set of accepted nodes S_{a}, and each neighbouring node $\mathbf{y} \notin S_a$ can be constructed by using the following second-order forward and backward finite difference approximations for $\phi_x(\mathbf{x}_{i,j})$ (Stolarska and Chopp 2003),

$$\begin{aligned}\phi_x(\mathbf{x}_{i,j}) &\approx D_x^{\mathrm{b}}\phi_{i,j} + \frac{a_1^{\mathrm{b}}\Delta x}{2} D_x^{\mathrm{b}}\, D_x^{\mathrm{b}}\phi_{i,j} \\ &= \frac{\phi_{i,j} - \phi_{i-1,j}}{\Delta x} + \frac{a_1^{\mathrm{b}}}{2}\left(\frac{\phi_{i,j} - 2\phi_{i-1,j} + \phi_{i-2,j}}{\Delta x}\right)\end{aligned} \tag{3.144}$$

$$\begin{aligned}\phi_x(\mathbf{x}_{i,j}) &\approx D_x^{\mathrm{f}}\phi_{i,j} + \frac{a_1^{\mathrm{f}}\Delta x}{2} D_x^{\mathrm{f}}\, D_x^{\mathrm{f}}\phi_{i,j} \\ &= \frac{\phi_{i+1,j} - \phi_{i,j}}{\Delta x} + \frac{a_1^{\mathrm{f}}}{2}\left(\frac{\phi_{i,j} - 2\phi_{i+1,j} + \phi_{i+2,j}}{\Delta x}\right)\end{aligned} \tag{3.145}$$

where D_x^{b} and D_x^{f} denote the backward and forward finite difference operators, respectively,

$$D_x^{\mathrm{b}}\phi_{i,j} = \frac{\phi_{i,j} - \phi_{i-1,j}}{\Delta x} \tag{3.146}$$

$$D_x^{\mathrm{f}}\phi_{i,j} = \frac{\phi_{i+1,j} - \phi_{i,j}}{\Delta x} \tag{3.147}$$

and

$$a_1^{\mathrm{b}} = \begin{cases} 1 & \mathbf{x}_{i-1,j} \in S_{\mathrm{a}} \\ 0 & \mathbf{x}_{i-1,j} \notin S_{\mathrm{a}} \end{cases} \tag{3.148}$$

$$a_1^{\mathrm{f}} = \begin{cases} 1 & \mathbf{x}_{i+2,j} \in S_{\mathrm{a}} \\ 0 & \mathbf{x}_{i+2,j} \notin S_{\mathrm{a}} \end{cases} \tag{3.149}$$

In order to compute $\phi_{i,j}$ with $\mathbf{x}_{i-1,j}, \mathbf{x}_{i,j+1} \in S_{\mathrm{a}}$, the following quadratic equation should be solved:

$$\left(D_x^{\mathrm{b}}\phi_{i,j} + \frac{a_1^{\mathrm{b}}\Delta x}{2} D_x^{\mathrm{b}}\, D_x^{\mathrm{b}}\phi_{i,j}\right)^2 + \left(D_y^{\mathrm{f}}\phi_{i,j} + \frac{a_2^{\mathrm{f}}\Delta y}{2} D_y^{\mathrm{f}}\, D_y^{\mathrm{f}}\phi_{i,j}\right)^2 = \frac{1}{\mathbf{v}_{ij}^2} \tag{3.150}$$

The procedure begins by taking the node $\mathbf{x} \in S_{\mathrm{c}}$ with the smallest value for $\phi(\mathbf{x})$ and moving it from the set S_{c} into S_{a}. Then, each node $\mathbf{y}$ adjacent to the node $\mathbf{x}$ is updated

according to Eq. (3.150). If $\mathbf{y} \in S_d$, it is moved from S_d to S_c. For further details see Sukumar *et al.* (2003).

3.8.3 Ordered upwind method

In FMM, the solution is systematically updated from known values to unknown spots. At each step, one exploits the fact that the gradient of the front is in the direction from which information must come.

This, however, is not true when the speed is not isotropic (Fig. 3.28). If the speed varies irregularly and depends on a number of other effects including the direction, then one can not assume that information always arrives at a trajectory perpendicular to the evolving wave front**.**

A possible solution is to keep track of the characteristic directions, defined as the ratio between the fastest and slowest speed at each point. Accordingly, the entire Dijkstra methodology can be held while modifying it to include anisotropic speeds. This method is called the ordered upwind method (OUM). This maintains the procedure of point ordering, while systematically computing the solution by relying on previously known computed information.

OUMs have been developed in both semi-Lagrangian and fully Eulerian versions. They use partial information about the characteristic directions, obtained by examining the anisotropy ratio between fastest and slowest speeds to decouple the large system of coupled nonlinear discretized equations, producing one pass algorithms of greatly reduced computational efforts of an order $O(n_t \log n_t)$ (Sethian 2001, 2006).

In order to provide a view on FMM extension by the OUM, a more general form of Eq. (3.150), which accounts for the change in direction, takes the following form (Sukumar *et al.* 2003a):

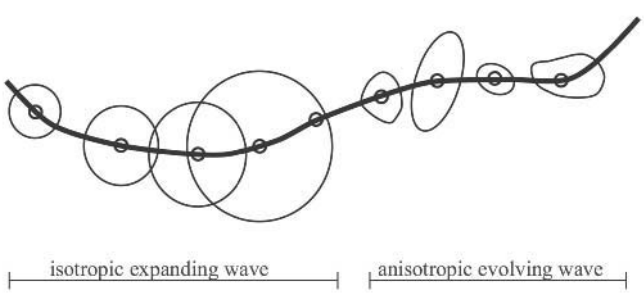

Figure 3.28 Isotropic expanding waves are always circular, even if they are different in size. In contrast, anisotropic evolving waves are irregularly shaped.

$$\left[\max\left(D_x^{\mathrm{b}}\phi_{i,j}+\frac{a_1^{\mathrm{b}}\Delta x}{2}D_x^{\mathrm{b}}D_x^{\mathrm{b}}\phi_{i,j},-D_x^{\mathrm{f}}\phi_{i,j}+\frac{a_1^{\mathrm{f}}\Delta x}{2}D_x^{\mathrm{f}}D_x^{\mathrm{f}}\phi_{i,j},0\right)\right]^2+\left[\max\left(D_y^{\mathrm{b}}\phi_{i,j}+\frac{a_2^{\mathrm{b}}\Delta y}{2}D_y^{\mathrm{b}}D_y^{\mathrm{b}}\phi_{i,j},-D_y^{\mathrm{f}}\phi_{i,j}+\frac{a_2^{\mathrm{f}}\Delta y}{2}D_y^{\mathrm{f}}D_y^{\mathrm{f}}\phi_{i,j},0\right)\right]^2=\frac{1}{\mathbf{v}_{ij}^2} \tag{3.151}$$

Similar methodology has been reported as part of the fast marching method by a number of references. For further details on the fast marching and ordered upwind methods see Sukumar *et al.* (2003a) and Sethian (2001, 2006).

3.9 NUMERICAL SIMULATIONS

In this section a number of classical examples of fracture mechanics are simulated by XFEM. For comparing results, stress intensity factors (SIFs) are calculated based on the equivalent domain integral method. They include:

1. A tensile plate with a central crack.
2. A double edge crack in a tensile plate.
3. A double internal collinear crack.
4. A central crack in an infinite plate.
5. An edge crack in a finite tensile plate.

In all examples, simulated by Ebrahimi (2007), the normalised stress intensity factors defined as $\overline{K}_{\mathrm{I}}=K_{\mathrm{I}}/(\sigma\sqrt{\pi a})$ are computed and compared to assess the performance of XFEM simulations. Further examination of XFEM performance will be provided in Chapters 4 and 5 for orthotropic and cohesive crack problems.

3.9.1 A tensile plate with a central crack

In order to verify the proposed approach, first a classical isotropic rectangular plate with a central crack is considered (Fig. 3.29a). The tensile plate is discretized by a structured finite element mesh. Different meshes of quadrilateral finite elements (24×50 and 48×90 elements) are used to assess the accuracy of results.

Fig. 3.30a shows the crack tip and Heaviside enrichment nodes. Elements that are fully cut by a crack are enriched by the Heaviside enrichment, whereas elements containing a crack tip are enriched by the crack tip enrichment functions. Element matrices are integrated over the set of Gauss points, as depicted in Fig. 3.30b.

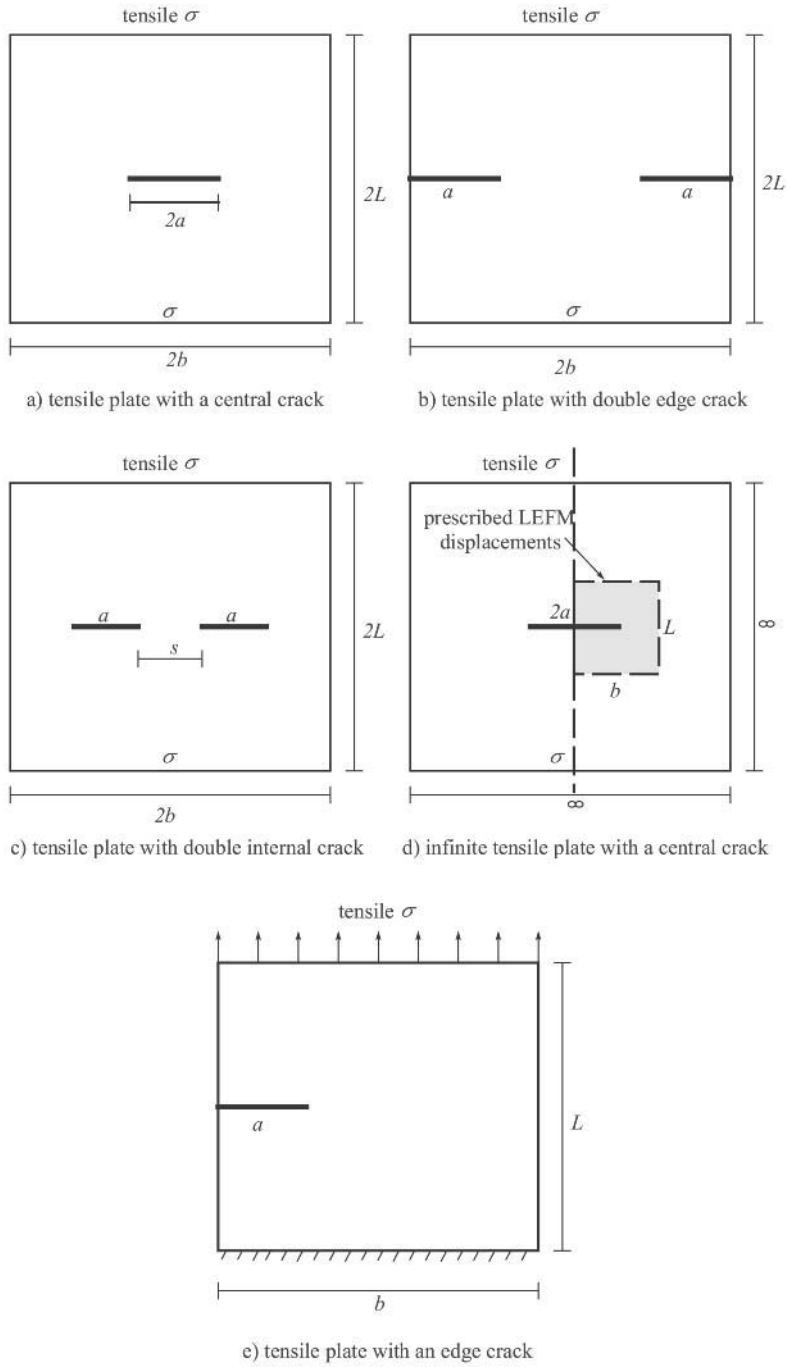

Figure 3.29 Geometry of the tensile plate with a central crack.

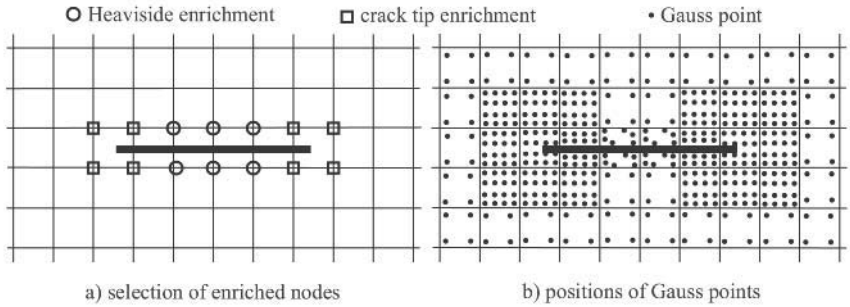

Figure 3.30 Selection of enrichment and position of Gauss points around the central crack.

Table 3.1 compares the normalised stress intensity factors for various meshes as well as different ratios of crack length a to plate width b. Computed errors show a close agreement between the numerical results and the exact solution, according to Irwin's classical solution.

Table 3.1 Normalised values of stress intensity factors.

a/b	Irwin	Mesh 24×50		Mesh 48×90	
	$\overline{K}_{\mathrm{I}}$	$\overline{K}_{\mathrm{I}}$	Error (%)	$\overline{K}_{\mathrm{I}}$	Error (%)
1/8	1.040	1.033	0.72	1.035	0.56
1/6	1.075	1.066	0.78	1.069	0.59
1/4	1.189	1.180	0.81	1.183	0.56

3.9.2 Double edge cracks

The second example is another classical problem of fracture mechanics. A double edge crack plate is subjected to tensile stresses, as depicted in Fig. 3.29b. Three different crack to width ratios are analysed and the normalised stress intensity factor is calculated for two different finite element discretizations (24×50 and 48×90 elements). They are compared to the classical solutions by Irwin, as illustrated in Table 3.2.

Table 3.2 Normalised values of stress intensity factors.

a/b	Irwin	Mesh 24×50		Mesh 48×90	
	$\overline{K}_{\mathrm{I}}$	$\overline{K}_{\mathrm{I}}$	Error (%)	$\overline{K}_{\mathrm{I}}$	Error (%)
1/8	1.129	1.103	2.34	1.108	1.90
1/6	1.130	1.112	1.60	1.116	1.29
1/4	1.170	1.163	0.59	1.166	0.30

Contours of σ_{xx} and σ_{yy} are shown in Fig. 3.31. In both cases, a stress concentration is observed around the crack tip. This is unlikely to be obtainable by similar finite elements with conventional formulation.

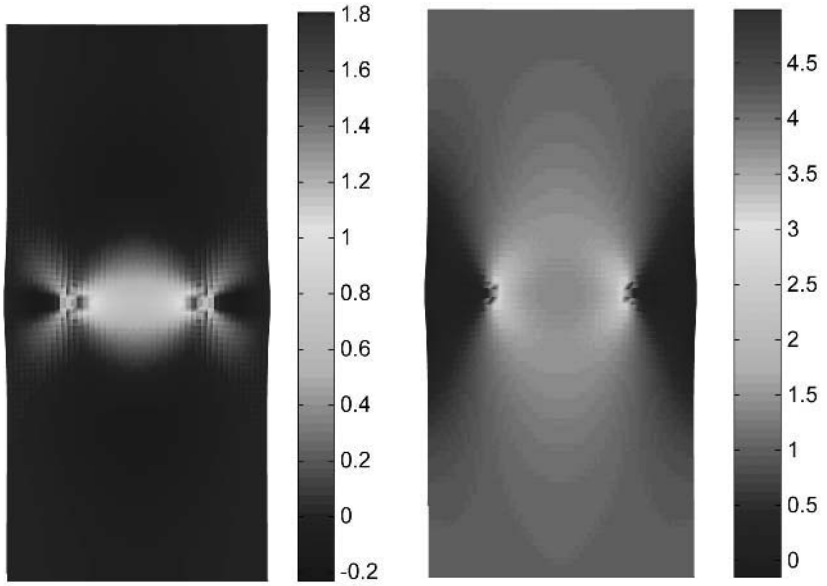

a) σ_{xx} b) σ_{yy}

Figure 3.31 Contours of stress distribution.

3.9.3 Double internal collinear cracks

A double internal collinear crack within an infinite tensile plate is considered (Fig. 3.29c). The same 70×70 finite element mesh is used to analyse different crack geometries (a/s ratios). Fig. 3.32 compares σ_x and σ_y stress contours for three different a/s ratios.

To investigate the effect of the mesh size on the solution, the $a/s=2$ case is analysed by two different mesh sizes, 70×70 and 120×120. Table 3.3 compares the normalised stress intensity factors for all four analyses. It can be clearly seen that the difference between the two meshes does not constitute a large error. This is an indication of the capability of the XFEM for calculation of different crack geometry problems with a single relatively coarse finite element mesh.

Table 3.3 Normalised values of stress intensity factors

Domain and crack				Mesh	$\overline{K}_{\mathrm{I}}$				Error (%)
a	s	b	L		Outer tip	Inner tip	Average	Exact	
1	2.0	3.0	10	70×70	0.722	0.727	0.725	0.743	2.4
1	1.0	2.0	10	70×70	0.738	0.750	0.744	0.800	6.8
1	0.5	1.5	10	70×70	0.754	0.801	0.777	0.910	14.5
1	0.5	1.5	10	120×120	0.755	0.800	0.777	0.910	14.6

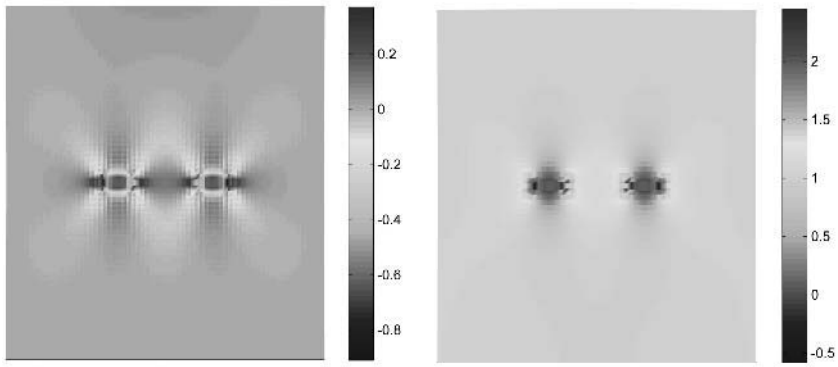

a) σ_{xx} for $a/s = 0.5$ b) σ_{yy} for $a/s = 0.5$

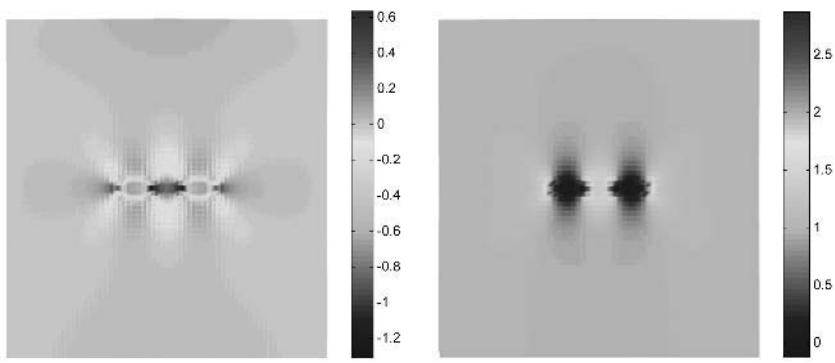

c) σ_{xx} for $a/s = 1$ d) σ_{yy} for $a/s = 1$

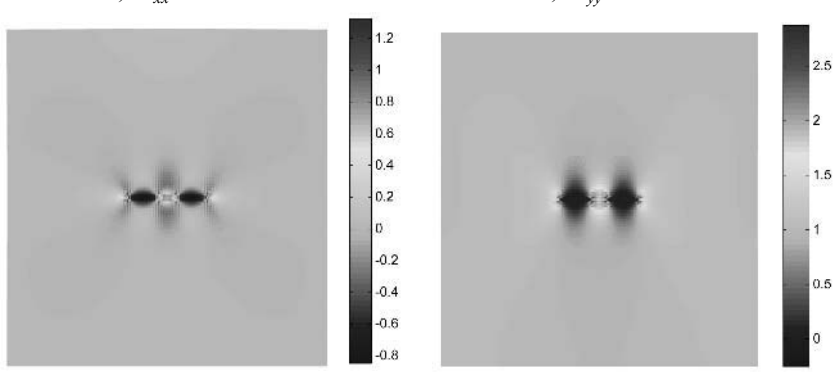

e) σ_{xx} for $a/s = 2$ f) σ_{yy} for $a/s = 2$

Figure 3.32 Stress distribution contours for different a/s ratios.

3.9.4 A central crack in an infinite plate

This test illustrates a different approach for analysis of an infinite plate. The exact elasticity solution is used as an input imposed displacement field on the boundaries of a finite plate to resemble an infinite plate with a central crack. Only half of the plate is modelled due to symmetry, as illustrated in Fig. 3.29d. Two different finite element meshes including 40×40 and 80×80 elements are used to assess the accuracy of results.

Fig. 3.33 illustrates the contours used for evaluation of the J integral for the two different finite element meshes.

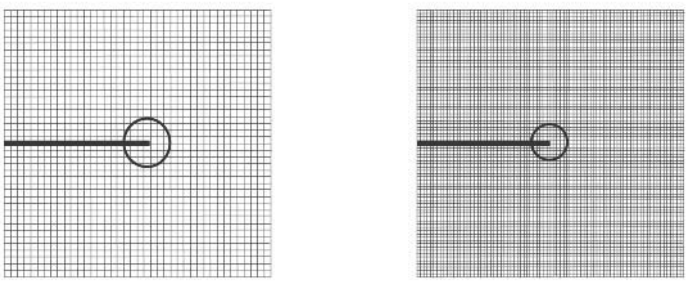

Figure 3.33 Contour domains for evaluation of the J integral on each crack tip.

Fig. 3.34 compares the exact deformed shape with the XFEM evaluation on a 30 times magnified shape for better illustration of the differences around the crack.

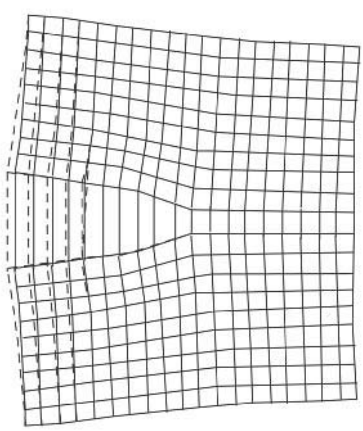

Figure 3.34 Comparison of the exact and predicted deformed shapes of the plate (magnified by 30).

Table 3.4 compares the normalised stress intensity factors for various meshes, as well as different ratios of crack length *a* to plate width *b*. It can be concluded that the accuracy of the results remains unaltered with the change in the crack length. It can be attributed to the imposition of the accurate boundary conditions, which avoids the dependency of the solution to the dimensions selected for modelling an infinite plate.

Table 3.4 Normalised values of stress intensity factors

a/b	Mesh 40×40		Mesh 80×80	
	$\overline{K}_{\mathrm{I}}$	Error (%)	$\overline{K}_{\mathrm{I}}$	Error (%)
1/10	17.281	2.5	17.242	2.6
1/20	17.281	2.5	17.242	2.6

3.9.5 An edge crack in a finite plate

The final test in this chapter is a finite tensile plate with an edge crack, as depicted in Fig. 3.29e. Fig. 3.35 illustrates the deformed shape of the plate. A magnification factor of 20 is used to enable a clear description of how the model performs around the crack.

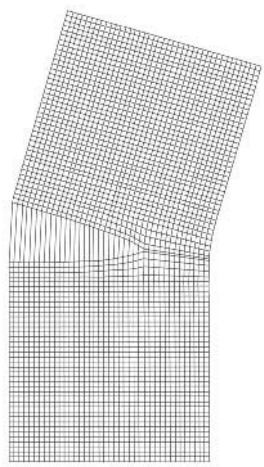

Figure 3.35 Deformed shape of the plate (magnified by 20).

Table 3.5 compares the normalised stress intensity factors for various meshes as well as different ratios of crack length *a* to plate width *b*. Computed errors show a close agreement between the numerical results and the exact solution according to Irwin's classical solution.

Distribution of the stress components in two cartesian coordinates, σ_{xx} and σ_{yy}, are illustrated in Fig. 3.36.

Table 3.5 Normalised values of stress intensity factors for various discretization and crack sizes

a/b	Irwin $\overline{K}_{\mathrm{I}}$	Mesh 20×40		Mesh 40×80	
		$\overline{K}_{\mathrm{I}}$	Error (%)	$\overline{K}_{\mathrm{I}}$	Error (%)
0.30	1.660	1.630	1.83	1.646	0.86
0.45	2.420	2.362	2.41	2.396	0.99
0.60	4.027	3.876	3.75	3.961	1.65

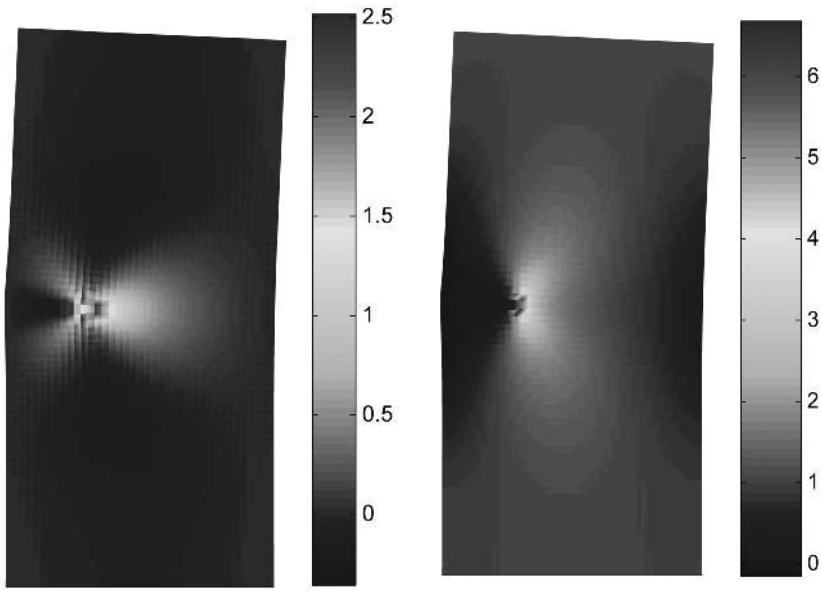

a) σ_{xx} b) σ_{yy}

Figure 3.36 σ_{xx} and σ_{yy} **s**tress contours.

Chapter 4

XFEM for Orthotropic Problems

4.1 INTRODUCTION

Orthotropic materials such as composites are widely used in different branches of engineering and structural systems like those in aerospace and automobile industries, power plants, etc. Since the ratio of strength to weight and stiffness of such materials in many cases is higher than other conventional engineering materials, applications of these orthotropic materials have been widely expanded. Generally, composite materials are utilised in thin shell forms, which are very defect susceptible. A major type of defect that is most likely to take place in these structures is cracking. Cracks can be initiated under different circumstances, such as initial weakness in material strength, fatigue, yielding and imperfection in production procedure. As a result, properties related to fracture mechanics of these types of material are highly prominent; reviving greatly the research efforts in this area.

Several analytical investigations have been reported on the fracture behaviour of composite materials such as the pioneering one by Muskelishvili (1953) dealing with isotropic elastic material, Sih *et al.* (1965), Tupholme (1974), Viola *et al.* (1989) and more recently Lim *et al.* (2001). Bogy (1972), Bowie and Freese (1972), Barnett and Asaro (1972) and Kuo and Bogy (1974) have worked on finding the stress and displacement fields around a linear crack in an anisotropic medium. More advanced contributions can be found in Carloni and Nobile (2002), Carloni *et al.* (2003) and Nobile and Carloni (2005).

Also, there are many numerical methods available for analysing orthotropic composites such as the boundary element method (BEM) (Cruse 1988), the finite element method (FEM) (Swenson and Ingraffea 1988), the finite difference method (FDM), and meshless methods such as the element-free Galerkin method (Belytschlo *et al.* 1994). Boundary element methods, regardless of all the benefits, are barely capable of being employed in nonlinear systems; furthermore, the majority of meshless methods are not sufficiently versatile to deal with arbitrary boundary conditions and geometries. In contrast, the finite element method is capable of analysis of nonlinear systems and can be easily adapted to general boundary conditions and complex geometries. Therefore, its extension to XFEM allows for new capabilities while preserving the finite element original advantages.

The development of XFEM has substantially contributed to new studies of fracture analysis of various types of composite materials. Dolbow and Nadeau (2002) and Dolbow and Gosz (2002) employed the extended finite element method to simulate fracture behaviour of microstructred materials, alleviating the need to remesh the domain between different microstructural realisations. They addressed some fundamental theoretical and numerical issues concerning the application of effective properties for the failure analysis of microstructured materials, with a focus on functionally graded materials.

In a related contribution by Remmers *et al.* (2003), a partition of unity finite element was presented for the simulation of delamination growth in thin layered composite structures. The delamination crack was incorporated in the element as a jump in the displacement field. Similar studies were performed by Nagashima and Suemasu (2004) who applied the extended finite element method to composites.

Development of orthotropic crack tip enrichment functions was reported in a series of papers by Asadpoure *et al.* (2006, 2007), Asadpoure and Mohammadi (2007) and Mohammadi and Asadpoure (2006). They developed three different sets of enrichment functions for various types of composites based on the analytical solutions recently developed for fracture analysis of anisotropic composites by Carloni and Nobile (2002), Carloni *et al.* (2003) and Nobile and Carloni (2005).

Recently, Piva *et al.* (2005) further extended the orthotropic crack tip solutions to elastodynamic problems. It is, therefore, expected that new dynamic orthotropic enrichment functions can be developed using the same methodology of elastic orthotropic enrichment functions.

This chapter begins with a review on anisotropic and orthotropic elasticity. It is followed by a comprehensive discussion on near crack tip fields for orthotropic materials, as a means of developing the necessary enrichment functions for the XFEM formulation, which will be briefly discussed in a separate section. Finally, a number of numerical simulations are provided to illustrate the validity, robustness and efficiency of the proposed approach for evaluation of mixed mode stress intensity factors and *J* integrals in composites and other orthotropic structures.

4.2 ANISOTROPIC ELASTICITY

4.2.1 Elasticity solution

The general form of an anisotropic stress–strain relationship can be defined as:

$$\boldsymbol{\sigma} = \mathbf{D}\boldsymbol{\varepsilon} \tag{4.1}$$

or

$$\boldsymbol{\varepsilon} = \mathbf{C}\boldsymbol{\sigma} \tag{4.2}$$

where $\mathbf{D}$ and $\mathbf{C}$ are anisotropic material stiffness and compliance matrices, respectively. Eq. (4.2) can also be written in a component form,

$$\varepsilon_i = c_{ij}\sigma_j \qquad i,j = 1,\ 2,\ 3,\ \ldots,\ 6 \tag{4.3}$$

which only requires 36 independent constants c_{ij} due to symmetry properties.

For an orthotropic material which has three mutually orthogonal planes of elastic symmetry, Eq. (4.3) is reduced to:

$$\begin{Bmatrix} \varepsilon_1 \\ \varepsilon_2 \\ \varepsilon_3 \\ \varepsilon_4 \\ \varepsilon_5 \\ \varepsilon_6 \end{Bmatrix} = \begin{bmatrix} c_{11} & c_{12} & c_{13} & 0 & 0 & 0 \\ c_{12} & c_{22} & c_{23} & 0 & 0 & 0 \\ c_{13} & c_{23} & c_{33} & 0 & 0 & 0 \\ 0 & 0 & 0 & c_{44} & 0 & 0 \\ 0 & 0 & 0 & 0 & c_{55} & 0 \\ 0 & 0 & 0 & 0 & 0 & c_{66} \end{bmatrix} \begin{Bmatrix} \sigma_1 \\ \sigma_2 \\ \sigma_3 \\ \sigma_4 \\ \sigma_5 \\ \sigma_6 \end{Bmatrix} \tag{4.4}$$

and there remain only 5 independent constants for a transversely isotropic material,

$$\begin{Bmatrix} \varepsilon_1 \\ \varepsilon_2 \\ \varepsilon_3 \\ \varepsilon_4 \\ \varepsilon_5 \\ \varepsilon_6 \end{Bmatrix} = \begin{bmatrix} c_{11} & c_{12} & c_{13} & 0 & 0 & 0 \\ c_{12} & c_{11} & c_{13} & 0 & 0 & 0 \\ c_{13} & c_{13} & c_{33} & 0 & 0 & 0 \\ 0 & 0 & 0 & 2(c_{11}-c_{12}) & 0 & 0 \\ 0 & 0 & 0 & 0 & c_{44} & 0 \\ 0 & 0 & 0 & 0 & 0 & c_{44} \end{bmatrix} \begin{Bmatrix} \sigma_1 \\ \sigma_2 \\ \sigma_3 \\ \sigma_4 \\ \sigma_5 \\ \sigma_6 \end{Bmatrix} \tag{4.5}$$

Eqs. (4.4) and (4.5) are valid for arbitrarily selected coordinate systems. Further simplification is obtained if Eq. (4.4) is written for the principal directions of orthotropy:

$$\begin{Bmatrix} \varepsilon_1 \\ \varepsilon_2 \\ \varepsilon_3 \\ \varepsilon_4 \\ \varepsilon_5 \\ \varepsilon_6 \end{Bmatrix} = \begin{bmatrix} \frac{1}{E_1} & -\frac{\nu_{21}}{E_2} & -\frac{\nu_{31}}{E_3} & 0 & 0 & 0 \\ -\frac{\nu_{12}}{E_1} & \frac{1}{E_2} & -\frac{\nu_{32}}{E_3} & 0 & 0 & 0 \\ -\frac{\nu_{13}}{E_1} & -\frac{\nu_{23}}{E_2} & \frac{1}{E_3} & 0 & 0 & 0 \\ 0 & 0 & 0 & \frac{1}{\mu_{23}} & 0 & 0 \\ 0 & 0 & 0 & 0 & \frac{1}{\mu_{31}} & 0 \\ 0 & 0 & 0 & 0 & 0 & \frac{1}{\mu_{12}} \end{bmatrix} \begin{Bmatrix} \sigma_1 \\ \sigma_2 \\ \sigma_3 \\ \sigma_4 \\ \sigma_5 \\ \sigma_6 \end{Bmatrix} \tag{4.6}$$

with the following additional relations to keep the number of independent constants unchanged:

$$E_1\nu_{21} = E_2\nu_{12} \tag{4.7}$$

$$E_2\nu_{32} = E_3\nu_{23} \tag{4.8}$$

$$E_3\nu_{13} = E_1\nu_{31} \tag{4.9}$$

4.2.2 Anisotropic stress functions

The Airy stress function is limited to isotropic problems. For an extension to more complex problems, including anisotropic problems, the stress function $\Phi(x,y)$ can be written as

$$\Phi(x,y) = 2\,\mathrm{Re}\left[\Phi_1(z_1) + \Phi_2(z_2)\right] \tag{4.10}$$

where $\Phi_1(z_1)$ and $\Phi_2(z_2)$ are arbitrary functions of $z_1 = x + s_1 y$ and $z_2 = x + s_2 y$, respectively. Combining the definition of stress components from the Airy stress function and satisfying the compatibility equation, the following relation is obtained for anisotropic solids in absence of body forces:

$$c_{22}\frac{\partial^4\Phi}{\partial x^4} - 2c_{26}\frac{\partial^4\Phi}{\partial x^3\partial y} + (2c_{12} + c_{66})\frac{\partial^4\Phi}{\partial x^2\partial y^2} - 2c_{16}\frac{\partial^4\Phi}{\partial x\partial y^3} + c_{22}\frac{\partial^4\Phi}{\partial y^4} = 0 \tag{4.11}$$

which reduces to the following simplified equation for isotropic problems,

$$\frac{\partial^4\Phi}{\partial x^4} + 2\frac{\partial^4\Phi}{\partial x^2\,\partial y^2} + \frac{\partial^4\Phi}{\partial y^4} = \nabla^2(\nabla^2\Phi) = 0 \tag{4.12}$$

The characteristic equation of the homogenous partial differential equation (4.11) is

$$c_{11}s^4 - 2c_{16}s^3 + (2c_{12} + c_{66})s^2 - 2c_{26}s + c_{22} = 0 \tag{4.13}$$

Lekhnitski (1968) discussed the availability and conditions for the roots of Eq. (4.13). Here, only the two isotropic and orthotropic cases are considered. For an isotropic case, the roots are $s_1 = s_2 = i$ and $\bar{s}_1 = \bar{s}_2 = -i$, whereas for an orthotropic material with axes of orthotropy (1,2) coinciding cartesian (x,y) axes, $c_{16} = c_{26} = 0$, the characteristic Eq. (4.13) is reduced to:

$$s^4 + \left(\frac{E_1}{\mu} - 2\nu_1\right)s^2 + \frac{E_1}{E_2} = 0 \tag{4.14}$$

Finally, the stress components are defined from the second derivatives of the complex stress function Φ_i'':

$$\sigma_x = 2\,\mathrm{Re}\left[s_1^2\Phi_1''(z_1) + s_2^2\Phi_2''(z_2)\right] \tag{4.15}$$

$$\sigma_y = 2\,\mathrm{Re}\left[\Phi_1''(z_1) + \Phi_2''(z_2)\right] \tag{4.16}$$

$$\sigma_{xy} = -2\,\mathrm{Re}\left[s_1\Phi_1''(z_1) + s_2\Phi_2''(z_2)\right] \tag{4.17}$$

and the displacements are obtained from the first derivatives of the complex stress function, Φ_i':

$$u_x = 2\,\mathrm{Re}\left[p_1\Phi_1'(z_1) + p_2\Phi_2'(z_2)\right] \tag{4.18}$$

$$u_y = 2\,\mathrm{Re}\left[q_1\Phi_1'(z_1) + q_2\Phi_2'(z_2)\right] \tag{4.19}$$

where

$$p_i = c_{11}s_i^2 + c_{12} - c_{16}s_i \qquad i = 1,2 \tag{4.20}$$

$$q_i = c_{12}s_i + \frac{c_{22}}{s_i} - c_{26} \qquad i = 1,2 \tag{4.21}$$

4.2.3 Orthotropic mixed mode problems

Saouma *et al.* (1987) extended the original isotropic maximum circumferential tensile stress theory to anisotropic solids.

In this case, the fracture toughness is no longer uniquely defined. Instead, two values of K_{Ic}^1 and K_{Ic}^2 are required for characterizing the brittle behaviour of the crack in a homogenous transversely isotropic solid with elastic constants E_1, E_2, and μ_{12} (Fig. 4.1).

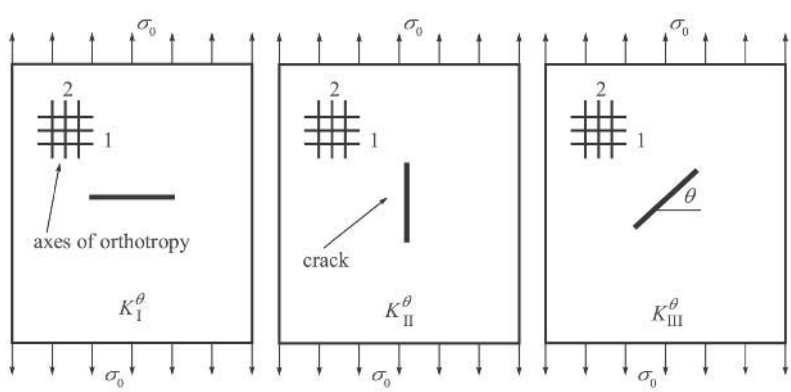

Figure 4.1 Fracture toughness for a homogeneous anisotropic solid.

For a crack arbitrarily oriented with respect to direction 1, K_{Ic}^{θ} would be a function of K_{Ic}^{1} and K_{Ic}^{2}:

$$K_{\mathrm{Ic}}^{\theta} = K_{\mathrm{Ic}}^{1}\cos^2\theta + K_{\mathrm{Ic}}^{2}\sin^2\theta \tag{4.22}$$

In order to avoid performing two separate fracture toughness tests, it is assumed that the ratio of the fracture toughness in both directions is equal to the ratio of the elastic modulus (Saouma *et al.* 1987):

$$K_{\mathrm{Ic}}^{2} = K_{\mathrm{Ic}}^{1}\frac{E_1}{E_2} \tag{4.23}$$

The crack propagation is assumed to be along the direction of the maximum tangential stress σ_θ, while the shear stress is zero:

$$\sigma_\theta = \frac{K_{\mathrm{I}}}{\sqrt{2\pi r}}\mathrm{Re}\left[\frac{s_1 t_1 - s_2 t_2}{s_1 - s_2}\right] + \frac{K_{\mathrm{II}}}{\sqrt{2\pi r}}\mathrm{Re}\left[\frac{t_1 - t_2}{s_1 - s_2}\right] \tag{4.24}$$

where

$$t_1^{\,2} = (s_2\sin\theta + \cos\theta)^3 \tag{4.25}$$

$$t_2^{\,2} = (s_1\sin\theta + \cos\theta)^3 \tag{4.26}$$

The angle of crack propagation θ' is found by maximizing:

$$\max\left\{\frac{1}{\cos^2\theta + \dfrac{K_{\mathrm{Ic}}^{1}}{K_{\mathrm{Ic}}^{2}}\sin^2\theta}\left[\mathrm{Re}\left[\frac{s_1 t_1 - s_2 t_2}{s_1 - s_2}\right] + \frac{K_{\mathrm{II}}}{K_{\mathrm{I}}\,\mathrm{Re}\left[\dfrac{t_1 - t_2}{s_1 - s_2}\right]}\right]\right\} \tag{4.27}$$

The estimated angle θ' has to be checked against the following condition:

$$\frac{\sigma_\theta}{\sigma_\theta^{\max}} = \frac{K_{\mathrm{I}}\,\mathrm{Re}\left[\dfrac{s_1 t_1 - s_2 t_2}{s_1 - s_2}\right] + K_{\mathrm{II}}\,\mathrm{Re}\left[\dfrac{t_1 - t_2}{s_1 - s_2}\right]}{K_{\mathrm{Ic}}^{1}\cos^2\theta + K_{\mathrm{Ic}}^{2}\sin^2\theta} = 1 \tag{4.28}$$

4.2.4 Energy release rate and stress intensity factor for anisotropic materials

Sih *et al.* (1965) extended Eqs. (2.159)–(2.160) for anisotropic materials:

$$\begin{cases} G_{\mathrm{I}} = -\dfrac{1}{2} K_{\mathrm{I}} c_{22} \operatorname{Im}\left[\dfrac{K_{\mathrm{I}}(s_1+s_2)+K_{\mathrm{II}}}{s_1 s_2}\right] \\ G_{\mathrm{II}} = \dfrac{1}{2} K_{\mathrm{II}} c_{11} \operatorname{Im}\left[K_{\mathrm{II}}(s_1+s_2)+K_{\mathrm{I}} s_1 s_2\right] \\ G_{\mathrm{III}} = \dfrac{1}{2} K_{\mathrm{III}}^2 \operatorname{Im}\left[s_3 c_{66} - c_{56}\right] \dfrac{1}{c_{55} c_{66}} \end{cases} \tag{4.29}$$

4.2.5 Anisotropic singular elements

The same idea of singular quarter point finite elements can be extended to anisotropic problems. Saouma *et al.* (1987) proposed the following procedure for anisotropic materials in the form of:

$$K_i = \sum_{j=1}^{3} \mathbf{Q}_{ij} \, \widetilde{u}_j \qquad i = 1(\mathrm{I}), 2(\mathrm{II}), 3(\mathrm{III}) \tag{4.30}$$

where $\widetilde{u}_j$ is the transformed displacement obtained from the displacements of those nodes along the crack in the singular quarter point element, as shown in Fig. 4.2:

$$\begin{aligned} \widetilde{u}_i &= 2u_{iA_1} - u_{iB_1} + 2u_{iA_2} - u_{iB_2} + u_{iF_1} \\ &+ \frac{1}{2}\eta(-4u_{iA_1} + u_{iB_1} + 4u_{iA_2} - u_{iB_2}) + \frac{1}{2}\eta^2(u_{iB_1} - 2u_{iF_1} + u_{iB_2}) \end{aligned} \tag{4.31}$$

and the matrix $\mathbf{Q}$ is obtained from the analytical solution to the displacements around the crack tip in homogeneous anisotropic solids (Saouma *et al.* 1987):

$$\mathbf{Q}^{-1} = \alpha\sqrt{2\pi} \begin{bmatrix} \operatorname{Re}\left[\dfrac{i}{s_1 - s_2}(q_2 - q_1)\right] & \operatorname{Re}\left[\dfrac{-i}{s_1 - s_2}(p_2 - p_1)\right] & 0 \\ \operatorname{Re}\left[\dfrac{-i}{s_1 - s_2}(s_1 q_2 - s_2 q_1)\right] & \operatorname{Re}\left[\dfrac{i}{s_1 - s_2}(s_1 p_2 - s_2 p_1)\right] & 0 \\ 0 & 0 & \dfrac{D}{c_{44}c_{55} - c_{66}^2} \end{bmatrix} \tag{4.32}$$

where p_i and q_i are defined in Eqs. (4.20) and (4.21), respectively, s_i are the roots of the characteristic equation (4.13) and α is determined from the size of the singular element and the elasticity parameters (Saouma *et al.* 1987).

It should be noted, however, that the problem is very complex and requires a number of different finite element models to verify the model and to assess the accuracy of the results.

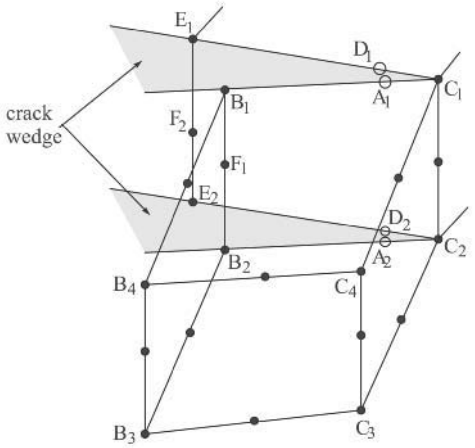

Figure 4.2 Displacement field around the crack tip.

4.3 ANALYTICAL SOLUTIONS FOR NEAR CRACK TIP

In the extended finite element method, near tip displacement fields are required to derive a basis for enrichment functions. Several analytical solutions for near crack tip fields in orthotropic materials have been proposed. Some of them can only be applied to specific applications, while others can be applied to general orthotropic media. In this section, three methods are discussed. The first two are each dedicated to a specific class of orthotropic materials, while the third approach can be used for all orthotropic problems.

4.3.1 Near crack tip displacement field (class I)

In this section, the analytical displacement fields derived by Carloni and Nobile (2002), Carloni *et al.* (2003) and Nobile and Carloni (2005) are discussed.

Consider a crack in an orthotropic medium with axes of elastic symmetry coincident with the cartesian coordinates axes ($x_1 = x$, $x_2 = y$) and the orthotropic body is subjected to a uniform biaxial load (σ_0 and $k\sigma_0$) at infinity, applied along X and Y directions, respectively (Fig. 4.3). The stress–strain equations can be defined as:

$$\sigma_{x_1} = c_{11}\frac{\partial u_1}{\partial x_1} + c_{12}\frac{\partial u_2}{\partial x_2} \tag{4.33}$$

$$\sigma_{x_2} = c_{12}\frac{\partial u_1}{\partial x_1} + c_{22}\frac{\partial u_2}{\partial x_2} \tag{4.34}$$

$$\tau_{x_1x_2} = c_{66}\left(\frac{\partial u_1}{\partial x_2} + \frac{\partial u_2}{\partial x_1}\right) \tag{4.35}$$

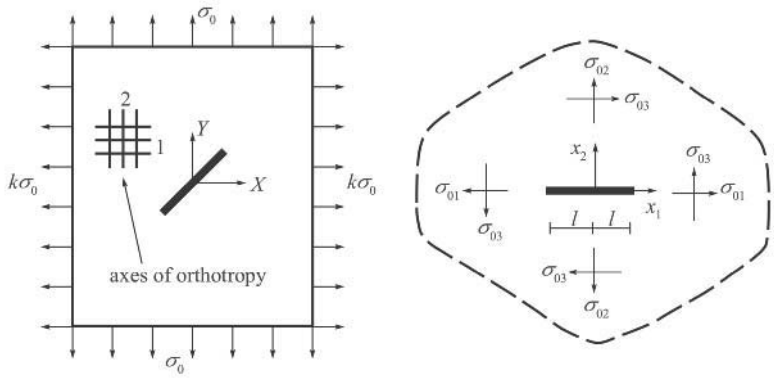

Figure 4.3 Crack positioning and implied stresses.

where c_{ij} $(i,\ j=1,\ 2,\ 6)$ are the relevant components of the compliance matrix of the material in x_1, x_2 directions. The set of equations for an inplane elastostatic problem can be expressed as:

$$\frac{\partial^2 u_1}{\partial {x_1}^2}+\left(\frac{c_{66}}{c_{11}}\right)\frac{\partial^2 u_1}{\partial {x_2}^2}+2\left(\frac{c_{12}+c_{66}}{2c_{11}}\right)\frac{\partial^2 u_2}{\partial x_1 \partial x_2}=0 \tag{4.36}$$

$$\frac{\partial^2 u_2}{\partial {x_1}^2}+\left(\frac{c_{22}}{c_{66}}\right)\frac{\partial^2 u_2}{\partial {x_2}^2}+2\left(\frac{c_{12}+c_{66}}{2c_{66}}\right)\frac{\partial^2 u_1}{\partial x_1 \partial x_2}=0 \tag{4.37}$$

Following the methodology proposed by Viola *et al.* (1989), a transformation is applied in order to express the formulation in terms of complex functions,

$$\frac{\partial \mathbf{\Phi}}{\partial x_1}+\mathbf{\Lambda}\frac{\partial \mathbf{\Phi}}{\partial x_2}=\mathbf{0} \tag{4.38}$$

where

$$\mathbf{\Phi}=\left\{\frac{\partial u_1}{\partial x_1},\frac{\partial u_1}{\partial x_2},\frac{\partial u_2}{\partial x_1},\frac{\partial u_2}{\partial x_2}\right\}^{\mathrm{T}} \tag{4.39}$$

$$\mathbf{\Lambda}=\begin{pmatrix} 0 & \alpha_1 & 2\beta_1 & 0 \\ -1 & 0 & 0 & 0 \\ 2\beta_2 & 0 & 0 & \alpha_2 \\ 0 & 0 & -1 & 0 \end{pmatrix} \tag{4.40}$$

and

$$\alpha_1 = \frac{c_{66}}{c_{11}} \qquad \alpha_2 = \frac{c_{22}}{c_{66}} \qquad \beta_1 = \frac{c_{12}+c_{66}}{2c_{11}} \qquad \beta_2 = \frac{c_{12}+c_{66}}{2c_{66}} \tag{4.41}$$

Eigenvalues λ of the matrix $\mathbf{\Lambda}$ can be obtained by

$$\lambda^4 + 2a_1\lambda^2 + a_2 = 0 \tag{4.42}$$

with

$$a_1 = \frac{(\alpha_1 + \alpha_2 - 4\beta_1\beta_2)}{2} \tag{4.43}$$

$$a_2 = \alpha_1\alpha_2 \tag{4.44}$$

Two types of orthotropic materials can be defined based on the existence of the real part of the solution: $a_1 > \sqrt{a_2}$ (type I) and $|a_1| < \sqrt{a_2}$ (type II). Only the first type is considered in this section. The second type will be dealt with in the next section.

According to Carloni and Nobile (2002), Carloni *et al.* (2003), Nobile and Carloni (2005) and Asadpoure (2006) and with reference to Fig. 4.3, the displacement field can be written as:

$$\begin{aligned} u_1 = {} & \frac{2m_2}{c_{66}(e_1-e_2)}\sqrt{2lr}\left\{\sigma_{02}\left[\frac{e_2\sqrt{g_2(\theta)}}{m_4(m_1-e_2^2)}\cos\frac{\theta_2}{2} - \frac{e_1\sqrt{g_1(\theta)}}{m_3(m_1-e_1^2)}\cos\frac{\theta_1}{2}\right]\right. \\ & \left. + e_1e_2\sigma_{03}\left[\frac{\sqrt{g_2(\theta)}}{m_4(m_1-e_2^2)}\sin\frac{\theta_2}{2} - \frac{\sqrt{g_1(\theta)}}{m_3(m_1-e_1^2)}\sin\frac{\theta_1}{2}\right]\right\} \\ & - \frac{2m_2e_1e_2(\sigma_{02}-e_1e_2\sigma_{01})}{c_{66}m_3m_4(m_1-e_1^2)(m_1-e_2^2)}(l+r\cos\theta) - \frac{m_2\sigma_{03}(e_1+e_2)^2}{c_{66}m_3m_4(m_1-e_1^2)(m_1-e_2^2)}r\sin\theta \end{aligned} \tag{4.45}$$

$$\begin{aligned} u_2 = {} & \frac{1}{c_{66}(e_1-e_2)}\frac{\sqrt{2lr}}{m_3m_4}\left\{\sigma_{02}\left[m_3\sqrt{g_2(\theta)}\sin\frac{\theta_2}{2} - m_4\sqrt{g_1(\theta)}\sin\frac{\theta_1}{2}\right]\right. \\ & \left. + \sigma_{03}\left[m_4e_2\sqrt{g_1(\theta)}\cos\frac{\theta_1}{2} - m_3e_1\sqrt{g_2(\theta)}\cos\frac{\theta_2}{2}\right]\right\} \\ & + \frac{\sigma_{03}(e_1+e_2)(m_3-m_4)}{2c_{66}m_3m_4(e_1-e_2)}(l+r\cos\theta) \\ & + \frac{(\sigma_{02}-e_1e_2\sigma_{01})}{c_{66}(e_1^2-e_2^2)}\left(\frac{e_2}{m_3e_1} - \frac{e_1}{m_4e_2}\right)\frac{m_2\sigma_{03}(e_1+e_2)^2}{c_{66}m_3m_4(m_1-e_1^2)(m_1-e_2^2)}r\sin\theta \end{aligned} \tag{4.46}$$

where m_1, m_2, m_3 and m_4 are coefficients related to material properties, defined in (Carloni *et al.* 2003), and:

$$e_1 = \left\{ \frac{1}{2}\left[\frac{c_{66}}{c_{11}} + \frac{c_{22}}{c_{66}} - \frac{(c_{12}+c_{66})^2}{c_{11}c_{66}} \right] - \left(\frac{1}{4}\left[\frac{c_{66}}{c_{11}} + \frac{c_{22}}{c_{66}} - \frac{(c_{12}+c_{66})^2}{c_{11}c_{66}} \right]^2 - \frac{c_{22}}{c_{11}} \right)^{1/2} \right\}^{1/2} \tag{4.47}$$

$$e_2 = \left\{ \frac{1}{2}\left[\frac{c_{66}}{c_{11}} + \frac{c_{22}}{c_{66}} - \frac{(c_{12}+c_{66})^2}{c_{11}c_{66}} \right] + \left(\frac{1}{4}\left[\frac{c_{66}}{c_{11}} + \frac{c_{22}}{c_{66}} - \frac{(c_{12}+c_{66})^2}{c_{11}c_{66}} \right]^2 - \frac{c_{22}}{c_{11}} \right)^{1/2} \right\}^{1/2} \tag{4.48}$$

and

$$g_j(\theta) = \left(\cos^2\theta + \frac{\sin^2\theta}{e_j^2} \right)^{1/2} \qquad j = 1,2 \tag{4.49}$$

$$\theta_j = \tan^{-1}\left(\frac{x_2}{e_j x_1} \right) = \tan^{-1}\left(\frac{\tan\theta}{e_j} \right) \qquad j = 1,2 \tag{4.50}$$

where r and θ are the polar coordinates and x_1 and x_2 are the cartesian coordinates in the local coordinate system at each crack tip (see Fig. 4.4).

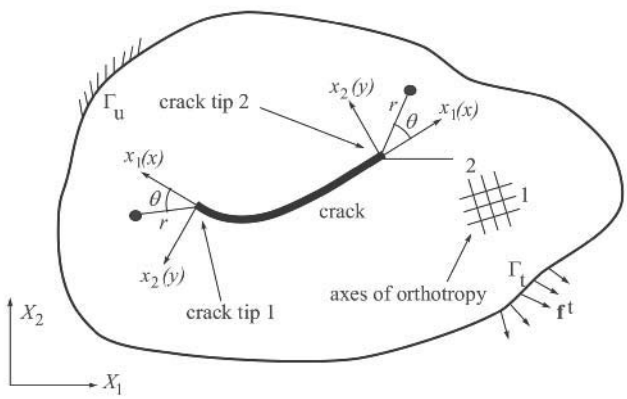

Figure 4.4 Local coordinates at both crack tips.

To extract near tip functions it is noted that these functions must span the displacement fields in Eqs. (4.45) and (4.46); therefore (Asadpoure *et al.* 2007):

$$\{F_l(r,\theta)\}_{l=1}^{4} = \left\{ \sqrt{r}\cos\frac{\theta_1}{2}\sqrt{g_1(\theta)}, \sqrt{r}\cos\frac{\theta_2}{2}\sqrt{g_2(\theta)}, \sqrt{r}\sin\frac{\theta_1}{2}\sqrt{g_1(\theta)}, \right. \\ \left. , \sqrt{r}\sin\frac{\theta_2}{2}\sqrt{g_2(\theta)} \right\} \tag{4.51}$$

According to Eq. (4.51), the first two terms are continuous across the crack faces while the remaining ones are discontinuous. It is important to note that the enrichment functions (4.51) can not be directly adopted for isotropic problems because Eqs. (4.45)–(4.46) become indefinite (0/0) expressions. The mathematical solution for the limiting isotopic case leads to similar results as those defined in Eq. (3.27):

$$\{F_l(r,\theta)\}_{l=1}^{4} = \left\{ \sqrt{r}\cos\frac{\theta}{2}, \sqrt{r}\sin\frac{\theta}{2}, \sqrt{r}\sin\theta\cos\frac{\theta}{2}, \sqrt{r}\sin\theta\sin\frac{\theta}{2} \right\} \tag{4.52}$$

4.3.2 Near crack tip displacement field (class II)

The same problem with the condition of $|a_1| < \sqrt{a_2}$ is now considered (type II). An infinite orthotropic plate, consisting of a traction free line crack, is subjected to uniform biaxial (σ_0 and $k\sigma_0$) and shear (τ_0) loads at infinity. Fig. 4.5 shows the crack geometry, loading conditions and the cartesian and polar coordinates utilised in this section.

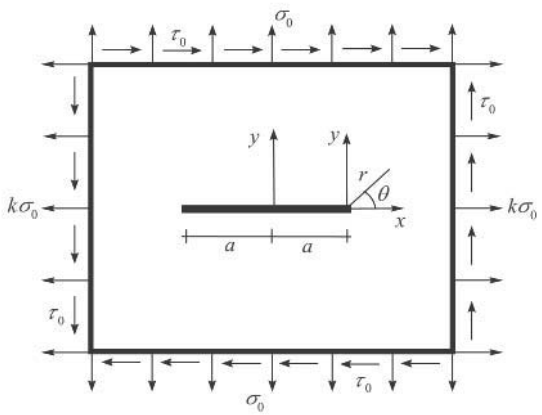

Figure 4.5 Crack geometry, loading condition and global and local coordinates.

The following complex variables are defined:

$$z_1 = \left(x - \frac{\gamma_1}{\gamma_1^2+\gamma_2^2} y \right) + i \left(\frac{\gamma_2}{\gamma_1^2+\gamma_2^2} y \right) \tag{4.53}$$

$$z_2 = \left(x + \frac{\gamma_1}{\gamma_1^2+\gamma_2^2} y \right) + i \left(\frac{\gamma_2}{\gamma_1^2+\gamma_2^2} y \right) \tag{4.54}$$

where

$$\gamma_1 = \left[\frac{1}{2} + \left(\sqrt{a_2} + a_1\right)\right]^{1/2} \tag{4.55}$$

$$\gamma_2 = \left[\frac{1}{2} + \left(\sqrt{a_2} - a_1\right)\right]^{1/2} \tag{4.56}$$

Viola *et al.* (1989) explained the procedure of obtaining the complex variables and functions. Neglecting the velocity of the crack propagation for the present static case, the basic solution proposed by Viola *et al.* (1989) results in the following displacement fields in the x and y directions,

$$\begin{aligned} u_1 = & -2\beta_1 d_5 + \frac{\beta\sigma_0}{c_{66}k_7}\left\{d_1\left[2(a + r\cos\theta) - \sqrt{2ar}\left(\sqrt{g_1(\theta)}\cos\frac{\theta_1}{2} + \sqrt{g_2(\theta)}\cos\frac{\theta_2}{2}\right)\right]\right. \\ & \left. - d_2\sqrt{2ar}\left(\sqrt{g_1(\theta)}\sin\frac{\theta_1}{2} - \sqrt{g_2(\theta)}\sin\frac{\theta_2}{2}\right)\right\} \\ & + \frac{\beta_1\tau_0}{c_{66}k_7}\left\{d_3\left[X_1 - X_2 + \sqrt{2ar}\left(\sqrt{g_2(\theta)}\cos\frac{\theta_2}{2} - \sqrt{g_1(\theta)}\cos\frac{\theta_1}{2}\right)\right]\right. \\ & \left. - d_4\left[2Y_1 - \sqrt{2ar}\left(\sqrt{g_1(\theta)}\sin\frac{\theta_1}{2} + \sqrt{g_2(\theta)}\sin\frac{\theta_2}{2}\right)\right]\right\} \end{aligned} \tag{4.57}$$

$$\begin{aligned} u_2 = & -h_5 + \frac{\sigma_0}{2c_{66}k_7}\left\{h_1\left[(X_1 - X_2) + \sqrt{2ar}\left(\sqrt{g_1(\theta)}\cos\frac{\theta_1}{2} - \sqrt{2ar}\cos\frac{\theta_2}{2}\right)\right]\right. \\ & \left. + h_2\left[2Y_1 - \sqrt{2ar}\left(\sqrt{g_1(\theta)}\sin\frac{\theta_1}{2} + \sqrt{g_2(\theta)}\sin\frac{\theta_2}{2}\right)\right]\right\} \\ & + \frac{\tau_0}{2c_{66}k_7}\left\{h_3\left[2(a + r\cos\theta) - \sqrt{2ar}\left(\sqrt{g_1(\theta)}\cos\frac{\theta_1}{2} + \sqrt{g_2(\theta)}\cos\frac{\theta_2}{2}\right)\right]\right. \\ & \left. + h_4\sqrt{2ar}\left(\sqrt{g_1(\theta)}\sin\frac{\theta_1}{2} + \sqrt{g_2(\theta)}\sin\frac{\theta_2}{2}\right)\right\} \end{aligned} \tag{4.58}$$

with (for the definition of β_1 see Eq. (4.41))

$$d_1 = t_3k_6 + t_4k_5\,,\ d_2 = t_3k_5 + t_4k_5\,, d_3 = t_3k_3 + t_4k_4\,,\ d_4 = t_3k_4 + t_4k_3 \tag{4.59}$$

$$d_5 = \left(t_3A_1 - t^4B_1 + t_4B_2\right)Y_1 + \left(t_3B_1 + t_4A_1\right)X_1 + t_3B_2X_2 \tag{4.60}$$

and

$$h_1 = \gamma_1k_6 + \gamma_2k\,,\ h_2 = \gamma_1k_5 - \gamma_2k_6\,,\ h_3 = \gamma_1k_3 - \gamma_2k_4\,,\ h_4 = \gamma_1k_4 + \gamma_2k_3 \tag{4.61}$$

$$h_5 = (\gamma_1 A_1 - \gamma_2 B_1 - \gamma_2 B_2) Y_1 + (\gamma_2 A_1 + \gamma_1 B_2) X_1 - \gamma_1 B_2 X_2 \tag{4.62}$$

where

$$t_1 + it_2 = \frac{(\gamma_1 + i\gamma_2)}{\alpha + (\gamma_1 + i\gamma_2)^2} \qquad t_3 + it_4 = (\gamma_1 + i\gamma_2)(t_1 - it_2) \tag{4.63}$$

$$k_1 = \frac{c_{12} - 2\beta_1 t_3 c_{11}}{c_{66}},\ k_2 = 2\beta_1 t_4 \frac{c_{11}}{c_{66}}, k_3 = \frac{c_{22} - 2\beta_1 t_3 c_{12}}{c_{66}},\ k_4 = 2\beta_1 t_4 \frac{c_{12}}{c_{66}} \tag{4.64}$$

$$k_5 = 2\beta_1 t_2 - \gamma_2,\ k_6 = 2\beta_1 t_1 - \gamma_1 \tag{4.65}$$

$$k_7 = k_3 k_6 - k_4 k_5 \tag{4.66}$$

and

$$X_1 = (a + r\cos\theta) - \gamma_1 l^2 r \sin\theta \tag{4.67}$$

$$X_2 = (a + r\cos\theta) + \gamma_1 l^2 r \sin\theta \tag{4.68}$$

$$Y_1 = \gamma_2 l^2 r \sin\theta \tag{4.69}$$

$$l^2 = \left(\gamma_1^2 + \gamma_2^2\right)^{-1} \qquad j = 1,2 \tag{4.70}$$

$$A_1 = \frac{(k_3 k - k_1)\sigma_0}{c_{66}(k_1 k_4 - k_2 k_3)} \tag{4.71}$$

$$B_1 = \frac{\tau_0}{2c_{66}k_6} + \frac{\sigma_0}{2c_{66}k_6} \frac{[k(k_4 k_6 - k_3 k_5) + (k_1 k_5 - k_2 k_6)]}{(k_1 k_4 - k_2 k_3)} \tag{4.72}$$

$$B_2 = -\frac{\tau_0}{2c_{66}k_6} + \frac{\sigma_0}{2c_{66}k_6} \frac{[k(k_4 k_6 - k_3 k_5) - (k_1 k_5 + k_2 k_6)]}{(k_1 k_4 - k_2 k_3)} \tag{4.73}$$

and the main contributing terms

$$g_j(\theta) = \left(\cos^2\theta + l^2 \sin^2\theta + (-1)^j l^2 \sin 2\theta\right)^{1/2} \qquad j = 1,2 \tag{4.74}$$

$$\theta_j = \arctan\left(\frac{\gamma_2 l^2 \sin\theta}{\cos\theta + (-1)^j \gamma_1 l^2 \sin\theta}\right) \qquad j = 1,2 \tag{4.75}$$

It is noted that the displacement fields in Eqs. (4.57)–(4.58) are only valid for $r/a<1$; near the crack tip and they should not be used elsewhere.

The analytical solution for displacement in the vicinity of the crack tip can be used to derive the crack tip enrichment functions which must span the possible displacement space that may have occurred in the analytical solution. Therefore, from Eqs. (4.57)–(4.58), the orthotropic enrichment functions can be defined as (Asadpoure *et al.* 2006):

$$\{F_l(r,\theta)\}_{l=1}^{4}=\left\{\sqrt{r}\cos\frac{\theta_1}{2}\sqrt{g_1(\theta)},\sqrt{r}\cos\frac{\theta_2}{2}\sqrt{g_2(\theta)},\sqrt{r}\sin\frac{\theta_1}{2}\sqrt{g_1(\theta)},\right.$$
$$\left.,\sqrt{r}\sin\frac{\theta_2}{2}\sqrt{g_2(\theta)}\right\} \tag{4.76}$$

4.3.3 Unified near crack tip displacement field (both classes)

In this section, a unified formulation is adopted to include both classes of orthotropic materials within a unified approach.

This formulation is based on the work by Sih *et al.* (1965) who used the stress function (4.10) for an infinite anisotropic plate with a central crack and solved the final displacement fields.

Assume an anisotropic body containing a crack is subjected to arbitrary forces with general displacement and traction boundary conditions. Global cartesian coordinates are (X_1,X_2) and local cartesian coordinate $(x_1=x,\ x_2=y)$ and local polar coordinate (r,θ) are defined on the crack tip as illustrated in Fig. 4.4. Recalling the characteristic equation (4.13) of the governing fourth-order partial differential equation (Lekhnitskii 1968)

$$c_{11}s^4-2c_{16}s^3+(2c_{12}+c_{66})s^2-2c_{26}s+c_{22}=0 \tag{4.77}$$

According to Lekhnitskii (1968), the roots of Eq. (4.77) are always complex or purely imaginary ($s_k=s_{kx}+is_{ky},\ k=1,2$) and occur in conjugate pairs as s_1, $\bar{s}_1$ and s_2, $\bar{s}_2$.

Sih *et al.* (1965) derived the two-dimensional displacement and stress fields in the vicinity of the crack tip by means of analytical functions and complex variables, $z_k=x+s_k y,\ k=1,2$. The stress components for pure mode I are defined as,

$$\sigma_{11}^{\mathrm{I}}=\frac{K_{\mathrm{I}}}{\sqrt{2\pi r}}\mathrm{Re}\left[\frac{s_1s_2}{s_1-s_2}\left(\frac{s_2}{(\cos\theta+s_2\sin\theta)^{1/2}}-\frac{s_1}{(\cos\theta+s_1\sin\theta)^{1/2}}\right)\right] \tag{4.78}$$

$$\sigma_{22}^{\mathrm{I}}=\frac{K_{\mathrm{I}}}{\sqrt{2\pi r}}\mathrm{Re}\left[\frac{1}{s_1-s_2}\left(\frac{s_1}{(\cos\theta+s_2\sin\theta)^{1/2}}-\frac{s_2}{(\cos\theta+s_1\sin\theta)^{1/2}}\right)\right] \tag{4.79}$$

$$\sigma_{12}^{\mathrm{I}}=\frac{K_{\mathrm{I}}}{\sqrt{2\pi r}}\mathrm{Re}\left[\frac{s_1s_2}{s_1-s_2}\left(\frac{1}{(\cos\theta+s_1\sin\theta)^{1/2}}-\frac{1}{(\cos\theta+s_2\sin\theta)^{1/2}}\right)\right] \tag{4.80}$$

and the displacements are

$$u_1^{\mathrm{I}} = K_{\mathrm{I}}\sqrt{\frac{2r}{\pi}}\,\mathrm{Re}\left\{\frac{1}{s_1-s_2}\left[s_1p_2\left(\cos\theta+s_2\sin\theta\right)^{\frac{1}{2}}-s_2p_1\left(\cos\theta+s_1\sin\theta\right)^{\frac{1}{2}}\right]\right\} \tag{4.81}$$

$$u_2^{\mathrm{I}} = K_{\mathrm{I}}\sqrt{\frac{2r}{\pi}}\,\mathrm{Re}\left\{\frac{1}{s_1-s_2}\left[s_1q_2\left(\cos\theta+s_2\sin\theta\right)^{\frac{1}{2}}-s_2q_1\left(\cos\theta+s_1\sin\theta\right)^{\frac{1}{2}}\right]\right\} \tag{4.82}$$

$$u_3^{\mathrm{I}} = 0 \tag{4.83}$$

and in the same way, for pure mode II (skew-symmetric loading), the stress and displacement fields are defined as:

$$\sigma_{11}^{\mathrm{II}} = \frac{K_{\mathrm{II}}}{\sqrt{2\pi r}}\,\mathrm{Re}\left[\frac{1}{s_1-s_2}\left(\frac{s_2^2}{\left(\cos\theta+s_2\sin\theta\right)^{1/2}}-\frac{s_1^2}{\left(\cos\theta+s_1\sin\theta\right)^{1/2}}\right)\right] \tag{4.84}$$

$$\sigma_{22}^{\mathrm{II}} = \frac{K_{\mathrm{II}}}{\sqrt{2\pi r}}\,\mathrm{Re}\left[\frac{1}{s_1-s_2}\left(\frac{1}{\left(\cos\theta+s_2\sin\theta\right)^{1/2}}-\frac{1}{\left(\cos\theta+s_1\sin\theta\right)^{1/2}}\right)\right] \tag{4.85}$$

$$\sigma_{12}^{\mathrm{II}} = \frac{K_{\mathrm{II}}}{\sqrt{2\pi r}}\,\mathrm{Re}\left[\frac{1}{s_1-s_2}\left(\frac{s_1}{\left(\cos\theta+s_1\sin\theta\right)^{1/2}}-\frac{s_2}{\left(\cos\theta+s_2\sin\theta\right)^{1/2}}\right)\right] \tag{4.86}$$

$$u_1^{\mathrm{II}} = K_{\mathrm{II}}\sqrt{\frac{2r}{\pi}}\,\mathrm{Re}\left\{\frac{1}{s_1-s_2}\left[p_2\left(\cos\theta+s_2\sin\theta\right)^{\frac{1}{2}}-p_1\left(\cos\theta+s_1\sin\theta\right)^{\frac{1}{2}}\right]\right\} \tag{4.87}$$

$$u_2^{\mathrm{II}} = K_{\mathrm{II}}\sqrt{\frac{2r}{\pi}}\,\mathrm{Re}\left\{\frac{1}{s_1-s_2}\left[q_2\left(\cos\theta+s_2\sin\theta\right)^{\frac{1}{2}}-q_1\left(\cos\theta+s_1\sin\theta\right)^{\frac{1}{2}}\right]\right\} \tag{4.88}$$

$$u_3^{\mathrm{II}} = 0 \tag{4.89}$$

The following equations can also be simply derived for mode III:

$$u_1^{\mathrm{III}} = 0 \tag{4.90}$$

$$u_2^{\mathrm{III}} = 0 \tag{4.91}$$

$$u_3^{\mathrm{III}} = K_{\mathrm{III}}\sqrt{\frac{2r}{\pi}}\left(c_{44}c_{55}-c_{45}^2\right)^{-\frac{1}{2}}\,\mathrm{Im}\left\{\left(\cos\theta+s_3\sin\theta\right)^{\frac{1}{2}}\right\} \tag{4.92}$$

where K_{I}, K_{II} and K_{III} are stress intensity factors for modes I, II and III, respectively, and p_k and q_k are defined in Eqs. (4.20) and (4.21).

In order to extract crack tip enrichment functions, Eqs. (4.81), (4.82), (4.87) and (4.88) are transformed into a simpler form by introducing two auxiliary complex variables in polar forms (Asadpoure and Mohammadi 2007)

$$z_k^{\mathrm{aux}} = r_k e^{i\theta_k} = r(\cos\theta + s_k \sin\theta) \tag{4.93}$$

$$r_k = r g_k(\theta) \tag{4.94}$$

and

$$g_k(\theta) = \sqrt{(\cos\theta + s_{kx}\sin\theta)^2 + (s_{ky}\sin\theta)^2} \tag{4.95}$$

$$\theta_k = \arctan\left(\frac{s_{ky}\sin\theta}{\cos\theta + s_{kx}\sin\theta}\right) \tag{4.96}$$

The imaginary and real parts of the main field of Eqs. (4.81), (4.82), (4.87) and (4.88) can be written as:

$$\mathrm{Im}(\sqrt{Z_k^{\mathrm{aux}}}) = r^{\frac{1}{2}}\sqrt{g_k(\theta)}\,\sin\frac{\theta_k}{2} \qquad k = 1,2 \tag{4.97}$$

$$\mathrm{Re}(\sqrt{Z_k^{\mathrm{aux}}}) = r^{\frac{1}{2}}\sqrt{g_k(\theta)}\,\cos\frac{\theta_k}{2} \qquad k = 1,2 \tag{4.98}$$

Eqs. (4.81), (4.82), (4.87), (4.88), (4.97) and (4.98) are used to extract crack tip enrichment functions (Asadpoure and Mohammadi 2007) as they should include all possible displacement states:

$$\begin{aligned} F_l(r,\theta) = \Bigg\{ & \sqrt{r}\cos\frac{\theta_1}{2}\sqrt{g_1(\theta)}, \sqrt{r}\cos\frac{\theta_2}{2}\sqrt{g_2(\theta)}, \sqrt{r}\sin\frac{\theta_1}{2}\sqrt{g_1(\theta)}, \\ & , \sqrt{r}\sin\frac{\theta_2}{2}\sqrt{g_2(\theta)} \Bigg\} \end{aligned} \tag{4.99}$$

Eq. (4.99) is in a similar form as those presented in Asadpoure *et al.* (2006, 2007). However, functions θ_k and $g_k(\theta)$ defined in Eqs. (4.95) and (4.96), have different definitions for different classes of composites. For the first class, Eqs. (4.45), (4.46), (4.49) and (4.50), define the first category $a_1 > \sqrt{a_2}$ (Asadpoure *et al.* 2007)

$$g_j(\theta) = \left(\cos^2\theta + \frac{\sin^2\theta}{e_j^2}\right)^{\frac{1}{2}} \qquad j = 1,2 \tag{4.100}$$

$$\theta_j = \arctan\left(\frac{y}{e_j x}\right) = \arctan\left(\frac{\tan\theta}{e_j}\right) \tag{4.101}$$

while $a_1 < \sqrt{a_2}$ represents the second branch (Asadpoure *et al.* 2006) based on Eq. (4.70),

$$g_j(\theta) = \left[\cos^2\theta + l^2\sin^2\theta + (-1)^j l^2 \sin 2\theta\right]^{\frac{1}{2}} \qquad j = 1,2 \tag{4.102}$$

$$\theta_j = \arctan\left[\frac{\gamma_2 l^2 \sin\theta}{\cos\theta + (-1)^j \gamma_1 l^2 \sin\theta}\right] \qquad j = 1,2 \tag{4.103}$$

The present formulation is capable of spanning the whole range of orthotropic media in a single unique formulation, Eq. (4.99).

4.4 ANISOTROPIC XFEM

The general methodology of isotropic extended finite element can be similarly extended to include anisotropic problems, if anisotropic enrichment functions are embedded into an anisotropic finite element procedure. Generalised Heaviside and near crack tip anisotropic enrichment functions are included as an extra few degrees of freedom in addition to the classical finite element model in selected nodes near the discontinuities.

4.4.1 Governing equation

The strong form of the equilibrium equation can be written as:

$$\nabla.\boldsymbol{\sigma} + \mathbf{f}^{\mathrm{b}} = 0 \qquad \text{in } \Omega \tag{4.104}$$

with the following boundary conditions:

$$\boldsymbol{\sigma}\cdot\mathbf{n} = \mathbf{f}^{\mathrm{t}} \qquad \text{on } \Gamma_{\mathrm{t}} \text{ : external traction} \tag{4.105}$$

$$\mathbf{u} = \overline{\mathbf{u}} \qquad \text{on } \Gamma_{\mathrm{u}} \text{ : prescribed displacement} \tag{4.106}$$

$$\boldsymbol{\sigma}\cdot\mathbf{n} = 0 \qquad \text{on } \Gamma_{\mathrm{c}} \text{ : traction free crack} \tag{4.107}$$

where Γ_{t}, Γ_{u} and Γ_{c} are traction, displacement and crack boundaries, respectively, $\boldsymbol{\sigma}$ is the stress tensor and $\mathbf{f}^{\mathrm{b}}$ and $\mathbf{f}^{\mathrm{t}}$ are the body force and external traction vectors, respectively (Fig. 3.20).

The variational formulation of the boundary value problem can be defined as:

$$W^{\text{int}} = W^{\text{ext}} \tag{4.108}$$

or

$$\int_{\Omega} \boldsymbol{\sigma} \cdot \delta\boldsymbol{\varepsilon} \; \mathrm{d}\Omega = \int_{\Omega} \mathbf{f}^{\mathrm{b}} \cdot \delta\mathbf{u} \; \mathrm{d}\Omega + \int_{\Gamma} \mathbf{f}^{\mathrm{t}} \cdot \delta\mathbf{u} \; \mathrm{d}\Gamma \tag{4.109}$$

4.4.2 XFEM discretization

Consider a body in the state of equilibrium with the boundary conditions in the form of traction and displacements that also include a crack, as depicted in Fig. 4.6.

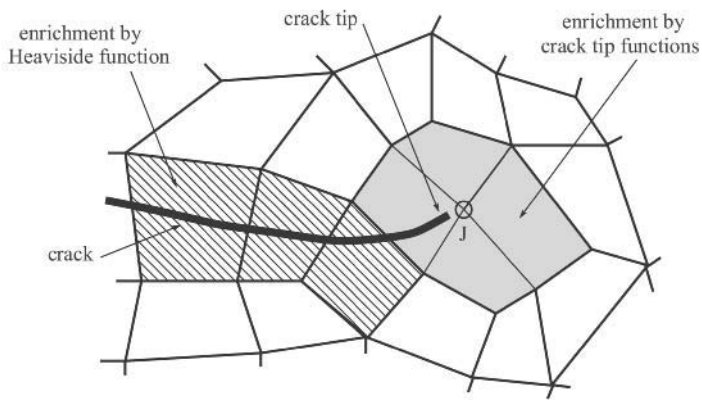

Figure 4.6 A crack within an orthotropic domain.

In the extended finite element method, in order to include the effects of crack surfaces and crack tips, the approximation (3.72) is utilised to calculate the displacement for point **x** locating within the domain (Moës *et al.* 1999)

$$\begin{aligned} \mathbf{u}^h(\mathbf{x}) = & \sum_{j=1}^{n} N_j(\mathbf{x})\mathbf{u}_j + \sum_{h=1}^{m} N_h(\mathbf{x}) H(\xi(x))\mathbf{a}_h \\ & + \sum_{k=1}^{mt_1} N_k(\mathbf{x}) \left(\sum_{l=1}^{mf} F_l^1(x)\mathbf{b}_k^{l1} \right) \\ & + \sum_{k=1}^{mt_2} N_k(\mathbf{x}) \left(\sum_{l=1}^{mf} F_l^2(x)\mathbf{b}_k^{l2} \right) \end{aligned} \tag{4.110}$$

where m is the set of nodes that have crack face (but not crack tip) in their support domain, while mt_1 and mt_2 are the set of nodes associated with crack tips 1 and 2 in their influence domain, respectively; $\mathbf{u}_j$ are the nodal displacements (standard degrees of

freedom); $\mathbf{a}_h$, $\mathbf{b}_k^1$ and $\mathbf{b}_k^2$ are vectors of additional degrees of nodal freedom for modelling crack faces and the two crack tips, respectively. $F_l^i(\mathbf{x})$, $i=1,2$ represent mf crack tip enrichment functions and $H(\mathbf{x})$ is the generalised Heaviside function.

The first term on the right-hand side of Eq. (4.110) is the classical finite element approximation to determine the displacement field, while the remaining terms are the enrichment approximation in order to take into account the existence of any discontinuities. They utilise additional degrees of freedom to facilitate modelling the existence of any discontinuous field, such as a crack, without modelling it explicitly in the finite element mesh.

Discretization of Eq. (4.109) using the XFEM procedure (4.110) results in a discrete system of linear equilibrium equations:

$$\mathbf{K}\mathbf{u}^h = \mathbf{f} \tag{4.111}$$

where $\mathbf{K}$ is the stiffness matrix, $\mathbf{u}^h$ is the vector of degrees of nodal freedom (for both classical and enriched ones) and $\mathbf{f}$ is the vector of external force. The global matrix and vectors are calculated by assembling matrices and vectors of each element. For each element, $\mathbf{K}$ and $\mathbf{f}$ are defined as:

$$\mathbf{K}_{ij}^e = \begin{bmatrix} \mathbf{K}_{ij}^{\mathbf{uu}} & \mathbf{K}_{ij}^{\mathbf{ua}} & \mathbf{K}_{ij}^{\mathbf{ub}} \\ \mathbf{K}_{ij}^{\mathbf{au}} & \mathbf{K}_{ij}^{\mathbf{aa}} & \mathbf{K}_{ij}^{\mathbf{ab}} \\ \mathbf{K}_{ij}^{\mathbf{bu}} & \mathbf{K}_{ij}^{\mathbf{ba}} & \mathbf{K}_{ij}^{\mathbf{bb}} \end{bmatrix} \tag{4.112}$$

$$\mathbf{f}_i^e = \left\{ \mathbf{f}_i^{\mathbf{u}} \quad \mathbf{f}_i^{\mathbf{a}} \quad \mathbf{f}_i^{\mathbf{b}1} \quad \mathbf{f}_i^{\mathbf{b}2} \quad \mathbf{f}_i^{\mathbf{b}3} \quad \mathbf{f}_i^{\mathbf{b}4} \right\}^{\mathrm{T}} \tag{4.113}$$

and $\mathbf{u}^h$ is the vector of nodal parameters:

$$\mathbf{u}^h = \{\mathbf{u} \quad \mathbf{a} \quad \mathbf{b}_1 \quad \mathbf{b}_2 \quad \mathbf{b}_3 \quad \mathbf{b}_4\}^T \tag{4.114}$$

with

$$\mathbf{K}_{ij}^{rs} = \int_{\Omega^e} (\mathbf{B}_i^r)^{\mathrm{T}} \mathbf{D} \mathbf{B}_j^s \, \mathrm{d}\Omega \qquad (r, s = \mathbf{u}, \mathbf{a}, \mathbf{b}) \tag{4.115}$$

$$\mathbf{f}_i^{\mathbf{u}} = \int_{\Gamma_t} N_i \mathbf{f}^{\mathrm{t}} \, \mathrm{d}\Gamma + \int_{\Omega^e} N_i \mathbf{f}^{\mathrm{b}} \, \mathrm{d}\Omega \tag{4.116}$$

$$\mathbf{f}_i^{\mathbf{a}} = \int_{\Gamma_t} N_i H \mathbf{f}^{\mathrm{t}} \, \mathrm{d}\Gamma + \int_{\Omega^e} N_i H \mathbf{f}^{\mathrm{b}} \, \mathrm{d}\Omega \tag{4.117}$$

$$\mathbf{f}_i^{\mathbf{b}\alpha} = \int_{\Gamma_t} N_i F_\alpha \mathbf{f}^{\mathrm{t}} \, \mathrm{d}\Gamma + \int_{\Omega^e} N_i F_\alpha \mathbf{f}^{\mathrm{b}} \, \mathrm{d}\Omega \qquad (\alpha = 1, 2, 3 \text{ and } 4) \tag{4.118}$$

where $\mathbf{B}_i^{\mathbf{u}}$, $\mathbf{B}_i^{\mathbf{a}}$ and $\mathbf{B}_i^{\mathbf{b}}$ are derivatives of shape functions defined in Eqs. (3.88), (3.89) and (3.90), respectively.

Crack tip enrichment functions are obtained from the analytical solution for displacement in the vicinity of the crack tip, Eqs. (4.51), (4.76) and (4.99):

$$\{F_l(r,\theta)\}_{l=1}^{4} = \left\{\sqrt{r}\cos\frac{\theta_1}{2}\sqrt{g_1(\theta)}, \sqrt{r}\cos\frac{\theta_2}{2}\sqrt{g_2(\theta)}, \sqrt{r}\sin\frac{\theta_1}{2}\sqrt{g_1(\theta)}, \right. \\ \left. , \sqrt{r}\sin\frac{\theta_2}{2}\sqrt{g_2(\theta)}\right\} \tag{4.119}$$

Eq. (4.119) can not be directly used in isotropic media because it may lead to indefinite $(0/0)$ expressions (Mohammadi and Asadpoure 2006). A straightforward remedy is to apply the original isotropic enrichment functions (3.100)

$$\{F_l(r,\theta)\}_{l=1}^{4} = \left\{\sqrt{r}\cos\frac{\theta}{2}, \sqrt{r}\sin\frac{\theta}{2}, \sqrt{r}\sin\theta\cos\frac{\theta}{2}, \sqrt{r}\sin\theta\sin\frac{\theta}{2}\right\} \tag{4.120}$$

4.4.3 SIF calculations

The stress intensity factor (SIF) is one of the important parameters representing fracture properties of a crack tip. Here, the domain integral method proposed by Kim and Paulino (2002) is adopted for evaluating the mixed mode stress intensity factors in homogenous orthotropic media.

Fig. 4.7 shows an arbitrary area surrounding a crack tip. The standard path independent *J* integral for the cracked body is defined as (Rice and Rosengren 1968):

$$J = \int_{\Gamma}\left(W_{\mathrm{s}}\delta_{1j} - \sigma_{ij}\frac{\partial u_j}{\partial x_1}\right)\mathbf{n}_j \mathrm{d}\Gamma \tag{4.121}$$

where $\mathbf{n}_j$ is the *j*th component of the outward unit normal to Γ, δ_{1j} is Kronecker delta, W_{s} is the strain energy density for linear elastic material, and Γ is an arbitrary contour around the crack tip which encloses no other cracks or discontinuities.

Eq. (4.121) is not well suited for the finite element solutions, and an equivalent form of the *J* integral can be obtained by exploiting the divergence theorem in the form of the domain integral approach (Kim and Paulino 2003)

$$J = -\int_{A}\left(W_{\mathrm{s}}\delta_{1j} - \sigma_{ij}\frac{\partial u_i}{\partial x_1}\right)\frac{\partial q}{\partial x_j}\mathrm{d}\Gamma \tag{4.122}$$

where A is an area surrounding the crack tip (the interior region of Γ) and q is a smoothly varying function. Γ is usually assumed as a circular or rectangular area whose centre locates on the crack tip.

As proposed by Dolbow (1999) and Moës *et al.* (1999), a simple function q, varying linearly from $q=1$ at the crack tip to $q=0$ at the exterior boundary Γ, is used in the finite element model (Fig. 4.8). Therefore, the elements away from the boundary can be

neglected. It is worth noting that the value within the parentheses in Eq. (4.122) is not necessary to be evaluated in the area that q is constant (and so its gradient vanishes). From a numerical aspect, in spite of the fact that the stress gradient in elements containing a crack tip is usually very high, it is more appropriate to avoid locating the contour on the elements including a crack tip (Asadpoure *et al.* 2007).

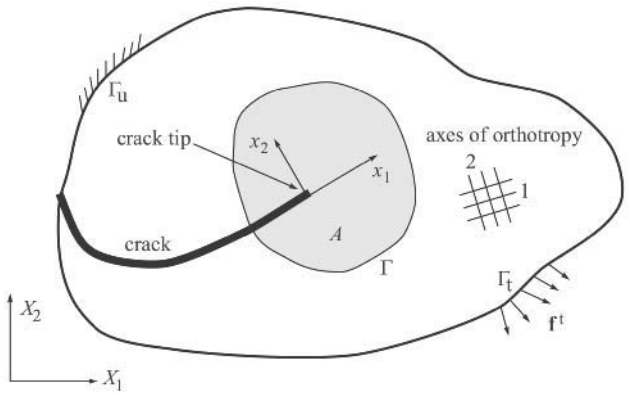

Figure 4.7 Local crack tip coordinates and the contour Γ and its interior area, A.

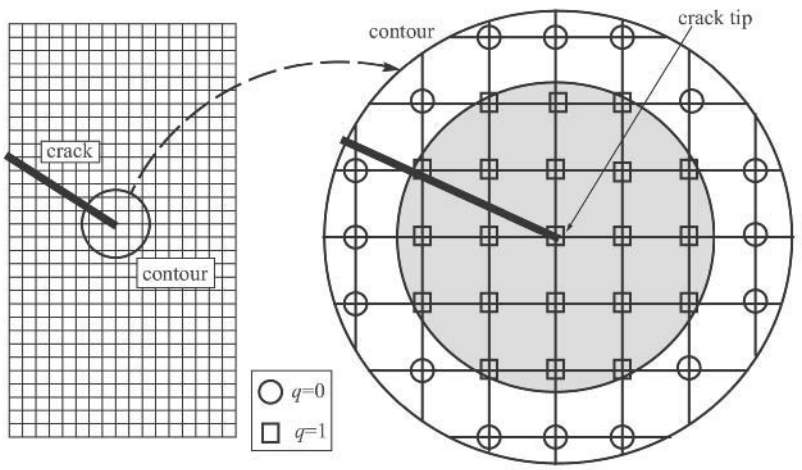

Figure 4.8 Nodal values for function q.

The method of interaction integral, based on the definition of an auxiliary state, is used to extract mixed mode stress intensity factors. Suppose there are two equilibrium states; state 1 corresponds to the actual state and state 2 corresponds to an auxiliary state for the given problem geometry.

Auxiliary stress and strain states should be chosen so as to satisfy both the equilibrium equation and the traction free boundary condition on the crack surface in the area A. One of the choices is the displacement and stress fields in the vicinity of the crack tip provided by Sih *et al.* (1965) and Asadpoure *et al.* (2007),

$$\sigma_{11}^{\text{aux}} = \frac{K_{\text{I}}^{\text{aux}}}{\sqrt{2\pi r}} \text{Re}\left[\frac{s_1 s_2}{s_1 - s_2}\left\{\frac{s_2}{\sqrt{\cos\theta + s_2 \sin\theta}} - \frac{s_1}{\sqrt{\cos\theta + s_1 \sin\theta}}\right\}\right] + \frac{K_{\text{II}}^{\text{aux}}}{\sqrt{2\pi r}} \text{Re}\left[\frac{1}{s_1 - s_2}\left\{\frac{s_2^2}{\sqrt{\cos\theta + s_2 \sin\theta}} - \frac{s_1^2}{\sqrt{\cos\theta + s_1 \sin\theta}}\right\}\right] \tag{4.123}$$

$$\sigma_{22}^{\text{aux}} = \frac{K_{\text{I}}^{\text{aux}}}{\sqrt{2\pi r}} \text{Re}\left[\frac{1}{s_1 - s_2}\left\{\frac{s_1}{\sqrt{\cos\theta + s_2 \sin\theta}} - \frac{s_2}{\sqrt{\cos\theta + s_1 \sin\theta}}\right\}\right] + \frac{K_{\text{II}}^{\text{aux}}}{\sqrt{2\pi r}} \text{Re}\left[\frac{1}{s_1 - s_2}\left\{\frac{1}{\sqrt{\cos\theta + s_2 \sin\theta}} - \frac{1}{\sqrt{\cos\theta + s_1 \sin\theta}}\right\}\right] \tag{4.124}$$

$$\sigma_{12}^{\text{aux}} = \frac{K_{\text{I}}^{\text{aux}}}{\sqrt{2\pi r}} \text{Re}\left[\frac{s_1 s_2}{s_1 - s_2}\left\{\frac{1}{\sqrt{\cos\theta + s_1 \sin\theta}} - \frac{1}{\sqrt{\cos\theta + s_2 \sin\theta}}\right\}\right] + \frac{K_{\text{II}}^{\text{aux}}}{\sqrt{2\pi r}} \text{Re}\left[\frac{1}{s_1 - s_2}\left\{\frac{s_1}{\sqrt{\cos\theta + s_1 \sin\theta}} - \frac{s_2}{\sqrt{\cos\theta + s_2 \sin\theta}}\right\}\right] \tag{4.125}$$

and

$$u_1^{\text{aux}} = K_{\text{I}}^{\text{aux}} \sqrt{\frac{2r}{\pi}} \text{Re}\left[\frac{1}{s_1 - s_2}\left\{s_1 p_2 \sqrt{\cos\theta + s_2 \sin\theta} - s_2 p_1 \sqrt{\cos\theta + s_1 \sin\theta}\right\}\right] + K_{\text{II}}^{\text{aux}} \sqrt{\frac{2r}{\pi}} \text{Re}\left[\frac{1}{s_1 - s_2}\left\{p_2 \sqrt{\cos\theta + s_2 \sin\theta} - p_1 \sqrt{\cos\theta + s_1 \sin\theta}\right\}\right] \tag{4.126}$$

$$u_2^{\text{aux}} = K_{\text{I}}^{\text{aux}} \sqrt{\frac{2r}{\pi}} \text{Re}\left[\frac{1}{s_1 - s_2}\left\{s_1 q_2 \sqrt{\cos\theta + s_2 \sin\theta} - s_2 q_1 \sqrt{\cos\theta + s_1 \sin\theta}\right\}\right] + K_{\text{II}}^{\text{aux}} \sqrt{\frac{2r}{\pi}} \text{Re}\left[\frac{1}{s_1 - s_2}\left\{q_2 \sqrt{\cos\theta + s_2 \sin\theta} - q_1 \sqrt{\cos\theta + s_1 \sin\theta}\right\}\right] \tag{4.127}$$

where superscript aux stands for the auxiliary state, s_1 and s_2 are crack tip material parameters evaluated by solving the characteristic equation of homogenous partial differential equation of anisotropic stress function (4.11) (Lekhnitskii 1968) and p_i and q_i are defined in Eqs. (4.20) and (4.21).

By combining the actual and auxiliary states for obtaining the J integral, one can write:

$$J = J^{\text{act}} + J^{\text{aux}} + M \tag{4.128}$$

where J corresponds to the superposition state, and J^{act} and J^{aux} are the actual and auxiliary states J integrals, respectively, and:

$$M = \int_A \left[\sigma_{ij} \frac{\partial u_i^{\text{aux}}}{\partial x_1} + \sigma_{ij}^{\text{aux}} \frac{\partial u_i}{\partial x_1} - W^{\text{M}} \delta_{1j} \right] \frac{\partial q}{\partial x_j} \mathrm{d}A \tag{4.129}$$

where $W^{\text{M}} = 0.5(\sigma_{ij}\varepsilon_{ij}^{\text{aux}} + \sigma_{ij}^{\text{aux}}\varepsilon_{ij})$ for linear elastic conditions.

The strain of the auxiliary field could be chosen by either the strain–stress relationship, i.e. $\varepsilon_{ij}^{\text{aux}} = C_{ijkl}\sigma_{kl}^{\text{aux}}$ or as the symmetric part of the displacement gradient, i.e. $\varepsilon_{ij}^{\text{aux}} = 0.5(u_{i,j}^{\text{aux}} + u_{j,i}^{\text{aux}})$; these are compatible with each other as long as the material is homogeneous and C_{ijkl} has one value in the domain. After some manipulations (Asadpoure *et al.* 2007 and Asadpoure and Mohammadi 2007):

$$M = 2t_{11}K_{\text{I}}K_{\text{I}}^{\text{aux}} + t_{12}\left(K_{\text{I}}K_{\text{II}}^{\text{aux}} + K_{\text{I}}^{\text{aux}}K_{\text{II}}\right) + 2t_{22}K_{\text{II}}K_{\text{II}}^{\text{aux}} \tag{4.130}$$

where

$$t_{11} = -\frac{c_{22}}{2}\,\text{Im}\left(\frac{s_1 + s_2}{s_1 s_2}\right) \tag{4.131}$$

$$t_{12} = -\frac{c_{22}}{2}\,\text{Im}\left(\frac{1}{s_1 s_2}\right) + \frac{c_{11}}{2}\,\text{Im}\left(s_1 s_2\right) \tag{4.132}$$

$$t_{22} = \frac{c_{11}}{2}\,\text{Im}\left(s_1 + s_2\right) \tag{4.133}$$

The stress intensity factor can then be obtained by considering the two states and solving a system of linear algebraic equations. These two states are state 1: $K_{\text{I}}^{\text{aux}} = 1; K_{\text{II}}^{\text{aux}} = 0$ and state 2: $K_{\text{I}}^{\text{aux}} = 0; K_{\text{II}}^{\text{aux}} = 1$. By calculating M from both Eqs. (4.129) and (4.130) and solving a system of linear algebraic equations, the actual mixed mode stress intensity factors associated with state 1 and state 2 are obtained (Asadpoure *et al.* 2007 and Asadpoure and Mohammadi 2007):

$$M^{(1)} = 2t_{11}K_{\text{I}} + t_{12} \tag{4.134}$$

$$M^{(2)} = t_{12}K_{\text{I}} + 2t_{22}K_{\text{II}} \tag{4.135}$$

4.5 NUMERICAL SIMULATIONS

In order to verify performance of the developed anisotropic XFEM approach, several examples with initial internal flaws are considered. They are:

1. An orthotropic plate with a crack parallel to one of the principle material orthotropic axes subjected to tensile stresses.

2. An orthotropic plate with various oblique principle material orthotropic axes with an edge crack subjected to tensile stresses.
3. An orthotropic plate with various oblique edge cracks subjected to tensile stresses.
4. An orthotropic plate with various central oblique cracks subjected to tensile stresses.
5. A circular plate with various oblique cracks subjected to a couple of concentrated forces.
6. A crack between orthotropic and isotropic materials subjected to tensile tractions.

All examples are solved with the following independent engineering constants $(E_{ij}, \nu_{ij}, G_{ij}, i, j = 1,2)$,

$$E = \sqrt{E_{11}E_{22}} \tag{4.136}$$

$$\nu = \sqrt{\nu_{12}\nu_{21}} \tag{4.137}$$

$$\delta = \frac{E_{11}}{E_{22}} = \frac{\nu_{12}}{\nu_{21}} \tag{4.138}$$

$$\kappa_0 = \frac{E}{2G_{12}} - \nu \tag{4.139}$$

where E is the efficient Young's modulus, ν is the effective Poisson's ratio, δ is the stiffness ratio and κ_0 is the shear parameter.

Stress intensity factors and J integrals are calculated for all examples using the proposed XFEM with associated enrichment functions and are compared to other available analytical and numerical solutions. Results are presented in terms of the stress intensity factors K_{I} and K_{II} and/or normalised stress intensity factors $\overline{K}_{\mathrm{I}} = K_{\mathrm{I}} / \sigma\sqrt{\pi a}$ and $\overline{K}_{\mathrm{II}} = K_{\mathrm{II}} / \sigma\sqrt{\pi a}$ for the applied uniform stress and $\overline{K}_{\mathrm{I}} = K_{\mathrm{I}}\delta^2 / \varepsilon_0 E\sqrt{\pi a}$ and $\overline{K}_{\mathrm{II}} = K_{\mathrm{II}}\delta^2 / \varepsilon_0 E\sqrt{\pi a}$ for fixed-grip loading.

A quadrature partitioning approach is used for integration over an element, if it contains a crack. Any element cut by a crack is numerically partitioned into ten sub-quads to accurately calculate the numerical integrals and a 2×2 Gauss rule is utilised for integrations in each one. Furthermore, a 2×2 Gauss rule is applied for other regular finite elements without any partitioning.

Finally, the effect of proposed XFEM enrichment functions is investigated for different problems. To simplify the illustrations, the following notations are assumed:

1. XFEM-I: Class I orthotropic materials using the enrichment functions (4.51) and (4.49)–(4.50) which are based on the displacement fields (4.45), (4.46) (Asadpoure *et al.* 2007).

2. XFEM-II: Class II orthotropic materials using the enrichment functions (4.76) and (4.74)–(4.75), which are based on the displacement fields (4.57), (4.58) (Asadpoure *et al.* 2006).
3. XFEM-III: All classes of orthotropic materials using the enrichment functions (4.99) and (4.95)–(4.96) based on the displacement and stress fields (4.78), (4.92) (Asadpoure and Mohammadi 2007).

4.5.1 Plate with a crack parallel to material axis of orthotropy

A very simple example, a crack aligned along one of the axes of orthotropy in the centre of a plate, is investigated. Fig. 4.9a illustrates the geometry and boundary conditions of the cracked plate with a fixed-grip loading, which is obtained by a constant tensile traction by utilizing a uniform unit stress ($\sigma = 1$), or a tensile load equivalent to uniform unit strain ($\varepsilon_0 = 1$) in the corresponding uncracked plate. The plate is composed of a graphite-epoxy material with the following orthotropic properties: $E_1 = 114.8$ GPa, $E_2 = 11.7$ GPa, $G_{12} = 9.66$ GPa, $\nu_{12} = 0.21$.

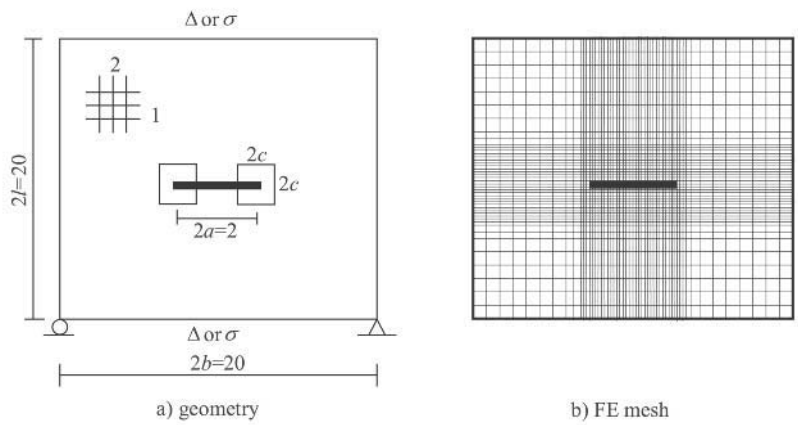

Figure 4.9 Geometry and boundary conditions for a plate with a crack parallel to material axis of orthotropy and the FE model.

Table 4.1 Values of the stress intensity factor K_I for a plate with a crack parallel to material orthotropic axes

Method	Number of elements	DOFs	K_I
Reference	2001	11702	1.767
XFEM-II	2025	4278	1.804
XFEM-III	2025	4278	1.807

The domain is discretized into 2025 quadrilateral finite elements and 2116 nodes (Fig. 4.9b). The size of the finite elements around the crack tip is set to one-sixteenth of the crack length. Stress intensity factors are calculated by XFEM-II (Asadpoure *et al.* 2006) and XFEM-III (Asadpoure and Mohammadi 2007) enrichments, and compared with the results provided by Kim and Paulino (2002) using a total of 2001 elements and 5851 nodes, as given in Table 4.1.

The mode I stress intensity factor predicted by XFEM-III (Asadpoure and Mohammadi 2007) is different by about 2.3% from Kim and Paulino's (2002) and 0.2% from the XFEM-II (Asadpoure *et al.* 2006); however, Kim and Paulino (2002) used almost three times the present degrees of freedom (DOF).

Two coarser finite element meshes are used to investigate the effect of the number of finite elements on stress intensity factors. According to Table 4.2, even with 4 times the reduction in the number of degrees of freedom, the computed SIFs have changed only 1.5%; illustrating the efficiency of the proposed enrichment approach in crack modelling. The results of Table 4.2 are associated to a specific value of *c/a* where a converged solution is obtained. In Fig. 4.10, the rate of convergence of the mode I stress intensity factor with respect to the relative integration domain size is illustrated.

Table 4.2 Values of the stress intensity factor K_I for a plate with a crack parallel to material axis of orthotropy for three different finite meshes

Mesh	Number of elements	DOFs	*c/a*	K_I
1	2025	4278	0.5	1.807
2	784	1712	0.5	1.800
3	400	904	1.5	1.781

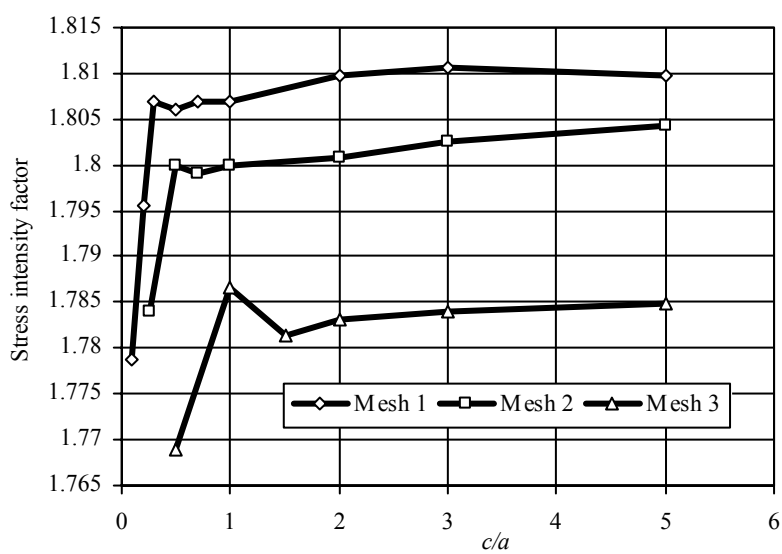

Figure 4.10 The rate of convergence of the mode I stress intensity factor with respect to the relative integration domain size.

Table 4.3 compares the computed stress intensity factors for enrichment with and without crack tip functions and shows the rate of convergence for various integration domain sizes (c). According to Table 4.3, small domain sizes cannot be used without the inclusion of crack tip enrichment functions, and in order to compensate for the local effects of the crack tip, larger domains should be selected.

Inclusion of crack tip enrichment functions allows for smaller domain sizes around the crack tip, as higher rates of convergence are anticipated. Numerical results show that when $c/a = 0.5$, the values of SIFs become nearly independent from the domain size (Asadpoure *et al.* 2006).

Table 4.3 Comparison of mode I stress intensity factors with and without crack tip functions for a plate with a crack parallel to material orthotropic axis

Relative domain size (c/a)	K_I without crack tip function	K_I with crack tip function
0.25	1.804	1.804
0.50	1.802	1.802
1	1.802	1.802
2	1.800	1.804

The effect of the number of elements in the numerical analysis is investigated by utilizing some coarser meshes. Table 4.4 compares the results for SIFs when isotropic and orthotropic enrichment functions are applied. According to Table 4.4, the results are only slightly different (0.2%).

Table 4.4 Comparison of stress intensity factors for orthotropic and isotropic enrichment functions

Mesh	Number of elements	Number of DOFs	K_I	
			XFEM-II	Isotropic enrichment
1	2025	4278	1.804	1.810
2	784	1712	1.803	1.806
3	400	904	1.802	1.801

4.5.2 Edge crack with several orientations of the axes of orthotropy

Consider a rectangular plane stress plate with an edge horizontal crack subjected to a tensile distributed load, as depicted in Fig. 4.11a. The width of the plate is one half of its height and the length of the crack is one fourth of its height. The plate is composed of a graphite-epoxy material with the following orthotropic properties: $E_1 = 114.8$ GPa, $E_2 = 11.7$ GPa, $G_{12} = 9.66$ GPa, $\nu_{12} = 0.21$. Several orientations of material elastic axes are studied.

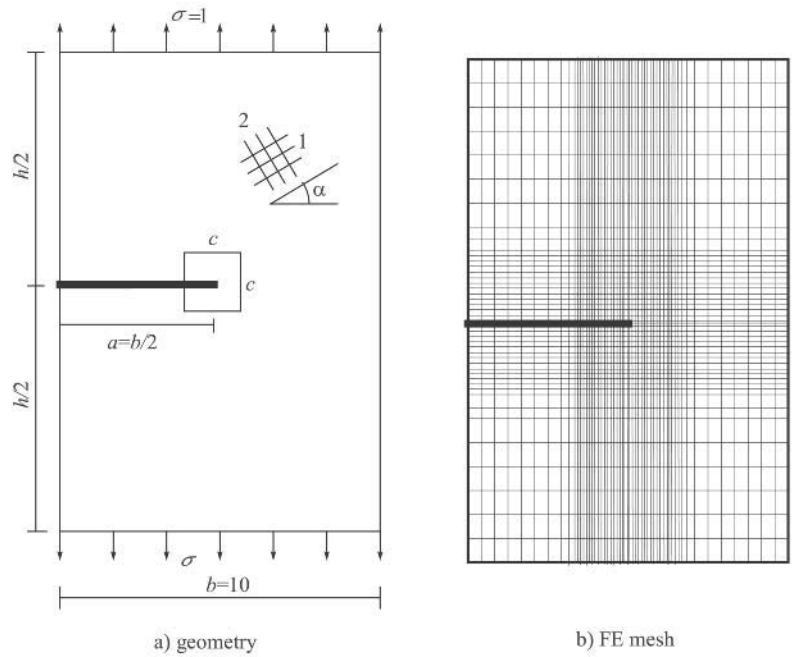

Figure 4.11 Geometry and loading of a single edge crack in a rectangular plate with several orientations of the axes of orthotropy and the finite element mesh.

The finite element model is composed of 1836 four-node elements with 1925 nodes (Fig. 4.11b). Forty-two additional degrees of freedom are associated with the enrichment part of the approximation. A 2×2 Gauss quadrature is adopted for finite elements, while a 5×5 Gauss quadrature is utilised for integration in elements containing Heaviside enriched nodes.

The effects of changing the material elastic angle on mixed mode stress intensity factors in the plate are investigated. The relative integration domain size (c/a) is about 0.12 of the crack's length. Moreover, a study of variations of stress intensity factors for different domain sizes has shown that the domain size does not substantially affect the value of SIFs. Fig. 4.12 compares the results by XFEM-I (Asadpoure *et al.* 2007) and XFEM-III (Asadpoure and Mohammadi 2007) enrichments with the reference results by Aliabadi and Sollero (1998) who performed similar studies on the same problem using the boundary element method.

The results show that the trend of mode I stress intensity factor changes around $\alpha=45^\circ$. It has an increasing trend in the span of $\alpha=0^\circ$ to $\alpha=45^\circ$ and then decreases in the span of $\alpha=45^\circ$ to $\alpha=90^\circ$. The turning point for the mode II stress intensity factor is about $\alpha=30^\circ$.

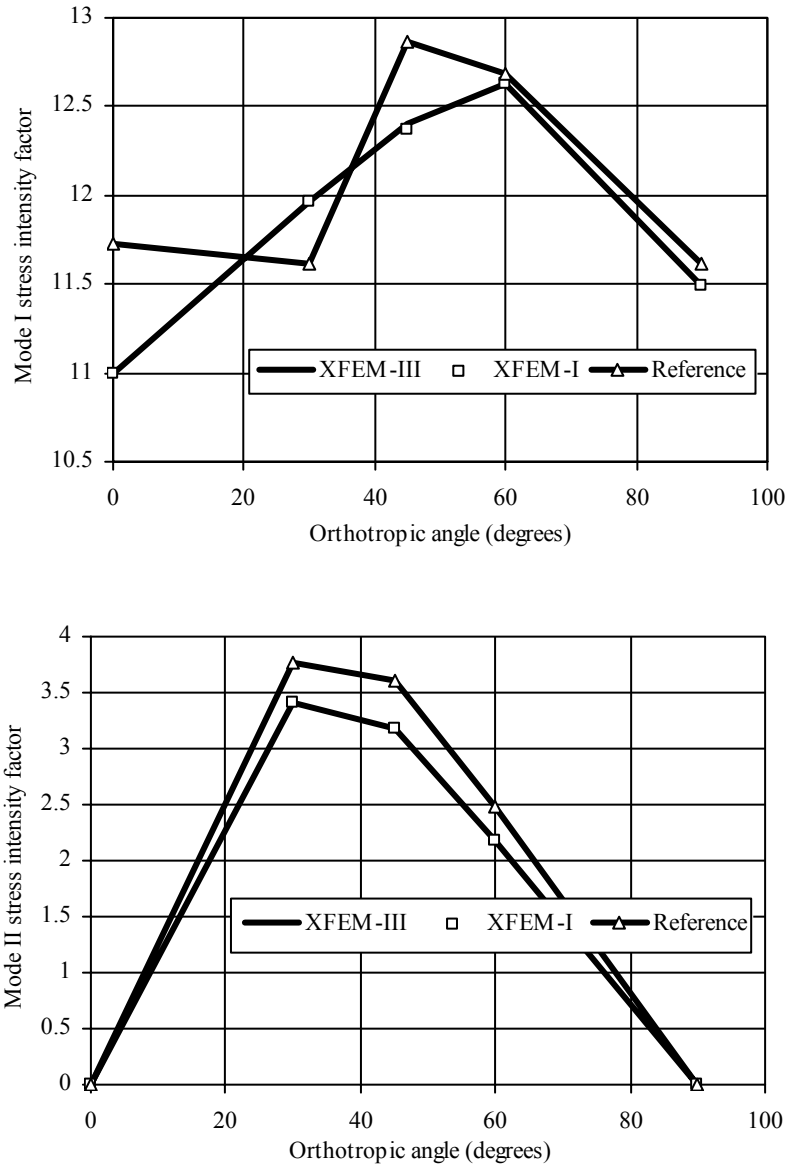

Figure 4.12 The effect of various inclinations of elastic material axes on the mode I and mode II stress intensity factors.

4.5.3 Single edge notched tensile specimen with crack inclination

Fig. 4.13 illustrates the geometry of a plate composed of Norway spruce (Picea abies) and a crack along one of the material elastic axes that emanates from the edge of the plate. Cracks usually propagate either along the wood fibres or perpendicular to them. A tensile uniform loading is applied and the analysis is performed in the plane strain state.

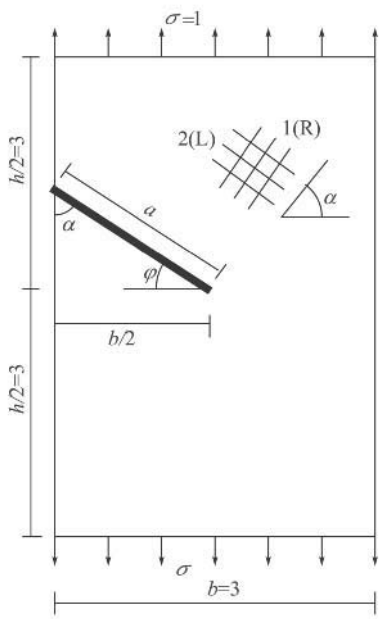

Figure 4.13 Specimen geometry used for mixed mode analysis in a rectangular plate with single notched crack.

Dimensions of the specimen are $h = 6cm$, $b = 3cm$, Poisson's ratios are $\nu_{LR} = 0.38$, $\nu_{LT} = 0.56$ and $\nu_{RT} = 0.4$, and elastic modulus are $E_R = 0.81$ GPa, $E_L = 11.84$ GPa, $E_T = 0.64$ GPa, $G_{LR} = 0.63$ GPa.

The same finite element model as in the previous example is utilised for all crack inclinations; showing the ability of analysing the XFEM for simulation of different crack patterns with the same finite element mesh. Mixed mode stress intensity factors are computed by both XFEM-I and XFEM-III enrichments and are compared with the similar effort made by Jernkvist (2001). The mesh presented by Jernkvist (2001) was focused at the crack tip, with 36 rows of elements in circumferential and 10 rows in radial direction, respectively. He correlated the mixed mode stress intensity factors to load through a simple procedure with six crack inclinations in the range of 0° to 45°.

A 2×2 Gauss quadrature rule is applied to evaluate the stiffness matrix of the classical finite element. Sub-quad partitioning is adopted for elements which have enriched nodes,

utilising ten sections in both directions and a 2×2 Gauss quadrature in each section.

The results are calculated on the base of converged values within the range of relative integration domain size, *c/a* of about 0.1 to 0.5 of crack length, which correspond to two to ten elements far from the crack tip position, respectively. Jernkvist (2001) proposed the following expressions to approximate stress intensity factors, based on a correlation approach through the usual procedure of identifying displacements of nodal points on the crack surfaces close to the crack tip by six crack inclinations φ in the range of 0° to 45° (φ in degrees):

$$K_{\mathrm{I}} = \sigma\sqrt{\pi a}\left(3.028 - 3.22\times10^{-3}\varphi + 3.73\times10^{-4}\varphi^2 - 9.14\times10^{-6}\varphi^3\right) \tag{4.140}$$

$$K_{\mathrm{II}} = \sigma\sqrt{\pi a}\left[\sin(2\varphi)\left(0.644 + 4.89\times10^{-3}\varphi\right)\right] \tag{4.141}$$

Table 4.5 shows that XFEM-I computes the mode I and II stress intensity factors by a margin of error within 0.2–2.0% and 0–3.6%, respectively. The maximum difference between the XFEM-III and Jernkvist (2001) for modes I and II are about 1.2% and 3.2%, respectively. It is clearly observed that XFEM-III (Asadpoure and Mohammadi 2007) and XFEM-I (Asadpoure *et al.* 2007) produce only slightly different results.

The maximum difference between the results of XFEM-III and Jernkvist (2001) for both stress intensity factors occurred at the maximum inclination $\varphi = 45^\circ$. The stress intensity factor for mode I has a maximum when crack inclination is about 30°; then, it decreases to lower values. In contrast, the values of K_{II} continue increasing from $\varphi = 0^\circ$ to $\varphi = 45^\circ$.

Fig. 4.14 illustrates the rate of convergence of the stress intensity factor for various relative integration domain sizes, *c/a*. It is found that the rate of convergence of XFEM-III is slightly higher than XFEM-I.

Fig. 4.15 illustrates the effect of the number of sub-quad partitioning in each element (ns) for an inclined crack $\varphi = 30^\circ$. It shows that the converged values for stress intensity factors for each mode can be obtained when ns is set to 6.

Table 4.5 The effect of crack angle on the stress intensity factors in a rectangular plate with single notched cracked

φ°	Jernkvist (2001)		XFEM-I		XFEM-III	
	K_{I}	K_{II}	K_{I}	K_{II}	K_{I}	K_{II}
0	6.573	0	6.449	0	6.454	0
15	6.699	0.793	6.617	0.795	6.620	0.797
30	7.045	1.598	7.059	1.612	7.052	1.612
45	7.244	2.230	7.391	2.310	7.378	2.303

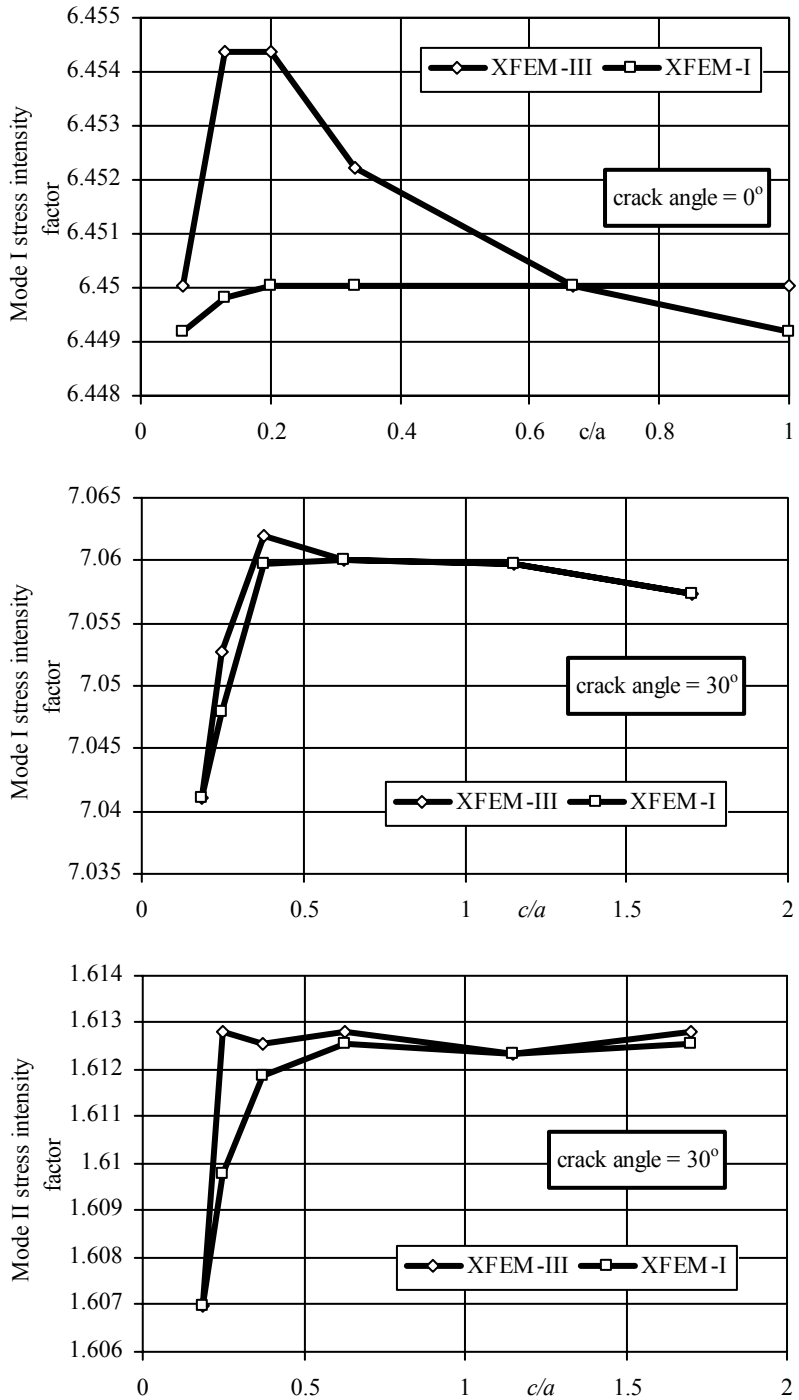

Figure 4.14 Variations of the mode I and II stress intensity factors with respect to *c/a* for a horizontal and an inclined $\varphi = 30^{\circ}$ crack, respectively.

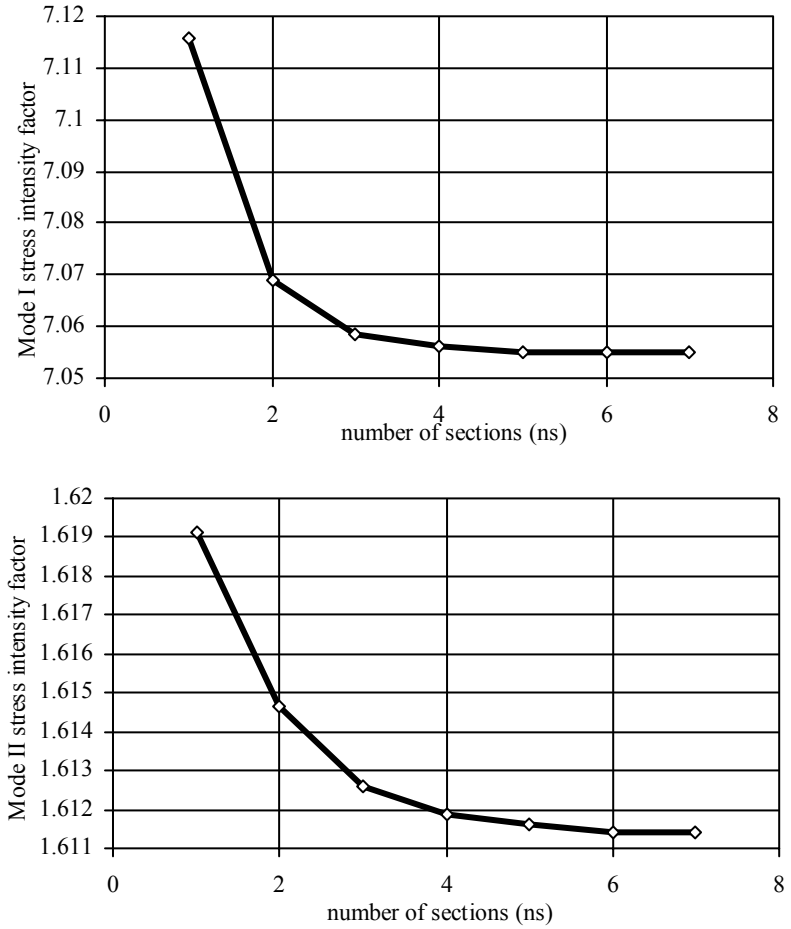

Figure 4.15 The effect of the number of sections (ns) in each element on mode I and II stress intensity factors for an inclined crack, $\varphi = 30^\circ$, when partitioning is applied.

Fig. 4.16 illustrates variations of the SIFs with respect to the order of Gauss quadrature rule without any partitioning. This is important in showing that a higher-order Gauss quadrature rule may not always replace the partitioning technique. According to Fig. 4.16, even by applying a 10×10 Gauss quadrature, a converged value for the normalised stress intensity factor in mode II cannot be achieved (Asadpoure *et al.* 2007).

4.5.4 Central slanted crack

Consider a rectangular tensile orthotropic plate with a central slanted crack, as depicted in Fig. 4.17a. The crack has a length of $2a = 2\sqrt{2}$ with the initial angle of 45°. Elastic properties are assumed as $E_1 = 3.5$ GPa, $E_2 = 12$ GPa, $G_{12} = 3$ GPa, $\nu_{21} = 0.7$.

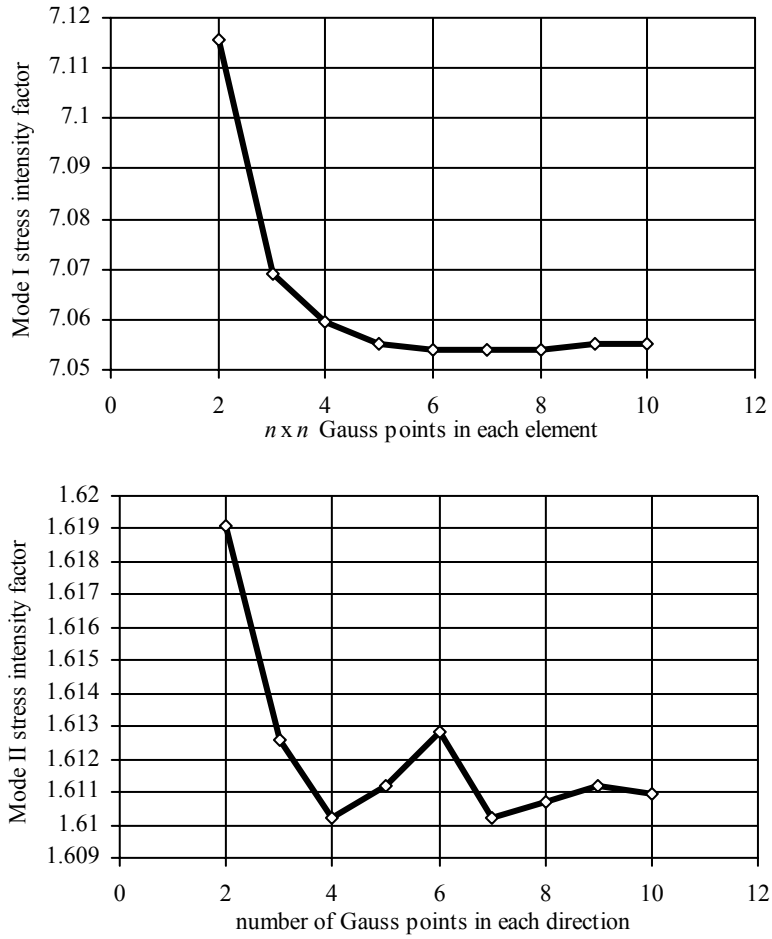

Figure 4.16 The influence of higher-order Gauss quadrature rules on stress intensity factors ($\varphi = 30^{\circ}$)**.**

The same problem, as a classic problem of mixed mode stress intensity factor, has been investigated by several others; Sih *et al.* (1965) utilised a complex variable method, Atluri *et al.* (1975) used hybrid-displacement finite element method, Wang *et al.* (1980) adopted a conservation law of elasticity, and Kim and Paulino (2002) employed two methodologies of the modified crack closure (MCC) and displacement correlation technique (DCT).

The finite element model is constructed by 2400 quadrilateral elements and 2501 nodes. Element sizes are smaller in the vicinity of the crack than the other parts of the model. The same mesh is used for all crack angles. In total, 5064 degrees of freedom are employed which include 5002 normal DOF and 62 enrichment DOF. The extended finite element method combined with the interaction integral method has been used by both XFEM-II (Asadpoure *et al.* 2006) and XFEM-III (Asadpoure and Mohammadi 2007) for solving this problem.

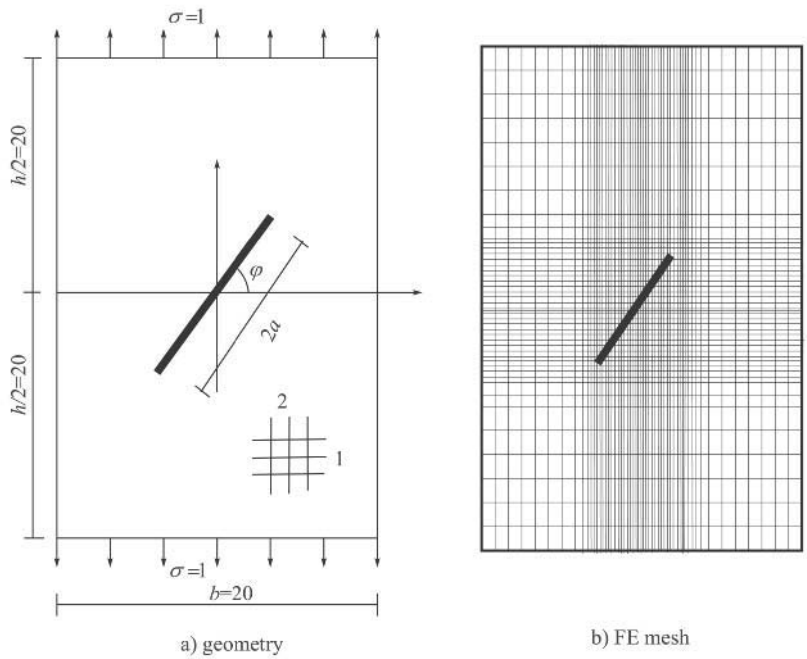

Figure 4.17 Geometry and applied loads of an orthotropic plate with a central slanted crack under remote tension and the finite element mesh.

Table 4.6 compares the results of XFEM simulations based on two types of orthotropic enrichment functions with the available reference results. XFEM analyses were performed by using a relative integration domain size, *c/a*, of about 0.85. The differences are about 2.6% and 3.9% for modes I and II, respectively, in comparison to the solution obtained by Sih *et al.* (1965). Again, both XFEM enrichments produce relatively similar results.

Table 4.6 Mixed mode stress intensity factors for an orthotropic plate with a central slanted crack under remote tension

Method	K_I	$\overline{K}_I$	K_{II}	$\overline{K}_{II}$
XFEM-II (Asadpoure *et al.* 2006)	1.081	0.513	1.092	0.518
XFEM-III (Asadpoure and Mohammadi 2007)	1.084	0.514	1.095	0.519
Sih *et al.* (1965)	1.0539	0.500	1.0539	0.500
Atluri *et al.* (1975)	1.0195	0.484	1.0795	0.512
Wang *et al.* (1980)	1.023	0.485	1.049	0.498
Kim and Paulino (2002) (DCT)	1.077	0.511	1.035	0.491
Kim and Paulino (2002) (MCC)	1.067	0.506	1.044	0.495

Fig. 4.18 illustrates the normalised SIFs corresponding to different crack angles $\varphi = 0^\circ - 90^\circ$. The mode I stress intensity factor reduces steadily by an increase in crack angle, whereas the mode II stress intensity factor increases and reaches its maximum value at $\varphi = 45^\circ$, and then decreases (Asadpoure *et al.* 2006).

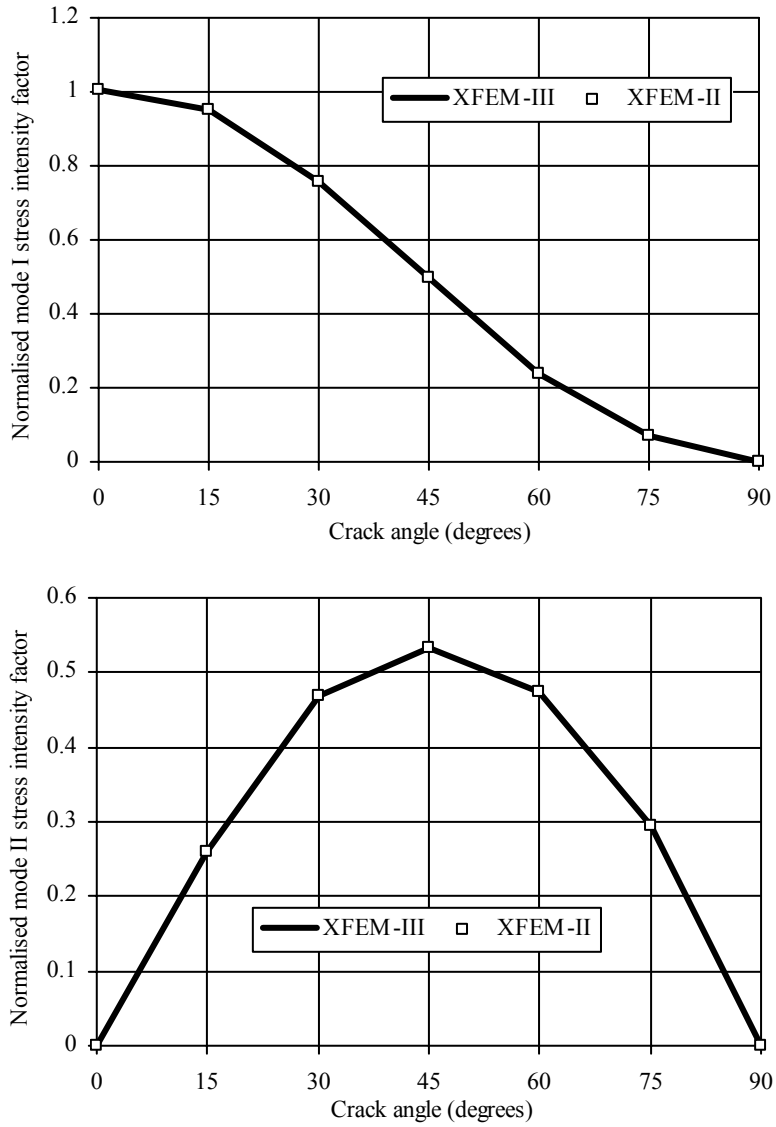

Figure 4.18 Normalised mode I and II stress intensity factors corresponding to different crack angles for a plate with a slanted crack subjected to remote tension.

Fig. 4.19 compares the value of J for various relative integration domain sizes for the crack angle 45°. Similar patterns are obtained for XFEM-II and XFEM-III orthotropic enrichments.

Values of SIFs corresponding to different sizes of the integration domain are illustrated in Fig. 4.20. As the domain size c reaches about $0.75a$, the results become almost domain-independent (Asadpoure *et al.* 2006).

If isotropic enrichment functions are applied, values for mixed mode SIFs for the case of $\varphi = 45^\circ$ are obtained as 1.083 and 1.074 for mode I and II, respectively. To further investigate the difference between orthotropic and isotropic enrichment functions, the rate of convergence of SIFs for both cases is studied for a crack angle $\varphi = 30^\circ$. According to Table 4.7, the differences of computed SIFs are not negligible and may exceed 5%. This is in contrast to the previous example where the differences were relatively small.

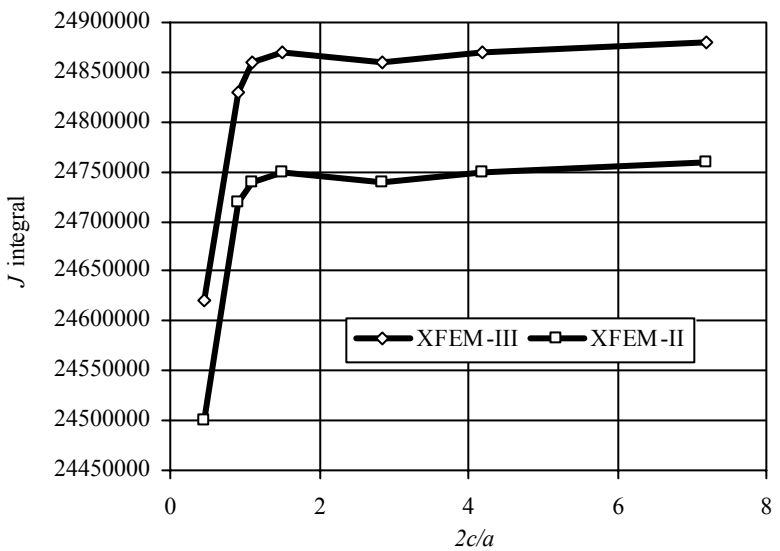

Figure 4.19 The value of the J integral for various relative integration domains for the crack angle $\varphi = 45^\circ$ (Asadpoure and Mohammadi 2007).

Table 4.7 Comparison of stress intensity factors for the proposed and isotropic enrichment functions when several meshes are used ($\varphi = 30^\circ$)

Number of elements	Number of DOFs	XFEM-II		Isotropic enrichment	
		K_{I}	K_{II}	K_{I}	K_{II}
816	1836	1.682	1.016	1.635	0.930
1496	3260	1.619	0.961	1.608	0.925
2400	5112	1.621	0.961	1.611	0.925

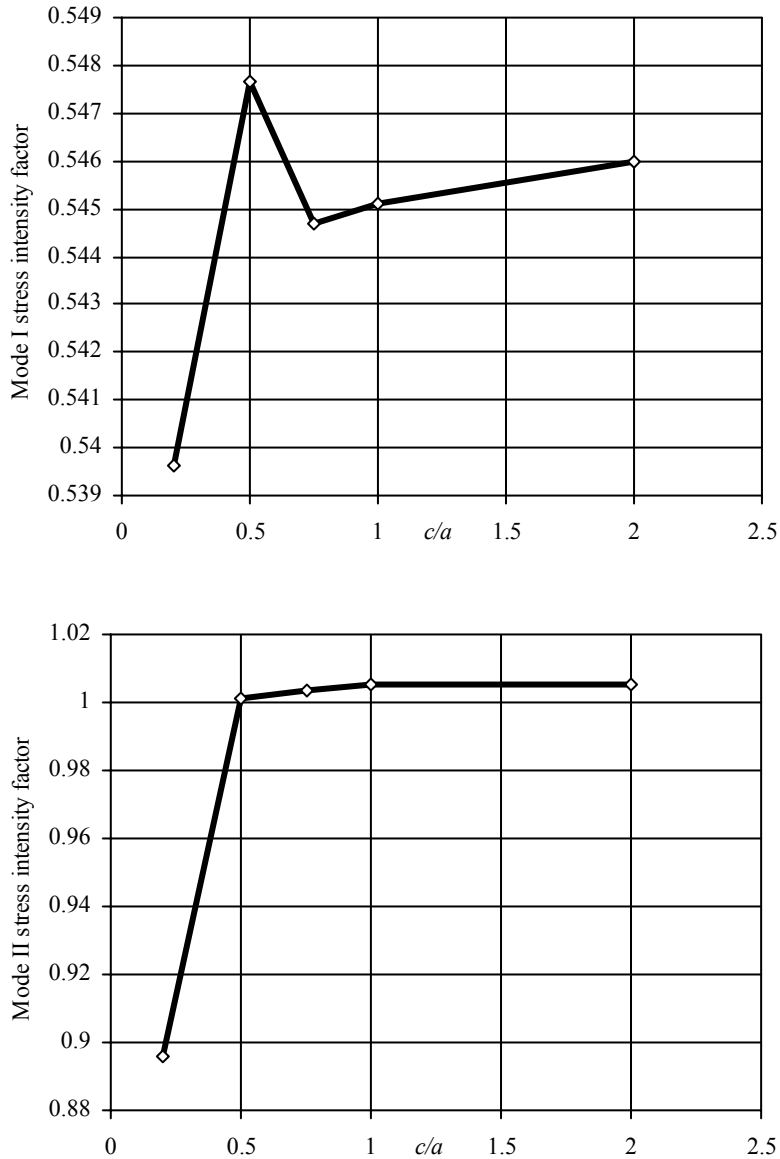

Figure 4.20 Rate of convergence of mode I and mode II stress intensity factors with $\varphi = 60^\circ$ with respect to relative domain size in a plate with a slanted crack under remote tension.

Finally, the rate of convergence of SIFs with respect to the relative domain size for a crack angle $\varphi = 30^\circ$ is illustrated in Fig. 4.21. Almost similar rates of convergence for both enrichment functions are obtained (Asadpoure *et al.* 2006).

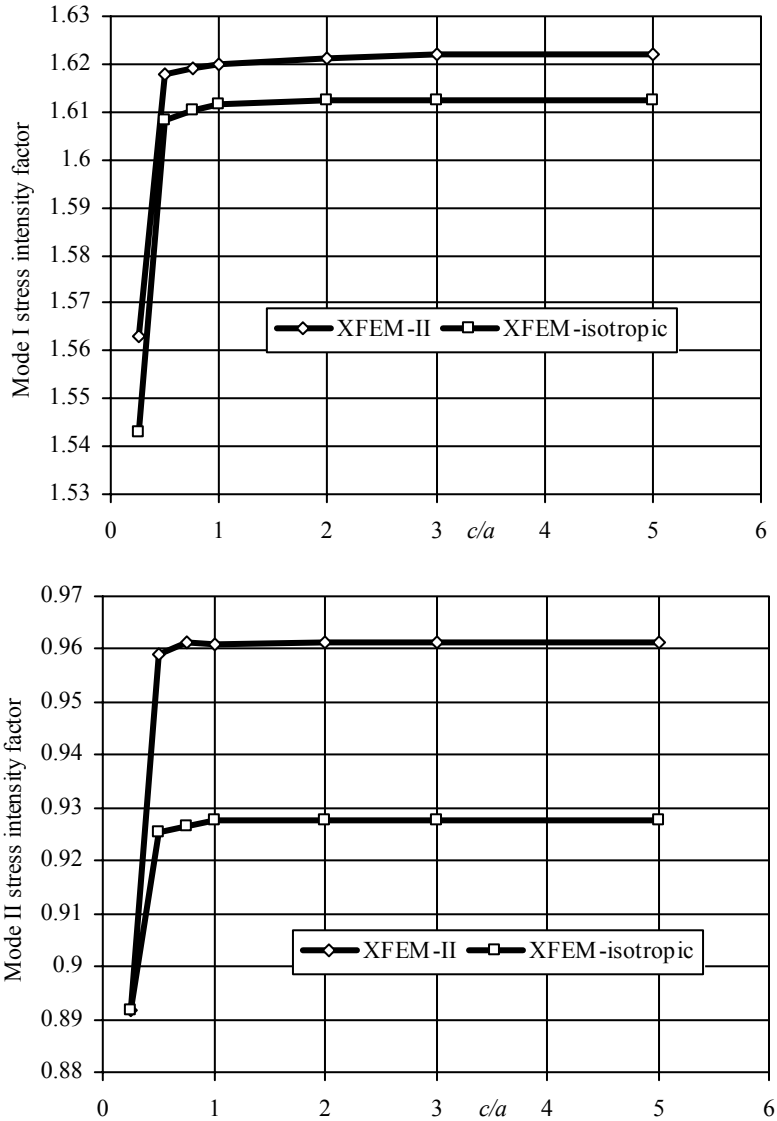

Figure 4.21 Rate of convergence of mode I and mode II stress intensity factors with $\varphi = 30^{\circ}$ with respect to relative domain size in a plate with a slanted crack under remote tension for isotropic and proposed enrichment functions using 1496 elements.

4.5.5 An inclined centre crack in a disk subjected to point loads

Consider a disk with an inclined central crack subjected to double point loads, as illustrated in Fig. 4.22. The material elastic axes are assumed to be coincident with x_1 and x_2 axes with the following material properties: $E_{11} = 0.1$, $E_{22} = 1.0$, $G_{12} = 0.5$, $\nu_{12} = 0.03$.

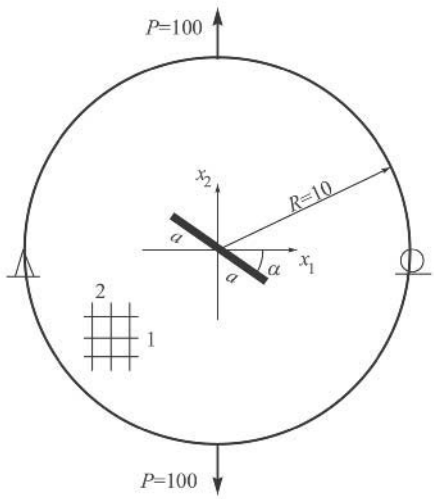

Figure 4.22 Geometry and boundary conditions for an inclined centre crack in a disk subjected to point loads.

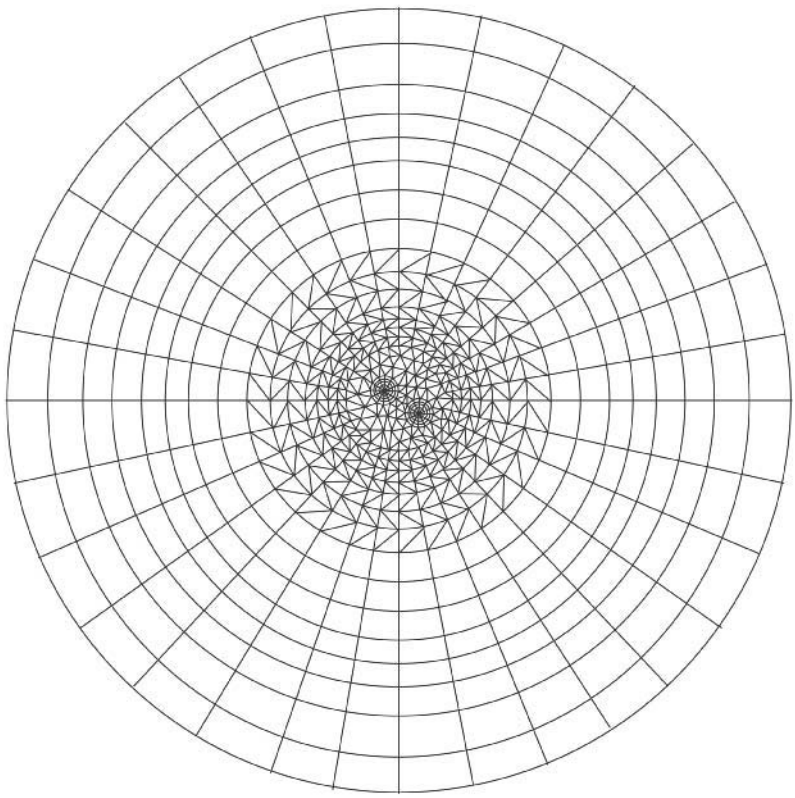

Figure 4.23 FEM discretization for an inclined centre crack in a disk subjected to point loads.

The finite element model is constructed by 920 finite elements with 1960 classical degrees of freedom, as depicted in Fig. 4.23. Only one finite element model is utilised for calculating the stress intensity factors for all crack inclinations.

Fig. 4.24 shows the value of mixed mode stress intensity factors while φ is in the range of 0° to 45°. Variations of mode I and mode II stress intensity factors appear to be sinusoidal in their quarter periods; which are in accordance with the classical results $K_{\mathrm{I}} = \sigma(\pi a)^{1/2} \sin^2 \varphi$ and $K_{\mathrm{II}} = \sigma(\pi a)^{1/2} \sin \varphi \cos \varphi$ in an infinite plate (Asadpoure and Mohammadi 2007).

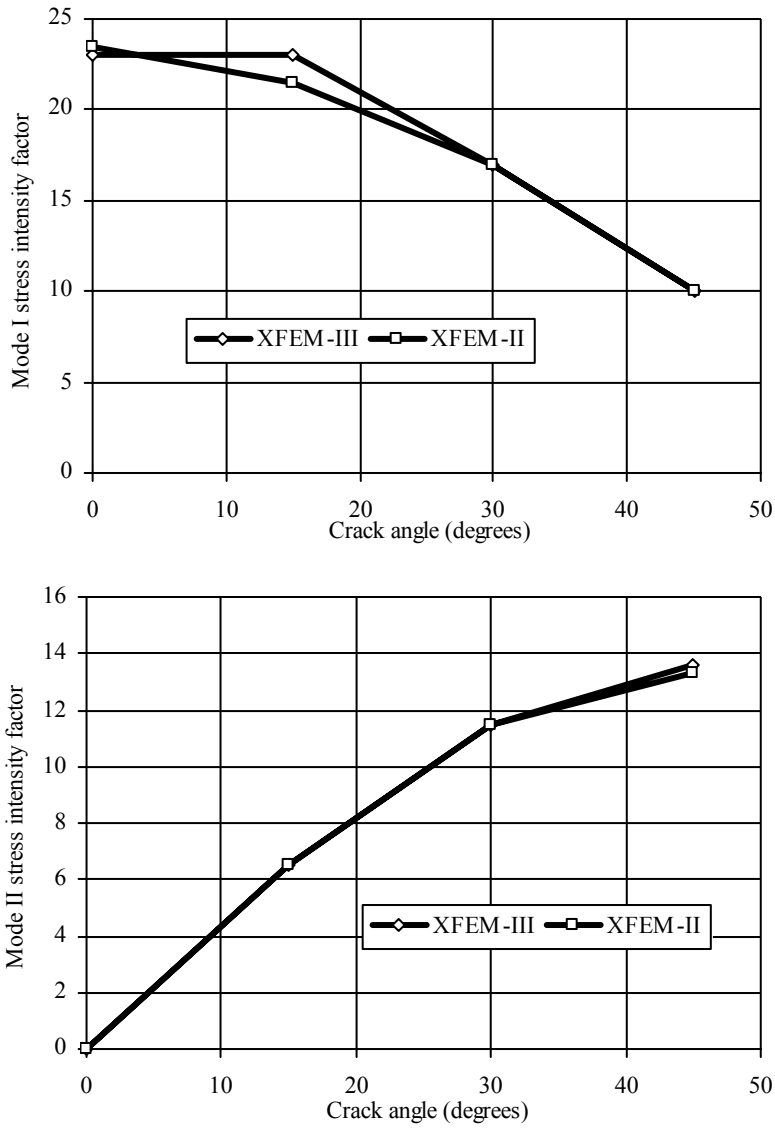

Figure 4.24 Effects of various crack inclinations on the mode I and II stress intensity factors.

Fig. 4.25 illustrates the rate of convergence for mode I and II stress intensity factors. The apparent oscillations may be attributed to sudden changes in the size of unstructured elements when different values of *c* are used (Asadpoure and Mohammadi 2007).

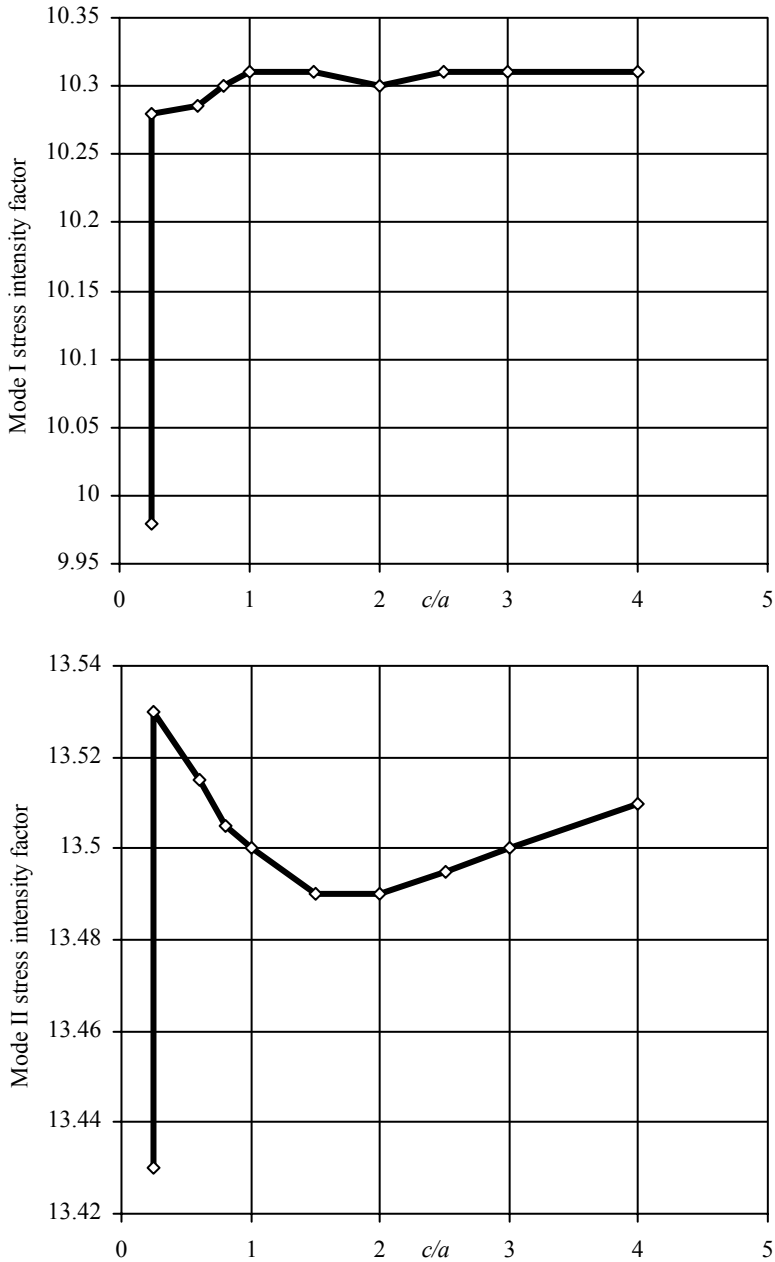

Figure 4.25 The rate of convergence of mode I and II stress intensity factors with respect to the relative integration domain size ($\varphi = 45^{\circ}$).

Mixed mode stress intensity factors for the case of $\varphi = 30^{\circ}$, evaluated by the XFEM-II and XFEM-III methods, are compared in Table 4.8 with Kim and Paulino (2002), using 999 elements and 2712 nodes for their classic finite element crack simulation. The difference of XFEM-II solutions is about 1.7–2.2% for mode I and 2.4–3.4% for mode II with respect to the solution proposed by Kim and Paulino (2002). The results show that while stress intensity factors decrease by increase of the crack inclination for mode I, they remain increasing for mode II (Asadpoure and Mohammadi 2007).

Table 4.8 Values of stress intensity factors for an inclined centre crack in a disk subjected to point loads when angle of crack alignment with respect to x_1 axis is $\varphi = 30^{\circ}$

Method	Number of elements	Number of DOFs	K_{I}	K_{II}
XFEM-II (Asadpoure *et al.* 2006)	920	1960	17.01	11.60
XFEM-III (Asadpoure and Mohammadi 2007)	920	1960	17.08	11.65
Kim and Paulino (2002) (MCC)	999	5424	16.73	11.33
Kim and Paulino (2002) (M- integral)	999	5424	16.75	11.38

4.5.6 A crack between orthotropic and isotropic materials subjected to tensile tractions

The last example of the chapter is dedicated to the analysis of a crack in between two orthotropic and isotropic materials, as depicted in Fig. 4.26. The infinite plate is subjected to far tensile stress traction $\boldsymbol{\sigma}^0$. The material properties are defined as: $E_L = 137$ GPa, $E_T = E_Z = 10.8$ GPa, $G_{ZT} = 3.36$ GPa, $G_{ZL} = G_{TL} = 5.65$ GPa, $\nu_{TZ} = 3.36$ GPa, $\nu_{ZL} = \nu_{TL} = 0.238$ and $t_{ply} = 0.127mm$, where L, T, Z are longitudinal, transverse and through the thickness axes, respectively.

A model similar to Fig. 4.9b with 1025 quadrilateral finite elements is used to simulate the plate with dimensions $b/a = h/a = 20$.

The stress intensity factors derived analytically by Qu and Bassani (1993) for a crack between two anisotropic materials in an infinite plate can be expressed as:

$$K^{\infty} = \sqrt{\pi a}\, Y(\omega)\left[(1+2i\omega)(2a)^{-i\omega}\right]\boldsymbol{\sigma}^0 \tag{4.142}$$

where ω is the index of oscillation (see Section 6.2.2), $Y(\omega)$ is a matrix function representing the oscillatory field (Chow and Atluri 1998), and

$$K^{\infty} = \left\{K_{\mathrm{I}} \quad K_{\mathrm{II}} \quad K_{\mathrm{III}}\right\}^{\mathrm{T}} \tag{4.143}$$

$$\boldsymbol{\sigma}^0 = \left\{\sigma_{22}^0 \quad \sigma_{12}^0 \quad \sigma_{23}^0\right\}^{\mathrm{T}} \tag{4.144}$$

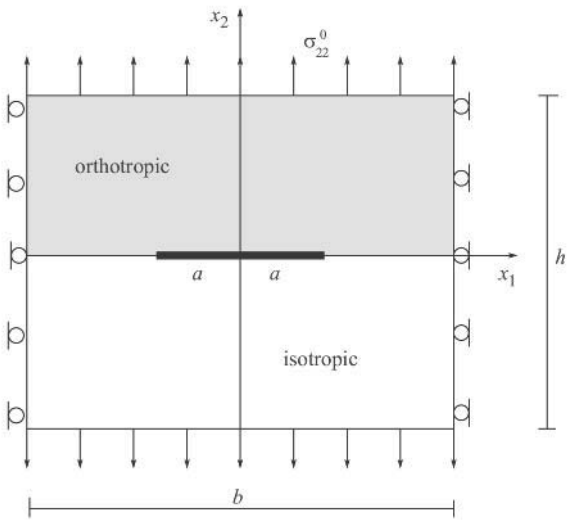

Figure 4.26 A crack between orthotropic and isotropic materials.

For the present problem $\sigma_{12}^0 = \sigma_{23}^0 = 0$. Table 4.9 compares the differences between the exact solution by Qu and Bassani (1993) with the mixed mode stress intensity factors obtained by XFEM and the one reported by Chow and Atluri (1998). Clearly, better results are obtained by XFEM.

Table 4.9 Comparison of the difference between the reference and XFEM results with the analytical stress intensity factor (Qu and Bassani 1993)

Method	Number of elements	Number of nodes	Error (K_{I})	Error (K_{II})
Chow and Atluri (1998)	216	2037	0.60	0.10
XFEM	852	2120	0.05	0.05

Chapter 5

XFEM for Cohesive Cracks

5.1 INTRODUCTION

In previous chapters, the fracture process was always considered to occur at the tip of a sharp crack. However, such models are strictly applicable only when the fracture process zone is small compared to the relevant dimensions of the specimen. Furthermore, they neglect a detailed description of what is happening in the fracture process zone.

Under the assumptions of linear elastic fracture mechanics, the stress at a crack tip becomes theoretically infinite. Form a physical point of view, however, no material can withstand such an infinite stress state, and a small plastic/fractured zone will be formed around the crack tip.

This chapter introduces some of the simplest models that describe the fracture process. Even if the fracture process zone is small, describing what is going on inside it may be convenient for the purpose of understanding the fracture mechanisms and designing appropriate modifications of the material.

The fracture process zone can be described by two simplified approaches:

1. The entire fracture process zone is lumped into the crack line and is characterised in the form of a stress–displacement law which exhibits softening. Different names have been used for this class of methods in the literature such as cohesive crack model, fictitious crack model, Dugdale–Barrenblatt model, and stress bridging model.
2. In the second approach, called the crack band model, the inelastic deformations in the process zone are smeared over a band of certain width, imagined to exist in front of the main crack.

Both approaches are capable of simulating the details of fracture process in the direction of crack. None of them can resolve the fracture process detail across the width of the fracture process zone. This chapter is mainly dedicated to the first approach and only briefly discusses some basic points regarding the second approach. It deals with the extension of the original idea of XFEM to include the effects of cohesive cracks where the type of discontinuity is different from normal cracks.

Historically, Moës and Belytschko (2002a), were the first to apply XFEM to modelling growth of arbitrary cohesive cracks, where the growth of the cohesive zone was governed by requiring the stress intensity factors at the tip of the cohesive zone to vanish.

Modelling cohesive cracks was further advanced by Zi and Belytschko (2003). They developed a new version of XFEM for applications of static cohesive cracks. All cracked elements were enriched by the sign function so that no blending of the local partition of unity was required. The entire crack was treated with only one type of enrichment function, including the elements containing the crack tip. This scheme was applied to linear 3-node triangular elements and quadratic 6-node triangular elements.

In a similar methodology, Mariani and Perego (2003) presented a methodology for the simulation of quasi-static cohesive crack propagation in quasi-brittle materials. Assumption of a cubic displacement discontinuity allowed reproducing the typical cusp-like shape of the process zone at the tip of a cohesive crack.

Further development was reported by Mergheim *et al.* (2005) who proposed the computational modelling of cohesive cracks in quasi-brittle materials, whereby the discontinuity was allowed to propagate freely through the elements. As a result, only two independent copies of the standard basis functions were required: one set was put to zero on one side of the discontinuity, while the other set took its usual values on the opposite side, and vice versa for the other set. In contrast to the classical XFEM, the suggested approach only relied exclusively on displacement degrees of freedom. On the discontinuity surface, the jump in the deformation is related to the cohesive tractions to account for smooth crack opening.

More recently, de Borst *et al.* (2004c) proposed a proper representation of the discrete character of cohesive zone formulations by the so-called cohesive crack segments, which avoided any mesh bias by exploiting the partition of unity property of finite element shape functions.

5.2 COHESIVE CRACKS

Analytical solutions for cracks based on the theory of elasticity leads to singular (infinite) strain and stress fields at the crack tip. Such an infinite stress cannot be tolerated by any material and the material has to undergo nonlinear behaviour in the vicinity of the crack. This nonlinear behaviour increases the strength of material to cracking and dissipation of energy. The cohesive crack model is one of the available approaches for solving this problem.

Effects of nonlinear behaviour around a crack tip can be classified into two classes. In the first class, all nonlinear behaviour of the material is utilised within a so-called fracture process zone (FPZ) on the crack surface (Fig. 5.1). Interactions between the aggregates and crack surfaces prevent further opening of the crack. The rest of the model is assumed to behave elastically. The point with zero displacement is called the fictitious or mathematical crack tip, while the physical crack tip is the point where the crack surface tractions vanish. According to Fig. 5.2, a variable traction field governs the crack face interactions.

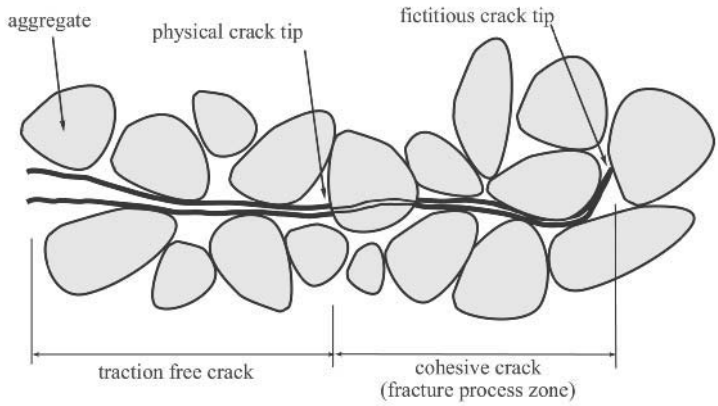

Figure 5.1 Interface cohesive behaviour due to aggregate interlocking, frictional contact, etc.

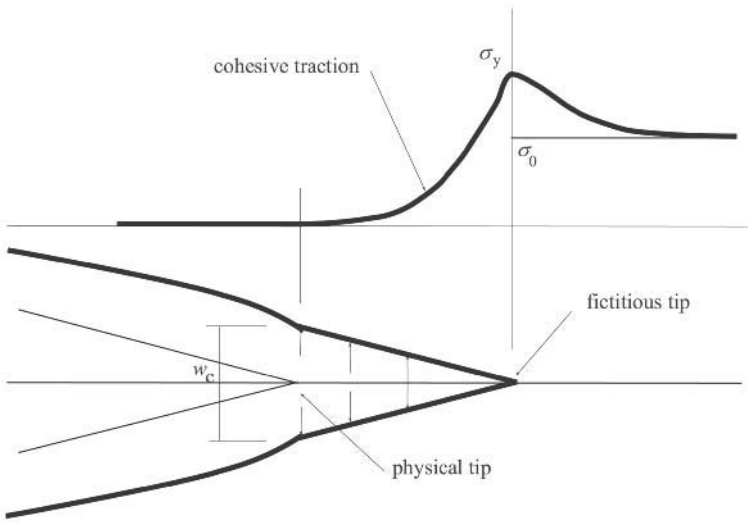

Figure 5.2 Fracture process zone for modelling a cohesive crack.

The second approach, called the smeared crack model, assumes that the plastic deformations are distributed in a specific domain around the crack tip. The method assumes that any discontinuity caused by the presence of a crack within a finite element, can be simulated as a smeared (distributed) strain field over the element. The next step is to set up a definition for the stress–strain relationship which leads to the evaluation of an equivalent stiffness matrix.

In addition to the nonlinear behaviour of a material, other effects may also contribute to the cohesive behaviour, such as aggregate locking, frictional contact, fibre bridging, atomic bonds and dislocation effects.

The main characteristic of a cohesive crack model is the removal of singularity at crack tips. As a result, the stress intensity factor at the crack tip should vanish, which implies that the crack closes smoothly. This condition is also called the zero stress intensity factor. Owing to the fact that the mode II stress intensity factor is typically negligible compared to the mode I stress intensity factor, only the mode I stress intensity factor can be taken into account:

$$K_{\mathrm{I}} = 0 \tag{5.1}$$

This condition is caused by the superposition of two independent stress fields; singular crack tip stress field and non-singular crack surface traction field:

$$K_{\mathrm{I}}^{\mathrm{crack}} + K_{\mathrm{I}}^{\mathrm{cohesion}} = 0 \tag{5.2}$$

The direction of a mixed mode crack growth can be determined by using the mode I and II stress intensity factors K_{I} and K_{II}:

$$\theta = 2\tan^{-1}\frac{1}{4}\left(\frac{K_{\mathrm{I}}}{K_{\mathrm{II}}} \pm \sqrt{\frac{K_{\mathrm{I}}^2}{K_{\mathrm{II}}^2} + 8}\right) \tag{5.3}$$

In an alternative approach, a stress condition can be adopted (Zi and Belytschko 2003). The zero stress intensity factor implies that the stress at the crack tip should be finite. As a result, the stress projection in the normal direction $\mathbf{n}$ of the crack can be assumed to equal the tensile strength of the material:

$$\boldsymbol{\sigma}_{\mathrm{tip}} = f_{\mathrm{t}} \tag{5.4}$$

where $\boldsymbol{\sigma}_{\mathrm{tip}}$ is the stress at the crack tip and f_{t} is the tensile strength of material. The crack propagation is then assumed to be in the direction perpendicular to the direction of the maximum principle stress.

Whilst the first criterion can be efficiently calculated by means of the domain integral technique, the second criterion is simpler and can be implemented readily.

5.2.1 Cohesive crack models

Several models have been proposed to simulate the complex behaviour of a cohesive crack and to simplify it into a more computationally friendly model. Barrenblatt (1959), Dugdale (1960), Willis (1967), Wunk (1974) and Hillerborg *et al.* (1976) were among the first to propose models for simulating the cohesive behaviour. Hong *et al.* (2003) presented an analytical approach defined within an inverse method to extract cohesive zone laws from elastic far fields using a field projection method.

Another formulation for cohesive interface element was proposed by Chowdhury and Narasimhan (2000), while de Borst *et al.* (2004c) studied the delaminaion buckling phenomena for crossing discontinuities. For a detailed review of other available models see Bazant and Planas (1997).

5.2.1.1 *Dugdale uniform traction model*

Dugdale proposed a simple uniform traction equal to the yield stress within the fracture process zone (Fig. 5.3a). The length of the process zone is determined to satisfy Eq. (5.2) and to avoid stress singularity at the crack tip.

Tractions are independent of the crack length in the Dugdale model and the model is more suited to ductile materials.

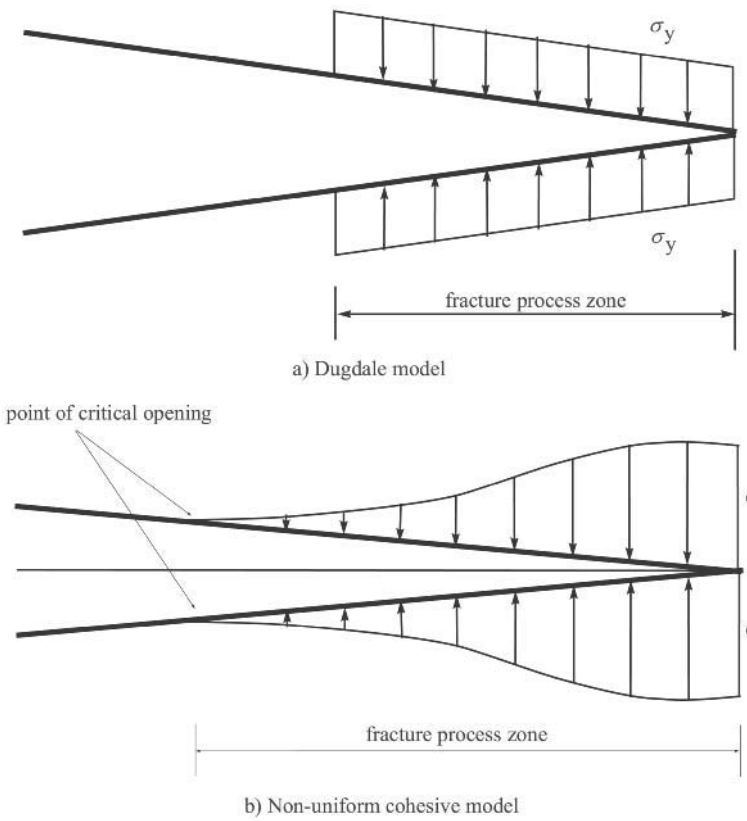

Figure 5.3 Cohesive crack models.

5.2.1.2 *Non-uniform traction models*

Owing to the fact that the material strength is reduced by an increase in crack opening, a number of non-uniform traction models have been proposed over the years. Their main difference is in how to define non-uniformity, but they share the same concept of softening behaviour whereby the traction has the maximum intensity at the crack tip and a minimum value (usually zero) at the point of critical crack opening, as illustrated in Fig. 5.3b.

Fig. 5.4 illustrates different non-uniform models in terms of traction-opening curves. They include linear, bilinear and exponential models in comparison to the uniform Dugdale model. Non-uniform models require extra experimentally determined material parameters to define their associated traction-opening curves.

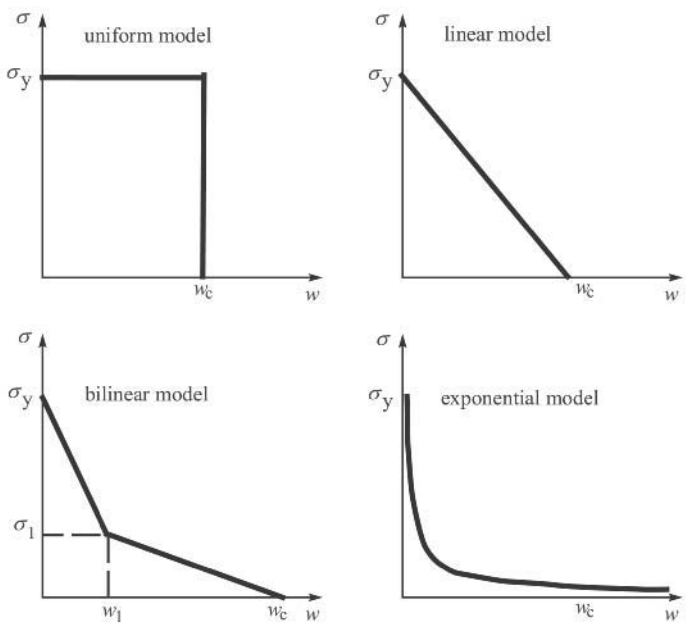

Figure 5.4 Non-uniform models in comparison to the uniform model.

5.2.2 Numerical models for cohesive cracks

Similar to other crack propagation problems, various methods have been successfully adopted for simulating the behaviour of cohesive cracks. Analytical, semi-analytical and numerical approaches, such as the boundary integral method, the boundary element method, the finite element method and recently a number of meshless methods, have been successfully used for modelling cohesive cracks; each one provide advantages and drawbacks in handling certain parts of the simulation.

In this book, the emphasis is only put on the finite element method as a basis for its extension into the extended finite element method. In the FEM, simulation of cohesive crack is performed by one of the following methods.

5.2.2.1 *Discrete inter-element crack model*

In this approach, cracks can only be defined along the finite element edges. As a result, a strong discontinuity is directly assumed in the displacement field. The cohesive behaviour is simulated by inter-element nonlinear springs/tractions, as depicted in Fig. 5.5.

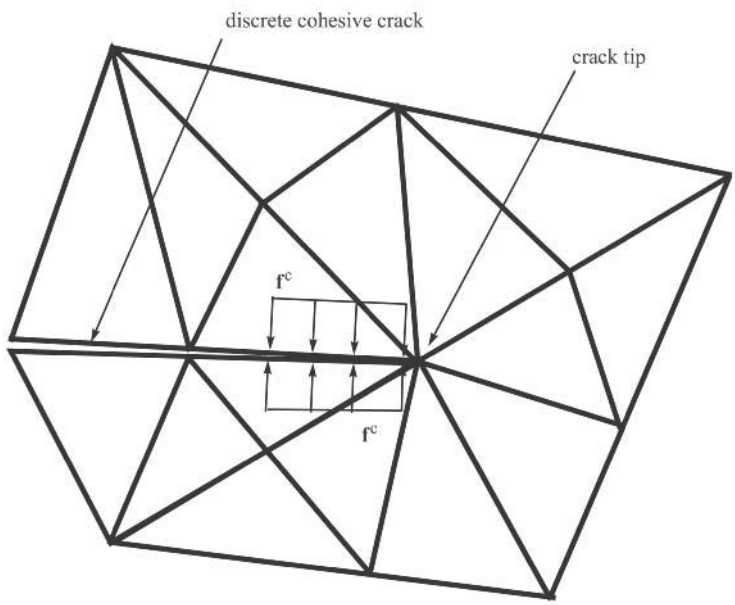

Figure 5.5 Discrete inter-element crack model.

The model is extremely simple for predefined crack paths along the element edges. It becomes rather difficult for general crack paths as it requires a remeshing of the model. Another major drawback of the model is its higher potential of mesh dependency (Mohammadi 2003).

5.2.2.2 *Smeared crack model*

In this model, the discontinuity caused by a discrete crack within an element, is simulated by a distributed (smeared) equivalent strain field over the entire domain of the element, as depicted in Fig. 5.6. The method uses a traction-opening law to derive the equivalent

stiffness matrix for each cracked element. The main advantage of the method is that it does not require any remeshing in the process of crack propagation.

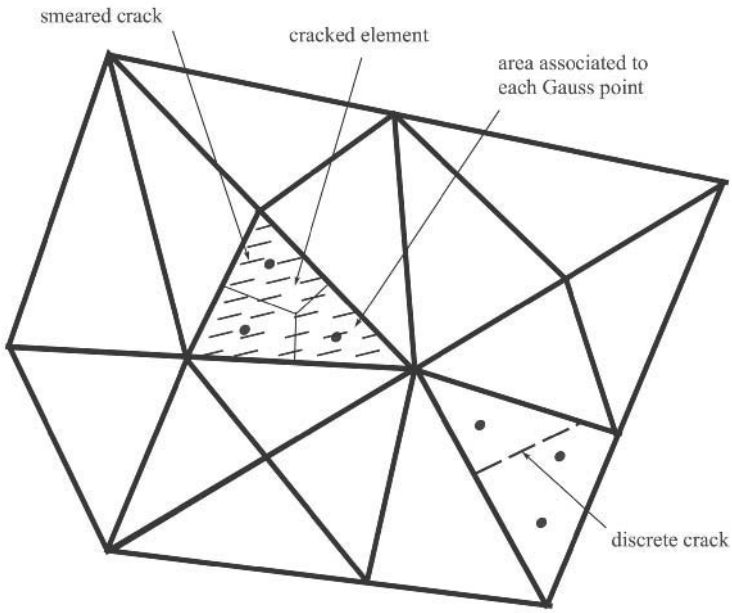

Figure 5.6 Discrete and smeared crack models.

5.2.2.3 *Discrete cracked element model*

Fig. 5.7 illustrates a model in which the crack path is through the middle of a finite element. In this model, a local remeshing technique combined with adaptivity techniques is required to create a new mesh by splitting the cracked element and dividing adjacent elements to ensure compatibility of the neighbouring finite elements. Adaptivity techniques are applied to compute the state variables within the newly created elements from the state variables of their parent elements. Combined finite/discrete element procedures have been successfully applied to these classes of problems and may take into account the effects of post-cracking interactions including fully nonlinear frictional behaviour (Mohammadi 2003).

The procedure usually avoids remeshing of the whole model by gradual local remeshing techniques according to the advancement of the crack. It may require, however, a global remeshing if the mesh becomes excessively distorted or includes elements with bad aspect ratios as a result of multiple cracking.

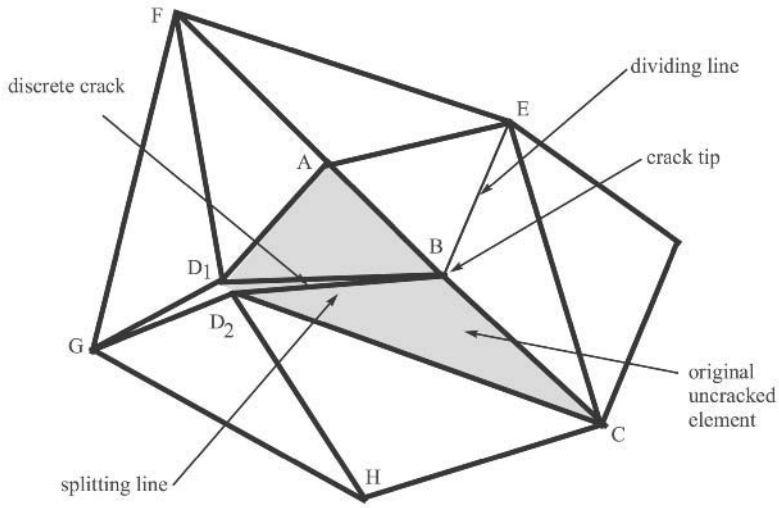

Figure 5.7 Discrete cracked element model.

5.2.2.4 *Enriched elements model*

Fig. 5.8 illustrates a model in which the crack path is through the middle of a finite element. In this model, the discontinuous displacement field within a finite element is simulated by a special set of shape functions. The main advantage of the method is that it does not require any remeshing in the process of crack propagation. Partition of unity finite element method and XFEM are among this set of models.

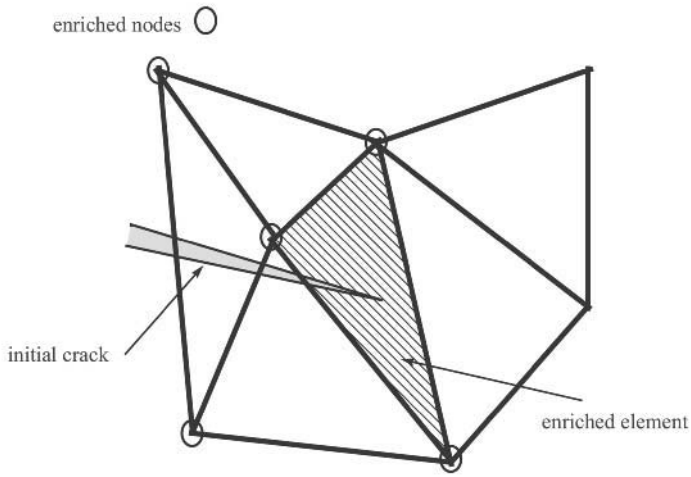

Figure 5.8 Enriched elements model.

5.2.3 Crack propagation criteria

The Rankine maximum tensile stress criterion is usually adopted to govern the behaviour of the mathematical crack tip in a cohesive crack model.

$$\boldsymbol{\sigma} = \max\{\sigma_{11}, \sigma_{22}, \sigma_{33}\} \tag{5.5}$$

In order to avoid the inaccuracy of direct evaluation of the local strain field at the crack tip, a non-local weighted approach is adopted to determine the stress field at the crack tip from the stress at neighbour Gauss points (Wells and Sluys 2001):

$$\boldsymbol{\sigma} = \sum_{g=1}^{ng} W_g^{\mathrm{r}} \boldsymbol{\sigma}_g \tag{5.6}$$

with the radial weight function W_g^{r} defined as:

$$W_g^{\mathrm{r}} = \frac{1}{(2\pi)^{2/3} l_c^3} \exp\left(-\frac{r_g^2}{2l_c^2}\right) \tag{5.7}$$

where $\boldsymbol{\sigma}_g$ is the stress tensor at a Gauss point g with a distance r_g from the crack tip and l_c is a characteristic length, assumed to be equal to the average element size. Fig. 5.9 illustrates the way the stress tensor at a crack tip can be evaluated from the stress tensors at Gauss points of neighbouring elements.

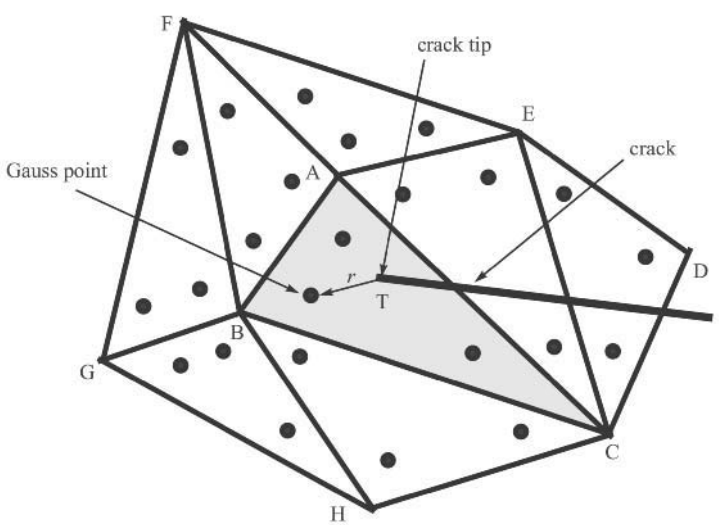

Figure 5.9 Non-local evaluation of stress at the crack tip.

Several studies in recent decades have shown that adoption of a non-local stress evaluation may drastically change the local path of the crack propagation (Tvergaard and Hutchinson 1992, Saleh and Aliabadi 1995, Wells and Sluys 2001, Dumstorff and Meschke 2003).

5.2.4 Snap-back behaviour

Snap-back phenomenon is one of the commonly observed response modes while investigating the equilibrium path of crack propagation. In a snap-back mode, the reduction in material stiffness caused by the crack propagation is smaller than the reduction in critical applied load.

Fig. 5.10 illustrates a simple description of snap-back behaviour. It is obvious that such a response cannot be simulated by using a load control or displacement control approach alone. Instead other methods such as the arc length method are usually preferred. Alternative methods in fracture mechanics are the so-called crack length control and the fracture process zone control.

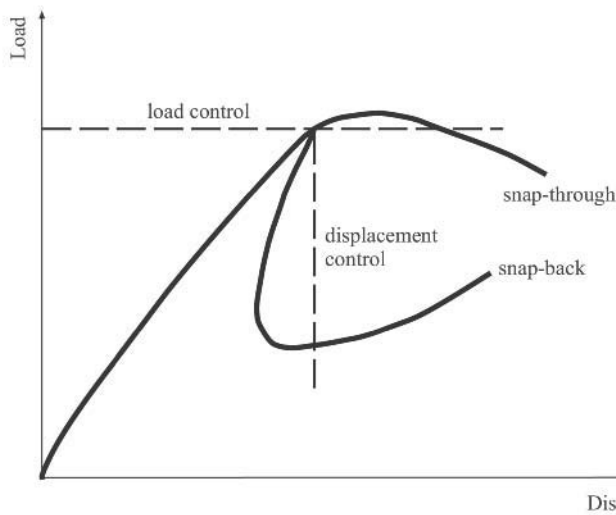

Figure 5.10 Snap-back and snap-through behaviours.

The method of crack length control is based on the superposition of two independent analyses of the model subject to external and internal loads. The procedure may be summarised as:

1. Initial estimates of the crack profile and fracture process zone are assumed. The results at the end of previous iteration are usually considered.
2. Calculation of cohesive stress according to the assumed crack profile.
3. Solving the model for the cohesive stress loading.

$$\mathbf{K}\mathbf{u}^{\text{coh}} = \mathbf{f}^{\text{coh}} \tag{5.8}$$

4. Solving the model for external loading.

$$\mathbf{K}\mathbf{u}^{\text{ext}} = \mathbf{f}^{\text{ext}} \tag{5.9}$$

5. Satisfying the maximum stress condition at the crack tip.

$$\boldsymbol{\sigma} = \alpha \boldsymbol{\sigma}^{\text{ext}} + \boldsymbol{\sigma}^{\text{coh}} \tag{5.10}$$

6. Solving for the nodal displacements.

$$\mathbf{K}\mathbf{u} = \alpha \mathbf{f}^{\text{ext}} + \mathbf{f}^{\text{coh}} \tag{5.11}$$

7. Evaluation of the loading coefficient from the crack propagation condition.

$$\boldsymbol{\sigma}^{\text{tip}} = f_{\text{t}} \tag{5.12}$$

8. Control of the fracture process zone and checking it against the initial estimate.
9. Repeat the procedure from step 2, if the solution has not converged.

5.2.5 Griffith criterion for cohesive crack

Assume a plate, containing a cohesive crack, is subjected to normal and tangential traction loadings, as illustrated in Fig. 5.11.

The J contour integral can be defined as:

$$J = \int_{\Gamma} \left(W_{\text{s}} \mathbf{n} - \mathbf{t} \frac{\partial \mathbf{u}}{\partial x} \right) \text{d}\Gamma \tag{5.13}$$

Path independency of the J integral allows for evaluation of J along the crack surfaces:

$$J_{\Gamma_{\text{c}}} = -\int_{\Gamma_{\text{c}}} \mathbf{f}^{\text{c}} \frac{\partial \mathbf{u}}{\partial x} \text{d}\Gamma \tag{5.14}$$

where Γ_{c} identifies the fracture process zone (FPZ), and Eq. (5.14) can be expressed as:

$$J_{\Gamma_{\text{c}}} = \int_{\Gamma_{\text{c}}} \left(\boldsymbol{\sigma}_{\text{c}} \frac{\partial u_y}{\partial x} \right) \text{d}\Gamma + \int_{\Gamma_{\text{c}}} \left(\boldsymbol{\tau}_{\text{c}} \frac{\partial u_x}{\partial x} \right) \text{d}\Gamma \tag{5.15}$$

Assuming that differentiation and integration can commute, Eq. (5.15) is transformed into (Saouma 2000):

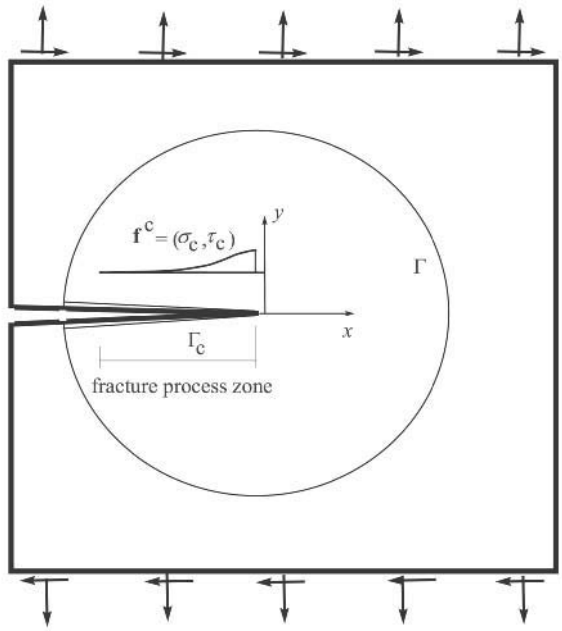

Figure 5.11 The contour *J* integral and Griffith criterion.

$$J_{\Gamma_{\mathrm{c}}} = \int_{\Gamma_{\mathrm{c}}} \left[\frac{\mathrm{d}}{\mathrm{d}x} \underbrace{\left(\int_0^{u_y} \boldsymbol{\sigma}_{\mathrm{c}} \mathrm{d}u_y \right)}_{\substack{\text{surface energy} \\ \text{dissipated in} \\ \text{mode I}}} \right] \mathrm{d}x + \int_{\Gamma_{\mathrm{c}}} \left[\frac{\mathrm{d}}{\mathrm{d}x} \underbrace{\left(\int_0^{u_x} \boldsymbol{\tau}_{\mathrm{c}} \mathrm{d}u_x \right)}_{\substack{\text{surface energy} \\ \text{dissipated in} \\ \text{mode II}}} \right] \mathrm{d}x \tag{5.16}$$

For the case of pure mode I and mode II, Eq. (5.16) is further simplified:

$$J_{\Gamma_{\mathrm{c}}}^{\mathrm{I}} = \int_{\Gamma_{\mathrm{c}}} \left[\frac{\mathrm{d}}{\mathrm{d}x} \left(\int_0^{u_y} \boldsymbol{\sigma}_{\mathrm{c}} \mathrm{d}u_y \right) \right] \mathrm{d}x = \int_0^{w_y} \boldsymbol{\sigma}_{\mathrm{c}}(u_y) \mathrm{d}u_y \tag{5.17}$$

$$J_{\Gamma_{\mathrm{c}}}^{\mathrm{II}} = \int_{\Gamma_{\mathrm{c}}} \left[\frac{\mathrm{d}}{\mathrm{d}x} \left(\int_0^{u_x} \boldsymbol{\tau}_{\mathrm{c}} \mathrm{d}u_x \right) \right] \mathrm{d}x = \int_0^{w_x} \boldsymbol{\tau}_{\mathrm{c}}(u_x) \mathrm{d}u_x \tag{5.18}$$

where w_y and w_x are the critical crack opening and sliding, respectively, for which normal and tangential stresses can no longer be transferred across the crack.

5.2.6 Cohesive crack model

A cohesive crack resists any relative displacement between crack faces. Referring to Fig. 5.12, the relative displacement can be decomposed into normal and tangential components $\delta \mathbf{u}_{\mathrm{n}}, \delta \mathbf{u}_{\mathrm{t}}$, respectively.

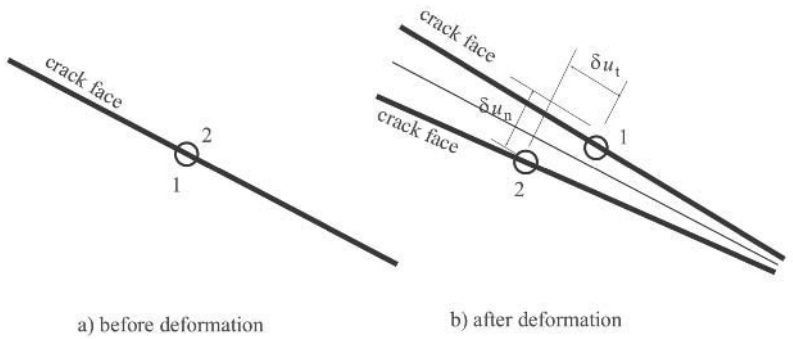

Figure 5.12 A cohesive crack before and after deformaion.

Interface forces between the crack surfaces can be defined as:

$$\mathbf{f}_{\mathrm{n}}^{\mathrm{c}} = \mathbf{f}_{\mathrm{n}}^{\mathrm{c}}\left(\delta \mathbf{u}_{\mathrm{n}}\right) \tag{5.19}$$

$$\mathbf{f}_{\mathrm{t}}^{\mathrm{n}} = \mathbf{f}_{\mathrm{t}}^{\mathrm{n}}\left(\delta \mathbf{u}_{\mathrm{n}}, \delta \mathbf{u}_{\mathrm{t}}\right) \tag{5.20}$$

It is important to note that the tangential force is a function of both the normal opening and the tangential sliding of crack faces. Any further opening of the crack reduces the aggregate interlocking and, therefore, reduces the interaction forces between crack faces.

5.3 XFEM FOR COHESIVE CRACKS

5.3.1 Enrichment functions

In the extended finite element method, approximation of a discontinuous displacement field is based on the definition of specially designed shape functions by the use of enrichment functions. The method operates on additional virtual degrees of freedom for the definition of the crack boundary and approximation of the displacement field.

Earlier models used a simple enrichment function in the form of:

$$N_i^h = \begin{cases} N_i - 1 & \mathbf{x} \in \Omega_i \\ N_i & \mathbf{x} \notin \Omega_i \end{cases} \tag{5.21}$$

where N_i is the conventional finite element shape function and Ω_i is part of the element in between the crack and node i, as illustrated in Fig. 5.13a. Fig. 5.13b shows how this jump enrichment can affect the shape functions for a simple one-dimensional case.

A problem with this type of jump function is that it provides similar strain fields (derivatives of the displacement field) in both sides of the crack. This is in contrast to the physical observations that both segments of a cracked element behave independently. Another drawback is the lower number of degrees of freedom required by this

approximation than other recently available techniques. This may directly affect the quality of approximation field and the crack analysis.

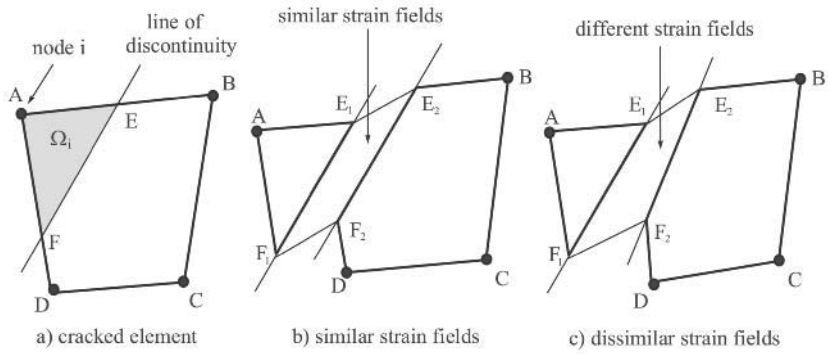

Figure 5.13 An element cut across by a crack.

The following Heaviside/jump function can also be used:

$$N_i^h = H_i(\mathbf{x})N_i(\mathbf{x}) \tag{5.22}$$

with

$$H_i(\mathbf{x}) = \begin{cases} 0 & \mathbf{x} \in \Omega_i \\ 1 & \mathbf{x} \notin \Omega_i \end{cases} \tag{5.23}$$

The present definition of the jump function allows for the discontinuity to be modelled across the crack over the points along the crack surface. The value of the modified shape function N_i^h is zero at all nodes and edges that do not intersect with the crack. This is important in satisfying the inter-element continuity requirements.

XFEM using classical jump functions applies the enrichment onto the nodal points. As a result, elements containing an enriched node are affected by the enrichment degrees of freedom. In contrast, the present approach only affects the element containing a crack, and does not directly influence other elements, even if they share a common node with the enriched element. Fig. 5.14 compares the effect of different definitions of the jump function on the final shape function for a simple one-dimensional problem.

Other effects include the influence of external forces on the enrichment degrees of freedom in classical jump functions, while the present approach avoids these direct interaction effects.

Application of the mentioned jump function on a quadrilateral element may lead to a discontinuous field as depicted in Fig. 5.13c. The deformation field includes all potential displacement fields independently for both sides of the crack. Strain fields also remain independent in both sides of the crack.

Fig. 5.15 illustrates the procedure for selection of nodes for enrichment. If a crack passes an edge of an element, nodes associated with that edge are selected for enrichment. Even if the crack tip locates on an edge, the corresponding nodes are not enriched.

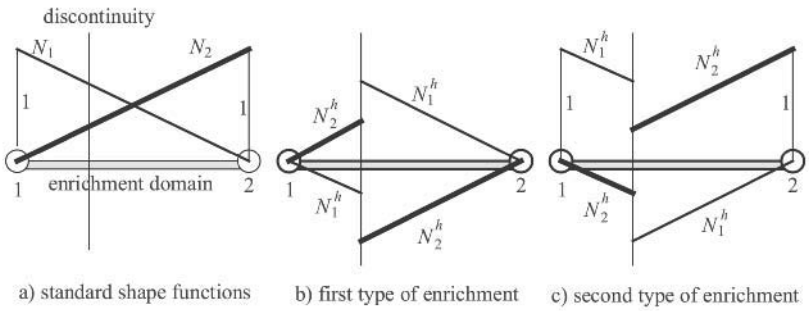

Figure 5.14 Comparison of shape functions based on different definitions of the jump function.

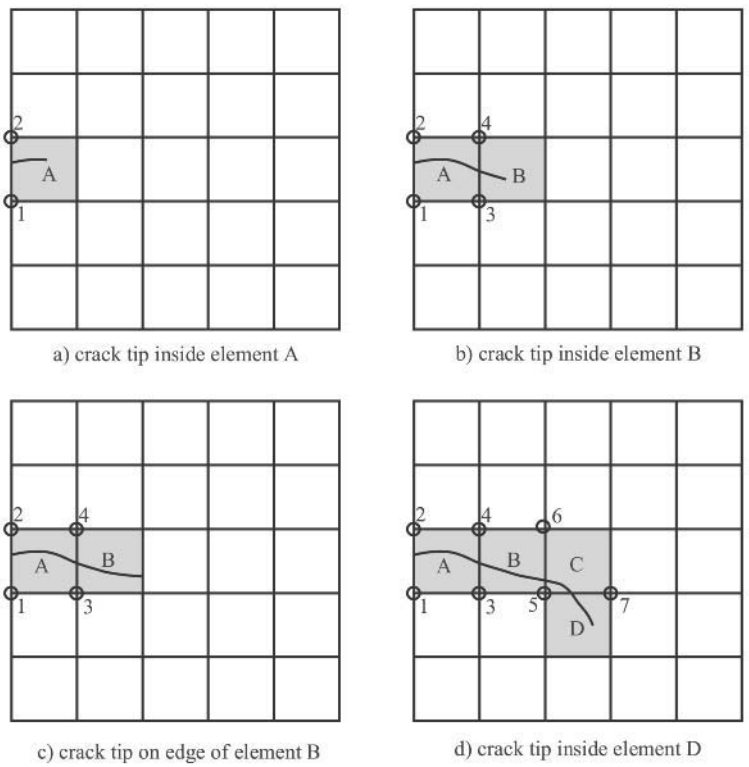

Figure 5.15 Enrichment nodes at different stages of crack propagation.

The present formulation adds two enrichment degrees of freedom to an element per any enriched node. As a result, for a quadrilateral element on the path of a crack, sixteen degrees of freedom including 8 classical DOFs and 8 enriched DOFs are assigned.

Efficiency of XFEM for crack propagation analysis can be simply explained from Fig. 5.15. At each stage of the propagation, nodes on edges cut by the crack path are enriched. Special attention is required because a potential source of instability and divergence is when a crack path passes along the finite element edges.

It should be noted that the procedure discussed in this section is only related to the Heaviside enrichment. Crack tip enrichments, if required, are applied to all nodes of the element that contains the crack tip. The discontinuous crack tip enrichment functions discussed in Section 3.5.1, however, can no longer be used for cohesive crack modelling, as they do not represent the displacement field around a cohesive crack tip.

5.3.2 Governing equations

A body in the state of equilibrium and subjected to body forces is assumed. The boundary conditions include the external traction and displacement conditions, as depicted in Fig. 5.16.

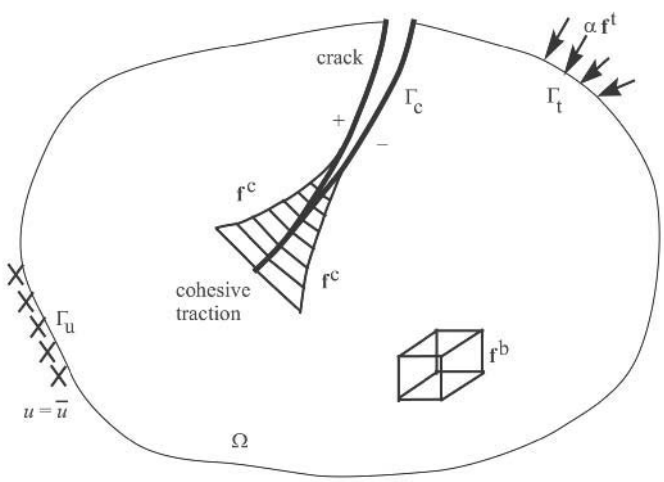

Figure 5.16 Deformation of a quadrilateral element with a jump function.

The virtual work of the boundary value problem can be defined as:

$$W^{\text{int}} = W^{\text{ext}} \tag{5.24}$$

or

$$\int_{\Omega} \boldsymbol{\sigma} \cdot \delta \boldsymbol{\varepsilon} \; \mathrm{d}\Omega = \int_{\Omega} \mathbf{f}^{\mathrm{b}} \cdot \delta \mathbf{u} \; \mathrm{d}\Omega + \int_{\Gamma_{\mathrm{t}}} \alpha \mathbf{f}^{\mathrm{t}} \cdot \delta \mathbf{u} \; \mathrm{d}\Gamma \tag{5.25}$$

where $\mathbf{f}^{\mathrm{b}}$ and $\alpha\mathbf{f}^{\mathrm{t}}$ are the body force and external traction vectors, respectively, and $\boldsymbol{\sigma}$ is the stress tensor; α is the load factor which controls the solution increments. In fact, both load and displacement controls can be activated at the same time.

Now, consider that the body also includes a cohesive crack with tractions $\mathbf{f}^{\mathrm{c}}$ along the fracture process zone Γ_{c} and $\mathbf{f}^{\mathrm{c}}$ is assumed to be functions of the crack opening w_{c}. The weak form of the equilibrium equation can then be modified to (Zi and Belytschko 2003):

$$W^{\mathrm{int}} = W^{\mathrm{ext}} + W^{\mathrm{coh}} \tag{5.26}$$

or

$$\int_{\Omega} \boldsymbol{\sigma} \cdot \delta\boldsymbol{\varepsilon} \, \mathrm{d}\Omega = \int_{\Omega} \mathbf{f}^{\mathrm{b}} \cdot \delta\mathbf{u} \, \mathrm{d}\Omega + \int_{\Gamma_{\mathrm{t}}} \alpha\mathbf{f}^{\mathrm{t}} \cdot \delta\mathbf{u} \, \mathrm{d}\Gamma + \int_{\Gamma_{\mathrm{c}}} \mathbf{f}^{\mathrm{c}} \cdot \left(\delta\mathbf{u}^{+} - \delta\mathbf{u}^{-}\right) \mathrm{d}\Gamma \tag{5.27}$$

Discretization of Eq. (5.27) using the XFEM procedure results in:

$$\mathbf{K}\mathbf{u} = \mathbf{f}^{\mathrm{ext}} + \mathbf{f}^{\mathrm{coh}} \tag{5.28}$$

with

$$\mathbf{K} = \int_{\Omega} \mathbf{B}^{\mathrm{T}} \mathbf{D} \mathbf{B} \, \mathrm{d}\Omega \tag{5.29}$$

$$\mathbf{f}^{\mathrm{ext}} = \alpha \int_{\Gamma_{\mathrm{t}}} N^{\mathrm{T}} \mathbf{f}^{\mathrm{t}} \mathrm{d}\Gamma + \int_{\Omega} N^{\mathrm{T}} \mathbf{f}^{\mathrm{b}} \mathrm{d}\Omega \tag{5.30}$$

$$\mathbf{f}^{\mathrm{coh}} = -2 \int_{\Gamma_{\mathrm{c}}} N^{\mathrm{T}} \mathbf{f}^{\mathrm{c}} \mathrm{d}\Gamma = -2 \int_{\Gamma_{\mathrm{c}}} N^{\mathrm{T}} \mathbf{T}^{\mathrm{c}} \mathbf{n} \, \mathrm{d}\Gamma \tag{5.31}$$

where $\mathbf{B}$ is the strain–displacement matrix, and $\mathbf{T}^{\mathrm{c}}(w_{\mathrm{c}})$ is a cohesive softening law relating the crack surface normal traction $\mathbf{f}^{\mathrm{c}}$ to the crack opening w_{c}.

The solution should simultaneously satisfy the equilibrium condition and a cohesive criterion such as the cohesive stress condition. The procedure for a given cohesive crack can be summarised as the following (Carpinteri and Colombo 1989):

1. An initial value of the load factor α is obtained from the condition that the stress at the notch tip should be equal to the strength f_{t}.
2. The stiffness matrix $\mathbf{K}$ is constructed.

$$\mathbf{K} = \int_{\Omega} \mathbf{B}^{\mathrm{T}} \mathbf{D} \mathbf{B} \, \mathrm{d}\Omega \tag{5.32}$$

3. The derivative of $\mathbf{f}^{\mathrm{coh}}$ with respect to nodal displacements u is calculated (Zi and Belytschko 2003):

$$\frac{\partial \mathbf{f}^{\mathrm{coh}}}{\partial \mathbf{u}} = -2 \int_{\Gamma_{\mathrm{c}}} \frac{\partial \mathbf{T}^{\mathrm{c}}(w_{\mathrm{c}})}{\partial w_{\mathrm{c}}} N^{\mathrm{T}} \cdot \mathbf{n} \cdot \mathbf{n}^{\mathrm{T}} \cdot N \, \mathrm{d}\Gamma \tag{5.33}$$

4. The Jacobian of the Newton–Raphson method, its residual and the increments are calculated.

$$\Lambda = \begin{bmatrix} \mathbf{K} - \dfrac{\partial \mathbf{f}^{\text{coh}}}{\partial \mathbf{u}} & -\mathbf{f}^{\text{ext}} \\ \dfrac{\partial \boldsymbol{\sigma}_{\text{t}}^{\text{tip}}}{\partial \mathbf{u}} & 0 \end{bmatrix} \tag{5.34}$$

$$\mathbf{r} = \begin{Bmatrix} \mathbf{K} \cdot \mathbf{u} - \mathbf{f}^{\text{ext}} - \mathbf{f}^{\text{coh}} \\ \boldsymbol{\sigma}_{\text{t}}^{\text{tip}} - f_{\text{t}} \end{Bmatrix} \tag{5.35}$$

where $\boldsymbol{\sigma}_{\text{t}}^{\text{tip}}$ is the normal tensile stress at the crack tip and f_{t} is the material tensile strength. The second row of Eq. (5.35) can be replaced by other sophisticated material models, if required.

5. Step 3 is iterated until $\mathbf{u}$ and α converge. The incremental solution for iteration i reads,

$$\begin{Bmatrix} \Delta \mathbf{u} \\ \Delta \alpha \end{Bmatrix}_{(i)} = -\left(\Lambda^{-1}\right)_{(i-1)} \cdot \mathbf{r}_{(i-1)} \tag{5.36}$$

6. The direction of the crack propagation and the crack extension is calculated.
7. The geometry of the model (for classical finite element method) is updated.

5.3.3 XFEM discretization

Recalling the XFEM approximation:

$$\mathbf{u}(\mathbf{x}) = \mathbf{N}(\mathbf{x})\mathbf{u} + \mathbf{N}(\mathbf{x})\left(H(\mathbf{x})\mathbf{a}\right) \tag{5.37}$$

where $\mathbf{u}$ and $\mathbf{a}$ are the real and enrichment degrees of freedom. The strain tensor can be defined from the derivative of $\mathbf{u}(\mathbf{x})$:

$$\boldsymbol{\varepsilon}(\mathbf{x}) = \mathbf{B}^{\mathbf{u}}(\mathbf{x})\mathbf{u} + \mathbf{B}^{\mathbf{u}}(\mathbf{x})\left(H(\mathbf{x})\mathbf{a}\right) + \mathbf{N}(\mathbf{x})\left(\delta(\mathbf{x})\mathbf{a}\right) \tag{5.38}$$

where δ is the Dirac delta function. Alternatively, from Section 3.7.2,

$$\boldsymbol{\varepsilon}(\mathbf{x}) = \mathbf{B}(\mathbf{x})\mathbf{u}^{h}(\mathbf{x}) \tag{5.39}$$

with

$$\mathbf{u}^{h} = \{\mathbf{u} \quad \mathbf{a}\}^{\text{T}} \tag{5.40}$$

and

$$\mathbf{B} = \left[\mathbf{B^u} \quad \mathbf{B^a}\right] \tag{5.41}$$

$$\mathbf{B}_i^{\mathbf{u}} = \begin{bmatrix} N_{i,x} & 0 \\ 0 & N_{i,y} \\ N_{i,y} & N_{i,x} \end{bmatrix} \tag{5.42}$$

$$\mathbf{B}_i^{\mathbf{a}} = \begin{bmatrix} N_{i,x}H & 0 \\ 0 & N_{i,y}H \\ N_{i,y}H & N_{i,x}H \end{bmatrix} \tag{5.43}$$

Using variational principles and assuming independent real and enrichment degrees of freedom $\mathbf{u}$ and $\mathbf{a}$, lead to the following equations:

$$\mathbf{f}^{\text{ext}} = \mathbf{f}_{\mathbf{u}}^{\text{int}} \tag{5.44}$$

$$\mathbf{f}^{\text{coh}} = \mathbf{f}_{\mathbf{a}}^{\text{int}} \tag{5.45}$$

with

$$\mathbf{f}^{\text{ext}} = \int_{\Gamma_t} N^{\text{T}} \alpha \mathbf{f}^{\text{t}} \text{d}\Gamma \tag{5.46}$$

$$\mathbf{f}^{\text{int}} = \int_{\Omega} (\mathbf{B^u})^{\text{T}} \boldsymbol{\sigma} \, \text{d}\Omega \tag{5.47}$$

$$\mathbf{f}^{\text{coh}} = \int_{\Gamma_c} N^{\text{T}} \mathbf{f}^{\text{c}} \text{d}\Gamma \tag{5.48}$$

$$\mathbf{f}_{\mathbf{a}}^{\text{int}} = \int_{\Omega_{\text{enr}}} (\mathbf{B^a})^{\text{T}} \boldsymbol{\sigma} \, \text{d}\Omega \tag{5.49}$$

The final incremental form of the equilibrium equations (5.44)–(5.45) takes the form of:

$$\begin{bmatrix} \mathbf{K^{uu}} & \mathbf{K^{ua}} \\ \mathbf{K^{ua}} & \mathbf{K^{aa}} \end{bmatrix} \begin{Bmatrix} \Delta\mathbf{u} \\ \Delta\mathbf{a} \end{Bmatrix} = \begin{Bmatrix} \mathbf{f}^{\text{ext}} \\ \mathbf{f}^{\text{coh}} \end{Bmatrix} - \begin{Bmatrix} \mathbf{f}_{\mathbf{u}}^{\text{int}} \\ \mathbf{f}_{\mathbf{a}}^{\text{int}} \end{Bmatrix} \tag{5.50}$$

with

$$\mathbf{K^{uu}} = \int_{\Omega} (\mathbf{B^u})^{\text{T}} \mathbf{D} \mathbf{B^u} \text{d}\Omega \tag{5.51}$$

$$\mathbf{K^{ua}} = \int_{\Omega_{\text{enr}}} (\mathbf{B^a})^{\text{T}} \mathbf{D} \mathbf{B^u} \, \text{d}\Omega \tag{5.52}$$

$$\mathbf{K}^{\mathbf{aa}} = \int_{\Omega_{\text{enr}}} (\mathbf{B}^{\mathbf{a}})^{\mathrm{T}} \mathbf{D}\mathbf{B}^{\mathbf{a}} \mathrm{d}\Omega + \int_{\Gamma_{\mathrm{c}}} N^{\mathrm{T}} \mathbf{T}^{\mathrm{c}} N \, \mathrm{d}\Gamma \tag{5.53}$$

where $\mathbf{T}^{\mathrm{c}}(w_{\mathrm{c}})$ is determined from the cohesive crack behaviour and its derivative with respect to the crack opening. The cohesive behaviour has direct effect on both the stiffness matrix and the nodal force vector.

5.4 NUMERICAL SIMULATIONS

5.4.1 Mixed mode bending beam

Fig. 5.17 shows a beam subjected to an un-symmetric loading which generates a mixed mode crack propagation. Material properties are assumed as: $E = 3.5\times10^6$ kg/cm^2, $\nu = 0.2$ and $f_t = 300$ kg/cm^2 with a linear softening model for the cohesive behaviour. Crack surfaces are assumed frictionless.

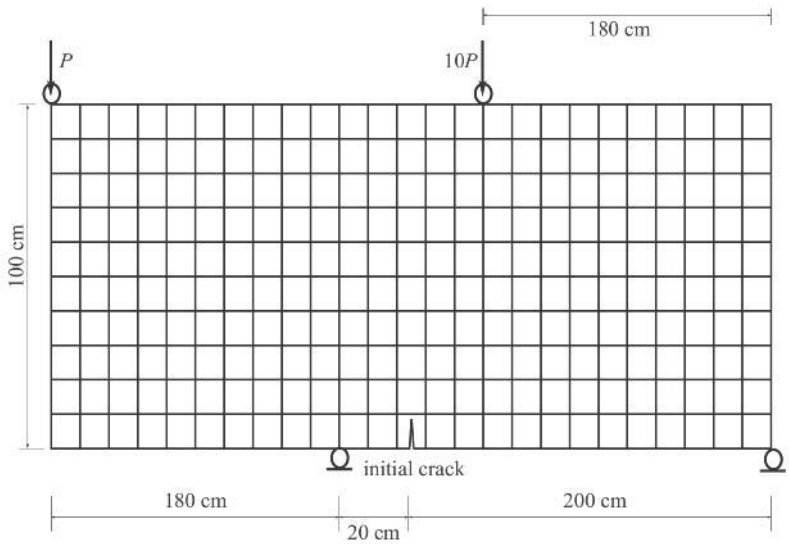

Figure 5.17 Geometry of the beam for mixed mode analysis.

Fig. 5.18 compares the crack propagation path predicted by XFEM with the results reported by (Wells and Sluys 2001). Again, close agreement is observed.

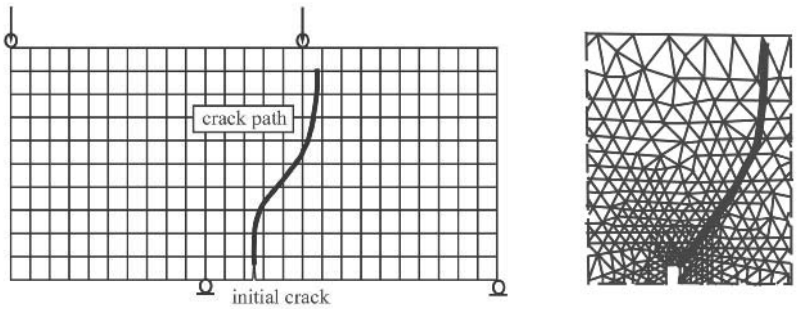

a) XFEM solution b) Reference results.

Figure 5.18 Crack propagation path obtained by XFEM (Forghani 2005) and the reference (Wells and Sluys 2001).

5.4.2 Four point bending beam

A four point bending beam, depicted in Fig. 5.19a, is considered. Material properties are assumed as: $E = 1.0\times10^6$ kg/cm^2, $\nu = 0.3$ and $f_t = 87.5$ kg/cm^2 with a linear softening model for the cohesive behaviour. The beam is subjected to a symmetric loading condition and behaves in pure mode I.

According to Fig. 5.20, the tensile stress in elements near the crack tip is decreased by the distance from the crack tip. The cohesive traction has practically vanished at a distance of four elements from the crack tip.

Fig. 5.21a compares the load–deflection curve obtained from the present XFEM analysis with the results of Carpinteri and Colombo (1989), which shows a close agreement. Also, the load–deflection behaviour for different values of the critical opening w_c is compared in Fig. 5.21b.

According to Fig. 5.21b, the snap-back behaviour is observed in all cases where the critical crack opening is a small value; an indication for a small value of critical energy of crack propagation. The response is, therefore, close to a linear elastic fracture mechanics (LEFM).

In contrast, for large values of the critical crack opening, the absorbed energy within the cohesive zone is relatively large, and the overall response is an elastoplastic behaviour. As a result, neither snap-back nor instability is expected to take place, and the LEFM cannot be used for simulation.

Any values in between the two limiting cases can be considered as a transition from the LEFM to the elastoplastic response, which gradually transforms the snap-back behaviour into a stable softening response.

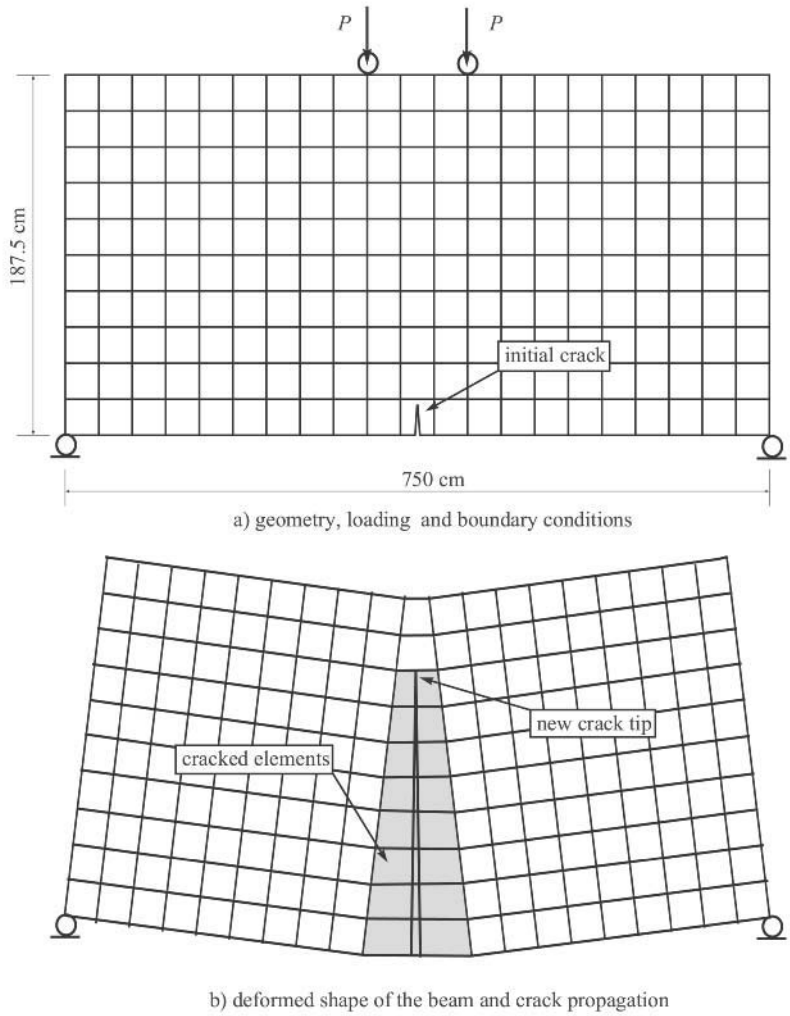

Figure 5.19 Geometry of the four point bending beam and its deformed shape (magnified by a factor of 10).

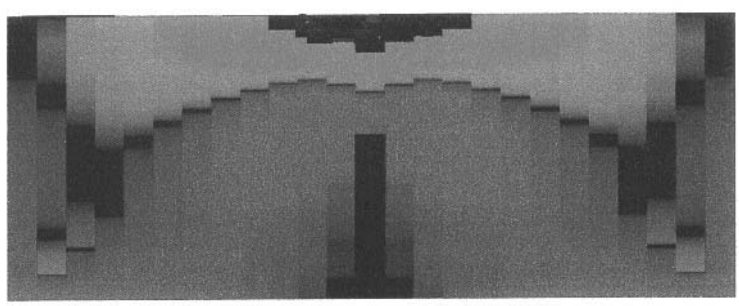

Figure 5.20 The σ_{xx} contour (Forghani 2005).

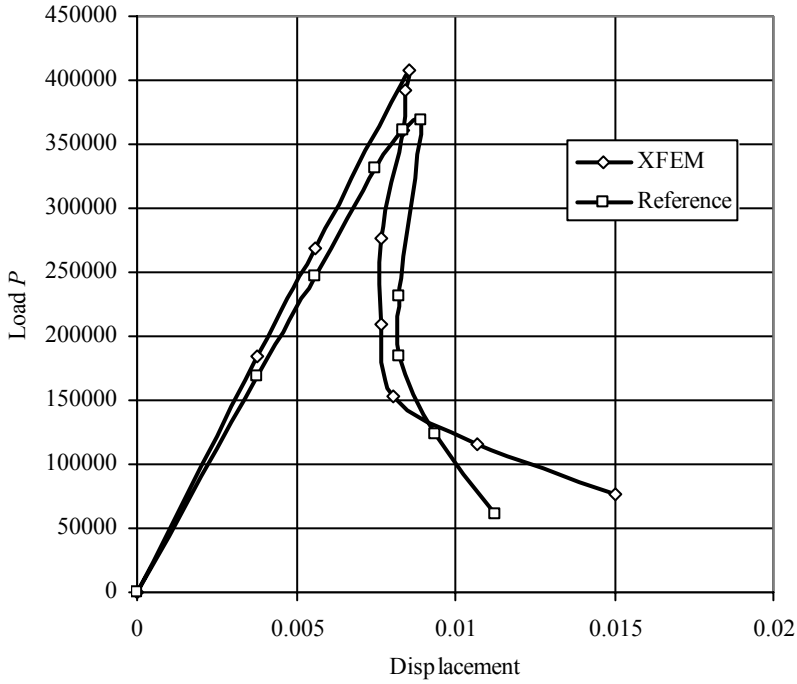

a) Comparison of XFEM with the reference results for $w_c = 0.023$

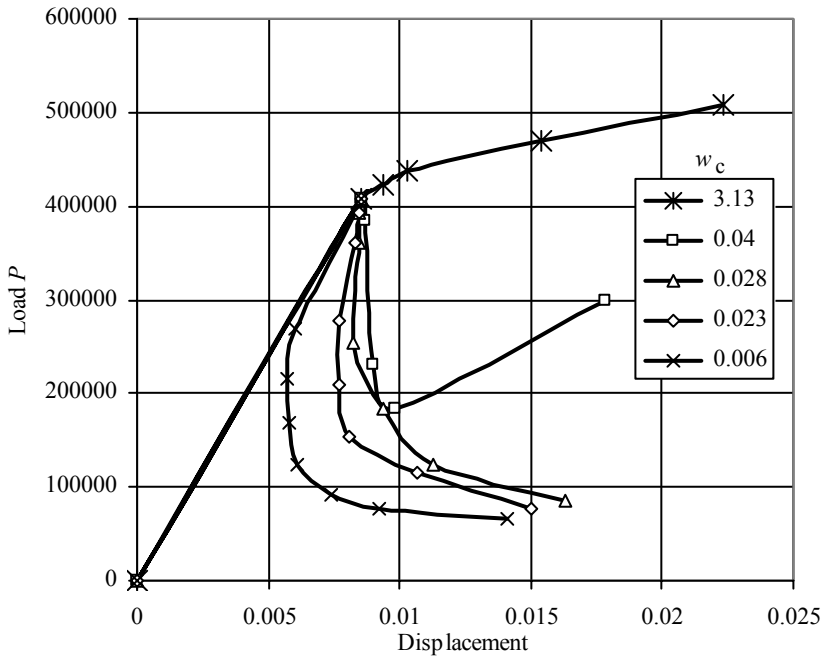

b) Load–deflection curves for different values of critical opening w_c

Figure 5.21 Comparison of XFEM and the reference (Carpinteri and Colombo 1989).

5.4.3 Double cantilever beam

The double cantilever beam has long been one of the main tests for determining the fracture mechanics parameters (Forghani 2005). Experimental tests induce a notch to facilitate crack extension in a straight path. Here, in contrast, there is no constraint to limit the crack extension path.

Fig. 5.22a depicts a $900 \times 330\,\text{cm}$ double cantilever beam with the following material properties: $E = 1.0 \times 10^6$ kg/cm^2, $\nu = 0.3$ and $f_t = 87.5$ kg/cm^2 with a linear softening model for the cohesive behaviour. The critical crack opening is set to $w_c = 0.004$ cm.

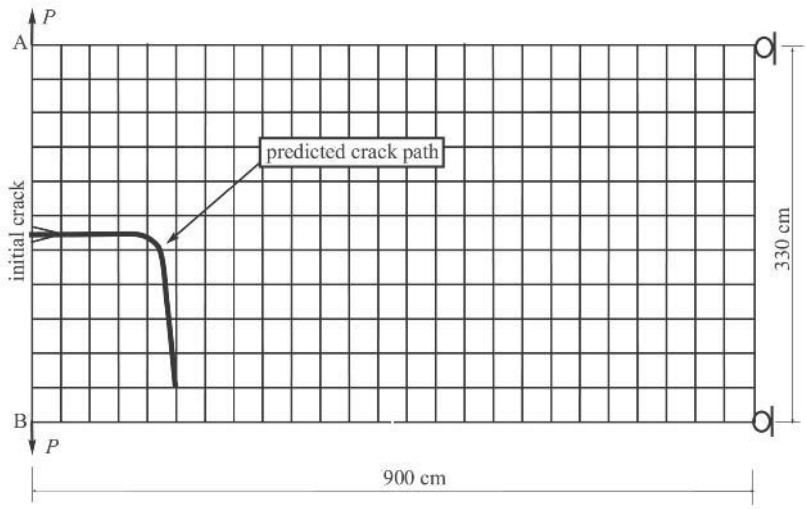

Figure 5.22 A double cantilever beam and predicted path of crack propagation.

Fig. 5.22 also shows the path of crack propagation predicted by the present XFEM. In contrast to the symmetry of the initial geometry and loading, the crack path has deviated from the symmetric solution.

In order to clarify how such an un-symmetric result has been obtained from a symmetric solution, it is necessary to discuss the requirements for one of the three possible crack propagation paths, as illustrated in Fig. 5.23.

Fig. 5.24 depicts the XFEM response prediction for each case. For path 1, an additional constraint is necessary to limit the crack path to a straight one. As a result, it requires the maximum level of energy to be activated, and so it is less probable to happen.

Any of the paths 2 or 3 is a result of local bending in each individual cantilever segment. The bending causes the extra tensile stress in far points across the height of the segment to be increased from the maximum tensile strength. As a result, the crack path turns to a curve. No distinction is theoretically possible for paths 2 or 3. Numerical errors or a small defect or perturbation in any part of the model may help to win the race for either path.

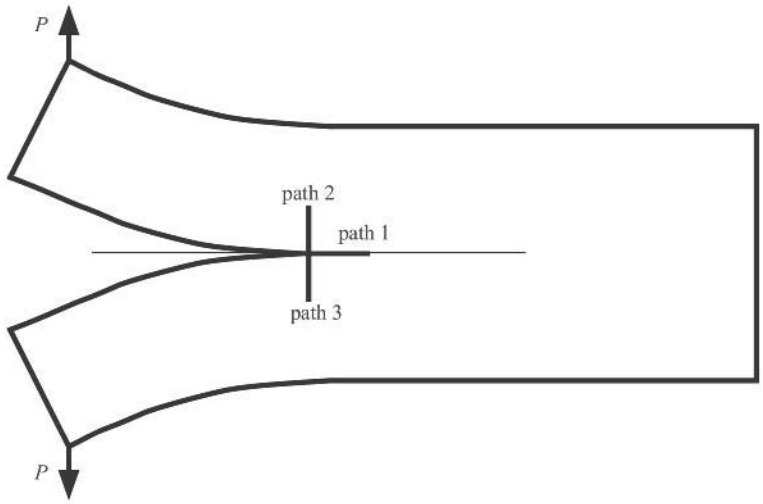

Figure 5.23 Potential crack propagation paths.

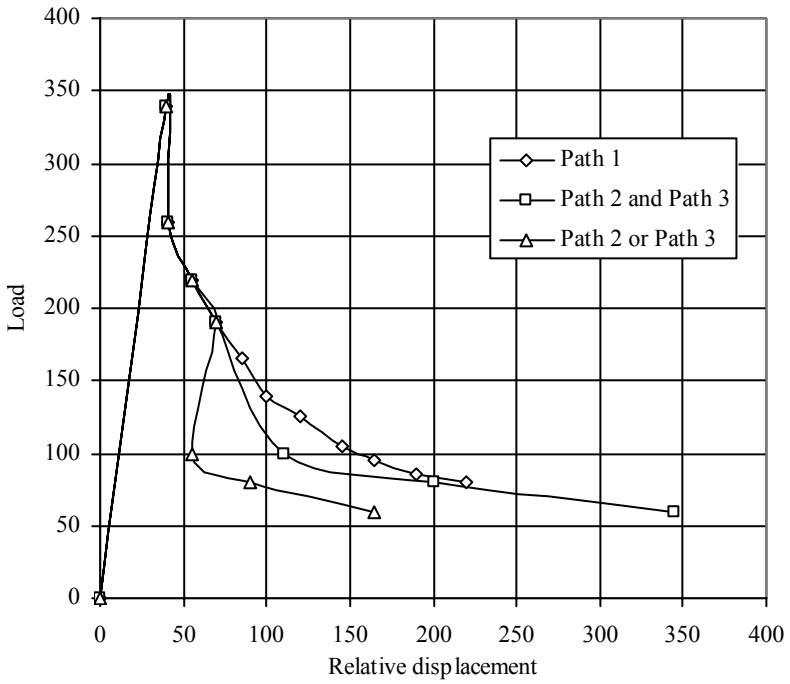

Figure 5.24 Load versus relative crack opening for different crack paths (Forghani 2005).

Chapter 6

New Frontiers

6.1 INTRODUCTION

This chapter is dedicated to describing new applications of the extended finite element method in different engineering applications.

Fundamental aspects of the extended finite element method were developed mainly for crack propagation problems. Then it was further extended to simulate other localisation problems in solid mechanics, especially in bimaterial and composite applications. However, the exceptional power of XFEM for modelling discontinuous fields has allowed for analysis of other engineering and physical applications. Problems involved with large deformations, plasticity and contact mechanics or in dynamic regimes have been extensively studied by many researchers based on the XFEM methodology. Multiphase problems naturally comprise internal discontinuous interfaces and can therefore be theoretically modelled by XFEM.

The first part of this chapter deals with interface cracks in solid media. It begins with classical elasticity and fracture mechanics solutions for an interface between isotropic materials and an extension to anisotropic materials. Available analytical displacement fields will then be used to present enrichment functions.

Contact problems constitute the second part of the chapter. It provides a review on available techniques for XFEM simulation of contact problems. Practically, strong and weak discontinuous enrichment functions are sufficient for most of the contact problems; the remaining aspects should be dealt with within the general concepts of contact kinematics and nonlinear frictional contact mechanics (Mohammadi 2003).

The next section is dedicated to dynamic fracture mechanics. Again, first classical concepts of fracture mechanics are extended to dynamic problems. Then an extension to include orthotropic effects is explained. The XFEM methodology for handling the dynamic fracture problems is then discussed comprehensively. In order to introduce the concepts of time discretization, the time integration schemes are briefly explained. Then, the new idea of time finite element method (TFEM) is introduced and followed by the time extended finite element method (TXFEM).

A brief discussion on multiscale applications constitutes the next part. The subject is too complicated to be discussed in detail in this book. Only the basic formulation and its XFEM approximation developed earlier by other authors are provided.

The final part of this chapter deals with the multiphase application. The strong and weak forms of the governing equations of solid–fluid multiphase solidification problems and the multiphase fluid flow simulations are provided, followed by the XFEM discretization. Again, the subject is too complex to be discussed in detail in this chapter, and only a very brief introduction is provided based on the original work of corresponding authors.

6.2 INTERFACE CRACKS

6.2.1 Elasticity solution for isotropic bimaterial interface

Interface crack propagation is rapidly gaining wide attention. Such a crack growth is exceedingly important for delamination and debonding analysis in composite materials, and can be extended to other brittle and semi-brittle materials such as concrete and rock crack interfaces.

Williams (1952) extended his early contribution on V notch to analyse a crack at the interface between two dissimilar materials, as depicted in Fig. 6.1. Following the classical elasticity procedures, two stress functions Φ_1 and Φ_2 are now required:

$$\Phi_i(r,\theta) = r^{\lambda+1} F_i(\theta,\lambda) \tag{6.1}$$

and

$$F_i(\theta,\lambda) = A_{1i}\cos(\lambda-1)\theta + A_{2i}\cos(\lambda+1)\theta + A_{3i}\sin(\lambda-1)\theta + A_{4i}\sin(\lambda+1)\theta \tag{6.2}$$

Solving for the unknown coefficients A_{1i}, A_{2i}, A_{3i} and A_{4i} allows for determination of near crack tip stresses for each material i:

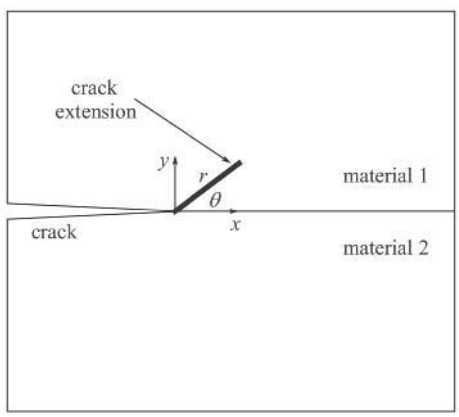

Figure 6.1 An interface crack between two dissimilar isotropic materials.

$$(\sigma_{rr})_i = r^{-\frac{1}{2}}\cos(\lambda_j \log(r))F_i''(\theta) + r^{-\frac{1}{2}}\left[\frac{3}{2}\cos(\lambda_j \log(r)) + \lambda_j \sin(\lambda_j \log(r))\right]F_i(\theta) \tag{6.3}$$

$$(\sigma_{\theta\theta})_i = r^{-\frac{1}{2}}\left[\left(\frac{3}{4} - \lambda_j^2\right)\cos(\lambda_j \log(r)) + \left(\frac{3}{2} + \frac{\lambda_j}{2}\right)\lambda_j \sin(\lambda_j \log(r))\right]F_i(\theta) \tag{6.4}$$

$$(\sigma_{r\theta})_i = r^{-\frac{1}{2}}\left\{\cos(\lambda_j \log(r))F_i'(\theta) + \left[\frac{3}{2}\cos(\lambda_j \log(r)) + \lambda_j \sin(\lambda_j \log(r))\right]F_i(\theta)\right\} \tag{6.5}$$

where the first and second derivatives of F are defined as:

$$\begin{aligned} F'(\theta) = a\Big\{&\cosh\lambda_j\theta\left[\frac{3}{2}\cos\frac{3\theta}{2} + \frac{1}{2}\cos\frac{\theta}{2}\right] + \lambda_j \sinh\lambda_j\theta\left[\sin\frac{3\theta}{2} + \sin\frac{\theta}{2}\right]\Big\} \\ + b\Big\{&\cosh\lambda_j\theta\left[-\frac{3}{2}\sin\frac{3\theta}{2} - \frac{3}{2}\sin\frac{\theta}{2}\right] + \lambda_j \sinh\lambda_j\theta\left[\cos\frac{3\theta}{2} + 3\cos\frac{\theta}{2}\right]\Big\} \end{aligned} \tag{6.6}$$

$$\begin{aligned} F''(\theta) = a\Big\{&\cosh\lambda_j\theta\left[-\frac{9}{4}\sin\frac{3\theta}{2} - \frac{1}{4}\sin\frac{\theta}{2}\right] + 2\lambda_j \sinh\lambda_j\theta\left[\frac{3}{2}\cos\frac{3\theta}{2} + \frac{1}{2}\sin\frac{\theta}{2}\right] \\ &+ \lambda_j^2 \cosh^2\lambda_j\theta\left[\sin\frac{3\theta}{2} + \sin\frac{\theta}{2}\right]\Big\} + b\Big\{\cosh\lambda_j\theta\left[-\frac{9}{4}\cos\frac{3\theta}{2} - \frac{3}{4}\cos\frac{\theta}{2}\right] \\ &+ 2\lambda_j \sinh\lambda_j\theta\left[-\frac{3}{2}\sin\frac{3\theta}{2} - \frac{3}{2}\sin\frac{\theta}{2}\right] + \lambda_j^2 \cosh^2\lambda_j\theta\left[\cos\frac{3\theta}{2} + 3\cos\frac{\theta}{2}\right]\Big\} \end{aligned} \tag{6.7}$$

λ_j are the roots of the following characteristic equation (Saouma 2000):

$$\cot^2\lambda\pi + \left[\frac{2\frac{\mu_1}{\mu_2}(1-\alpha_2) - 2(1-\alpha_1) - (\frac{\mu_1}{\mu_2} - 1)}{2\frac{\mu_1}{\mu_2}(1-\alpha_2) + 2(1-\alpha_1)}\right]^2 = 0 \tag{6.8}$$

with

$$\alpha_i = \frac{\nu_i}{1+\nu_i} \tag{6.9}$$

6.2.2 Stability of interface cracks

After evaluation of displacement and stress fields, a criterion is required to determine whether an interface crack is either stable or propagates in an unstable manner. The unstable crack can propagate along the interface, kink into one of the materials, or branch

out along the interface and then kink, depending on the relative toughness of the interface and both materials.

Consider a bimaterial interface crack, as depicted in Fig. 6.1. Hutchinson and Sue (1992) expressed the near tip normal and shear stresses in a complex form,

$$\sigma_{yy} + i\tau_{xy} = \frac{Kr^{i\varepsilon}}{\sqrt{2\pi r}} \tag{6.10}$$

where the complex stress intensity factor K is defined in terms of its components:

$$K = K_1 + iK_2 \tag{6.11}$$

and ω is the oscillation index defined as (Nagashima *et al.* 2003):

$$\omega = \frac{1}{2\pi} \ln\left(\frac{\frac{\kappa_1}{\mu_1} + \frac{1}{\mu_2}}{\frac{\kappa_2}{\mu_2} + \frac{1}{\mu_1}}\right) \tag{6.12}$$

It should be noted that the present definition of K, Eq. (6.11), is proportional to $(length)^{1/(2-i\varepsilon)}$, which is different from the classical stress intensity factor as of $(length)^{1/2}$ (Sukumar *et al.* 2004). Eq. (6.10) implies a high frequency stress noise around the crack tip. Furthermore, the relative proportion of interfacial normal and shear stresses varies slowly with distance from the crack tip. Therefore, K_1 and K_2 cannot be decoupled; they are not the familiar mode I and II stress intensity factors, respectively.

The energy release rate G for extension of the crack along the interface for a plane strain problem is defined by (Carlsson and Prasad 1993)

$$G = \frac{1}{2\cosh^2(\pi\omega)}\left(\frac{1}{E_1'} + \frac{1}{E_2'}\right)\left(K_1^2 + K_2^2\right) \tag{6.13}$$

The phase angle φ that is an important parameter in the characterisation of interfacial fracture toughness, and measures the relative proportion of shear to normal tractions at a characteristic length l ahead of the crack tip can be defined as (Sukumar *et al.* 2004):

$$\varphi = \tan^{-1}\left[\frac{\mathrm{Im}\,(Kl^{i\omega})}{\mathrm{Re}\,(Kl^{i\omega})}\right] \tag{6.14}$$

or

$$Kl^{i\omega} = (K_i^2 + K_2^2)e^{i\varphi} \tag{6.15}$$

According to Rice (1988), near crack tip asymptotic displacement fields within the material $m = 1, 2$ can be written as:

$$u_j^m = \frac{1}{2\mu_1}\sqrt{\frac{r}{2\pi}}\left\{\mathrm{Re}(Kr^{i\omega})u_j^{m,\mathrm{I}} + \mathrm{Im}(Kr^{i\omega})u_j^{m,\mathrm{II}}\right\} \qquad j=1,2 \tag{6.16}$$

with (Nagashima *et al.* 2003 and Sukumar *et al.* 2004)

$$u_1^{m,\mathrm{I}} = \frac{e^{-\omega(\pi-\theta)}}{(1+4\omega^2)\cosh(\pi\omega)}\left[-e^{2\omega(\pi-\theta)}A_1 + \kappa_1 A_2 + C_2\right] \tag{6.17}$$

$$u_2^{m,\mathrm{I}} = \frac{e^{-\omega(\pi-\theta)}}{(1+4\omega^2)\cosh(\pi\omega)}\left[e^{2\omega(\pi-\theta)}B_1 + \kappa_1 B_2 - C_1\right] \tag{6.18}$$

$$u_1^{m,\mathrm{II}} = \frac{e^{-\omega(\pi-\theta)}}{(1+4\omega^2)\cosh(\pi\omega)}\left[e^{2\omega(\pi-\theta)}B_1 + \kappa_1 B_2 + C_1\right] \tag{6.19}$$

$$u_2^{m,\mathrm{II}} = \frac{e^{-\omega(\pi-\theta)}}{(1+4\omega^2)\cosh(\pi\omega)}\left[-e^{2\omega(\pi-\theta)}A_1 - \kappa_1 A_2 + C_2\right] \tag{6.20}$$

and

$$\begin{cases} A_k = \cos\dfrac{\theta}{2} + (-1)^{k+1}2\omega\sin\dfrac{\theta}{2} \\ B_k = \sin\dfrac{\theta}{2} + (-1)^{k}2\omega\cos\dfrac{\theta}{2} \\ C_k = (1+4\omega^2)\sin(k\dfrac{\pi}{2} - \dfrac{\theta}{2})\sin\theta \end{cases} \qquad k=1,2 \tag{6.21}$$

The same equations can be used for material 2 by replacing $\omega\pi$ with $-\omega\pi$.

6.2.3 XFEM approximation for interface cracks

The standard XFEM approximation (3.72) for crack analysis can be extended to include new enrichment terms according to Eq. (6.22)

$$\begin{aligned} \mathbf{u}^h(\mathbf{x}) = &\sum_{j=1}^{n} N_j(\mathbf{x})\mathbf{u}_j + \sum_{h=1}^{m} N_h(\mathbf{x})H(\xi(x))\mathbf{a}_h \\ &+ \sum_{k=1}^{mt_1} N_k(\mathbf{x})\left(\sum_{l=1}^{12} F_l^1(x)\mathbf{b}_k^{l1}\right) \\ &+ \sum_{k=1}^{mt_2} N_k(\mathbf{x})\left(\sum_{l=1}^{12} F_l^2(x)\mathbf{b}_k^{l2}\right) \end{aligned} \tag{6.22}$$

where F_l^j, $j=1,2$ are the new enrichment functions for crack tips 1 and 2, respectively, defined in terms of the local polar coordinate system (r,θ) and the oscillation index ω (Sukumar *et al.* 2004),

$$\begin{aligned}\left[F_l^j(\mathbf{x})\right]_{j=1,2} = \Bigg\{ & \sqrt{r}\cos(\omega\log r)e^{-\omega\theta}\sin\frac{\theta}{2}, \sqrt{r}\cos(\omega\log r)e^{-\omega\theta}\cos\frac{\theta}{2}, \\ & \sqrt{r}\cos(\omega\log r)e^{\omega\theta}\sin\frac{\theta}{2}, \sqrt{r}\cos(\omega\log r)e^{\omega\theta}\cos\frac{\theta}{2}, \\ & \sqrt{r}\sin(\omega\log r)e^{-\omega\theta}\sin\frac{\theta}{2}, \sqrt{r}\sin(\omega\log r)e^{-\omega\theta}\cos\frac{\theta}{2}, \\ & \sqrt{r}\sin(\omega\log r)e^{\omega\theta}\sin\frac{\theta}{2}, \sqrt{r}\sin(\omega\log r)e^{\omega\theta}\cos\frac{\theta}{2}, \\ & \sqrt{r}\cos(\omega\log r)e^{\omega\theta}\sin\frac{\theta}{2}\sin\theta, \\ & \sqrt{r}\cos(\omega\log r)e^{\omega\theta}\cos\frac{\theta}{2}\sin\theta, \\ & \sqrt{r}\sin(\omega\log r)e^{\omega\theta}\sin\frac{\theta}{2}\sin\theta, \\ & \sqrt{r}\sin(\omega\log r)e^{\omega\theta}\cos\frac{\theta}{2}\sin\theta\Bigg\}\end{aligned} \tag{6.23}$$

Sukumar *et al.* (2004) provided the cartesian derivatives of the interface enrichment functions for use in XFEM discretization and evaluation of the system matrices, as discussed in Section 3.7.2.

In a rather complicated problem, Asadpoure (2006) solved the problem of an interface crack between two orthotropic materials (see Section 4.5.6).

A more complicated problem of a cracked sliding interface between anisotropic bimaterials was studied by Wang and Zhong (2003). This class of problems may also be studied in the next section, as the problem of contact is investigated.

6.3 CONTACT

6.3.1 Numerical models for a contact problem

Contact between two deformable bodies is one of the important subjects in computational mechanics. Among them are the behaviour of a cracked structure, metal forming, moulding and frictional contact between a concrete dam and its foundation, etc.

Contact mechanics plays an important role in metal forming processes, where the existing differences between the elasticity modulus and deformability of the tool and workpiece leads to the occurrence of relative tangential displacement at the interface of die and plate. Existence of surface asperities further complicates the frictional contact phenomenon and may result in the development of local plastic zones and the generation of new microcracks.

In its simplest form, a contact interaction between two bodies can be represented simply by a series of normal and tangential linear or nonlinear springs connecting the two

objects. These additional stiffness terms prevent the bodies from getting too close or too far from each other according to a predefined load–displacement law for the springs.

The contact can be assumed to be occurring in a virtually zero thickness or very thin interface layer. As a result, the normal finite elements cannot be used directly for simulation of such tiny long zones because their aspect ratios become unacceptably large, causing numerical instabilities.

Finite element procedures, however, adopt the concept of interface (contact) elements defined between the nodes on both sides of the interface. Efficient large deformation formulations are now available in practically all general-purpose finite element software packages. A problem with this kind of modelling is that the nodes on both sides of the interface must match each other, limiting the contact procedure to be further extended for multiple crack propagations and progressive fracture analysis of structures.

More advanced procedures are also available which include general node-to-node, node-to-face and face-to-face contacts based on the penalty, Lagrange and augmented Lagrangian constraint enforcement methods (Mohammadi 2003). They are designed to undergo large deformations and may response in a fully nonlinear frictional contact both in hardening and softening regimes. Such a nonlinear response usually requires iterative contact stress update procedures to achieve quadratic rate of convergence based on evaluation of the consistent contact modulus.

A complex aspect of contact problems is the governing kinematics. Rigidity and deformability of both or any of the contact couples change the way the deformation kinematics is formulated. Also, smooth and non-smooth contacts have to be addressed (Wriggers 2002). In general, the contact surface is not always a predefined known part of the problem, and the contact boundary conditions may have to be determined within the solution process. Consequently, by its nature the contact is a mathematically nonlinear problem.

Another important contribution of contact mechanics is in analysing multibody dynamics for simulation of granular flow by the discrete element technique. Extremely large numbers of contacts take place at any time, which requires an expensive efficient contact detection procedure. Nevertheless, each contact interaction is usually simple and associated computations remain fast, non-iterative and clear.

In a dynamic contact problem, the contact surface changes by time, and in addition to a contact detection approach, an efficient algorithm is required to transfer the history dependent contact state variables from the old position to a new one. This may itself become a main source of error in the overall numerical solution. The problem is further complicated for curved deformable objects and around sharp corners.

6.3.2 XFEM modelling of a contact problem

In this section, a fundamentally different approach based on the concepts of extended finite element method is presented. The inspiration is to avoid explicit definition of the contact surface by adopting a similar procedure of modelling cracks by XFEM. Therefore, the whole domain can be discretized by a finite element mesh regardless of the size, extent and position of the contact interface. Standard XFEM procedure is followed to simulate the discontinuity path within the finite elements by enriching the classical finite

element approximation. Level set methods have been successfully used for tracking the moving contact interfaces, and its combination with XFEM can be efficiently used for solving complex contact problems.

Dolbow *et al.* (2000c) extended XFEM for modelling of crack growth with frictional contact on the crack faces. The subject of contact mechanics was further investigated by Dolbow *et al.* (2001) and Belytschko *et al.* (2002a). Recently, Shamloo *et al.* (2005), Khoei and Nikbakht (2006) and Khoei *et al.* (2006a, 2006b) applied the extended finite element method to modelling frictional contact in elastoplastic behaviour of pressure-sensitive material for powder compaction problems.

Beginning with the extended finite element approximation at a point $\mathbf{x}$,

$$\mathbf{u}^h(\mathbf{x}) = \sum_{j=1}^{n} N_j(\mathbf{x})\, \mathbf{u}_j + \sum_{k=1}^{m} N_k(\mathbf{x}) \psi(\mathbf{x}) \mathbf{a}_k \tag{6.24}$$

the enrichment function $\psi(\mathbf{x})$ for approximating a contact interface is assumed to be the Heaviside function $H(\xi)$,

$$\mathbf{u}^h(\mathbf{x}) = \sum_{j=1}^{n} N_j(\mathbf{x})\, \mathbf{u}_j + \sum_{k=1}^{m} N_k(\mathbf{x}) H(\xi) \mathbf{a}_k \tag{6.25}$$

where n is the number of nodes in a standard finite element and m is the number of enrichment terms. The Heaviside enrichment function is assumed to be the signed function defined in terms of the signed distance function $\xi(\mathbf{x})$ from the interface

$$H(\xi) = \text{sign}(\xi) = \begin{cases} 1 & \forall \xi > 0 \\ -1 & \forall \xi < 0 \end{cases} \tag{6.26}$$

Similar improvements as (3.59) can also be used to satisfy the interpolation requirements for the enriched solution.

Alternatively, a weak discontinuity enrichment (Section 3.6.4) can also be used, if an adhesive interface is being modelled:

$$\mathbf{u}^h(\mathbf{x}) = \sum_{j=1}^{n} N_j(\mathbf{x})\, \mathbf{u}_j + \sum_{k=1}^{m} N_k(\mathbf{x}) \chi(\mathbf{x}) \mathbf{a}_k \tag{6.27}$$

where $\chi(\mathbf{x})$ is the weak discontinuous enrichment function defined in terms of the signed distance function $\xi(\mathbf{x})$:

$$\chi_k(\mathbf{x}) = \left|\xi(\mathbf{x})\right| - \left|\xi(\mathbf{x}_k)\right| \tag{6.28}$$

The rest of the procedure is basically similar to the XFEM procedure for cracks. Similar sub-triangle or sub-quad methods have to be used to facilitate the Gauss quadrature rule and to provide acceptable levels of accuracy for the integration of the discretized system equation.

The only difference is that instead of using the material properties of the bodies in contact, one has to use the so-called interface properties. For an interface with normal and tangential material properties k_{n} and k_{t}, the following compliance matrix can be defined (Nikbakht 2005)

$$D = \frac{1}{1-\nu^2}\begin{bmatrix} k_{\mathrm{n}}\cos\theta & \nu k_{\mathrm{n}}\sin\theta & 0 \\ \nu k_{\mathrm{n}}\sin\theta & k_{\mathrm{n}}\cos\theta & 0 \\ 0 & 0 & k_{\mathrm{t}} \end{bmatrix} \tag{6.29}$$

where θ is the angle of interface with the x-axis. These properties are applied to the Gauss points defined in the sub-quad or sub-triangle within a predefined contact zone, as depicted in Fig. 6.2. The size of the contact zone depends on the interface properties and the magnitude of the shear force. No specific size can be recommended and a comprehensive sensitivity study is required to assess its effects.

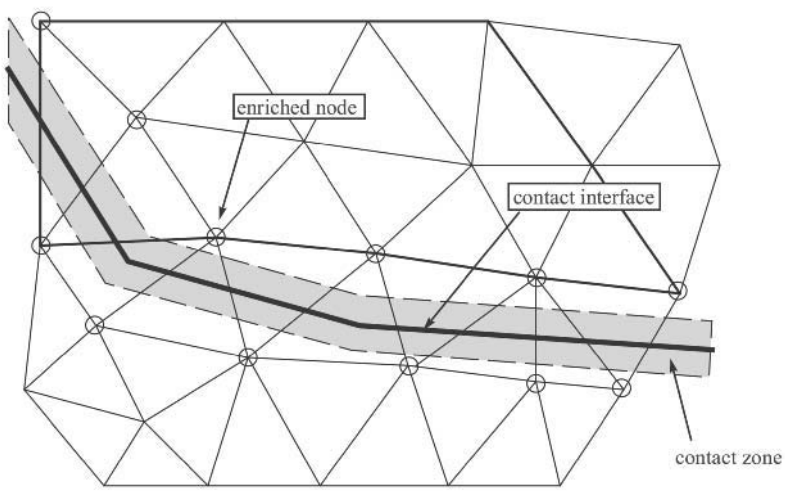

Figure 6.2 Definition of a contact zone.

Discussion on the details of contact mechanics procedures is out of the scope of this book. They are still among the most complicated problems in computational mechanics. Here, only the basic steps for a contact stress update procedure are provided. Assume that a system comprising of two contacting objects is in a state of equilibrium at an increment j, and the new displacement, strain and stress states are sought for a new increment $(j+1)$:

1. The stiffness of elements containing part of the interface is updated according to the interface property at corresponding Gauss points within the contact zone.
2. The global stiffness matrix is assembled and the incremental equilibrium equation is solved for the incremental displacements $\Delta\mathbf{u}_j$.

$$\mathbf{K}\,\Delta\mathbf{u}_j = \Delta\mathbf{f}_j \tag{6.30}$$

3. The incremental and total strains are then evaluated and their components in normal and tangential directions (with respect to the interface) are determined.
4. The normal and tangential contact stresses are then estimated using the converged solution at the end of increment j. Non-associated slip rules are usually adopted.
5. Nonlinear frictional contact procedures based on non-associated slip rules are used to correct the predicted trial stress state to determine the final normal and tangential contact stresses.
6. The residual force vector is computed and the convergence of the solution is examined.

The above approach has the least modification in a standard XFEM methodology, if any at all. Reports by Shamloo *et al.* (2005), Khoei and Nikbakht (2006) and Khoei *et al.* (2006a, 2006b) seem to be using this methodology.

6.4 DYNAMIC FRACTURE

6.4.1 Dynamic crack propagation by XFEM

Static and quasi-crack analyses have been widely used for fracture analysis of structures. Nevertheless, they do not represent real world crack problems; they are only used as efficient simplified models for other highly complex dynamic phenomena.

The usual approach for solving dynamic problems in the finite element method is to discretize the time and space independently. Discretization in time is performed by means of implicit or explicit time integration techniques, while the discretization in space is carried out by standard finite element shape functions. In this section, the problem of dynamic crack analysis by the extended finite element method is briefly reviewed.

Two independent parts are involved in dynamic crack analysis by XFEM. First, a crack tracking procedure is required to represent an existing crack and its evolution by time. Fortunately, the level set method and the fast marching approach are available. They have been successfully implemented in the XFEM codes and can be used for quasi-static or dynamic crack evolution problems. Short descriptions of these methods have been given in Sections 3.8.1 and 3.8.2, respectively, and are not repeated.

The second part is related to the way dynamic crack propagation is formulated. Belytschko *et al.* (2003) developed a methodology for switching from a continuum to a discrete discontinuity where the governing partial differential equation loses hyperbolicity for rate independent materials. They adopted the technique of loss of hyperbolicity in combination with the XFEM cohesive crack models. The idea was to track the change of a hyperbolicity indicator to compute the direction and velocity of dynamic crack propagation. They applied the method to solve problems involving crack branching. The idea of loss of hyperbolicity was previously developed by Gao and Klein (1998) for analysing dynamic crack propagations. Later, Peerlings *et al.* (2002) and Oliver *et al.*

(2003) further studied the loss of hyperbolicity and added this technique into equilibrium equations.

Further improvements were reported by Chessa and Belytschko (2004) and Chessa and Belytschko (2006). They presented a locally enriched space–time extended finite element method for solving hyperbolic problems with discontinuities. The coupling was implemented through a weak enforcement of the continuity of the flux between the space–time and semi-discrete domains in a manner similar to discontinuous Galerkin methods. They successfully applied the TXFEM to the Rankine–Hugoniot jump conditions to linear first order wave and nonlinear Burgers equations.

Furthermore, Réthoré *et al.* (2005b) proposed a combined space–time extended finite element method, based on the idea of the time extended finite element method (TXFEM), allowing a suitable form of the time stepping formulae to satisfy stability and energy conservation criteria. XFEM was used to implicitly define a virtual crack field tangential to the crack front. The concept of a virtual field allowed for separation of mixed modes of fracture.

Other contributions include the work by Belytschko and Chen (2004) who developed a singular enrichment finite element method for elastodynamic crack propagation, Zi *et al.* (2005) who presented a method for modelling arbitrary growth of dynamic cracks without remeshing, and Menouillard *et al.* (2006) who introduced a lumped mass matrix for enriched elements, which allowed the use of a pure explicit formulation in XFEM applications.

6.4.2 Dynamic LEFM

The concept of dynamic stress intensity factors can be directly derived from the classical definition of stress intensity factors in linear elastic fracture mechanics:

$$K_{\mathrm{I}}^{\mathrm{dyn}} = \lim_{\substack{r\to 0\\ \theta=0}} \sqrt{2\pi r}\,\sigma_{yy} \tag{6.31}$$

$$K_{\mathrm{II}}^{\mathrm{dyn}} = \lim_{\substack{r\to 0\\ \theta=0}} \sqrt{2\pi r}\,\sigma_{xx} \tag{6.32}$$

Evaluation of dynamic stress intensity factors are indirectly made by computation of the J integral using the domain integral approach or the interaction integral method. The latter is based on the definition of auxiliary fields defined by Piva *et al.* (2005), as discussed in previous sections.

The mixed mode crack propagation is investigated by similar forms of static mixed mode criteria (2.126), (2.127), etc., except for using dynamic stress intensity factors.

Once the direction of crack propagation and its corresponding dynamic stress intensity factor are obtained, the speed of the crack tip $\dot{a}$ can be determined from the dynamic fracture toughness $K_{\mathrm{C}}^{\mathrm{dyn}}$. For example, if the maximum circumferential tensile stress $(\sigma_\theta)_{\max}$ is used as the mixed mode criterion, the following simplified equation can be used (Piva *et al.* 2005):

$$K_{\theta\theta}^{\text{dyn}} = K_{\text{C}}^{\text{dyn}} = \frac{K_{\text{IC}}}{1 - \left(\dfrac{\dot{a}}{c_{\text{R}}} \right)} \tag{6.33}$$

where c_{R} is the Rayleigh wave speed.

6.4.3 Dynamic orthotropic LEFM

The methodology described in Section 4.3.1 for an orthotropic near crack tip displacement field is now briefly extended to dynamic problems. Using the same notation, the steady-state equations of motion can be expressed as (Piva *et al.* 2005):

$$\frac{\partial \boldsymbol{\Phi}}{\partial x_1} + \boldsymbol{\Lambda} \frac{\partial \boldsymbol{\Phi}}{\partial x_2} = \mathbf{0} \tag{6.34}$$

where

$$\boldsymbol{\Phi} = \left\{ \frac{\partial u_1}{\partial x_1}, \frac{\partial u_1}{\partial x_2}, \frac{\partial u_2}{\partial x_1}, \frac{\partial u_2}{\partial x_2} \right\}^{\text{T}} \tag{6.35}$$

$$\boldsymbol{\Lambda} = \begin{pmatrix} 0 & \alpha_1 & 2\beta_1 & 0 \\ -1 & 0 & 0 & 0 \\ 2\beta_2 & 0 & 0 & \alpha_2 \\ 0 & 0 & -1 & 0 \end{pmatrix} \tag{6.36}$$

Coefficients α_i and β_i are different from Eq. (4.41) and are defined as:

$$\alpha_1 = \frac{c_{66}}{c_{11}(1 - \text{M}_1^2)},\ \alpha_2 = \frac{c_{22}}{c_{66}(1 - \text{M}_2^2)},\ \beta_1 = \frac{c_{12} + c_{66}}{2c_{11}(1 - \text{M}_1^2)},\ \beta_2 = \frac{c_{12} + c_{66}}{2c_{66}(1 - \text{M}_2^2)} \tag{6.37}$$

The Mach numbers M_j are defined as:

$$\text{M}_j = \frac{c}{v_j} \qquad j = 1,2 \tag{6.38}$$

where c is a constant velocity and v_1, v_2 are the longitudinal and shear wave velocities, respectively, defined in terms of the material density ρ

$$v_1 = \sqrt{\frac{c_{11}}{\rho}} \tag{6.39}$$

$$v_2 = \sqrt{\frac{c_{66}}{\rho}} \tag{6.40}$$

The characteristic equation of the matrix $\mathbf{\Lambda}$ remains similar to Eq. (4.42),

$$\lambda^4 + 2a_1\lambda^2 + a_2 = 0 \tag{6.41}$$

with

$$a_1 = \frac{\left(\alpha_1 + \alpha_2 - 4\beta_1\beta_2\right)}{2} \tag{6.42}$$

$$a_2 = \alpha_1\alpha_2 \tag{6.43}$$

Piva *et al.* (2005) derived the displacement and stress fields in terms of analytical solutions of Eq. (6.34). Those highly complex solutions are further simplified for an infinite plane orthotropic problem containing a steadily propagating semi-infinite crack subjected to traction σ_0. The dominant displacement fields near the crack tip can be expressed as (Piva *et al.* 2005):

$$u_1 = \frac{2\gamma(\gamma+1)K_{\mathrm{I}}}{c_{66}\left(l_3l_6 + l_4l_5\right)}\sqrt{\frac{r_1}{2\pi}}\cos\frac{\varphi}{2}\left[\frac{\alpha_1(1+\gamma)+a_1(1-\gamma)}{(a_1-\alpha_1)(1+\gamma)} + \sin^2\frac{\varphi}{2}\right] \tag{6.44}$$

$$u_2 = \frac{2(\gamma+1)K_{\mathrm{I}}}{c_{66}\left(l_3l_6 + l_4l_5\right)}\sqrt{\frac{r_1}{2\pi a_1}}\sin\frac{\varphi}{2}\left[\frac{\alpha_1(1+\gamma)+a_1(3\gamma-1)}{(a_1-\alpha_1)(1+\gamma)} - \cos^2\frac{\varphi}{2}\right] \tag{6.45}$$

and the dominant stress fields (Piva *et al.* 2005):

$$\sigma_{11} = \frac{K_{\mathrm{I}}}{\left(l_3l_6 + l_4l_5\right)\sqrt{2\pi r_1}}\cos\frac{\varphi}{2}\left[\left(l_1l_6 + l_2l_5\right) - \frac{l_2l_6}{\sqrt{a_1}}\sin\frac{\varphi}{2}\cos\frac{3\varphi}{2}\right] \tag{6.46}$$

$$\sigma_{22} = \frac{K_{\mathrm{I}}}{\sqrt{2\pi r_1}}\cos\frac{\varphi}{2}\left[1 - \frac{l_4l_6}{\left(l_3l_6 + l_4l_5\right)\sqrt{a_1}}\sin\frac{\varphi}{2}\cos\frac{3\varphi}{2}\right] \tag{6.47}$$

$$\sigma_{12} = \frac{K_{\mathrm{I}}l_6^2}{\left(l_3l_6 + l_4l_5\right)\sqrt{2\pi r_1 a_1}}\sin\frac{\varphi}{2}\cos\frac{\varphi}{2}\cos\frac{3\varphi}{2} \tag{6.48}$$

where

$$l_1 = \frac{c_{11}}{c_{66}}\frac{\gamma^2\alpha_1}{\beta_1} \qquad l_2 = \frac{c_{11}}{c_{66}}\gamma\sqrt{a_1} - \frac{c_{12}}{c_{66}}\frac{1}{\sqrt{a_1}} \qquad l_3 = \frac{c_{12}}{c_{66}}\frac{\gamma^2\alpha_1}{\beta_1}$$
$$l_4 = \frac{c_{12}}{c_{66}}\gamma\sqrt{a_1} - \frac{c_{22}}{c_{66}}\frac{1}{\sqrt{a_1}} \qquad l_5 = \frac{2\beta_1 - \gamma^2(\alpha_1+\alpha_2)}{2\beta_1\sqrt{a_1}} \qquad l_6 = \gamma + 1 \tag{6.49}$$
$$\gamma = \left[1 - M_2^2\right]^{\frac{1}{2}}$$

$K_I = 2\sigma_0\sqrt{2a/\pi}$ is the mode I stress intensity factor and $r_1 = rg(\theta)$ is defined with respect to the crack tip polar coordinates (r,θ)

$$g(\theta) = \left[\cos^2\theta + \frac{1}{a_1}\sin^2\theta\right]^{\frac{1}{2}} \tag{6.50}$$

$$\varphi = \tan^{-1}\left[\frac{\tan\theta}{\sqrt{a_1}}\right] \tag{6.51}$$

The dynamic energy release rate can also be obtained as (Piva *et al.* 2005):

$$G_I^{dyn} = \frac{\left(\alpha_2/\alpha_1\right)^{\frac{1}{4}}}{c_{66}(\gamma+1)\left[2\gamma\left(\sqrt{\alpha_2}-\sqrt{\alpha_1}\right)+(\gamma-1)\left(\sqrt{\alpha_2}+\sqrt{\alpha_1}\right)\right]}K_I^2 \tag{6.52}$$

A procedure similar to the one presented in Section 4.3.1 is expected to provide a basis for deriving the enrichment functions from the dominant displacement fields (6.44)–(6.45) for a dynamic crack analysis in orthotropic media.

6.4.4 Basic formulation of dynamic XFEM

Consider a body Ω with an initial traction-free crack Γ_c in the state of dynamic equilibrium, as depicted in Fig. 3.20. The fundamental elastodynamic equation can be expressed as:

$$\nabla\cdot\boldsymbol{\sigma} + \mathbf{f}^b = \rho\ddot{\mathbf{u}} \tag{6.53}$$

with the following boundary conditions:

$$\mathbf{u}(\mathbf{x},t) = \bar{\mathbf{u}}(\mathbf{x},t) \qquad \text{on}\,\Gamma_u \tag{6.54}$$

$$\boldsymbol{\sigma}\cdot\mathbf{n} = \mathbf{f}^t \qquad \text{on}\,\Gamma_t \tag{6.55}$$

$$\boldsymbol{\sigma}\cdot\mathbf{n} = 0 \qquad \text{on}\,\Gamma_c \tag{6.56}$$

and initial conditions:

$$\mathbf{u}(\mathbf{x}, t=0) = \overline{\mathbf{u}}(0) \tag{6.57}$$

$$\dot{\mathbf{u}}(\mathbf{x}, t=0) = \overline{\dot{\mathbf{u}}}(0) \tag{6.58}$$

where Γ_t, Γ_u and Γ_c are traction, displacement and crack boundaries, respectively; $\boldsymbol{\sigma}$ is the stress tensor and $\mathbf{f}^b$ and $\mathbf{f}^t$ are the body force and external traction vectors, respectively.

The variational formulation of the initial/boundary value problem of Eq. (6.53) can be written as:

$$\int_\Omega \rho \ddot{\mathbf{u}} \cdot \delta \mathbf{u} \, d\Omega + \int_\Omega \boldsymbol{\sigma} \cdot \delta \boldsymbol{\varepsilon} \, d\Omega = \int_\Omega \mathbf{f}^b \cdot \delta \mathbf{u} \, d\Omega + \int_\Gamma \mathbf{f}^t \cdot \delta \mathbf{u} \, d\Gamma \tag{6.59}$$

6.4.5 XFEM discretization

In the extended finite element method, approximation (3.42) is utilised to calculate the displacement $\mathbf{u}^h(\mathbf{x})$ for a typical point $\mathbf{x}$

$$\mathbf{u}^h(\mathbf{x}) = \sum_{j=1}^{n} N_j(\mathbf{x}) \mathbf{u}_j + \sum_{k=1}^{m} N_k(\mathbf{x}) \psi(\mathbf{x}) \mathbf{a}_k \tag{6.60}$$

or in a compact form

$$\mathbf{u}^h(\mathbf{x}) = \mathbf{N}^h \mathbf{u}^h = \mathbf{N} \left(\mathbf{u} + \sum_{k=1}^{m} \psi(\mathbf{x}) \mathbf{a}_k \right) \tag{6.61}$$

where $\mathbf{u}$ is the vector of regular degrees of nodal freedom in finite element method, $\mathbf{a}_k$ is the added set of degrees of freedom to the standard finite element model and $\psi(x)$ is the discontinuous enrichment function defined for the set of nodes that the discontinuity is in its influence (support) domain.

$\mathbf{N}^h$ is regarded as the global matrix of shape functions relating the generalised unknowns at each point $\mathbf{x}$ to their nodal values.

The discretized form of Eq. (6.59) using the XFEM procedure (6.61) can be written as:

$$\mathbf{M}\ddot{\mathbf{u}}^h + \mathbf{K}\mathbf{u}^h = \mathbf{f} \tag{6.62}$$

where $\mathbf{u}^h$ and $\ddot{\mathbf{u}}^h$ denote the vector of nodal parameters (displacements $\mathbf{u}$ and enrichment degrees of freedom $\mathbf{a}$) and its second time derivative, respectively:

$$\mathbf{u}^h = \{\mathbf{u}, \mathbf{a}\}^T \tag{6.63}$$

The stiffness matrix $\mathbf{K}$, mass matrix $\mathbf{M}$ and the external load vector $\mathbf{f}$ are defined as:

$$\mathbf{K}_{ij} = \begin{bmatrix} \mathbf{K}_{ij}^{\mathbf{uu}} & \mathbf{K}_{ij}^{\mathbf{ua}} \\ \mathbf{K}_{ij}^{\mathbf{au}} & \mathbf{K}_{ij}^{\mathbf{aa}} \end{bmatrix} \tag{6.64}$$

$$\mathbf{M}_{ij} = \begin{bmatrix} \mathbf{M}_{ij}^{\mathbf{uu}} & \mathbf{M}_{ij}^{\mathbf{ua}} \\ \mathbf{M}_{ij}^{\mathbf{au}} & \mathbf{M}_{ij}^{\mathbf{aa}} \end{bmatrix} \tag{6.65}$$

$$\mathbf{f}_i = \left\{ \mathbf{f}_i^{\mathbf{u}}, \mathbf{f}_i^{\mathbf{a}} \right\}^{\mathrm{T}} \tag{6.66}$$

where the stiffness components $\mathbf{K}_{ij}^{\mathbf{uu}}$, $\mathbf{K}_{ij}^{\mathbf{ua}}$ and $\mathbf{K}_{ij}^{\mathbf{aa}}$ associated with the classical FEM, coupled and enrichment parts of XFEM approximation, respectively, can be defined from Eq. (3.84):

$$\mathbf{K}_{ij}^{\mathbf{uu}} = \int_{\Omega} (\mathbf{B}_i^{\mathbf{u}})^{\mathrm{T}} \mathbf{D} \mathbf{B}_j^{\mathbf{u}} \, \mathrm{d}\Omega \tag{6.67}$$

$$\mathbf{K}_{ij}^{\mathbf{ua}} = \int_{\Omega} (\mathbf{B}_i^{\mathbf{u}})^{\mathrm{T}} \mathbf{D} \mathbf{B}_j^{\mathbf{a}} \, \mathrm{d}\Omega \tag{6.68}$$

$$\mathbf{K}_{ij}^{\mathbf{aa}} = \int_{\Omega} (\mathbf{B}_i^{\mathbf{a}})^{\mathrm{T}} \mathbf{D} \mathbf{B}_j^{\mathbf{a}} \, \mathrm{d}\Omega \tag{6.69}$$

where $\mathbf{B} = \nabla \mathbf{N}$ is the matrix of derivatives of shape functions, defined in Eqs. (3.88) and (3.89). Classical and enrichment components of the consistent mass matrix can be expressed as:

$$\mathbf{M}_{ij}^{\mathbf{uu}} = \int_{\Omega} \rho N_i \, N_j \mathrm{d}\Omega \tag{6.70}$$

$$\mathbf{M}_{ij}^{\mathbf{ua}} = \mathbf{M}_{ij}^{\mathbf{au}} = \int_{\Omega} \rho N_i \left(N_j \psi_j \right) \mathrm{d}\Omega \tag{6.71}$$

$$\mathbf{M}_{ij}^{\mathbf{aa}} = \int_{\Omega} \rho \left(N_i \psi_i \right) \left(N_j \psi_j \right) \mathrm{d}\Omega \tag{6.72}$$

Finally the force vectors associated with the classical and enrichment degrees of freedom are defined as:

$$\mathbf{f}_i^{\mathbf{u}} = \int_{\Gamma_{\mathrm{t}}} N_i \mathbf{f}^{\mathrm{t}} \, \mathrm{d}\Gamma + \int_{\Omega^e} N_i \mathbf{f}^{\mathrm{b}} \, \mathrm{d}\Omega \tag{6.73}$$

$$\mathbf{f}_i^{\mathbf{a}} = \int_{\Gamma_{\mathrm{t}}} N_i \psi \mathbf{f}^{\mathrm{t}} \, \mathrm{d}\Gamma + \int_{\Omega^e} N_i \psi \mathbf{f}^{\mathrm{b}} \, \mathrm{d}\Omega \tag{6.74}$$

6.4.6 Time integration

The Newmark time integration scheme is usually used in dynamic analysis, because it can be designed to remain unconditionally stable. Eq. (6.62) for a specific time $(n+1)$ can be expressed as:

$$\mathbf{M}_{n+1}\ddot{\mathbf{u}}_{n+1} + \mathbf{K}_{n+1}\mathbf{u}_{n+1} = \mathbf{f}_{n+1} \tag{6.75}$$

$$\mathbf{u}_{n+1} = \mathbf{u}_n + \Delta t\dot{\mathbf{u}}_n + \frac{\Delta t^2}{2}\ddot{\mathbf{u}}_n + \Delta t^3\left(\beta_n \frac{\ddot{\mathbf{u}}_{n+1} - \ddot{\mathbf{u}}_n}{\Delta t}\right) \tag{6.76}$$

$$\dot{\mathbf{u}}_{n+1} = \dot{\mathbf{u}}_n + \Delta t\ddot{\mathbf{u}}_n + \Delta t^2\left(\gamma_n \frac{\ddot{\mathbf{u}}_{n+1} - \ddot{\mathbf{u}}_n}{\Delta t}\right) \tag{6.77}$$

The method is unconditionally (with respect to the size of timestep) stable if $0.5 \le \gamma \le 2\beta$.

In the special case of $\beta = 0$ and $\gamma = 0.5$, the Newmark approach becomes similar to the central difference technique, which is only conditionally stable. Nevertheless, the central difference technique combined with a lumped mass matrix allows for decoupling the solution of degrees of freedom. As a result, the solution of the simultaneous system of equations can be avoided and a very fast explicit approach suitable for vectorise and parallel processing systems is obtained. Another important advantage of such explicit algorithms is that it does not require storage of the global stiffness matrix, and the process of assembly/solution is separately performed for each individual degree of freedom.

There are a number of techniques for constructing the lumped mass matrix from the standard finite element consistent mass matrix. They, however, cannot be used directly in the extended finite element method. Menouillard *et al.* (2006) have recently proposed a lumped mass matrix to be used instead of Eq. (6.65) that allows for adoption of an explicit time integration technique. They used the idea of exact discrete kinetic energy to derive their lumped mass matrix (Menouillard *et al.* 2006):

$$\mathbf{M}_i = \frac{M_0}{n_n}\frac{1}{l_e}\int_{\Omega_e} \psi_i^2 \mathrm{d}\Omega \tag{6.78}$$

where M_0 is the total mass of element, n_n is the number of nodes and:

$$l_e = \begin{cases} \text{length} & \text{1D} \\ \text{area} & \text{2D} \\ \text{volume} & \text{3D} \end{cases} \tag{6.79}$$

They discussed the effect of enrichment and mass lumping on the size of the critical timestep required for stability of an explicit dynamic analysis. For further details, see Menouillard *et al.* (2006).

6.4.7 Time finite element method

The idea of time finite element method (TFEM) was first proposed by Zienkiewicz (1977). Beginning with the elastodynamics equation in terms of the displacement $\mathbf{u}(\mathbf{x},t)$

$$\mathbf{M}\ddot{\mathbf{u}}(\mathbf{x},t)+\mathbf{K}\mathbf{u}(\mathbf{x},t)=\mathbf{f}(t) \tag{6.80}$$

The basic equation is to interpolate the displacement in time according to:

$$\mathbf{u}(\mathbf{x},t)=\sum_{i=n-1}^{n+1} T_i(t)\mathbf{u}_i(t) \tag{6.81}$$

where $T_i(t)$ are the time shape functions. Eq. (6.80) is then solved in a weighted residual form:

$$\int_{-\Delta t}^{\Delta t} W_t(t)\left[\mathbf{M}\sum_{i=n-1}^{n+1}\ddot{T}_i(t)\mathbf{u}_i(t)+\mathbf{K}\sum_{i=n-1}^{n+1}T_i(t)\mathbf{u}_i(t)\right]\mathrm{d}t=\int_{-\Delta t}^{\Delta t} W_t(t)\mathbf{f}(t)\mathrm{d}t \tag{6.82}$$

where $W_t(t)$ is an appropriate weight function in time. The solution will depend on the selection of the weight function. Eq. (6.81) replaces the conventional set of Newmark equations ((6.76) and (6.77)).

Later, Wood (1984) modified the original approach to include the velocity terms in the time interpolation:

$$\mathbf{u}(\mathbf{x},t)=\mathbf{u}_n(t)+t\,\mathbf{u}_n(t)+\left(\frac{t}{\Delta t}\right)^2\left[\mathbf{u}_{n+1}(t)-\mathbf{u}_n(t)-\Delta t\,\dot{\mathbf{u}}_n(t)\right] \tag{6.83}$$

The rest of the procedure is similar to the original approach.

Alternatively, Réthoré *et al.* (2005b) presented a new formulation in terms of the velocity field $\mathbf{v}(t)$:

$$\mathbf{v}(t)=\mathbf{v}_n\tau_n(t)+\mathbf{v}_{n+1}\tau_{n+1}(t) \tag{6.84}$$

where

$$\tau_n(t)=\frac{t_{n+1}-t}{t_{n+1}-t_n}\qquad \tau_{n+1}(t)=\frac{t-t_n}{t_{n+1}-t_n} \tag{6.85}$$

and the displacement is obtained by integration of Eq. (6.84)

$$\mathbf{u}(t)=\mathbf{u}_n+\int_{t_0}^{t}\mathbf{v}(t)\,\mathrm{d}t \tag{6.86}$$

6.4.8 Time extended finite element method

The same procedure as discussed in the previous section was extended to the XFEM formulation by Réthoré *et al.* (2005b), which was motivated by the fact that polynomial interpolation cannot approximate time discontinuities well.

The fundamental XFEM approximation of the velocity field $\mathbf{v}^h(t)$ is defined in terms of n classical and m enrichment degrees of freedom $\mathbf{v}$ and $\mathbf{a}$, respectively (Réthoré *et al.* 2005b):

$$\mathbf{v}^h(t) = \sum_{j=0}^{n} \tau_j(t)\,\mathbf{v}_j + \sum_{j=0}^{n}\sum_{k=1}^{m} \tau_j(t)\psi_k(t)\,\mathbf{a}_{jk} \tag{6.87}$$

which can be assumed to be an extension of Eq. (6.84).

6.5 MULTISCALE XFEM

6.5.1 Basic formulation

The finite element method has recently been applied to multiscale analysis, in which different levels of accuracy are sought through appropriate formulations ranging from atomic scales to macro simulations of usual engineering problems.

The original idea of global–local approximation was introduced to enhance the FEM over the entire region or part of the domain. Hirari *et al.* (1985) proposed a family of so-called zooming methods, using refined finite element meshes for the local regions containing stress concentrations.

In a superposition multiscale approach, global and local parts are modelled independently, and then superimposed to provide the final solution by satisfying the compatibility equations. An alternative approach is the multiple scale expansion technique based on homogenisation of field variables at each scale. Finally, domain decomposition techniques divide the domain into several subdomains connected to each other with interface elements (Haidar *et al.* 2003)

Multiscale analyses have been performed using the partition of unity approach by a number of researchers. A micro–macro approach for crack propagation with local partition of unity enrichment was developed by Guidault *et al.* (2004). Haidar *et al.* (2003) proposed a two-scale approach for modelling crack propagation in concrete structures. Recently, Fish and Yuan (2005) developed a new multiscale enrichment based on the concept of partition of unity. A multifield XFEM approach was also presented by Mariano and Stazi (2004) to solve the problem of strain localisation due to crack–microcrack interactions.

Fig. 6.3 illustrates the multiscale methodology for a crack analysis. Part of the domain that requires an accurate approximation is simulated by a fine scale approach (Guidault *et al.* 2004).

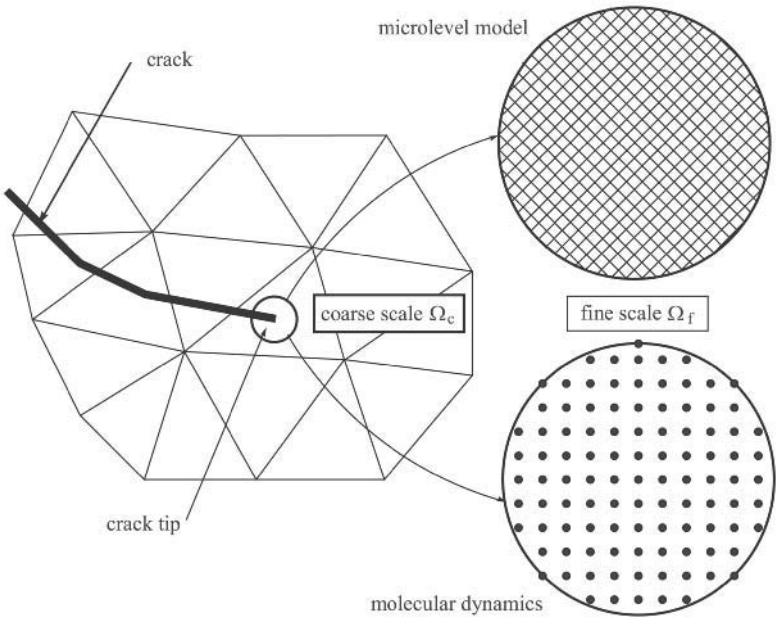

Figure 6.3 A simple illustration of multiscale analysis.

6.5.2 The zoom technique

Consider a solid domain Ω descretized by a finite element mesh, as depicted in Fig. 6.3. The equilibrium equation of the system can be written as:

$$\delta \mathbf{u}^{\mathrm{T}} \int_{\Omega} \mathbf{B}^{T} \boldsymbol{\sigma} \, \mathrm{d}\Omega = \delta \mathbf{u}^{\mathrm{T}} \mathbf{f} \tag{6.88}$$

where $\delta \mathbf{u}^{\mathrm{T}}$ is the variation of nodal displacement vector. The domain is split into a coarse scale linear elastic part Ω_c and a fine scale nonlinear part Ω_f with an interface Γ_{int}. Eq. (6.88) can then be transformed into the followings (Hirari *et al.* 1985):

$$\delta \mathbf{u}_c^{\mathrm{T}} \int_{\Omega_c} \mathbf{B}_c^{\mathrm{T}} \mathbf{D}_c \mathbf{B}_c \mathbf{u}_c \mathrm{d}\Omega + \delta \mathbf{u}_c^{\mathrm{T}} \int_{\Omega_f} \mathbf{B}_c^{\mathrm{T}} \boldsymbol{\sigma}_f \mathrm{d}\Omega = \delta \mathbf{u}^{\mathrm{T}} \mathbf{f} \tag{6.89}$$

and

$$\int_{\Omega_f} \mathbf{B}_f^{\mathrm{T}} \boldsymbol{\sigma}_f \mathrm{d}\Omega = \int_{\Gamma_{\mathrm{int}}} N_f^{\mathrm{T}} \mathbf{p}_f \mathrm{d}\Gamma \tag{6.90}$$

$$\boldsymbol{\sigma}_f = \mathbf{D}_f \mathbf{B}_f \mathbf{u}_f \tag{6.91}$$

where subscripts c, f represent the corresponding variables in coarse and fine scales, respectively.

Applying the boundary conditions along the internal interface of the coarse and fine scales, results in the following form of the governing equations (Haidar *et al.* 2003):

$$\int_{\Omega_c} \mathbf{B}_c^{\mathrm{T}} \boldsymbol{\sigma}_c \mathrm{d}\Omega = \mathbf{f} + \mathbf{f}_c \tag{6.92}$$

$$\mathbf{f}_c + \int_{\Gamma_{\mathrm{int}}} N_f^{\mathrm{T}} \mathbf{t}^{\mathrm{int}} \mathrm{d}\Gamma = 0 \tag{6.93}$$

where $\mathbf{t}^{\mathrm{int}}$ denotes the internal surface traction along the fine/coarse boundary Γ_{int}.

6.5.3 Homogenisation based techniques

The fact that the presence of a crack in a macro–micro or coarse–fine approach may influence both the coarse and fine scales, raises questions regarding the kinematics and the description of forces on the two scales. A solution for keeping the structure of the global coarse scale solution unchanged is to introduce a displacement discontinuity on the fine scale (Guidault *et al.* 2004).

Assume $\mathbf{x}_c$ and $\mathbf{x}_f$ denote the coordinates at coarse and fine scales, respectively. Macroscopic stress and strain fields $\boldsymbol{\sigma}_c, \boldsymbol{\varepsilon}_c$ are determined from the average (homogenised) Ξ microscopic stress and strain fields $\boldsymbol{\sigma}_f$, $\boldsymbol{\varepsilon}_f$,

$$\boldsymbol{\sigma}_c(\mathbf{x}_c) = \Xi\left[\boldsymbol{\sigma}_f(\mathbf{x}_c, \mathbf{x}_f)\right] \tag{6.94}$$

$$\boldsymbol{\varepsilon}_c(\mathbf{x}_c) = \Xi\left[\boldsymbol{\varepsilon}_f(\mathbf{x}_c, \mathbf{x}_f)\right] \tag{6.95}$$

where Ξ is the average/homogenisation operator. One of the important features of homogenisation based methods is that any fine scale solution can be completely described by the coarse scale (Fish and Yuan 2005).

Assuming a periodic microstructure allows for a homogenisation procedure that is built on a single basic cell. Denoting the periodic displacement by $\mathbf{u}_p$, the displacement field can now be decomposed into (Mariano and Stazi 2004)

$$\mathbf{u}(\mathbf{x}_c, \mathbf{x}_f) = \boldsymbol{\varepsilon}_c(\mathbf{x}_c) \cdot \mathbf{x}_f + \mathbf{u}_p(\mathbf{x}_f) \tag{6.96}$$

and the fine scale strain can be computed from its derivative,

$$\boldsymbol{\varepsilon}_f(\mathbf{x}_f) = \boldsymbol{\varepsilon}_c(\mathbf{x}_c) + \boldsymbol{\varepsilon}_p \tag{6.97}$$

The governing equation for a basic cell can then be defined as (Moës *et al.* 2003):

$$\mathrm{div}\,\boldsymbol{\sigma}(\mathbf{x}_f) = 0 \tag{6.98}$$

with

$$\boldsymbol{\sigma}_f(\mathbf{x}_f) = \mathbf{D}_f(\mathbf{x}_f)\boldsymbol{\varepsilon}_f(\mathbf{x}_f) \tag{6.99}$$

where $\mathbf{D}_f$ is the fine scale constitutive matrix. The strain localisation tensor can also be defined:

$$\boldsymbol{\varepsilon}_f(\mathbf{x}_f) = \mathbf{D}_{\text{loc}}(\mathbf{x}_f)\boldsymbol{\varepsilon}_c(\mathbf{x}_c) \tag{6.100}$$

and the effective homogenised stiffness matrix $\mathbf{K}_{\text{hom}}$ as (Moës *et al.* 2003):

$$\mathbf{K}_{\text{hom}} = \Xi\left[\mathbf{D}_f(\mathbf{x}_f)\mathbf{D}_{loc}(\mathbf{x}_f)\right] \tag{6.101}$$

6.5.4 XFEM discretization

In order to allow for variation of the coarse scale solution over the unit cell domain, the dependency of the fine scale functions on the coarse scale solutions should be removed (Fish and Yuan 2005). The partition of unity feature of XFEM allows for replacing $\boldsymbol{\varepsilon}_c(\mathbf{x}_c)$ with an independent set of degrees of freedom.

Alternatively, the standard form of XFEM can be used to approximate the displacement field around any discontinuity boundary:

$$\mathbf{u}^h(\mathbf{x}) = \sum_{j=1}^{n} N_j(\mathbf{x})\mathbf{u}_j + \sum_{k=1}^{m} N_k(\mathbf{x})\psi(\mathbf{x})\mathbf{a}_k \tag{6.102}$$

Moës *et al.* (2003) proposed the following enrichment functions $\psi(\mathbf{x})$ instead of using the conventional Heaviside functions:

$$\psi(\mathbf{x}) = \left|\sum_{i=1}^{m} \phi_i N_i(\mathbf{x})\right| \tag{6.103}$$

and

$$\psi(\mathbf{x}) = \sum_{i=1}^{m} \left|\phi_i\right| N_i(\mathbf{x}) - \left|\sum_{i=1}^{m} \phi_i N_i(\mathbf{x})\right| \tag{6.104}$$

The rest of the procedure remains similar to the finite element modelling of multiscale problems. For further details see Moës *et al.* (2003), Mariano and Stazi (2004) and Fish and Yuan (2005).

6.6 MULTIPHASE XFEM

6.6.1 Basic formulation

Consider a domain Ω consisting of two phases of fluid Ω_f and solid Ω_s, as depicted in Fig. 6.4.

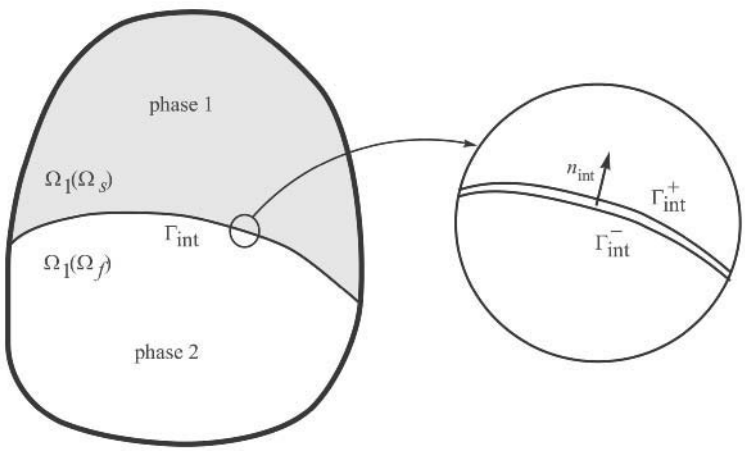

Figure 6.4 A two-phase problem with an internal interface.

Governing equations for the temperature T evolution in the fluid and solid phases can be defined as (Zabaras *et al.* 2006):

$$\frac{\partial T}{\partial t} + \mathbf{v}_{\text{n}} \cdot \nabla T = \alpha_f \nabla^2 T \qquad \mathbf{x} \in \Omega_f \tag{6.105}$$

$$\frac{\partial T}{\partial t} = \alpha_s \nabla^2 T \qquad \mathbf{x} \in \Omega_s \tag{6.106}$$

where α_f and α_s are thermal diffusivities of liquid and solid phases, respectively, and $\mathbf{v}_{\text{n}}$ is the normal interface speed. The conditions on solid–fluid interface Γ_{int} can be expressed as:

$$T_s = T_f = T_{\text{m}} - \varepsilon_{\text{c}} \rho_{\text{int}} - \varepsilon_{\text{v}} v \qquad \text{on } \Gamma_{\text{int}} \tag{6.107}$$

and the jump in the heat flux normal to the interface

$$< q > = q^{+} - q^{-} = -H_{\text{l}} \mathbf{v}_{\text{n}} \qquad \text{on } \Gamma_{\text{int}} \tag{6.108}$$

where ε_c and ε_v are the surface tension coefficient and the kinetic mobility coefficients, respectively, and ρ_{int} is the curvature of the propagating interface. H_l is the latent heat for the phase change, T_m is the melting/fusion temperature and q is the heat flux.

Neglecting any material transport caused by an expansion or shrinkage due to phase change or buoyancy effects, the energy conservation equation in Ω can be defined as (Ji *et al*. 2002):

$$\rho_i \frac{\partial}{\partial t}(c_i T_i) = \nabla \cdot (k_i \nabla T_i) + s_i \quad \text{in } \Omega_i, \ i = s, f \tag{6.109}$$

where ρ, c, k and s are density, specific heat, thermal conductivity, and the heat source, respectively. The conditions on solid–fluid interface Γ_{int} can then be expressed as:

$$T_s = T_f = T_m \quad \text{on } \Gamma_{int} \tag{6.110}$$

$$< q > = q^+ - q^- = \left[k_f \nabla T_f - k_s \nabla T_s\right] \cdot \mathbf{n}_{int} \quad \text{on } \Gamma_{int} \tag{6.111}$$

Chessa *et al.* (2002) developed a backward difference formula for the time derivative to derive the following weak form for solving Eq. (6.109):

$$\begin{aligned} &\frac{1}{\Delta T}\int_\Omega \delta T \rho\left[(cT)^{n+1} - (cT)^n\right] d\Omega + \int_\Omega \nabla \delta T \cdot (k \nabla T)^{n+1} d\Omega \\ &\quad = -\int_{\Gamma_q} \delta T q^{n+1} d\Gamma + \int_\Omega \delta T s^{n+1} d\Omega \end{aligned} \tag{6.112}$$

Solid and fluid parameters are used for evaluation of Eq. (6.112) at corresponding gauss integration points.

Alternatively, Ji *et al.* (2002) used a trapezoidal time stepping rule. They also proposed an independent approximation for the time derivative of the temperature field $T^n_{,t}(\mathbf{x})$ to account for its discontinuity across the phase boundary using the Heaviside function, $H(\mathbf{x})$ (Ji *et al.* 2002):

$$\frac{\partial T^n(\mathbf{x})}{\partial t} = \sum_{i=1}^{4}\left(M_i^1 a_i^1 + M_i^2 a_i^2 + M_i^3 a_i^3\right) + \sum_{k=1}^{m}\left(M_k^1 \mathbf{b}_k\right) H(\mathbf{x}) \tag{6.113}$$

where M_i^j are tensor products of the one-dimensional Hermite interpolants (Ji *et al.* 2002).

6.6.2 XFEM approximation

The extended finite element approximation for the temperature field $T^h(\mathbf{x},t)$ can be defined as:

$$T^h(\mathbf{x},t)=\sum_{j=1}^{n}N_j(\mathbf{x})T_j(t)+\sum_{k=1}^{m}N_k(\mathbf{x})\psi(\mathbf{x},t)\mathbf{a}_k(t)=\mathbf{N}^h(\mathbf{x})\overline{T}(t) \tag{6.114}$$

where $\mathbf{a}_k$ are the added set of degrees of freedom to the standard finite element model, $\psi(\mathbf{x})$ is the discontinuous enrichment function and $\mathbf{N}^h$ can be regarded as the global matrix of shape functions:

$$\overline{T}(t)=\left\{T_1(t),T_2(t),\ldots,T_n(t),\mathbf{a}_1(t),\ldots,\mathbf{a}_m(t)\right\}^{\mathrm{T}} \tag{6.115}$$

$$\mathbf{N}^h(\mathbf{x})=\left\{N_1(\mathbf{x}),N_2(\mathbf{x}),\ldots,N_n(\mathbf{x}),N_1(\mathbf{x})\,\psi(\mathbf{x},t),\ldots,N_m(\mathbf{x})\,\psi(\mathbf{x},t)\right\}^{\mathrm{T}} \tag{6.116}$$

Arbitrary material interfaces can be modelled through the use of an enrichment function with discontinuous derivatives (Ji *et al.* 2002). This can be examined by the gradient of the XFEM approximation Eq. (6.114),

$$\nabla T^h(\mathbf{x},t)=\sum_{j=1}^{n}\nabla N_j(\mathbf{x})T_j(t)+\sum_{k=1}^{m}\left[\nabla N_k(\mathbf{x})\psi(\mathbf{x},t)+N_k(\mathbf{x})\nabla\psi(\mathbf{x},t)\right]\mathbf{a}_k(t) \tag{6.117}$$

which reveals that gradient discontinuities will arise in the approximation for the temperature field wherever they exist in the enrichment function. As a result, weak discontinuous enrichment functions similar to Eq. (3.61) have to be adopted.

Eq. (6.114) is not an interpolation and $T_j(t)$ do not return the exact nodal temperatures. An alternative solution is to use the interpolating XFEM formulation:

$$T^h(\mathbf{x},t)=\sum_{j=1}^{n}N_j(\mathbf{x})T_j(t)+\sum_{k=1}^{m}N_k(\mathbf{x})\left[\psi(\mathbf{x},t)-\psi_k(\mathbf{x},t)\right]\mathbf{a}_k(t) \tag{6.118}$$

Substituting Eq. (6.114) into the weak form (6.112) results in the following discretized system of equations (Chessa *et al.* 2002):

$$\frac{1}{\Delta t}\mathbf{M}\overline{T}^{n+1}+\mathbf{K}\overline{T}^{n+1}=\frac{1}{\Delta t}\overline{\mathbf{M}}\overline{T}^{n}+\mathbf{f}_q^{n+1}+\mathbf{f}_s^{n+1} \tag{6.119}$$

where

$$\mathbf{K}=\int_{\Omega}\left(\mathbf{B}^{h,n+1}\right)^{\mathrm{T}}k^{n+1}\mathbf{B}^{h,n+1}\mathrm{d}\Omega \tag{6.120}$$

$$\mathbf{M}=\int_{\Omega}\left(\mathbf{N}^{h,n+1}\right)^{\mathrm{T}}c^{n+1}\rho\mathbf{N}^{h,n+1}\mathrm{d}\Omega \tag{6.121}$$

$$\overline{\mathbf{M}} = \int_{\Omega} \left(\mathbf{N}^{h,n+1}\right)^{\mathrm{T}} c^n \rho \mathbf{N}^{h,n} \mathrm{d}\Omega \tag{6.122}$$

$$\mathbf{f}_q^{n+1} = -\int_{\Gamma_q} \left(\mathbf{N}^{h,n+1}\right)^{\mathrm{T}} q^{n+1} \mathrm{d}\Gamma \tag{6.123}$$

$$\mathbf{f}_s^{n+1} = -\int_{\Omega} \left(\mathbf{N}^{h,n+1}\right)^{\mathrm{T}} s^{n+1} \mathrm{d}\Gamma \tag{6.124}$$

with

$$\mathbf{B}^{h,n+1} = \nabla \mathbf{N}^{h,n+1} \tag{6.125}$$

The level set method is used to explicitly track Γ_{int}. The location of the boundary Γ_{int} is defined with a signed distance function ϕ. The basic idea is to determine the movement of the interface with a correct speed $\mathbf{v}$ to satisfy (6.105) in a weak form. For further details see Chessa *et al.* (2002) and Ji *et al.* (2002).

6.6.3 Two-phase fluid flow

Chessa and Belytschko (2003a, 2003b) developed an extended finite element procedure for simulation of two-phase fluids. Consider a domain Ω partitioned into two time-varying subdomains Ω_1 and Ω_2, corresponding to fluids 1 and 2, respectively, with an interface Γ_{int} between the two phases, as depicted in Fig. 6.4.

In the absence of surface tractions, the Navier–Stokes equations for a two-phase incompressible flow take the following forms for the velocity field $\mathbf{v}$,

$$\rho\left[\frac{\partial \mathbf{v}}{\partial t} + \nabla \cdot (\mathbf{v} \otimes \mathbf{v}) - \mathbf{g}\right] - \nabla \cdot \boldsymbol{\sigma} = 0 \tag{6.126}$$

$$\nabla \cdot \mathbf{v} = 0 \tag{6.127}$$

where ρ is the fluid density, $\mathbf{g}$ is the applied body force, and $\boldsymbol{\sigma}$ is the Cauchy stress tensor,

$$\boldsymbol{\sigma} = \boldsymbol{\tau} - p\mathbf{I} \tag{6.128}$$

$$\boldsymbol{\tau} = \mu(\nabla \mathbf{v} + \mathbf{v}\nabla) \tag{6.129}$$

which is valid for Newtonian fluids. The governing Eq. (6.126) can now be rewritten as (Lin *et al.* 2005):

$$\rho\left[\frac{\partial \mathbf{v}}{\partial t}+\nabla\cdot(\mathbf{v}\otimes\mathbf{v})\right]+\nabla p=\nabla\cdot(\mu\nabla\mathbf{v})+\rho\mathbf{g} \tag{6.130}$$

The main boundary conditions can be defined as:

$$\mathbf{v}(\mathbf{x},t)=\overline{\mathbf{v}} \quad \text{on} \quad \Gamma_v \tag{6.131}$$

$$\mathbf{n}\cdot\boldsymbol{\sigma}(\mathbf{x},t)=\mathbf{f}^t \quad \text{on} \quad \Gamma_t \tag{6.132}$$

or in terms of the hydrostatic pressure p and deviatoric stress $\boldsymbol{\tau}$:

$$p(\mathbf{x},t)=\overline{p} \quad \text{on} \quad \Gamma_t \tag{6.133}$$

$$\mathbf{n}\cdot\boldsymbol{\tau}(\mathbf{x},t)=\mathbf{f}^t \quad \text{on} \quad \Gamma_t \tag{6.134}$$

The internal boundary conditions are expressed as:

$$<\boldsymbol{\sigma}\cdot\mathbf{n}_{\text{int}}>=0 \quad \text{on} \quad \Gamma_{\text{int}} \tag{6.135}$$

$$<\mathbf{v}>=0 \quad \text{on} \quad \Gamma_{\text{int}} \tag{6.136}$$

6.6.4 XFEM approximation

It is obvious that discontinuous derivatives of velocity and pressure may occur at the interface (Kolke *et al.* 2003). To capture these discontinuous gradient fields, the following weak discontinuity form of XFEM approximation is adopted:

$$\mathbf{v}^h(\mathbf{x},t)=\sum_{j=1}^{n}N_j(\mathbf{x})\mathbf{v}_j(t)+\sum_{k=1}^{m}N_k(\mathbf{x})\psi_k(\mathbf{x},t)\mathbf{a}_k(t)=\mathbf{N}^h(\mathbf{x})\mathbf{V}(t) \tag{6.137}$$

where $\mathbf{N}^h(\mathbf{x})$ and $\mathbf{V}(t)$ are the global shape functions and degrees of freedom, respectively, and the enrichment function $\psi_k(\mathbf{x},t)$ is defined in terms of the level set distance function $\phi(\mathbf{x},t)$ (see Eq. (3.62)):

$$\psi_k(\mathbf{x},t)=\left|\phi(\mathbf{x},t)\right|-\left|\phi(\mathbf{x}_k,t)\right| \tag{6.138}$$

Chessa and Belytschko (2003b) derived the following discretized form of the governing equations using a characteristic based split (CBS) algorithm (Chorin 1968 and Zienkiewicz and Codina 1995),

$$\overline{\mathbf{M}}\mathbf{V} = \mathbf{M}\mathbf{V}^n - \Delta t\left[\mathbf{C}\mathbf{V}^n + \mathbf{K}\mathbf{V}^n - \mathbf{f}^n - \frac{\Delta}{2}\left(\mathbf{K}_u\mathbf{V}^n + \mathbf{f}_s^n\right)\right] \tag{6.139}$$

$$\Delta t\,\mathbf{K}_p p^{n+1} = \mathbf{G}_u\mathbf{V} - \mathbf{f}_p \tag{6.140}$$

$$\mathbf{V}^{n+1} = \mathbf{V} - \Delta t\,\mathbf{M}^{-1}\mathbf{G}^T p^{n+1} \tag{6.141}$$

where (Chessa and Belytschko 2003b)

$$\mathbf{K} = \int_\Omega \left(\mathbf{B}^{h,n+1}\right)^{\mathrm{T}} \mu^n \begin{bmatrix} 1 & -1 & 0 \\ -1 & 1 & 0 \\ 0 & 0 & 1 \end{bmatrix} \mathbf{B}^{h,n}\mathrm{d}\Omega \tag{6.142}$$

$$\mathbf{K}_u = -\frac{1}{2}\int_\Omega \left(\nabla^{\mathrm{T}}\left(\mathbf{v}^n\mathbf{N}^{h,n+1}\right)\right)^{\mathrm{T}} \rho^n \left(\nabla^{\mathrm{T}}\left(\mathbf{v}^n\mathbf{N}^{h,n}\right)\right)\mathrm{d}\Omega \tag{6.143}$$

$$\mathbf{K}_p = \int_\Omega \mathbf{B}^{\mathrm{T}}\mathbf{B}\,\mathrm{d}\Omega \tag{6.144}$$

$$\mathbf{M} = \int_\Omega \left(\mathbf{N}^{h,n+1}\right)^{\mathrm{T}} \rho^n \mathbf{N}^{h,n+1}\mathrm{d}\Omega \tag{6.145}$$

$$\overline{\mathbf{M}} = \int_\Omega \left(\mathbf{N}^{h,n+1}\right)^{\mathrm{T}} \rho^n \mathbf{N}^{h,n1}\mathrm{d}\Omega \tag{6.146}$$

$$\mathbf{C} = \int_\Omega \left(\mathbf{N}^{h,n+1}\right)^{\mathrm{T}} \nabla\left(\rho^n\mathbf{v}^n\mathbf{N}^{h,n}\right)\mathrm{d}\Omega \tag{6.147}$$

$$\mathbf{G} = \int_\Omega \left(\mathbf{B}^{h,n+1}\right)^{\mathrm{T}} \mathbf{N}^h\mathrm{d}\Omega \tag{6.148}$$

$$\mathbf{G}_u = \int_\Omega \left(\mathbf{B}^{h,n}\right)^{\mathrm{T}} \rho^n N^n\mathrm{d}\Omega \tag{6.149}$$

$$\mathbf{f} = \int_\Omega \mathbf{N}^{h,n+1}\rho g\,\mathrm{d}\Omega + \int_{\Gamma_{\mathrm{t}}} \mathbf{N}^{h,n+1}\bar{\mathbf{t}}\,\mathrm{d}\Gamma \tag{6.150}$$

$$\mathbf{f}_p = \int_{\Gamma_{\mathrm{t}}} \mathbf{N}^{\mathrm{T}}\mathbf{n}\cdot\mathbf{v}^{n+1}\mathrm{d}\Gamma \tag{6.151}$$

with

$$\mathbf{B} = \nabla\mathbf{N} \tag{6.152}$$

$$\mathbf{B}^h = \nabla \mathbf{N}^h \tag{6.153}$$

Wagner *et al.* (2001, 2003) developed new formulations based on the XFEM enrichment procedure to simulate the fluid flow around rigid particles. The fluid flow was governed by the Stokes formulation, and a lubrication theory was adopted to allow for a combined fluid-particle model.

Chapter 7

XFEM Flow

7.1 INTRODUCTION

Previous chapters have comprehensively discussed various aspects of the extended finite element methodology for fracture analysis of structures. Other aspects of XFEM for simulation of different engineering and physical applications have also been addressed.

This chapter is designed to summarise a successful XFEM application in a step-by-step algorithmic approach. The aim has been to briefly provide a general overview of the whole process of code implementation for the XFEM methodology.

It is not intended to go into the details of the programming techniques, as they depend on the artistry and experience of the programmer and the level of smartness and genius put forward. Additionally, no specific XFEM source code is provided, and the reader may refer to a number of freely available source codes, if necessary. Instead, only the general algorithms and the main solution procedures are explained.

First, the general parts of a finite element analysis are described briefly. They cover the linear elastic solution, large deformation and elastoplastic analysis within a conventional finite element analysis.

Then, the basic steps of XFEM simulation are provided. Subsections are included on front tracking algorithms, criteria for selection of enrichment nodes/elements, definition and determination of various enrichment functions, including crack tip asymptotic functions, strong and weak discontinuous enrichments, biomaterial and orthotropic enrichments, and elastoplastic enrichments algorithms.

The next section deals with the items related to solving governing equations, which includes solution of static simultaneous equations, dynamic time integration techniques, and the crack length control for large deformation snap-back response.

The post-processing section addresses the main objectives of a fracture analysis by determining the mixed mode stress intensity factors, and controlling the crack growth criteria. Other applications of XFEM require a redesign for this section.

The final section briefly discusses the configuration update. Such an update is necessary if a large deformation analysis is performed or if a crack propagation criterion is met. The update procedure may be involved with geometric entities, or require the handling of complex data structures for updating the internal variables.

7.2 AVAILABLE OPEN-SOURCE XFEM

There are several freely available XFEM software packages on the internet. Both executable files and open-source files may be obtained and used, of course with great caution. FORTRAN, C++ and MATLAB source codes are available and may be used appropriately.

MATLAB is popular and highly appropriate for the development stages of any novel numerical approach. It facilitates the vector and matrix manipulations and is capable of powerful debugging of the code. However, for practical large-scale simulations, a move to FORTRAN or C++ implementations seems unavoidable.

7.3 FINITE ELEMENT ANALYSIS

7.3.1 Defining the model

The first step is to define the finite element model:

1. Define the boundary of the physical model.
2. Define different zones of the model, for which different finite element sizes are to be used. This is usually based on the experience of the analyst and an anticipation of the potential concentration or singular regions.
3. Ignore the presence of any predefined crack, hole or interface if the XFEM methodology is used.
4. Define the loading conditions:
    a. Static loading.
    b. Quasi-static incremental loading conditions.
    c. Loading–time curves for dynamic analysis.
5. Assign the appropriate material models to the finite elements.
    a. Linear elastic model.
    b. Nonlinear elastoplastic models.
6. Define the boundary conditions.
    a. Essential boundary conditions (displacements).
    b. Natural boundary conditions (tractions).
7. Define the contact surfaces.

7.3.2 Creating the finite element mesh

The finite element model is constructed according to the following steps:

1. Generate the finite element mesh using a conventional structured or unstructured mesh generator based on descriptions of Section 7.3.1.

2. The mesh generation is performed while ignoring the presence of any cracks or discontinuity.
3. There is basically no major difference between the triangular or quadrilateral elements in XFEM.
4. Both linear and higher-order finite elements can be used. Linear elements, however, have been more common and easier to implement.
5. The data structure related to the degrees of freedom should be designed to account for the additional variable number of unknowns in XFEM.

7.3.3 Linear elastic analysis

The following steps are usually taken for a classical linear elastic finite element analysis:

1. Determination of the equivalent nodal force vector.
2. Derivation of the stiffness matrix:

$$\mathbf{K} = \int \mathbf{B}^{\mathrm{T}}\mathbf{D}\mathbf{B}\,\mathrm{d}\Omega \tag{7.1}$$

   a. Constructing element stiffness matrices.

$$\mathbf{K}^{e} = \sum \left(\mathbf{B}^{\mathrm{T}}\mathbf{D}\mathbf{B}\right)_{g} \det \mathbf{J}\; W_{g} \tag{7.2}$$

   b. Assembling $\mathbf{K}^{e}$ into the global stiffness matrix $\mathbf{K}$.
3. Imposition of boundary conditions.
4. Solving the set of simultaneous equations $\mathbf{K}\mathbf{u} = \mathbf{f}$ for the unknown field variable $\mathbf{u}$ (displacements).
5. Computing the nodal internal forces:

$$\mathbf{f} = \int \mathbf{B}^{\mathrm{T}}\boldsymbol{\sigma}\; \mathrm{d}\Omega \tag{7.3}$$

7.3.4 Large deformation

There are a number of advanced algorithms for the finite element analysis in the large deformation regime. Here, a rather simple updated Lagrangian approach based on the predictor-corrector methodology is explained:

1. The loading is defined in a number of increments. For each increment, the following steps have to be taken:
2. Beginning of the iteration loop.
   a. Compute the stiffness matrix of the system using a standard or modified Newton–Raphson approach or a secant stiffness.

b. Solve the set of simultaneous equations for the displacements.
c. Compute the strain and stiffness tensors, based on the nonlinear Green strain.
d. Compute the equivalent internal nodal force vector.
e. Determine the residual force vector (difference between the internal nodal force vector and the external loading vector). This is also used as part of the loading for the next iteration.
f. Check for a convergence criterion based on appropriate norm of displacement, residual, energy, etc.
g. GOTO 3 if the convergence criterion is met.
h. GOTO 2 for new trial iteration.

3. Update the geometry.
4. GOTO 1 for the next incremental loading.

7.3.5 Nonlinear (elastoplastic) analysis

In order to explain the methodology of an elastoplastic update procedure, a rather simple description of the elastic prediction-plastic correction approach is briefly explained:

1. The external force vector is divided into a predefined number of load increments. For each increment, the following steps are considered.
2. Beginning of the iteration loop.
    a. Determine the initial or tangential stiffness matrix.
    b. Solve the set of simultaneous equations to compute the displacements.
    c. Assume a Green definition of strain tensor, and compute the strain field at the quadrature points.
    d. Compute a trial stress increment by assuming an elastic material response.
    e. Compute the total trial stress at the quadrature points.
    f. Perform the stress update procedure:
        i. Compute the failure criterion.
        ii. Follow the linearisation procedure to determine new stress state.
        iii. Determine new consistent stiffness.
        iv. Check for the stress convergence.
        v. If the convergence is not met, return to (2d) using an updated material stiffness.
    g. The final updated stress state is available at the end of the iteration.
    h. Compute the nodal internal force vector from the elasoplastic updated stress state.
    i. Evaluate an index of convergence using an appropriate global norm.
    j. If the convergence is not achieved, GOTO 2.
3. Update the geometry to include the effects of large deformation.

7.3.6 Material constitutive matrix

If a material point, usually a Gauss integration point, is due to undergo plastic deformations, the material stiffness matrix must be updated accordingly. The procedure should be basically designed for any specified type of plastic rule.

7.4 XFEM

7.4.1 Front tracking

In order to define various object entities such as cracks, holes, etc., an automatic procedure is required to first define the so-called front within an independent finite element mesh, and then to track any potential changes that may occur in time or subject to incremental loading conditions. The following steps are followed:

1. Defining various object entities:
    a. Cracks
    b. Holes
    c. Inclusions
    d. Interfaces
    e. …
2. Objects can be represented by explicit mathematical functions, adopting general curve defining algorithms such as B-splines, or as a collection of discrete points.
3. Tracking potential changes of the object geometry (front).

Tree data structures are required for efficient data management and reduction of various search times by invoking a hierarchical domain decomposition and data structure at the same time.

7.4.1.1 *Standard method*

For simple shaped cracks, the problem of defining and tracking the crack evolution is simple and straightforward and does not require any sophisticated tracking approach. In the case of more complicated problems, the standard approach for front tracking can be summarised as:

1. Define the front by one of the B-spline, NURBS or similar techniques by setting a number of marker nodes on the front.
2. Define a regular set of finite difference grid on the front.
3. Move the marker points in accordance with the finite difference approximation of the equation of the motion.

7.4.1.2 *Level set approach*

The level set method solves the problem of a moving interface on a fixed Eulerian mesh. The following steps are followed to define the level set approach:

1. Define the level set ϕ in terms of the signed distance function ξ

$$\phi(\mathbf{x}) = \xi(\mathbf{x}) \tag{7.4}$$

2. The front can be defined as the zero level set $\phi = 0$.
3. The level set ϕ is descretized in terms of the nodal values

$$\phi(\mathbf{x}) = \sum_{j=1}^{n} N_j(\mathbf{x})\phi(\mathbf{x}_j) \tag{7.5}$$

4. The Hamilton–Jacobi equation of motion (3.131) is solved for determining the front evolution with the velocity v

$$\dot{\phi} + \phi_{,i}\, \mathbf{v}_{,i} = 0 \tag{7.6}$$

or in an incremental form

$$\phi^{n+1} = \phi^{n} - \Delta t_{,i}^{n}\, \mathbf{v}_{,i}^{n} \tag{7.7}$$

7.4.1.3 *Vector level set approach*

A crack growth is modelled by appropriately updating the crack tip level set ψ and crack level set ϕ. At a step n:

1. The prescribed velocity vector $\mathbf{v} = (\mathbf{v}_x, \mathbf{v}_y)$ (normal to the front interface) is known.
2. Determine the rotated level set of ϕ_n^k

$$\phi^{k,r} = (x - x_k)\frac{\mathbf{v}_x}{\|\mathbf{v}\|} + (y - y_k)\frac{\mathbf{v}_y}{\|\mathbf{v}\|} \tag{7.8}$$

3. Determine ψ_{n+1}

$$\psi_{n+1} = \pm\left|(x - x_k)\frac{\mathbf{v}_y}{\|\mathbf{v}\|} + (y - y_k)\frac{\mathbf{v}_x}{\|\mathbf{v}\|}\right| \tag{7.9}$$

4. The updated location of the crack tip ϕ_{n+1}^k can be computed:

$$\phi_{n+1}^{k} = \phi^{k,r} - \Delta t \left\| \mathbf{v} \right\| \tag{7.10}$$

5. Update ϕ_{n+1} for more than one crack tip:

$$\phi(\mathbf{x},t) = \max_{k}(\phi^{k}) \tag{7.11}$$

6. The location of the new crack tip k is determined by finding the intersection of the zero level sets of ϕ_{n+1}^{k} and ψ_{n+1}.

7.4.1.4 *Fast marching method*

The following simple procedure describes the way a fast marching algorithm is constructed:

1. Initialise the crack front given by $\phi^{-1}(0)$.

$$\phi^{-1}(0) = \varphi_1^{-1}(0) \tag{7.12}$$

$$\left\| \nabla \varphi_1 \right\| = 1 \tag{7.13}$$

2. Use the FMM to compute the signed distance function.
3. Compute crack front speed $\mathbf{v}$ using the XFEM.
4. Use the FMM to extend the front speed:

$$\nabla \mathbf{v} \cdot \nabla \varphi_1 = 0 \tag{7.14}$$

5. Use the FMM to compute the location of the advancing crack front at time Δt:

$$\left\| \nabla \phi \right\| = \frac{1}{\mathbf{v}(\mathbf{x})} \tag{7.15}$$

6. Advance crack front by the time step size Δt

$$\phi = \phi - \Delta t \tag{7.16}$$

7.4.2 Enrichment detection

An efficient XFEM analysis requires a systematic algorithm for detection of the nodes or elements for enrichment. Such an algorithm must take into account:

1. Different enrichment types (crack tip, discontinuity, etc.) in the detection procedure.

2. The detection approach must also be capable of properly defining the transition domain between the classical finite element and the enriched domain, and specifying normal and enriched nodes associated to any transitional element.
3. The detection process must also be updated in time by any change in crack path due to the crack propagation.
4. Some of the previously enriched nodes may no longer be a candidate for enrichment or may require a different type of enrichment function.
5. The detection procedure should also prepare a list of interacted elements and nodes to facilitate application of the enrichment functions and assembly procedures.
6. A criterion is required to decide on whether to include interior nodes of higher-order elements in the enrichment process.
7. A fixed enrichment domain such as a circle centred at the crack tip can be used to determine the candidates for crack tip enrichments.
8. For Heaviside enrichments, only the nodes that belong to an element split by a discontinuity may be used.
9. Alternatively, a boundary zone close to the interface can well work for specific problems.

7.4.3 Enrichment functions

Both the enrichment functions and their derivatives should be evaluated. The following sections summarise the most important enrichment functions.

7.4.3.1 *Isotropic crack tip enrichment*

Eq. (3.27) for the isotropic crack tip enrichment, and Eqs. (3.101)–(3.110) for the derivatives can be used.

$$\{F_l(r,\theta)\}_{l=1}^{4} = \left\{\sqrt{r}\cos\frac{\theta}{2}, \sqrt{r}\sin\frac{\theta}{2}, \sqrt{r}\sin\theta\cos\frac{\theta}{2}, \sqrt{r}\sin\theta\sin\frac{\theta}{2}\right\} \tag{7.17}$$

7.4.3.2 *Orthotropic crack tip enrichment*

Three different classes of orthotropic crack tip enrichment functions have been presented in Chapter 4. The first two classes are associated with only part of the composite problems, whereas the third one can be adopted for any orthotropic crack simulation.

The procedure for an inclined crack in an orthotropic medium can be summarised as:

1. Select the appropriate class of orthotropic formulations.
2. Determine the function g_j and angles θ_j from Eqs. (4.49)–(4.50), (4.74)–(4.75) or (4.95)–(4.96) for class I, II and III orthotropic XFEM, respectively.

3. Use Eq. (4.99) to compute the orthotropic enrichment functions:

$$F(r,\theta)=\left\{\sqrt{r}\cos\frac{\theta_1}{2}\sqrt{g_1(\theta)},\sqrt{r}\cos\frac{\theta_2}{2}\sqrt{g_2(\theta)},\right.$$
$$\left.\sqrt{r}\sin\frac{\theta_1}{2}\sqrt{g_1(\theta)},\sqrt{r}\sin\frac{\theta_2}{2}\sqrt{g_2(\theta)}\right\} \tag{7.18}$$

7.4.3.3 *Strong discontinuity enrichment*

Eqs. (3.47) and (3.57) or their smoothed approximations can be used as the strong discontinuity enrichments:

$$\psi(\mathbf{x})=H(\xi)=\begin{cases}1 & \forall\xi>0\\ 0 & \forall\xi<0\end{cases} \tag{7.19}$$

$$\psi(\mathbf{x})=H(\xi)=\operatorname{sign}(\xi)=\begin{cases}1 & \forall\xi>0\\ -1 & \forall\xi<0\end{cases} \tag{7.20}$$

For the derivatives, Eqs. (3.94) and (3.95) should also be used.

7.4.3.4 *Weak discontinuity enrichment*

In order to define a weak discontinuity enrichment, Eqs. (3.61) and (3.62) are used.

$$\psi(\mathbf{x})=\chi_k(\mathbf{x})=\left|\xi(\mathbf{x})\right|-\left|\xi(\mathbf{x}_k)\right| \tag{7.21}$$

The derivatives are computed similarly.

7.4.3.5 *Frictional contact interface*

Most of the existing studies on contact interfaces have used the Heaviside enrichment to simulate a sliding contact interface. This will then resemble the strong or weak discontinuity enrichments. It is anticipated that a new class of contact interface enrichment functions are evolving from the available analytical solutions. When published, they should replace the conventional approach to contact enrichment.

7.4.3.6 *Bimaterial interface enrichment*

Various types of bimaterial interfaces such as solid–solid, solid–fluid and fluid–fluid interfaces can be considered. Each one may require its own set of enrichment functions. For a solid–solid bimaterial interface, Eq. (6.23) is adopted:

$$\begin{aligned}\left[F_l^j(\mathbf{x})\right]=\Bigg\{&\sqrt{r}\cos(\omega\log r)e^{-\omega\theta}\sin\frac{\theta}{2},\sqrt{r}\cos(\omega\log r)e^{-\omega\theta}\cos\frac{\theta}{2},\\&\sqrt{r}\cos(\omega\log r)e^{\omega\theta}\sin\frac{\theta}{2},\sqrt{r}\cos(\omega\log r)e^{\omega\theta}\cos\frac{\theta}{2},\\&\sqrt{r}\sin(\omega\log r)e^{-\omega\theta}\sin\frac{\theta}{2},\sqrt{r}\sin(\omega\log r)e^{-\omega\theta}\cos\frac{\theta}{2},\\&\sqrt{r}\sin(\omega\log r)e^{\omega\theta}\sin\frac{\theta}{2},\sqrt{r}\sin(\omega\log r)e^{\omega\theta}\cos\frac{\theta}{2},\\&\sqrt{r}\cos(\omega\log r)e^{\omega\theta}\sin\frac{\theta}{2}\sin\theta,\sqrt{r}\cos(\omega\log r)e^{\omega\theta}\cos\frac{\theta}{2}\sin\theta,\\&\sqrt{r}\sin(\omega\log r)e^{\omega\theta}\sin\frac{\theta}{2}\sin\theta,\sqrt{r}\sin(\omega\log r)e^{\omega\theta}\cos\frac{\theta}{2}\sin\theta\Bigg\}\end{aligned} \tag{7.22}$$

7.4.3.7 *Elastoplastic enrichment*

Elastoplastic enrichment functions are computed from Eqs. (3.68)–(3.71):

$$\left[F_l^j(\mathbf{x})\right]=r^{\frac{1}{n+1}}\left\{\left(\cos\frac{k\theta}{2},\sin\frac{k\theta}{2}\right);k\in[1,\ 3,\ 5,\ 7]\right\} \tag{7.23}$$

An iterative approach is required to perform the elastoplastic stress update procedure in combination with the elastoplastic crack enrichment functions:

1. A trial solution is computed from the elastic solution.
2. XFEM enrichments are applied and the new set of incremental equilibrium equations is formed.
3. The solution for the displacement increments is used to evaluate the strain and stress rates (increments).
4. The Newton–Raphson approach should be used with a consistent elastoplastic material modulus to satisfy both the equilibrium and consistency conditions in an iterative converging procedure (see Section 7.3.3).
5. The method should be adapted according to each specific elastoplasic material model.

7.4.4 Ramp (transition) functions

The ramp functions are defined according to Eq. (3.40). Linear and spline functions are frequently used. Derivatives of the ramp functions are also required.

1. Define the appropriate ramp function to satisfy the C^0 or C^1 continuity between the enriched and classical finite element approximations.
2. Linear and spline functions are usually preferred.
3. The size of the transition zone should be selected.
4. Compute the necessary terms associated with the transition domain.
5. The number of enriched and classical nodes in a transitional finite element may suddenly change in nearby elements. Special precautions are required to avoid potential mistakes in defining the correct numbers for different summations.

7.4.5 Evaluation of the B matrix

Evaluation of the **B** matrix is an essential part of constructing the stiffness matrix. This is achieved by computing the derivative of the finite element shape function and the enrichment functions.

$$\mathbf{B}_i^{\mathbf{u}} = \begin{bmatrix} N_{i,x} & 0 \\ 0 & N_{i,y} \\ N_{i,y} & N_{i,x} \end{bmatrix} \tag{7.24}$$

$$\mathbf{B}_i^{\mathbf{a}} = \begin{bmatrix} (N_i H)_{,x} & 0 \\ 0 & (N_i H)_{,y} \\ (N_i H)_{,y} & (N_i H)_{,x} \end{bmatrix} \tag{7.25}$$

$$\mathbf{B}_i^{\alpha} = \begin{bmatrix} (N_i F_\alpha)_{,x} & 0 \\ 0 & (N_i F_\alpha)_{,y} \\ (N_i F_\alpha)_{,y} & (N_i F_\alpha)_{,x} \end{bmatrix} \tag{7.26}$$

7.5 NUMERICAL INTEGRATION

To form the discretized set of equilibrium equations and the system matrices, numerical integration techniques have to be used to evaluate the existing integrals defined over the global or local domains. The Gauss quadrature rule is usually preferred for finite element analysis.

The Gauss quadrature rule can provide accurate numerical solutions for integrands of polynomial nature. Unfortunately, this is not the case for enriched finite element solutions as they include highly nonlinear and even discontinuous functions. Two approaches are available for improving the accuracy of the Gauss integration scheme.

7.5.1 Sub-quads

In this method:

1. The element domain is uniformly partitioned into a regular subgrid of quadrature elements (sub-quads).
2. Each sub-quad is assigned a predefined set of Gauss quadrature points and weights.
3. The integrand and the weight function are computed at each Gauss point.
4. The final solution of the integral is obtained from the summation over all Gauss points within the element.
5. A node is enriched only if there exists at least one Gauss point on both sides of the crack.

7.5.2 Sub-triangles

This is an alternative to the sub-quad approach by construction of a local mesh of triangular quadrature elements between the crack and the element boundaries:

1. Determine whether the crack crosses an element.
2. If the area between the crack and a corner node is very small compared to the element area, neglect the presence of crack and avoid sub-triangulation.
3. Use a simple triangulation technique by adding a limited predefined number of points inside the element and on its boundaries and connecting them to form consistent well shaped triangles.
4. A local Delaunay triangulation scheme may always be used as an automatic approach for creation of quadrature sub-triangles.
5. Each sub-triangle is assigned a predefined set of Gauss quadrature points and weights.
6. The integrand and the weight function are computed at the Gauss points.
7. The final solution of the integral is obtained from the summation over all Gauss points within the element.

7.6 SOLVER

7.6.1 XFEM degrees of freedom

One of the complicated aspects of XFEM is the use of different types of degrees of freedom (DOF) that may change by time or by propagation of a crack. As a result, a systematic way of handling the normal degrees of freedom (displacements) and the enrichment degrees of freedom are required. The following remarks should be considered:

1. Different types of degrees of freedom.
    a. Displacements, $\mathbf{u}_j$
    b. Heaviside related DOFs, $\mathbf{a}_k$
    c. Crack tip related DOFs, $\mathbf{b}_k$
2. Different number of DOFs.
3. The number of DOFs may change by time or by crack evolution.
4. Applying the boundary conditions may affect the enriched DOFs.
5. Special techniques such as lumping should be avoided or reformulated for the enrichment DOFs.

7.6.2 Time integration

There are a number of different time integration schemes for a dynamic XFEM analysis. Among them the Newmark method and a simplified explicit approach can be adopted:

1. For a Newmark approach,
    a. The approximation in time takes the following forms:

$$\mathbf{u}_{n+1} = \mathbf{u}_n + \Delta t\,\dot{\mathbf{u}}_n + \frac{\Delta t^2}{2}\ddot{\mathbf{u}}_n + \Delta t^3\left(\beta_n \frac{\ddot{\mathbf{u}}_{n+1} - \ddot{\mathbf{u}}_n}{\Delta t}\right) \tag{7.27}$$

$$\dot{\mathbf{u}}_{n+1} = \dot{\mathbf{u}}_n + \Delta t\,\ddot{\mathbf{u}}_n + \Delta t^2\left(\gamma_n \frac{\ddot{\mathbf{u}}_{n+1} - \ddot{\mathbf{u}}_n}{\Delta t}\right) \tag{7.28}$$

    b. The solution has to be obtained by one of the following assumptions for the stiffness update in nonlinear analyses:
        i. Constant stiffness
        ii. Newton approach
        iii. The modified Newton.
2. In a central difference explicit analysis,
    a. Compute the approximation for any degrees of freedom i:

$$\dot{\mathbf{u}}^i_{n+\frac{1}{2}} = \dot{\mathbf{u}}^i_{n-\frac{1}{2}} + \Delta t\left(m^i\right)^{-1}\left(\mathbf{f}_n^{ext,i} - \mathbf{f}_n^{\text{int},i}\right) \tag{7.29}$$

b. The appropriate lumped mass matrix (6.78) must be used:

$$m^i = \frac{M_0}{n_n}\frac{1}{l_e}\int_{\Omega_e}\psi_i^2 \mathrm{d}\Omega \tag{7.30}$$

3. Alternative techniques such as TFEM and TXFEM can be designed based on sections 6.4.7 and 6.4.8.

7.6.3 Simultaneous equations solver

The solution of the simultaneous equations of the system can be performed by any of the well developed available techniques. The following notes should be considered:

1. The system of equations involves different types of unknowns (DOFs).
2. The symmetry/asymmetry of the system matrices is not changed by the introduction of the enrichment approximations.
3. There is a possibility of ill conditioning if proper enrichments are not adopted in accordance with appropriate domains of influence.

7.6.4 Crack length control

A stable crack path, as discussed in Section 5.2.4, can be associated to a snap-back response. As a result neither the displacement control nor the force control solutions can simulate the whole stable path of crack propagation. Instead, the following simplified crack length control can be used:

1. Apply crack initiation preferences.
2. Compute/update the stiffness matrix of the system. Evaluate new stiffness matrix if the geometry has been changed due to crack propagation.
3. Beginning of the iteration loop.
    a. Solve the system under internal loadings from cohesive crack tractions. The final converged configuration of the system at the previous step can be assumed as a basis for evaluation of crack profile and cohesive forces. The stress state at the crack tip is obtained for this system of internal loading.

$$\mathbf{K}\mathbf{u}^{\mathrm{coh}} = \mathbf{f}^{\mathrm{coh}} \tag{7.31}$$

    b. The system is then solved under the external loading. Again, the stress state is computed at the crack tip.

$$\mathbf{K}\mathbf{u}^{\mathrm{ext}} = \mathbf{f}^{\mathrm{ext}} \tag{7.32}$$

c. The maximum crack tip stress criterion is used to evaluate the external load factor α. As a result, the set of coupled external and internal loadings that satisfy the crack propagation criterion is obtained.

$$\mathbf{Ku} = \alpha \mathbf{f}^{\text{ext}} + \mathbf{f}^{\text{coh}} \tag{7.33}$$

$$\boldsymbol{\sigma} = \alpha \boldsymbol{\sigma}_1 + \boldsymbol{\sigma}_2 \tag{7.34}$$

d. The crack propagation criterion is satisfied if the maximum tensile stress at the crack tip, $\boldsymbol{\sigma}^{\text{tip}}$, reaches to the material tensile strength f_{t}:

$$\boldsymbol{\sigma}^{\text{tip}} = f_{\text{t}} \tag{7.35}$$

4. The convergence is verified by comparing the computed load factors at the present iteration with the previous one.
5. If the crack propagation criterion is satisfied, it is extended along the plane of maximum tensile stress.

7.7 POST-PROCESSING

7.7.1 Stress intensity factor

To determine the stress intensity factor, the interaction integral approach is used to evaluate the *J* integral:

1. An appropriate line contour is set around the crack tip.
2. The finite elements and associated Gauss integration points within the contour area are determined.
3. The appropriate auxiliary field is set according the interaction integral approach. For the case of orthotropic crack analysis, the auxiliary fields defined in Section 4.4.2 have to be used.
4. Numerically evaluate *J* using a conventional Gauss integration rule.
5. Relate the computed *J* to its associated stress intensity factor.

7.7.2 Crack growth

The following steps are followed for each crack tip:

1. Check if the crack is unstable by comparing the computed stress intensity factor with the critical stress intensity factor.
2. Compute the propagation direction.
3. Adopt one of the available rules for crack increment length.

7.7.3 Other applications

Other applications require specific post-processing procedures. For example, multiphase interactions may require post-solution computations to handle further macro- or micro-scale phenomena.

7.8 CONFIGURATION UPDATE

In a standard finite element method, the geometry of a model has to be updated if a crack is initiated or an existing crack is to propagate. In contrast, no remeshing is required in the XFEM simulation of crack propagation.

In an updated Lagrangian formulation of large deformation analysis, however, the converged configuration of the model has to be updated by computed nodal displacements. This is also the case for an XFEM analysis.

The final point is that even in the case of a crack analysis, where no remeshing and geometry update is necessary, XFEM may require an update procedure for handling the database changes associated with evolving cracks and changing DOFs.

References

Adalsteinsson, D. and Sethian, J.A. (2003) Transport and diffusion of material quantities on propagating interfaces via level set methods. *Journal of Computational Physics*, **85 (**1), 271–288.

Aliabadi, M.H. and Sollero, P. (1998) Crack growth analysis in homogeneous orthotropic laminates. *Composites Science and Technology*, **58,** 1697–1703.

Anderson, T. (1995) *Fracture Mechanics: Fundamentals and Applications*, CRC Press, USA.

Areias, P.M.A. and Belytschko, T. (2005a) Non-linear analysis of shells with arbitrary evolving cracks using XFEM. *International Journal for Numerical Methods in Engineering*, **62**, 384–415.

Areias, P.M.A. and Belytschko, T. (2005b) Analysis of three-dimensional crack initiation and propagation using the extended finite element method. *International Journal for Numerical Methods in Engineering*, **63** (55), 760–788.

Areias, P.M.A. and Belytschko, T. (2006) Two-scale shear band evolution by local partition of unity. *International Journal for Numerical Methods in Engineering*, **66**, 878–910.

Areias, P.M.A., Song, J.H. and Belytschko, T. (2006) Analysis of fracture in thin shells by overlapping paired elements. *Computer Methods in Applied Mechanics and Engineering*, **195**, 5343–5360.

Asadpoure, A. (2006) *Analysis of layered composites by the extended finite element method*. MSc thesis, Sharif University of Technology, Tehran, Iran.

Asadpoure, A. and Mohammadi, S. (2007) A new approach to simulate the crack with the extended finite element method in orthotropic media. *International Journal for Numerical Methods in Engineering*, **69**, 2150–2172.

Asadpoure, A., Mohammadi, S. and Vafai, A. (2006) Modeling crack in orthotropic media using a coupled finite element and partition of unity methods. *Finite Elements in Analysis and Design*, **42 (**13), 1165–1175.

Asadpoure, A., Mohammadi and S., Vafai, A. (2007) Crack analysis in orthotropic media using the extended finite element method. *Thin Walled Structures*, **44** (9), 1031–1038.

Atluri, S.N., Kobayashi, A.S. and Nakagaki, M.A. (1975) Finite element program for fracture mechanics analysis of composite material. *Fracture Mechanics of Composites*, ASTM STP, **593,** 86–98.

Atluri, S.N. (1982) Path-independent integrals in finite elasticity and inelasticity, with body forces, inertiam and arbitrary crack-face conditions. *Engineering Fracture Mechanics*, **16** (3), 341–364.

Atluri, S.N. and Shen, S. (2002) *The Meshless Local Petrov–Galerkin (MLPG) Method.* Tech Science Press, USA.

Babuska, I. and Miller, A. (1984) The post-processing approach to finite element method – part II. *International Journal for Numerical Methods in Engineering*, **20**, 1111–1129.

Barnett, D.M. and Asaro, R.J. (1972) The fracture mechanics of slit-like cracks in anisotropic elastic media. *Journal of the Mechanics and Physics of Solids*, **20**, 353–66.

Barrenblatt, G.I. (1959) The formation of equilibrium cracks during brittle fracture: general ideas and hypotheses for axially symmetric cracks. *Journal of Applied Mathematics and Mechanics*, **23**, 622–636.

Barsoum, R. (1974) Application of quadratic isoparametric finite elements in linear fracture mechanics. *International Journal of Fracture*, **10**, 603–605.

Barsoum, R. (1975) Further application of quadratic isoparametric finite elements to linear fracture mechanics of plate bending and general shells. *International Journal of Fracture*, **11**, 167–169.

Barsoum, R. (1976a) On the use of isoparametric finite elements in linear fracture mechanics. *International Journal for Numerical Methods in Engineering*, **10**, 25–37.

Barsoum, R. (1976b) A degenerate solid element for linear fracture analysis of plate bending and general shells. *International Journal for Numerical Methods in Engineering*, **10**, 551–564.

Barsoum, R. (1977) Triangular quarter point elements as elastic and perfectly plastic crack tip elements. *International Journal for Numerical Methods in Engineering*, **11**, 85–98.

Barsoum, R. (1981) An assessment of the quarter-point elements in pressure vessel fracture analysis. *Sixth International Conference on Structural Mechanics in Reactor Technology*, Paris.

Bazant, Z.P. and Planas, J. (1997) *Fracture and Size Effects in Concrete and Other Quasibrittle Materials.* CRC Press, USA.

Béchet, E., Minnebo, H., Moës, N. and Burgardt, B. (2005) Improved implementation and robustness study of the X-FEM for stress analysis around cracks. *International Journal for Numerical Methods in Engineering*, **64**, 1033–1056.

Bellec, J. and Dolbow, J.E. (2003) A note on enrichment functions for modelling crack nucleation. *Communications in Numerical Methods in Engineering*, **19**, 921–932.

Belytschko, T. and Black, T. (1999) Elastic crack growth in finite elements with minimal remeshing. *International Journal of Fracture Mechanics*, **45**, 601–620.

Belytschko, T. and Chen, H. (2004) Singular enrichment finite element method for elastodynamic crack propagation. *International Journal of Computational Methods*, **1** (1), 1–15.

Belytschko, T., Lu, Y.Y. and Gu, L. (1994) Element-free Galerkin methods. *International Journal for Numerical Methods in Engineering*, **37**, 229–256.

Belytschko, T., Krongauz, Y., Organ, D., Fleming, M. and Krysl, P. (1996) Meshless methods: an overview and recent developments. *Computer Methods in Applied Mechanics and Engineering*, **139**, 3–47.

Belytschko, T., Moës, N., Usui, S. and Parimik, C. (2001) Arbitrary discontinuities in finite elements. *International Journal for Numerical Methods in Engineering*, **50**, 993–1013.

Belytschko, T., Daniel, W.J.T. and Ventura, G. (2002a) A monolithic smoothing-gap algorithm for contact-impact based on the signed distance function. *International Journal for Numerical Methods in Engineering*, **55**, 101–125.

Belytschko, T., Xu, J.X., Chessa, J., Moës, N. and Gravouil, A. (2002b) Recent developments in meshless and extended finite element methods. *Second International Conference on Advanced Computational Methods in Engineering*, Eindhoven, The Netherlands.

Belytschko, T., Chen, H., Xu, J. and Zi, G. (2003) Dynamic crack propagation based on loss of hyperbolicity and a new discontinuous enrichment. *International Journal for Numerical Methods in Engineering*, **58**, 1873–1905.

Bogy, D.B. (1972) The plane solution for anisotropic elastic wedges under normal and shear traction. *Journal of Applied Mechanics*, **39**,1103–9.

Bordas, S. and Legay, A. (2005) *X-FEM Mini-Course.* EPFL, Lausanne, Switzerland.

Bordas, S. and Moran, B. (2006) Enriched finite elements and level sets for damage tolerance assessment of complex structures. *Engineering Fracture Mechanics*, **73**, 1176–1201.

de Borst, R., Remmers, J.J.C. and Needleman, A. (2004a) Computational aspects of cohesive-zone models. *Fifteenth European Conference of Fracture*, Sweden.

de Borst, R., Gutiérrez, M.A., Wells, G.N., Remmers, J.J.C. and Askes, H. (2004b) Cohesive-zone models, higher-order continuum theories and reliability methods for computational failure analysis. *International Journal for Numerical Methods in Engineering*, **60**, 289–315.

de Borst, R., Remmers, J.J.C., Needleman A. and Abellan, M.A. (2004c) Discrete vs smeared crack models for concrete fracture: bridging the gap. *International Journal for Numerical and Analytical Methods in Geomechanics*, **28**, 583–607.

Bowie, O.L. and Freese, C.E. (1972) Central crack in plane orthotropic rectangular sheet. *International Journal of Fracture Mechanics*, **8**, 49–58.

Budyn, E., Zi, G., Moës, N. and Belytschko, T. (2004) A method for multiple crack growth in brittle materials without remeshing. *International Journal for Numerical Methods in Engineering*, **61**, 1741–1770.

Carloni, C. and Nobile, L. (2002) Crack initiation behaviour of orthotropic solids as predicted by the strain energy density theory. *Theoretical and Applied Fracture Mechanics*, **38**, 109–119.

Carloni, C., Piva, A. and Viola, E. (2003) An alternative complex variable formulation for an inclined crack in an orthotropic medium. *Engineering Fracture Mechanics*, **70**, 2033–2058.

Carlsson, L.A. and Prasad, S. (1993) Interfacial fracture of sandwich beams. *Engineering Fracture Mechanics*, **44** (4) 581–590.

Carpinteri, A. and Colombo, G. (1989) Numerical analysis of catastrophic softening behaviour (snap-back instability). *Computers and Structures*, **31** (4), 607–636.

Chahine, E., Laborde, P. and Renard, Y. (2006) A quasi-optimal convergence result for fracture mechanics with XFEM. *Academie des Sciences*, Paris, Ser. **I 342**, 527–532.

Chan, S.K., Tuba, I.S. and Wilson, W.K. (1970) On the finite element method in liner fracture mechanics: Finite element method with first order displacement functions to compute crack tip stress intensity factors in various shapes under different loading conditions. *Engineering Fracture Mechanics*, **2**, 1–17.

Chen, T., Minev, P.D. and Nandakumar, K. (2004) A projection scheme for incompressible multiphase flow using adaptive Eulerian grid. *International Journal for Numerical Methods in Fluids*, **45**, 1–19.

Chessa, J. and Belytschko, T. (2003a) An enriched finite element method and level sets for axisymmetric two-phase flow with surface tension. *International Journal for Numerical Methods in Engineering*, **58**, 2041–2064.

Chessa, J. and Belytschko, T. (2003b) An extended finite element method for two-phase fluids. *Transactions of the ASME*, **70**, 10–18.

Chessa, J. and Belytschko, T. (2004) Arbitrary discontinuities in space–time finite elements by level sets and X-FEM. *International Journal for Numerical Methods in Engineering*, **61**, 2595–2614.

Chessa, J. and Belytschko, T. (2006) A local space–time discontinuous finite element method. *Computer Methods in Applied Mechanics and Engineering*, **195**, 1325–1343.

Chessa, J., Smolinski, P. and Belytschko, T. (2002) The extended finite element method (XFEM) for solidification problems. *International Journal for Numerical Methods in Engineering*, **53**, 1959–1977.

Chessa, J., Wang, H. and Belytschko, T. (2003) On the construction of blending elements for local partition of unity enriched finite elements. *International Journal for Numerical Methods in Engineering*, **57**, 1015–1038.

Chopp, D.L. (2001) Some improvements on the fast marching method. *SIAM Journal of Scientific Computations*, **23** (1), 230–244.

Chopp, D.L. and Sukumar, N. (2003) Fatigue crack propagation of multiple coplanar cracks with the coupled extended finite element/fast marching method. *International Journal of Engineering Science*, **41**, 845–869.

Chorin, A. J. (1968) Numerical solution of the Navier–Stokes equation. *Mathematical Computations*, **23**, 745–762.

Chow, W.T. and Atluri, S.N. (1998) Stress intensity factors as the fracture parameters for delamination crack growth in composite laminates. *Computational Mechanics*, **21**, 1–10.

Chowdhury, S.R. and Narasimhan, R. (2000) A cohesive finite element formulation for modeling fracture and delamination in solids. *Saadhana*, **25 (**6), 561–587.

Cottrell, A.H. (1961) Theoretical aspects of radiation damage and brittle fracture in steel pressure vessels. *Iron and Steel Institute Special Report* No. 69, pp. 281–296. Iron and Steel Institute, London, UK.

Cruse, T. (1988) *Boundary Element Analysis in Computational Fracture Mechanics*. Kluwer, Dordrecht, The Netherlands.

Daux, C., Moës, N., Dolbow, J., Sukumark, N. and Belytschko, T. (2000) Arbitrary branched and intersecting cracks with the extended finite element method. *International Journal for Numerical Methods in Engineering*, **48**, 1741–1760.

Dolbow, J.E. (1999) *An extended finite element method with discontinuous enrichment for applied mechanics.* PhD dissertation, Theoretical and Applied Mechanics, Northwestern University, USA.

Dolbow, J.E. and Nadeau, J.C. (2002) On the use of effective properties for the fracture analysis of microstructured materials. *Engineering Fracture Mechanics*, **69**, 1607–1634.

Dolbow, J.E. and Gosz, M. (2002) On the computation of mixed-mode stress intensity factors in functionally graded materials. *International Journal of Solids and Structures*, **39**, 2557–2574.

Dolbow, J.E. and Devan, A. (2004) Enrichment of enhanced assumed strain approximations for representing strong discontinuities: addressing volumetric incompressibility and the discontinuous patch test. *International Journal for Numerical Methods in Engineering*, **59**, 47–67.

Dolbow, J., Moës, N. and Belytschko, T. (2000a) Discontinuous enrichment in finite elements with a partition of unity method. *Finite Elements in Analysis and Design*, **36**, 235–260.

Dolbow, J., Moës, N. and Belytschko, T. (2000b) Modeling fracture in Mindlin–Reissner plates with the extended finite element method. *International Journal of Solids and Structures*, **37**, 7161–7183.

Dolbow, J., Moës, N. and Belytschko, T. (2000c) An extended finite element method for modeling crack growth with frictional contact. *Finite Elements in Analysis and Design*, **36** (3) 235–260.

Dolbow, J., Moës, N. and Belytschko, T. (2001) An extended finite element method for modeling crack growth with frictional contact. *Computer Methods in Applied Mechanics and Engineering*, **190**, 6825–6846.

Dolbow, J., Fried, E. and Ji, H. (2004) Chemically induced swelling of hydrogels. *Journal of the Mechanics and Physics of Solids*, **52**, 51–84.

Dolbow, J., Fried, E. and Ji, H. (2005) A numerical strategy for investigating the kinetic response of stimulus-responsive hydrogels. *Computer Methods in Applied Mechanics and Engineering*, **194**, 4447–4480.

Duarte, C.A. and Oden, J.T. (1995) Hp clouds – a meshless method to solve boundary-value problems. *TICAM Report* 95-05.

Duarte, C.A. and Oden, J.T. (1996) An H-p adaptive method using clouds. *Computer Methods in Applied Mechanics and Engineering*, **139**, 237–262.

Dugdale, D. (1960) Yielding of steel sheets containing slits. *Journal of Mechanics and Physics of Solids*, **8**, 100–108.

Dumstorff, P. and Meschke, G. (2003) Finite element modelling of cracks based on the partition of unity method. *Proceedings of Applied Mathematics and Mechanics (PAMM)*, **2**, 226–227.

Ebrahimi, S.H. (2007) *Extended finite element analysis of cracking with frictional contact.* MSc thesis, University of Tehran, Tehran, Iran.

Elguedj, T., Gravouil, A. and Combescure, A. (2006) Appropriate extended functions for X-FEM simulation of plastic fracture mechanics. *Computer Methods in Applied Mechanics and Engineering*, **195**, 501–515.

Erdogan, F. and Sih, G.C. (1963) On the crack extension in plates under plane loading and transverse shear. *Journal of Basic Engineering*, **85**, 519–527.

Eshelby, J.D. (1956) The continuum theory of lattice defects. In: *Solid State Physics*, Vol. 3, (eds F. Seitz and D. Turnbull), pp. 79–141, Academic Press, New York.

Eshelby, J.D. (1974) Calculation of energy release rate. In: *Prospect of Fracture Mechanics,* pp. 69–84, Nordhoff, UK.

Evans, R.H. and Marathe, M.S. (1968) Microcracking and stress–strain curves for concrete in tension. *Materials and Structures Research and Testing*, **1** (1), 61–64.

Fagerström, M. and Larsson, R. (2006) Theory and numerics for finite deformation fracture modelling using strong discontinuities. *International Journal for Numerical Methods in Engineering*, **66**, 911–948.

Fawkes, A., Owen, D.R.J. and Luxmoore, A. (1979) An assessment of crack tip singularity models for use with isoparamtreic elements. *Engineering Fracture Mechanics*, **11**, 143–159.

Ferrie, E., Buffiere, J.Y., Ludwig, W., Gravouil, A. and Edwards, L. (2006) Fatigue crack propagation: In situ visualization using X-ray microtomography and 3D simulation using the extended finite element method. *Acta Materialia*, **54**, 1111–1122.

Fish, J. and Yuan, Z. (2005) Multiscale enrichment based on partition of unity. *International Journal for Numerical Methods in Engineering*, **62**, 1341–1359.

Forghani, A. (2005) *Application of the extended finite element method for modeling cohesive crack problems.* MSc thesis, Sharif University of Technology, Tehran, Iran.

Fries, T.P. and Belytschko, T. (2006) The intrinsic XFEM: a method for arbitrary discontinuities without additional unknowns. *International Journal for Numerical Methods in Engineering*, **68** (13) 1358–1385.

Gao, H. and Klein, P. (1998) Numerical simulation of crack growth in an isotropic solid with randomized internal cohesive bonds. *Journal of the Mechanics and Physics of Solids*, **42** (6), 187–218.

Gravouil, A., Moës, N. and Belytschko, T. (2002) Non-planar 3D crack growth by the extended finite element and level sets–Part II: Level set update. *International Journal for Numerical Methods in Engineering*, **53**, 2569–2586.

Griffith, A.A. (1921) The phenomena of rupture and flow in solids. *Philosophical Transactions of the Royal Society A: Mathematical, Physical and Engineering*, **221**, 163–197.

Griffith, A.A. (1924) The theory of rupture. *Proceedings of International Congress on Applied Mechanics*, Delft, pp. 55–62.

Gtoudos, E. (1993) *Fracture Mechanics: An Introduction*. Kluwer Academic Press, The Netherlands.

Guidault, P.A., Allix, O., Champaney, L. and Navarro, J.P. (2004) A micro-macro approach for crack propagation with local enrichment. In: *Proceedings of the Seventh International Conference on Computational Structures Technology*, (eds B.H.V. Toppings and C.A. Mota Soares), Paper 199, Civil-Comp Press, Scotland.

Gutierrez, L.M.G. and Bermejo, R. (2005) A semi-Lagrangian level set method for incompressible Navier–Stokes equations with free surface. *International Journal for Numerical Methods in Fluids*, **49**, 1111–1146.

Haidar, K., Dube, J.F. and Pijaudier-Cabot, G. (2003) Modelling crack propagation in concrete structures with a two scale approach. *International Journal for Numerical and Analytical Methods in Geomechanics*, **27**, 1187–1205.

Hellen, T.K. and Blackburn, W.S. (1975) The calculation of stress intensity factors for combined tensile and shear loading. *International Journal of Fracture*, **11** (4), 605–617.

Henshell, R.D. and Shaw, K.G. (1975) Crack tip elements are unnecessary. *International Journal of Numerical Methods in Engineering*, **9** (3), 495–509.

Hettich, T. and Ramm, E. (2006) Interface material failure modeled by the extended finite-element method and level sets. *Computer Methods in Applied Mechanics and Engineering*, **195**, 4753–4767.

Hibbit, H. (1977) Some properties of singular isoparametric elements. *International Journal for Numerical Methods in Engineering*, **11**, 180–184.

Hillerborg, A., Modeer, M. and Peterson, P.E. (1976) Analysis of crack formation and crack growth in concrete by means of fracture mechanics and finite elements. *Cement and Concrete Research*, **6**, 733–782.

Hirari, I., Uchiyama, Y., Mizuta, Y. and Pilkey, W.D. (1985) An exact zooming method. *Finite Elements in Analysis and Design*, **1**, 61–69.

Hong, S. and Kim, K.S. (2003) Extraction of cohesive-zone laws from elastic far-fields of a cohesive crack tip: a field projection method. *Journal of the Mechanics and Physics of Solid*s, **51,** 1267–1286.

Huang, R., Sukumar, N. and Prevost, J.H. (2003) Modeling quasi-static crack growth with the extended finite element method, Part II: Numerical applications. *International Journal of Solids and Structures*, **40**, 7539–7552.

Hussain, M., Pu, S. and Underwood, J. (1974) Strain energy release rate for a crack under combined mode I and mode II. *ASTM, STP*, **560**, 2–28.

Hutchinson, J. (1968) Singular behavior at the end of a tensile crack tip in a power-law hardening material. *Journal of Mechanics and Physics of Solids*, **16**, 13–31.

Hutchinson, J. (1990) Mixed mode cracking in layered materials. *Advances in Applied Mechanics*, **29**, 63–191.

Hutchinson, J.W. and Sue, Z. (1992) Mixed mode cracking in layered materials. In: *Advances in Applied Mechanics*, Vol. 29, (eds J.W. Hutchinson and T.Y. Wu), pp. 63–191. Academic Press, Orlando, USA.

Inglis, C.E. (1913) Stresses in a plate due to the presence of cracks and sharp corners. *Transactions of Institute of Naval Architects*, **55**, 219–241.

Irwin, G.R. (1957) Analysis of stresses and strains near the end of a crack transversing a plate. *Journal of Applied Mechanics, Transactions ASME*, **24**, 361–364.

Irwin, G.R. (1958) Fracture. In: *Handbuch der Physik*, Vol. **6**, (ed. Flugge), pp. 551–590. Springer-Verlag, Berlin, Germany.

Irwin, G.R. (1960) Plastic zone near a crack tip and fracture toughness. *Proceedings of the 7th Sagamore Conference*, New York, USA, p. 63.

Irwin, G.R., Kies, G.A. and Smith, H.L. (1958) Fracture strength relative to the onset and arrest of crack propagation. *Proceedings of ASTM*, **58**, 640–657.

Ishikawa, H. (1980) A finite element analysis of stress intensity factors for combined tensile and shear loading by only a virtual crack extension. *International Journal of Fracture* **16**, (5) 243–246.

Jernkvist, L.O. (2001) Fracture of wood under mixed mode loading II, Experimental investigation of Picea abies. *Engineering Fracture Mechanics*, **68**, 565–576.

Ji, H. and Dolbow, J.E. (2004) On strategies for enforcing interfacial constraints and evaluating jump conditions with the extended finite element method. *International Journal for Numerical Methods in Engineering*, **61**, 2508–2535.

Ji, H., Chopp, D. and Dolbow, J.E. (2002) A hybrid extended finite element-level set method for modeling phase transformations. *International Journal for Numerical Methods in Engineering*, **54**, 1209–1233.

Ji, H., Mourad, H., Fried, E. and Dolbow, J. (2006) Kinetics of thermally induced swelling of hydrogels. *International Journal of Solids and Structures*, **43**, 1878–1907.

Jirásek, M. (2002) Numerical modeling of strong discontinuities. *Revue Française de Génie Civil*, **6** (6).

Jirásek, M. and Zimmermann, T. (2001a) Embedded crack model. Part I: Basic formulation. *International Journal for Numerical Methods in Engineering*, **50**, 1269–1290.

Jirásek, M. and Zimmermann, T. (2001b) Embedded crack model. Part II: Combination with smeared cracks. *International Journal for Numerical Methods in Engineering*, **50**, 1291–1305.

Kanninen, M. (1984) Application of fracture mechanics to fiber composite materials and adhesive joint, a review. *Third International Conference on Numerical Methods in Fracture Mechanics*, Swansea, UK.

Karihaloo, B.L. and Xiao, Q.Z. (2003) Modelling of stationary and growing cracks in FE framework without remeshing: a state-of-the-art review. *Computers and Structures*, **81**, 119–129.

Karlsson, A. and Backlund, J. (1978) J-integral at loaded crack surfaces. *International Journal of Fracture*, **14** (6), R311–R314.

Khoei, A.R. and Nikbakht, M. (2006) Contact friction modeling with the extended finite element method (X-FEM). *Journal of Materials Processing Technology*, **177**, 58–62.

Khoei, A.R., Shamloo, A. and Azami, A.R. (2006a) Extended finite element method in plasticity forming of powder compaction with contact friction. *International Journal of Solids and Structures*, **43** (18–19), 5421–5448.

Khoei, A.R., Shamloo, A., Anahid, M. and Shahim, K. (2006b) The extended finite element method (X-FEM) for powder forming problems. *Journal of Materials Processing Technology*, **177**, 53–57.

Kim, J.H. and Paulino, G.H. (2002) Mixed-mode fracture of orthotropic functionally graded materials using finite elements and the modified crack closure method. *Engineering Fracture Mechanics*, **69**, 1557–1586.

Kim, J.H. and Paulino, G.H. (2003) The interaction integral for fracture of orthotropic functionally graded materials: evaluation of stress intensity factors. *International Journal of Solids and Structures*, **40**, 3967–4001.

Kolke, A., Walhorn, E., Hubner, B. and Dinkler, D. (2003) Numerical modeling of fluid-structure interaction with free surface flows. *Proceedings of Applied Mathematics and Mechanics (PAMM)*, **3**, 412–413.

Kuo, M.C. and Bogy, D.B. (1974) Plane solutions for the displacement and traction-displacement problem for anisotropic elastic wedges. *Journal of Applied Mechanics*, **41**, 197–203.

Laborde, P., Pommier, J., Renard, Y. and Salaün, M. (2005) High-order extended finite element method for cracked domains. *International Journal for Numerical Methods in Engineering*, **64**, 354–381.

Larsson, R. and Fagerström, M. (2005) A framework for fracture modelling based on the material forces concept with XFEM kinematics. *International Journal for Numerical Methods in Engineering*, **62**, 1763–1788.

Lee, S.H., Song, J.H., Yoon, Y.C., Zi, G. and Belytschko, T. (2004) Combined extended and superimposed finite element method for cracks. *International Journal for Numerical Methods in Engineering*, **59**, 1119–1136.

Legay, A., Wang, H.W. and Belytschko, T. (2005) Strong and weak arbitrary discontinuities in spectral finite elements. *International Journal for Numerical Methods in Engineering*, **64**, 991–1008.

Legrain, G., Moës, N. and Verron, E. (2005) Stress analysis around crack tips in finite strain problems using the extended finite element method. *International Journal for Numerical Methods in Engineering*, **63**, 290–314.

Lekhnitskii, S.G. (1968) *Anisotropic Plates*. Gordon and Breach Science Publishers, New York, USA.

Li, F.Z., Shih, C.F. and Needleman, A. (1985) A comparison of methods for calculating energy release rates. *Engineering Fracture Mechanics*, **21** (2), 405–421.

Lim, W.K., Choi, S.Y. and Sankar, B.V. (2001) Biaxial load effects on crack extension in anisotropic solids. *Engineering Fracture Mechanics*, **68**, 403–416.

Lin, C.L., Lee, H., Lee, T. and Weber, L.J. (2005) A level set characteristic Galerkin finite element method for free surface flows. *International Journal for Numerical Methods in Fluids*, **49**, 521–547.

Liu, W.K., Chen, Y., Jun, S., Chen, J.S., Belytschko, T., Pan, C., Uras, R.A. and Chang, C.T. (1996) Overview and applications of the reproducing kernel particle methods. *Archives of Computational Methods in Engineering*; State of the Art Reviews, **3**, 3–80.

Liu, X.Y., Xiao, Q.Z. and Karihaloo, B.L. (2004) XFEM for direct evaluation of mixed mode SIFs in homogeneous and bi-materials. *International Journal for Numerical Methods in Engineering*, **59**, 1103–1118.

Macneal, R.H. (1994) *Finite Elements: Their Design and Performance.* Marcell Dekker, Inc., USA.

Mariani, S. and Perego, U. (2003) Extended finite element method for quasi-brittle fracture. *International Journal for Numerical Methods in Engineering*, **58**, 103–126.

Mariano, P.M. and Stazi, F.L. (2004) Strain localization due to crack–microcrack interactions: X-FEM for a multifield approach. *Computer Methods in Applied Mechanics and Engineering*, **193**, 5035–5062.

Meguid, S.A. (1989) *Engineering Fracture Mechanics.* Elsevier Applied Science, UK.

Melenk, J.M. and Babuska, I. (1996) The Partition of Unity Finite Element Method: Basic Theory and Applications. *Seminar fur Angewandte Mathematik, Eidgenossische Technische Hochschule,* Research Report No. 96-01, January, CH-8092 Zurich, Switzerland.

Menouillard, T., Réthoré, J., Combescure A. and Bung, H. (2006) Efficient explicit time stepping for the extended finite element method (X-FEM). *International Journal for Numerical Methods in Engineering*, **68** (9) 911–939.

Mergheim, J., Kuh, E. and Steinmann, P. (2005) A finite element method for the computational modelling of cohesive cracks. *International Journal for Numerical Methods in Engineering*, **63**, 276–289.

Mergheim, J., Kuh, E. and Steinmann, P. (2006) Towards the algorithmic treatment of 3D strong discontinuities. *Communications in Numerical Methods in Engineering*, **23** (2) 97–108.

Moës, N. and Belytschko, T. (2002a) Extended finite element method for cohesive crack growth. *Engineering Fracture Mechanics*, **69**, 813–833.

Moës, N. and Belytschko, T. (2002b) X-FEM: De nouvelles frontières pour les éléments finis. *Revue Européenne des Éléments Finis*, **11**, 305–318.

Moës, N., Dolbow, J. and Belytschko, T. (1999) A finite element method for crack growth without remeshing. *International Journal for Numerical Methods in Engineering*, **46**, 131–150.

Moës, N., Gravouil, A. and Belytschko, T. (2002) Non-planar 3D crack growth by the extended finite element and level sets–Part I: Mechanical model. *International Journal for Numerical Methods in Engineering*, **53**, 2549–2568.

Moës, N., Cloirec, M., Cartraud, P. and Remacle, J.F. (2003) A computational approach to handle complex microstructure geometries. *Computer Methods in Applied Mechanics and Engineering*, **192**, 3163–3177.

Moës, N., Béchet, E. and Tourbier, M. (2006) Imposing Dirichlet boundary conditions in the extended finite element method. *International Journal for Numerical Methods in Engineering*, **67** (12), 1641–1669.

Mohammadi, S. (2003) *Discontinuum Mechanics by Combined Finite/Discrete Elements*. WIT Press, UK.

Mohammadi, S. and Asadpoure, A. (2006) A novel approach to analyze a crack with XFEM in composite meida. *International Conference on Computational Methods in Engineering* (ICOME), Hefei, China.

Muskelishvili, N.I. (1953) *Some Basic Problems on the Mathematical Theory of Elasticity*. Translated by J.R.M. Radok, Noordhoof, Groningen, The Netherlands.

Nagashima, T. and Suemasu, H. (2004) Application of extended finite element method to fracture of composite materials. *European Congress on Computational Methods in Applied Sciences and Engineering* (ECCOMAS), Jyväskylä, Finland.

Nagashima, T., Omoto, Y. and Tani, S. (2003) Stress intensity factor analysis of interface cracks using X-FEM. *International Journal for Numerical Methods in Engineering*, **56**, 1151–1173.

Nikbakht, M. (2005) *Application of the extended finite element method for numerical simulation of contact problems*. MSc thesis, Sharif University of Technology, Tehran, Iran.

Nobile, L. and Carloni, C. (2005) Fracture analysis for orthotropic cracked plates. *Composite Structures*, **68** (33) 285–293.

Oliver, J., Huespe, A.E., Pulido, M.D.G. and Samaniego, E. (2003) On the strong discontinuity approach in finite deformation settings. *International Journal for Numerical Methods in Engineering*, **56**, 1051–1082.

Onate, E., Idelsohn, S., Fischer, T. and Zienkiewicz, O.C. (1995) A finite point method for analysis of fluid flow problems. *Ninth International Conference on Finite Elements in Fluids*, Venice, Italy, pp. 15–21.

Osher, S. and Sethian, J.A. (1988) Fronts propagating with curvature-dependent speed: algorithms based on Hamilton–Jacobi formulations. *Journal of Computational Physics*, **79** (1), 12–49.

Owen, D.R.J. and Hinton, E. (1980) *Finite Elements in Plasticity: Theory and Practice.* Pineridge Press Ltd, Swansea, UK.

Owen, D.R.J. and Fawkes, A. (1983) *Engineering Fracture Mechanics: Numerical Methods and Applications*. Pineridge Press Ltd, Swansea, UK.

Parks, D. (1974) A stiffness derivative finite element technique for determination of crack tip stress intensity factors. *International Journal of Fracture*, **10** (4) 487–502.

Patrikalakis, N.M. (2003) *Computational Geometry*. Lecture Notes, Massachusetts Institute of Technology, USA.

Patzak, B. and Jirásek, M. (2003) Process zone resolution by extended finite elements. *Engineering Fracture Mechanics*, **70**, 957–977.

Peerlings, R.H.J., de Borst, R., Brekelmans, W.A.M. and Geers, M.G.D. (2002) Localisation issues in local and nonlocal continuum approaches to fracture. *European Journal of Mechanics – A: Solids*, **21**, 175–189.

Peters, M. and Hack, K. (2005) Numerical aspects of the extended finite element method. *Proceedings of Applied Mathematics and Mechanics*, **5**, 355–356.

Peters, M., Hoppe, U. and Hack, K. (2004) Simulation of crack–propagation using embedded discontinuities. *Proceedings of Applied Mathematics and Mechanics (PAMM)*, **4**, 366–367.

Piva, A., Viola, E. and Tornabene, F. (2005) Crack propagation in an orthotropic medium with coupled elastodynamic properties. *Mechanics Research Communications*, **32**, 153–159.

Qu, J. and Bassani, J.L. (1993) Interfacial fracture mechanics for anisotropic biomaterials, *Journal of Applied Mechanics*, **60**, 422–431.

Rabczuk, T. and Wall, W.A. (2006) Extended finite element and meshfree methods. Technical University of Munich, Germany, WS200/2007.

Remmers, J.J.C., Wells, G.N. and de Borst, R. (2003) A solid-like shell element allowing for arbitrary delaminations. *International Journal for Numerical Methods in Engineering*, **58**, 2013–2040.

Réthoré, J., Gravouil, A. and Combescure, A. (2005a) An energy-conserving scheme for dynamic crack growth using the extended finite element method. *International Journal for Numerical Methods in Engineering*, **63**, 631–659.

Réthoré, J., Gravouil, A. and Combescure, A. (2005b) A combined space–time extended finite element method. *International Journal for Numerical Methods in Engineering*, **64**, 260–284.

Rice, J.R. (1968) Path-independent integral and the approximate analysis of strain concentration by notches and cracks. *Journal of Applied Mechanics, Transactions ASME*, **35** (2), 379–386.

Rice, J.R. (1988) Elastic fracture mechanics concepts for interfacial cracks. *Journal of Applied Mechanics, Transactions ASME*, **55**, 98–103.

Rice, J.R. and Rosengren, G.F. (1968) Plane strain deformation near a crack tip in a power-law hardening material. *Journal of Mechanics and Physics of Solids*, **16**, 1–12.

Rice, J.R. and Levy, N. (1972) The part-through surface crack in an elastic plate. *Journal of Applied Mechanics, Transactions ASME*, **39**, 185–194.

Sadeghirad, A. and Mohammadi, S. (2007) Equilibrium on the line method (ELM) for imposition of Neumann boundary conditions in the finite point method (FPM). *International Journal for Numerical Methods in Engineering*, **69**, 60–86.

Saleh, A.L. and Aliabadi, M.A. (1995) Crack growth analysis in concrete using boundary element method. *Engineering Fracture Mechanics*, **51**, 533–545.

Samaniego, E. and Belytschko, T. (2005) Continuum–discontinuum modelling of shear bands. *International Journal for Numerical Methods in Engineering*, **62**, 1857–1872.

Saouma, V.E. (2000) *Fracture mechanics*. Lecture notes CVEN-6831, Univesity of Colorado, USA.

Saouma, V.E., Ayari, M. and Leavell, D. (1987) Mixed mode crack propagation in homogeneous anisotropic solids. *Engineering Fracture Mechanics*, **27** (2), 171–184.

Sethian, J.A. (1987) Numerical methods for propagating fronts. In: *Variational Methods for Free Surface Interfaces*, (eds P. Concus and R. Finn), pp. 155–164. Springer, New York, USA.

Sethian, J.A. (1996) A marching level set method for monotonically advancing fronts. *Proceedings of National Academy of Science*, **93** (4), 1591–1595.

Sethian, J.A. (1999a) Fast marching methods. *SIAM Review*, **41** (2), 199–235.

Sethian, J.A. (1999b) Level set methods and fast marching methods: evolving interfaces. *Computational Geometry Fluid Mechanics Computer Vision and Materials Science*. Cambridge University Press, Cambridge, UK.

Sethian, J.A. (2001) Evolution, implementation, and application of level set and fast marching methods for advancing fronts. *Journal of Computational Physic*s, **169** (2), 503–555.

Sethian, J.A. (2006) *Moving interfaces and boundaries: level set methods and fast marching methods*. http://math.berkeley.edu/~sethian/Explanations/level_set_explain.html.

Sethian, J.A. and Wilkening, J. (2004) A numerical model of stress driven grain boundary diffusion. *Journal of Computational Physics*, **193** (1), 275–305.

Sha, G. (1984) On the virtual crack extension technique for stress intensity factors and energy release rate calculation for mixed fracture modes. *International Journal of Fracture*, **25** (2) 33–42.

Shamloo, A., Azami, A.R. and Khoei, A.R. (2005) Modeling of pressure-sensitive materials using a cap plasticity theory in extended finite element method. *Journal of Materials Processing Technology*, **164–165**, 1248–1257.

Sharifabadi, H. (1990) *Theory of Elasticity*. Lecture Notes, University of Tehran, Iran.

Shih, C., de Lorenzi, H. and German, M. (1976) Crack extension modelling with singular quadratic isoparametric elements. *International Journal of Fracture*, **12**, 647–651.

Sih, G.C. (1973) *Handbook of Stress Intensity Factors for Researchers and Engineers.* Lehigh University, Bethlehem, PA, USA.

Sih, G.C. (1974) Strain energy density factors applied to mixed mode crack problems. *International Journal of Fracture*, **10**, 305–321.

Sih, G.C., Paris, P. and Irwin, G. (1965) On cracks in rectilinearly anisotropic bodies. *International Journal of Fracture Mechanics*, **1** (3) 189–203.

Song, J.H., Areias, P.M.A. and Belytschko, T. (2006) A method for dynamic crack and shear band propagation with phantom nodes. *International Journal for Numerical Methods in Engineering*, **67**, 868–893.

Stazi, F.L., Budyn, E., Chessa, J. and Belytschko, T. (2003) An extended finite element method with higher-order elements for curved cracks. *Computational Mechanics*, **31**, 38–48.

Stolarska, M. and Chopp, D.L. (2003) Modeling thermal fatigue cracking in integrated circuits by level sets and the extended finite element method. *International Journal of Engineering Science*, **41**, 2381–2410.

Stolarska, M., Chopp, D.L., Moës, N. and Belytschko, T. (2001) Modelling crack growth by level sets in the extended finite element method. *International Journal for Numerical Methods in Engineering*, **51**, 943–960.

Sukumar, N. and Prevost, J.H. (2003) Modeling quasi-static crack growth with the extended finite element method, Part I: Computer implementation. *International Journal of Solids and Structures*, **40**, 7513–7537.

Sukumar, N., Moës, N., Moran, B. and Belytschko, T. (2000) Extended finite element method for three-dimensional crack modeling. *International Journal for Numerical Methods in Engineering*, **48**, 1549–1570.

Sukumar, N., Chopp, D.L., Moës, N. and Belytschko, T. (2001) Modeling holes and inclusions by level sets in the extended finite-element method. *Computer Methods in Applied Mechanics and Engineering*, **190**, 6183–6200.

Sukumar, N., Chopp, D.L. and Moran, B. (2003a) Extended finite element method and fast marching method for three-dimensional fatigue crack propagation. *Engineering Fracture Mechanics*, **70**, 29–48.

Sukumar, N., Srolovitz, D.J., Baker, T.J. and Prevost, J.H. (2003b) Brittle fracture in polycrystalline microstructures with the extended finite element method. *International Journal for Numerical Methods in Engineering*, **56**, 2015–2037.

Sukumar, N., Huang, Z., Prevost, J.H. and Suo, Z. (2004) Partition of unity enrichment for bimaterial interface cracks. *International Journal for Numerical Methods in Engineering*, **59**, 1075–1102.

Swenson, D. and Ingraffea, A. (1988) Modeling mixed mode dynamic crack propagation using finite elements: Theory and applications. *Computational Mechanics*, **3**, 381–397.

Tupholme, G.E. (1974) A study of cracks in orthotropic crystals using dislocations layers. *Journal of Engineering and Mathematics*, **8**, 57–69.

Tvergaard, V. and Hutchinson, J. (1992) The relation between crack growth resistance and fracture process parameters in elastic-plastic solids. *Journal of Mechanics and Physics of Solids*, **40** (6) 1377–1397.

Ventura, G. (2006) On the elimination of quadrature subcells for discontinuous functions in the extended finite-element method. *International Journal for Numerical Methods in Engineering*, **66**, 761–795.

Ventura, G., Budyn, E. and Belytschko, T. (2003) Vector level sets for description of propagating cracks in finite elements. *International Journal for Numerical Methods in Engineering*, **58**, 1571–1592.

Ventura, G., Moran, B. and Belytschko, T. (2005) Dislocations by partition of unity. *International Journal for Numerical Methods in Engineering*, **62**, 1463–1487.

Viola, A., Piva, A. and Radi, E. (1989) Crack propagation in an orthotropic medium under general loading. *Engineering Fracture Mechanics*, **34** (5), 1155–1174.

Wagner, G.J., Moës, N., Liu, W.K. and Belytschko, T. (2001) The extended finite element method for rigid particles in Stokes flow. *International Journal for Numerical Methods in Engineering*, **51**, 293–313.

Wagner, G.J., Ghosal, S. and Liu, W.K. (2003) Particulate flow simulations using lubrication theory solution enrichment. *International Journal for Numerical Methods in Engineering*, **56**, 1261–1289.

Wang, S.S., Yau, J.F. and Corten, H.T. (1980) A mixed mode crack analysis of rectilinear anisotropic solids using conservation laws of elasticity. *International Journal of Fracture*, **16**, 247–259.

Wang, X. and Zhong, Z. (2003) A cracked sliding interface between anisotropic bimaterials. *Mechanics Research Communications*, **30**, 387–393.

Wells, A. (1963) *Application of fracture mechanics at and beyond general yielding*. British Welding Research Association, Report M13, UK.

Wells, G.N. and Sluys, L.J. (2001) A new method for modeling cohesive cracks using finite elements. *International Journal for Numerical Methods in Engineering*, **50**, 2667–2682.

Westergaard, H. (1939) Bearing pressures and cracks. *ASME Journal of Applied Mechanics*, **6**, 49–53.

Whittaker, B.N. and Singh, R.N. (1992) *Rock Fracture Mechanics, Principles, Design and Applications*. Elsevier, The Netherlands.

Williams, M.L. (1952) Stress singularities resulting from various boundary conditions in angular corners of plates in extension. *Journal of Applied Mechanics, Transactions ASME*, **19**, 526–528.

Willis, J.R. (1967) A comparison of the fracture criteria of Griffith and Barenblatt. *Journal of Mechanics and Physics of Solids*, **15**, 151–162.

Wood, W.L. (1984) A further look at Newmark, Houbolt, etc., time-stepping formulae. *International Journal for Numerical Methods in Engineering*, **20**, 1009–1017.

Wriggers, P. (2002) *Computational Contact Mechanics*. John Wiley and Sons, UK.

Wunk, M.P. (1974) Quasi-static extension of a tensile crack contained in a viscoelastic-plastic solid. *Journal of Applied Mechanics*, **41**, 234–242.

Xiao, Q.Z. and Karihaloo, B.L. (2006) Improving the accuracy of XFEM crack tip fields using higher order quadrature and statically admissible stress recovery. *International Journal for Numerical Methods in Engineering*, **66**, 1378–1410.

Xu, J. (2005) *Meshfree methods and extended finite element methods for arbitrary discontinuities*. PhD dissertation, Theoretical and Applied Mechanics, Northwestern University, USA.

Ying, L. (1982) A note on the singularity and the strain energy of singular elements. *International Journal for Numerical Methods in Engineering*, **18**, 31–39.

Zabaras, N., Ganapathysubramanian, B. and Tan, L. (2006) Modelling dendritic solidification with melt convection using the extended finite element method. *Journal of Computational Physics*, **218** (1), 200–227.

Zi, G. and Belytschko, T. (2003) New crack-tip elements for XFEM and applications to cohesive cracks. I*nternational Journal for Numerical Methods in Engineering*, **57**, 2221–2240.

Zi, G., Song, J.H., Budyn, E., Lee, S.H. and Belytschko, T. (2004) A method for growing multiple cracks without remeshing and its application to fatigue crack growth. *Modeling and Simulations for Matererial Science and Engineering*, **12**, 901–915.

Zi, G., Chen, H., Xu, J. and Belytschko, T. (2005) The extended finite element method for dynamic fractures. *Shock and Vibration*, **12**, 9–23.

Zienkiewicz, O.C. (1977) A new look at Newmark, Houbolt and other time stepping formulae, a weighted residual approach. *Earthquake Engineering and Structural Dynamics*, **5**, 413–418.

Zienkiewicz, O.C. and Codina, R. (1995) A general algorithm for compressible and incompressible flow, Part I. The split characteristic based scheme. *International Journal for Numerical Methods in Fluids*, **20**, 869–885.

Zienkiewicz, O.C., Taylor, R.L. and Zhu, J.Z. (2005) *The Finite Element Method*, 6th edn. Elsevier, USA.

Author Index

E

F

G

H

I

J

K

L

M

N

O

P

Q

R

S

T

U

V

W

X

Y

Z

Subject Index

D

E

F

G

H

I

J

K

L

M

N

O

P

Q

R

S

T

U

V

W

X

Y

Z